

**Optimising the Use and Assessing  
the Value of Intraoperative Shear  
Wave Elastography in  
Neurosurgery**

A thesis submitted to University College London

for the degree of

Doctor of Philosophy in Physics and Neurosurgery

by

**Huan Wee Chan**

*Department of Clinical Neuroscience (Hampstead Campus)*

*UCL Institute of Neurology*

*Queen Square, London WC1N 3BG, United Kingdom*

September 2016

## **Author's declaration**

I declare that I performed the work in this thesis at Great Ormond Street Hospital, the National Hospital for Neurology and Neurosurgery, and the Institute of Cancer Research from 3rd August 2011 to 4<sup>th</sup> August 2014, unless otherwise stated. Where information has been derived from other sources, I confirm that this has been indicated in the thesis.

*Huan Wee Chan*

# Abstract

The clinical outcomes for epilepsy and brain tumour surgery depend on the extent of resection. Neurosurgeons frequently rely on subjective assessment of stiffness and adherence to achieve maximal resection. However, due to similarity in tactile texture and visual appearance of these lesions to normal brain, this can lead to inadequate resection. Magnetic resonance imaging (MRI) has not completely solved this problem for various reasons, including the existence of MRI-negative lesions.

Shear wave elastography (SWE) is an ultrasound-based quantitative elasticity imaging technique that provides an objective assessment of stiffness, which has not previously been applied intraoperatively during neurosurgery. This thesis describes the optimisation and assessment of implementing intraoperative SWE in neurosurgery.

The aims of the work described in this thesis were to validate SWE measurements; to optimise intraoperative applications by investigating the artefacts of SWE; to evaluate SWE performance in detecting epileptogenic lesions, residual tumour and slippery boundaries; and to determine the histopathological correlation with SWE measurements.

Using gelatine phantoms and post-mortem mouse brains, SWE measurements were validated. Through phantom models and *ex vivo* porcine brains and spinal cords, the factors affecting SWE measurements were established and SWE settings optimised. In addition, novel features of slippery tumour-brain interface were demonstrated *in vitro* and confirmed intraoperatively.

Clinical implementation of SWE in epilepsy (38 patients) and brain tumour surgery (34 patients), demonstrated SWE's capability in differentiating epileptogenic lesions ( $p < 0.001$ ) and brain tumours ( $p = 0.003$ ) from normal brain. SWE was shown to be superior to MRI in detecting epileptogenic lesions ( $p = 0.001$ ), in particular MRI-negative cases where SWE managed to demonstrate lesions in 4 cases with positive histology. For detecting residual tumour, SWE was shown to be superior to surgeons' opinion ( $p = 0.001$ ), and similar to MRI ( $p = 1.000$ ) and intraoperative B-mode ultrasound ( $p = 0.727$ ). Histopathologically, there was no correlation with SWE measurements, except for proliferation ( $p = 0.007$ ).

In conclusion, this thesis demonstrated potential patient benefit of integrating intraoperative SWE into neurosurgical practice, and therefore, a compelling reason to continue development and optimisation of this technology.

## Acknowledgement

I would like to express my gratitude to my four supervisors – Mr Neil Dorward, Dr Jeff Bamber, Mr Aabir Chakraborty and Mr Chris Uff – for their relentless support and guidance throughout my PhD. This project would not have been possible otherwise. I am also grateful to Mr Neil Dorward for organising the funding from the Royal Free Charity (G90), which has helped me tremendously in continuing this project.

I would like to thank the neurosurgeons at the Great Ormond Street Hospital (Messrs William Harkness, Dominic Thompson, Owase Jeelani, and Kristian Aquilina) and at the National Hospital for Neurology and Neurosurgery (Messrs Andrew McEvoy, Lewis Thorne, Robert Bradford, and George Samandouras, and Miss Anna Miserocchi) for their assistance and patience in accommodating my request to acquire clinical scans for my project despite the time pressure imposed on by the theatre staff. I would like to specifically extend my thanks to Mr William Harkness, who has provided tremendous support and assistance to this project as well as excellent teaching on epilepsy cases. I would also like to thank histopathologist Dr Tom Jacques for his assistance with further analysis of histopathological features, and Dr Zoe Fox for her help with statistical analysis.

I would also like to thank Drs Erwin Alles and Jérémie Fromageau, both post-doctoral fellows at the Institute of Cancer Research for their help in MATLAB programming and writing the scripts for freehand drawing of ROI for YM calculations. I also appreciate the help from Mr Chris Bunton for creating phantom moulds and probe holder for my laboratory experiments. I would also like to extend my thanks to Mr Boniface Mburaburirwe, veterinarian at PC Turner abattoir, for providing me with *ex vivo* pig's brains and spinal cords. My thanks also go to the physics team at the Institute of Cancer Research for their invaluable input and suggestions during my team meetings: Dr Jérémie Fromageau, Mr Nigel Bush, Mr Anant Shah, Dr David Birtill-Harris, Dr Elí Elyas, Dr Erwin Alles, Dr Efthymia Papaevangelou, Miss Maria Theodorou, Miss Ramona DeLuca, Dr Leo

Garcia, Dr Tuathan O'Shea, Dr Emma Harris, Mr Michele DiFoggia, Dr Prabhjot Juneja, Dr Jin Li and Mr Alessandro Messa.

Last but not least, I would like to thank my family for their unwavering support and encouragement. Especially to my wife Madeline, thank you for your patience, love and understanding. To my daughter Zoe, thank you for putting a smile on my face with your mere presence.

## Dedication

I would like to dedicate this thesis to my wife Madeline and to our daughter Zoe.

## Table of Contents

<b>Author's declaration .....</b>	<b>2</b>
<b>Abstract.....</b>	<b>3</b>
<b>Acknowledgement.....</b>	<b>5</b>
<b>Dedication.....</b>	<b>7</b>
<b>Table of Contents .....</b>	<b>8</b>
<b>List of Tables.....</b>	<b>18</b>
<b>List of Figures.....</b>	<b>21</b>
<b>List of Symbols and Abbreviations.....</b>	<b>39</b>
<b>1 Introduction.....</b>	<b>43</b>
1.1 Medical Ultrasound .....	44
1.2 Ultrasound Elastography.....	45
1.3 Motivation.....	46
1.4 Previous work.....	47
1.5 Aims .....	48
1.6 Thesis outline .....	50
<b>2 Literature Review.....</b>	<b>52</b>
2.1 Brain tumour resection.....	53
2.1.1 Extrinsic brain tumours .....	53
2.1.2 Intrinsic brain tumours .....	54
2.1.2.1 High grade glioma .....	54
2.1.2.2. Low-grade glioma .....	58
2.1.3 Current techniques to improve extent of resection .....	61

---

2.1.3.1	Frameless stereotactic neuronavigation .....	62
2.1.3.2	Intra-operative CT (iCT) .....	64
2.1.3.3	Intra-operative MRI (iMRI) .....	64
2.1.3.4	Fluorescence imaging.....	65
2.1.3.5	Intra-operative ultrasound (IOUS).....	66
2.2	Epileptogenic foci resection .....	68
2.2.1	Refractory epilepsy.....	68
2.2.2	Temporal lobe epilepsy and surgery.....	69
2.2.3	Extratemporal epilepsy and surgery.....	70
2.2.3.1	Cortical zones in epilepsy .....	71
2.2.4	Neuroimaging techniques for MRI-defined non-lesional cases .....	72
2.2.4.1	MRI sequence and image postprocessing.....	72
2.2.4.2	Fluorodeoxyglucose positron emission tomography (FDG-PET) .....	73
2.2.4.3	Single photon emission computed tomography (SPECT).....	73
2.2.4.4	Magnetoencephalography (MEG) and Magnetic source imaging (MSI).....	74
2.2.5	Invasive intracranial recording.....	75
2.3	Motivation for intraoperative ultrasound elastography .....	77
2.4	Ultrasound elastography.....	78
2.5	Intra-operative ultrasound elastography in neurosurgery.....	79
2.5.1	Intra-operative ultrasound elastography in brain tumour resection.....	79
2.5.2	Intra-operative ultrasound elastography in epileptogenic foci resection.....	83
2.5.3	Shear wave elastography (SWE).....	84
2.6	Hypotheses .....	86
<b>3</b>	<b>Physics of Ultrasound Elastography .....</b>	<b>88</b>
3.1	Theory of elasticity.....	89

---

3.2	Types of ultrasound elastography .....	98
3.2.1	Quasistatic strain elastography (QSE).....	101
3.2.1.1	Vibrography.....	106
3.2.2	Acoustic radiation force impulse (ARFI) imaging.....	108
3.2.3	Shear wave elastography (SWE).....	110
3.2.3.1	Transient elastography (Fibroscan®) .....	113
3.2.3.2	Crawling wave imaging .....	114
3.2.3.3	SuperSonic shear imaging (SSI).....	117
3.2.4	SuperSonic Aixplorer® scanner .....	124
<b>4</b>	<b>Verification of Shear Wave Elastography Measurements.....</b>	<b>131</b>
4.1	Introduction.....	132
4.2	Nomenclature .....	132
4.3	Gelatine phantom manufacture .....	132
4.4	Temperature dependence of gelatine phantoms.....	133
4.4.1	Introduction .....	133
4.4.2	Materials and methods.....	133
4.4.3	Results .....	134
4.4.4	Discussion.....	134
4.4.5	Conclusion.....	134
4.5	Gelatin concentration dependence of gelatine phantoms.....	138
4.5.1	Introduction .....	138
4.5.2	Materials and methods.....	138
4.5.3	Results .....	141
4.5.4	Discussion.....	141
4.5.5	Conclusions .....	142

---

4.6	Time dependence of gelatine phantoms.....	149
4.6.1	Introduction .....	149
4.6.2	Materials and methods.....	149
4.6.3	Results .....	150
4.6.4	Discussion.....	154
4.6.5	Conclusion.....	154
4.7	Cross validation of SWE with MRE in post-mortem mouse brains .....	154
4.7.1	Introduction .....	154
4.7.2	Methods .....	155
4.7.2.1	Mouse studies .....	155
4.7.2.2	MRE acquisition.....	156
4.7.2.3	SWE acquisition .....	157
4.7.3	Results .....	159
4.7.4	Discussion.....	160
4.7.5	Conclusion.....	162
4.8	Conclusions.....	162
<b>5</b>	<b>Early Clinical Experience .....</b>	<b>164</b>
5.1	Introduction.....	165
5.2	Methods.....	165
5.2.1	Ethics Approval .....	165
5.2.2	Patient selection.....	165
5.2.3	Scanning protocol.....	165
5.2.4	Settings on the scanner .....	166
5.2.5	Grading of surgical findings .....	166
5.3	Results.....	167

---

5.3.1	Summary of cases.....	167
5.3.2	Lack of shear wave signal.....	169
5.3.3	Areas of increased Young's modulus by increasing SWE gain.....	169
5.3.4	Decreased Young's modulus of tumour after manipulation and dissection and during resection .....	169
5.3.5	Decreased Young's modulus of surrounding brain after manipulation and dissection .....	169
5.3.6	Increased Young's modulus of cortex in contact with ultrasound transducer ..	173
5.3.7	Young's moduli of grey and white matter.....	175
5.3.8	Correlation between surgical findings and measured Young's modulus .....	177
5.4	Discussion.....	178
5.4.1	Lack of shear wave signal.....	179
5.4.2	Artefactually increased Young's modulus when increasing SWE gain.....	180
5.4.3	Decreased Young's modulus of tissue after manipulation and dissection.....	180
5.4.4	Increased Young's modulus of brain in contact with ultrasound transducer ..	181
5.4.5	Young's moduli of normal brain.....	181
5.4.6	Correlation between surgical findings and SWE measurement .....	182
5.5	Conclusions.....	183
<b>6</b>	<b>Characterisation of Shear Wave Elastography Appearance .....</b>	<b>184</b>
6.1	Introduction.....	185
6.2	Aims .....	185
6.3	Methods.....	186
6.3.1	Effect of changing the region-of-interest (ROI) size.....	186
6.3.2	Effect of varying the water standoff.....	187
6.3.3	Lack of shear wave signals .....	188

---

6.3.3.1	Attenuation in superficial tissue .....	188
6.3.4	Effect of adjusting SWE gain .....	190
6.3.5	Effects of manipulations on SWE measurements .....	191
6.3.6	Effect of strain on SWE measurements.....	192
6.3.7	Varying the tumour-brain interface conditions .....	194
6.3.8	Resolution of shear wave elastography.....	195
6.3.9	Other factors affecting SWE measurements.....	197
6.3.9.1	Inclusion size .....	197
6.3.9.2	Inclusions at different depths .....	201
6.3.9.3	Anisotropy of tissue.....	203
6.4	Results.....	204
6.4.1	Effect of changing the region-of-interest (ROI) size.....	204
6.4.2	Effect of varying the water standoff.....	204
6.4.3	Attenuation in superficial tissue .....	205
6.4.4	Effect of adjusting SWE gain.....	208
6.4.5	Effects of manipulations on SWE measurements .....	211
6.4.6	Effect of strain on SWE measurements.....	217
6.4.7	Varying the tumour-brain interface conditions.....	223
6.4.8	Resolution of SWE.....	233
6.4.9	Other factors affecting SWE measurements.....	237
6.4.9.1	Inclusion sizes .....	237
6.4.9.2	Inclusions at different depths .....	243
6.4.9.3	Anisotropy of tissue.....	245
6.5	Discussion.....	247
6.5.1	Effect of changing the region-of-interest (ROI) size.....	247

---

6.5.2	Effect of varying the water standoff.....	248
6.5.3	Attenuation in superficial tissue .....	248
6.5.4	Effect of adjusting SWE gain.....	249
6.5.5	Effects of manipulations on SWE measurements .....	249
6.5.6	Effect of strain on SWE measurements.....	251
6.5.7	Varying the tumour-brain interface conditions .....	251
6.5.8	Resolution of SWE.....	252
6.5.9	Other factors affecting shear wave measurements .....	256
6.5.9.1	Inclusion sizes .....	256
6.5.9.2	Inclusions at different depths .....	261
6.5.9.3	Anisotropy of tissue.....	261
6.5	Conclusions.....	261
6.6	Recommendations.....	263
<b>7</b>	<b>Clinical Application of Intra-operative Shear Wave Elastography in Epilepsy Surgery .....</b>	<b>265</b>
7.1	Introduction.....	266
7.2	Aims .....	267
7.3	Methods.....	267
7.3.1	Patient selection.....	267
7.3.2	Operating room protocol.....	268
7.3.3	Data acquisition .....	269
7.3.4	Data analysis.....	269
7.4	Results.....	270
7.4.1	Comparison of Young's modulus measurements with surgical findings .....	275
7.4.2	Comparison between SWE and MRI gradings.....	277

---

7.4.2.1 MRI-negative cases.....	277
7.4.2.2 MRI-positive cases.....	281
7.4.2.3 Overall comparison between SWE and MRI gradings.....	286
7.4.3 Histopathological correlation.....	287
7.5 Discussion.....	292
7.5.1 Comparison of Young’s modulus measurements with surgical findings .....	292
7.5.2 Comparison of SWE and MRI gradings.....	294
7.5.3 Histopathological correlation.....	296
7.6 Conclusions.....	298
<b>8 Clinical Application of Intra-operative Shear Wave Elastography in Brain Tumour Resection .....</b>	<b>299</b>
8.1 Introduction.....	300
8.2 Aims .....	301
8.3 Methods.....	302
8.3.1 Patient selection.....	302
8.3.2 Operating room protocol.....	302
8.3.3 Data acquisition .....	303
8.3.4 Data analysis.....	303
8.4 Results.....	304
8.4.1 Comparison of Young’s modulus measurements with surgical findings .....	307
8.4.2 Residual tumour detection .....	310
8.4.3 Characterisation of tumour-brain interface.....	311
8.4.4 Histopathological correlation.....	314
8.4.5 Correlation of Young’s modulus and histopathological features for combined epileptogenic lesions and brain tumours.....	319

---

8.5	Discussion.....	322
8.5.1	Comparison of Young’s modulus measurements with surgical findings .....	322
8.5.2	Residual tumour detection .....	322
8.5.3	Characterisation of tumour-brain interface.....	324
8.5.4	Histopathological correlation.....	324
8.6	Conclusions.....	326
<b>9</b>	<b>Discussion and Conclusion.....</b>	<b>328</b>
9.1	Introduction.....	329
9.2	Summary, significance and limitations .....	330
9.3	Future work.....	336
9.3.1	Physics behind the ‘soft bracket’ sign in slip interfaces .....	336
9.3.2	Clinical studies using intra-operative SWE in neurosurgery .....	336
9.3.3	Integrating MRE with intra-operative SWE.....	337
9.3.4	Validation aspiration rheometer with SWE measurements.....	337
9.4	Conclusions.....	338
9.4.1	Hypothesis 1: SWE can quantify stiffness of normal brain tissue, different epileptogenic lesions and brain tumours.....	338
9.4.2	Hypothesis 2: SWE measurements are different between epileptogenic lesions and normal brain.....	338
9.4.3	Hypothesis 3: SWE measurements are different between brain tumours and normal brain.....	339
9.4.4	Hypothesis 4: SWE appearances are different for mobile and adhered interface. 339	
9.4.5	Hypothesis 5: SWE can visualise epileptogenic lesions better than MRI.....	339
9.4.6	Hypothesis 6: SWE-quantified elasticity of brain tumours and epileptogenic lesions is correlated with histopathological findings.....	339

---

9.4.7	Hypothesis 7: SWE can detect the residual tumour post-resection better than surgeon.	340
9.4.8	Hypothesis 8: SWE can detect the residual tumour post-resection better than ultrasound B-mode.	340
<b>10</b>	<b>References</b>	<b>341</b>
<b>A</b>	<b>The Correction of SWE for Frequency Dispersion</b>	<b>358</b>
<b>B</b>	<b>List of Publications originating from this thesis</b>	<b>361</b>
B.1	Peer-reviewed paper (from work described in chapter 7)	361
B.2	Presentations with published abstracts	366
B.3	Book Chapter	387
<b>C</b>	<b>Guide to setting up Supersonic Aixplorer® for intraoperative shear wave elastography in neurosurgery</b>	<b>388</b>

## List of Tables

Table 2.1. Table summarising the studies since 2000 looking at survival and extent of resection of high-grade glioma. AA = anaplastic astrocytoma; GBM = glioblastoma multiforme. ....	57
Table 2.2: Summary of the series of low grade glioma evaluated in Keles et al. (2001) for the effect of extent of resection on survival. Abbreviations: MST=median survival time; PFS=progression-free survival; res=resection; S=survival. (Adapted from Keles et al., 2001) .....	59
Table 2.3. Summary of studies since 2000 looking at extent of resection of low-grade glioma on survival. GTR = gross total resection; NTR = near total resection; STR = subtotal resection; Bx = biopsy; NA = not available. NB. The prefix “~” symbol represent approximate value from interpretation of the graph as value is not available in the text or table.....	60
Table 2.4. Different facets of refractory epilepsy. (Reproduced from Kwan & Brodie, 2002)	69
Table 2.5. Summary of histopathological findings of extratemporal lobe epilepsy. *WHO indicates World Health Organisation. (Reproduced from Frater et al., 2000) .....	70
Table 2.6: The definitions of the cortical zones detected by different diagnostic methods. (Adapted from (Rosenow & Lüders, 2001)). *functional MRI; §magnetoencephalogram. ....	72
Table 3.1. Description of different components of stress tensors. Bolded components are normal stresses whereas the rest are shear stresses. (Adapted from Fung (1993)) .....	93
Table 5.1: Summary of the initial 10 cases scanned at Great Ormond Street Hospital. *Dysembryoplastic neuroepithelial tumour. §Focal cortical dysplasia. ¶Primitive neuroectodermal tumour.....	168
Table 7.1. Summary of epilepsy surgery cases recruited into the study. §Dysembryoplastic neuroepithelial tumour. §§Focal cortical dysplasia. **Malformation of cortical development. ‡The resection was not performed due to location in the eloquent cortex. %Temporo-parieto-occipital. *These cases underwent either hemispherotomy or TPO disconnection. §This case was not epileptogenic because it was in the posterior fossa.....	272

Table 7.2. The summary of cases included for analysis. <sup>§</sup> Dysembryoplastic neuroepithelial tumour. <sup>§§</sup> Focal cortical dysplasia. <sup>¶</sup> Standard deviation. <sup>§</sup> Young's modulus contrast. <sup>£</sup> Engel's classification is used to group seizure outcomes. ....	274
Table 7.3: Contingency table for comparing SWE with MRI gradings. ....	286
Table 7.4: The result of Wilcoxon signed-rank test overall. <sup>a</sup> SWE < MRI; <sup>b</sup> SWE > MRI; <sup>c</sup> SWE = MRI. ....	287
Table 7.5: The result of Wilcoxon signed-rank test for just the lesional cases. <sup>a</sup> SWE < MRI; <sup>b</sup> SWE > MRI; <sup>c</sup> SWE = MRI. ....	287
Table 8.1: Summary of brain resection cases recruited into this study. <sup>¶</sup> Standard deviation. * It was converted to biopsy due to excessive bleeding. <sup>§</sup> It was a case of known residual due to invasion into brainstem. <sup>&amp;</sup> The patient developed air embolus during surgery so the post-operative scan was abandoned. <sup>§</sup> The calculation of YMC for these cases was not possible as the lesions were subventricular and the adjacent brain was too deep for shear wave to penetrate. <sup>£</sup> Supratentorial primitive neuroectodermal tumour. <sup>§§</sup> Subependymal giant cell astrocytoma. <sup>&amp;&amp;</sup> Atypical teratoid/rhabdoid tumour. <sup>§§</sup> Glioblastoma multiforme. <sup>££</sup> Embryonal tumour with abundant neuropil and true rosettes. ....	306
Table 8.2: McNemar's 2×2 contingency table comparing intra-operative SWE with post-operative MRI for detecting residual tumour. No statistically significant difference was detected between SWE and MRI for detecting residual tumour (p = 1.000). ....	310
Table 8.3: McNemar's 2×2 contingency table for comparing intra-operative US B-mode with post-operative MRI scan in detecting residual tumour. No statistically significant difference was detected between US B-mode and MRI for detecting residual tumour (p = 1.000). ....	310
Table 8.4: McNemar's 2×2 contingency table for comparing surgeon's intra-operative opinion with post-operative MRI scan in detecting residual tumour. A statistically significant difference was detected between surgeons's opinion and MRI for determining whether there was residual tumour or not (p < 0.001). ....	311
Table 8.5: McNemar's 2×2 contingency table for comparing intra-operative SWE with B-mode in detecting residual tumour. No statistically significant difference was detected for SWE and B-mode for detecting residual tumour (p = 0.727). ....	311

Table 8.6: McNemar's  $2 \times 2$  contingency table for comparing intra-operative SWE and surgeon's opinion in detecting residual tumour. A statistically significant difference was detected for SWE and surgeon's opinion of the presence of residual tumour. ( $p = 0.001$ ). ...311

## List of Figures

Figure 3.1. The illustration of Hooke's law with spring and load. Each load has the same weight, therefore the same force. With one load, the spring extends by distance $x$ . By doubling the load, the spring extends twice as much $- 2x$ .....	89
Figure 3.2. Notations of different components of the stress tensor in 3D space. (Adapted from Fung (1993)). .....	90
Figure 3.3. Shear modulus is characterised by the amount of force ( $F$ ) required to act on the surface area ( $A$ ) tangentially to create a displacement ( $\Delta x$ ) in a material with a height ( $L$ ). $\theta$ is the slanting angle of the material subjected to shear stress, and is dependent on $\Delta x$ and $L$ . .....	93
Figure 3.4. When the compressional force (depicted by red arrow) acts on the surface (blue) to produce a displacement of ( $\Delta L_{axial}$ ) there is an expansion of the material in the perpendicular direction ( $\Delta L_{transverse}$ ), resulting in the cuboid depicted by dashed outline.....	95
Figure 3.5. The illustration of longitudinal wave propagation. The compressed tissue elements are at maximum pressure whereas the dilated tissue elements just prior to these are at minimum pressure. The left image (a) is the 3D grid representation while the right image (b) is the simulated histological sections from liver tissue. (Reproduced from Bamber et al. (2013)).....	98
Figure 3.6. Schematic diagram of the cross-correlation technique with the pre-compression (a) and post-compression (b) RF A-line signal. The brown window in (a) is the reference window and the light green window in (b) is the search window. The bottom brown window is the congruent segment with the reference window identifying its location in the compressed RF line. $\delta t$ is the infinitesimal time delay detected.....	99
Figure 3.7. Diagrammatic representation of compression with force ( $F$ ) on a soft background (blue) with a stiff inclusion (yellow). The pre-compression image is on the left and post-compression image on the right. ....	102
Figure 3.8. Graphs of displacement-depth (a) and strain-depth (b) plots. Note that the displacement was negative because of compression. ....	103

Figure 3.9. The corresponding grey scale image of displacement (a) and strain (b) of simulated soft background with stiff inclusion. (Reproduced from Uff (2011))	104
Figure 3.10. The illustration of the concept of vibrography.	107
Figure 3.11. Shear waves (black solid line) produced by the displacement force (red arrow), which travels perpendicular to the force (blue arrows).	111
Figure 3.12. $S_1$ and $S_2$ are shear wave sources. The antinode lines can be illustrated as hyperbolae. (Adapted from Wu Z. et al. (2006))	115
Figure 3.13. The illustration of shear wave generation with ARF sweep focused at different depths. The resultant shear waves have the conical shape travelling in opposite directions. The angle $\theta$ depends on the speed of focus moving axially and the speed of the propagating shear waves; and is directly linked to the Mach number. (Adapted from Bercoff et al., 2004b)	118
Figure 3.14. The supersonic imaging regime. Initial reference insonification (step 1) is performed to obtain a reference image before any “pushes” are initiated. The pushing sequence (step 2) is performed by applying "pushes" at different depths, each lasting $\sim 100 \mu\text{s}$ . In between the “pushes”, ultrafast frames can be acquired to monitor the activation of the supersonic ARF. This is followed by imaging of the propagation shear wave (step 3) to estimate the shear wave velocity and elastic modulus. (Adapted from Bercoff et al. (2004))	120
Figure 3.15. The supersonic regime for different Mach number: (a) Mach 3 (b) Mach 10 (c) Mach -3. Note that Mach -3 is the inverse of Mach 3, with the Mach cone converges towards the transducer.	122
Figure 3.16. The operating room setup at Great Ormond Street Hospital. The Supersonic Aixplorer® scanner (orange) is placed next to the patient body (beige) with the monitor swivelled to face the surgeon. I stand next to the scanner so that I can optimise the scanner settings as well as acquire images for this thesis.	124
Figure 3.17. A photograph showing the surgeon performing the scan.	125
Figure 3.18. The buttons on the Supersonic Aixplorer scanner. (Adapted from SuperSonic Imagine (2010))	129
Figure 3.19. The display on Supersonic Aixplorer® scanner on SWE mode, showing SWE gain, SWE scale, focal depth, ROI box and Q-box.	130

Figure 3.20. This photograph shows the 4 grey knobs just beneath the display. The leftmost knob controls the SWE mode while the rightmost knob controls the SWE scale. (Adapted from SuperSonic Imagine (2010)) .....	130
Figure 4.1. Measured Young's modulus for gelatine phantoms with 8%, 10% and 14% gelatin concentrations with respect to temperature. ....	136
Figure 4.2. Comparison of rigidities of a mixed sample and its components at concentration of 5.75g/100 ml. (Reproduced from Ferry (1948)).....	137
Figure 4.3: This is a photograph showing the set up for measuring the Young's modulus of the gelatine phantom using the compressive rheometer. Vegetable oil was used to lubricate the top and bottom surface of the phantom to reduce frictional force. ....	140
Figure 4.4. The force-displacement data for 10% gelatin concentration phantom for the first 4 measurements. The slope of the graph is the Young's modulus. ....	143
Figure 4.5: Plot of SWE and compressive rheometer (Instron) measurements of Young's modulus in gelatine of different concentrations at 16 °C. The linear-fit line is forced through intercept (0,0). Pearson's correlation was statistically significant ( $p < 0.001$ ).....	144
Figure 4.6. Plot of SWE and compressive rheometer (Instron) measurements of Young's modulus in gelatine of different concentrations at 16 °C. The linear-fit line is not forced through intercept (0,0). Pearson's correlation was statistically significant ( $p < 0.001$ ).....	145
Figure 4.9: The plot of corrected Young's moduli measured using shear wave elastography with respect to those measured with compressive rheometer. The linear-fit line is forced through intercept (0,0). Pearson's correlation was statistically significant ( $p < 0.001$ ).....	148
Figure 4.10. Young's moduli of gelatine phantoms with respect to time held at 4 °C. ....	151
Figure 4.11. This is a plot of the change in weight of gelatine phantoms with polypropylene mould with respect to incubation time. The phantoms scanned at 12-hour interval lost more weight overall than those scanned at 24-hour interval. ....	152
Figure 4.12. This graph shows the Young's modulus expected from weight loss and Young's modulus measured with SWE. The Young's modulus rise from 36 hours onwards was higher than expected rise from just weight loss.....	153
Figure 4.13. A photograph showing the craniectomy for exposure prior to scanning with SWE. ....	156

Figure 4.14. Diagrammatic representation of the MRE setup. (Reproduced from Li (2015)) .....	157
Figure 4.15. A coronal slice of the MRE data. ....	157
Figure 4.16. A photograph of the setup for SWE acquisition in the brain of a dead mouse.	158
Figure 4.17. An example of the SWE image exported to MATLAB® and a region of interest drawn by hand (white outline) based on B-mode on the upper pane, which corresponds to the region on SWE in the lower pane. The Young's modulus measurements are given as mean $\pm$ SD, with the number of pixel in the region of interest in brackets. ....	159
Figure 4.18. Graph of SWE measurements plotted against MRE measurements. The standard errors were within the markers. ....	160
Figure 5.1: There was lack of shear wave signal in deeper areas, especially the region to the right of the tumour (asterisk). This particular case was an image taken from GOSH 1. ....	170
Figure 5.2: The areas surrounding the lesion were artefactually stiff, with a mean of 294 kPa. These areas did not display any elasticity information prior to increasing the SWE gain. The lesion in this case had a Young's modulus of $22.5 \pm 4.0$ kPa (mean $\pm$ SD). ....	170
Figure 5.3: This image was acquired before any manipulation or dissection into the tumour. The Young's modulus was $65.54 \pm 5.45$ kPa (mean $\pm$ SD). ....	171
Figure 5.4: This image was acquired after slight manipulation of the tumour and dissection around the medial aspect of the tumour. The Young's modulus was $56.57 \pm 10.59$ kPa (mean $\pm$ SD). The surgical patty (arrow) was placed medial to the tumour, which was where the dissection had been performed. ....	171
Figure 5.5: This image was taken after partial resection of the tumour. The Young's modulus was $36.10 \pm 11.00$ kPa (mean $\pm$ SD). ....	172
Figure 5.6: Compared to pre-resection scan, the brain surface had a lower Young's modulus during resection of astrocytoma in GOSH 1. The dark blue region superficially within the white circle had a Young's modulus of $6.49 \pm 8.47$ kPa (mean $\pm$ SD), compared to Young's modulus of $39.39 \pm 12.64$ kPa (mean $\pm$ SD) pre-manipulation or dissection. ....	172
Figure 5.7: There was a further decrease of the Young's modulus of the surrounding brain after complete resection of the lesion. The Young's modulus within the white circle was $1.33 \pm 1.83$ kPa (mean $\pm$ SD). ....	173

Figure 5.8: This is an image acquired for GOSH 7. The cortex in contact with the transducer appeared stiff with a Young's modulus of $51.62 \pm 16.28$ kPa (mean $\pm$ SD), compared to the adjacent cortex away from the transducer with a Young's modulus of $28.55 \pm 8.97$ kPa (mean $\pm$ SD). .....	174
Figure 5.9: This is the image acquired for GOSH 1. The cortex in contact with the transducer appeared stiff with Young's modulus of $59.7 \pm 2.50$ kPa (mean $\pm$ SD), compared to the cortex away from the transducer with a Young's modulus of $16.51 \pm 14.30$ kPa (mean $\pm$ SD). .....	175
Figure 5.10: SWE image from GOSH 10. The area scanned is frontal lobe where the brain appears normal. Circular ROIs indicate the grey and white matter where the measurements were made.....	176
Figure 5.11: The whisker box plot for the mean Young's moduli of normal cortical grey matter and subcortical white matter. The upper and lower bounds of the box were the third and first quartiles, respectively, while the line within the box was the median. The upper and lower whiskers were maximum and minimum, respectively. *Wilcoxon's signed ranks test showed the difference in the mean Young's moduli between the two regions of the normal brain were statistically significant ( $p = 0.008$ ).....	177
Figure 5.12: The distribution of measured Young's modulus for lesions grouped according to subjective surgical opinion of stiffness relative to brain. The upper and lower bounds of the box were the third and first quartiles, respectively while the line within the box was the median. The upper and lower whiskers were maximum and minimum values, respectively. There was a significant correlation between stiffness grading and Young's modulus measurements ( $\rho = 0.532$ ; $p = 0.004$ ).....	178
Figure 6.1. This is the top half of the display on the ultrasound scanner where it shows the B-mode image with superimposed colour SWE image within the ROI. ....	186
Figure 6.2. The experimental setup to investigate the effect of water standoff on the Young's modulus measurements.....	187
Figure 6.3. The experimental set-up for investigating the effect of attenuating layers on shear wave signal. ....	190
Figure 6.4: <i>Ex vivo</i> porcine brain with pia mater removed on the left and preserved on the right.....	192

Figure 6.5 Experimental set up for the porcine brain to investigate the effect of strain on the Young's modulus measurements. The ultrasound probe is attached to the compressive rheometer to enable controlled application of strain. ....	193
Figure 6.6 The experimental set up for investigating the effect of strain on the gelatine phantoms. The housing for the ultrasound probe extends the footplate of the ultrasound probe to exert a uniform strain in the phantom. ....	194
Figure 6.7. The gelatine phantom with small cylindrical inclusions (1mm, 1.8mm, 3mm, 4mm and 5mm diameter). ....	197
Figure 6.8. Gelatine phantom with large cylindrical inclusions (10mm, 15mm and 20mm diameter). ....	199
Figure 6.9. The setup for ultrasound scanning of a 3D phantom (a), and repeated but with scan plane coloured transparent green (b).....	199
Figure 6.10. The view of the 3D phantom from the top when the inclusion is large. The horizontal dashed lines indicate the outline of the SWE image slice thickness while the vertical dashed lines show the width of the inclusion on ultrasound B-mode image. The transparent green rectangle indicates the area of the projected volume included in the calculation of Young's modulus. ....	200
Figure 6.11. The view from the top of the 3D phantom for a small inclusion. The horizontal dashed lines indicate the outline of the SWE image slice thickness while the vertical dashed lines show the width of the inclusion on ultrasound B-mode image. The transparent green rectangle indicates the area of the projected volume included in the calculation of Young's modulus. ....	200
Figure 6.12. Three-dimensional (3D) phantom with small spheres measuring 12 mm, 8.5 mm, 6 mm and 2.5 mm in diameter, from the left, placed on a partially solidified background gelatine. More gelatine will be poured over it to make the phantom. ....	201
Figure 6.13. Gelatine phantom with cylindrical inclusions of 5 mm in diameter arranged at various depths.....	202
Figure 6.14. Gelatine phantom with 1-cm diameter cylindrical inclusions arranged in diagonal fashion. ....	203
Figure 6.16. Mean Young's modulus measured as a function of water standoff height for 3 different phantoms (n=3). The continuous and dashed lines represent 'standard' and	

'penetration' modes, respectively. The error bars are plus and minus one standard deviation. .....	205
Figure 6.17. Young's modulus measured for inclusion and background, for standard and penetration mode, as a function of the thickness of the overlying attenuating layer composed of 14% gelatine concentration phantom (n=3). .....	206
Figure 6.18. SWE appearance with surgicel as an attenuating layer, using standard mode.	207
Figure 6.19. SWE appearance with surgicel as an attenuating layer, using the penetration mode. ....	207
Figure 6.20. SWE appearance with duragen as an additional attenuating layer, using penetration mode. ....	208
Figure 6.21. Display on Supersonic Aixplorer® for SWE gain of 70%.....	209
Figure 6.22. Display on Supersonic Aixplorer for SWE gain of 80%. Note the previously areas void of SWE signal are now filled with artefactually high Young's modulus values (white arrows). ....	209
Figure 6.23. Display on Supersonic Aixplorer for SWE gain of 90%. Note more areas of previously void of SWE signal are appearing as artefactually stiff regions. ....	210
Figure 6.24. Display on Supersonic Aixplorer for SWE gain of 100%. Note the areas previously void of SWE signal are filled with artefactually high Young's modulus values...	210
Figure 6.25. SWE of the phantom with stiff inclusion simulating a tumour before resection. ....	211
Figure 6.26. SWE during resection of the inclusion.....	212
Figure 6.27. SWE after complete removal of the stiff inclusion. Notice the decrease in the Young's modulus in the surrounding tissue compared with previous 3 images. ....	212
Figure 6.28. Mean and plus and minus one standard deviation of Young's modulus measured by SWE before and during resection of the stiff inclusion for inclusion (n=3). There is no statistically significant difference ( $p = 0.802$ , paired t-test).....	213
Figure 6.29. Mean and plus and minus one standard deviation of Young's modulus measured by SWE of the background gelatine for different stages of inclusion removal (n=3). * denotes a statistically significant difference between pre-resection and post-resection ( $p < 0.001$ , paired t-test). However, the difference between during resection and post-resection is not statistically significant ( $p = 0.087$ , paired t-test). ....	213

Figure 6.30: The SWE images for porcine brain scanned in coronal section with the pia mater removed on the right side of the image. The pia mater on the left side of the image was intact. ....	214
Figure 6.31: Mean and plus and minus one standard deviation of Young's modulus measured by SWE for grey and white matter with pia mater intact and removed (n=3). *There was a statistically significant difference between the grey matter with and without pia mater (p = 0.011, Wilcoxon's signed-ranks test). However, there was no statistically significant difference between the white matter with and without pia mater (p = 0.314, Wilcoxon's signed-ranks test).....	215
Figure 6.32. Mean and plus and minus one standard deviation of Young's modulus measurements of porcine brains before and after compression (n=3). The difference was not statistically significant (p = 0.485, Wilcoxon's signed-ranks test).....	216
Figure 6.33. Mean and plus and minus one standard deviation of the Young's modulus of porcine brain heights before and after compression. * There was a statistically significant difference (p < 0.05, Wilcoxon's signed-ranks test).....	216
Figure 6.34. SWE display showing the apparently softer top layer of the homogeneous gelatine phantom compared to the rest of the phantom when the probe is used with water standoff.....	218
Figure 6.35. SWE display showing the homogeneous Young's modulus measurement when the probe is touching the phantom.....	218
Figure 6.36. The SWE Young's modulus measurements of the top layer of 8% and 14% gelatine phantoms using a water standoff and with the probe touching the phantoms. The Young's modulus seemed to decrease when a water standoff was used. * denotes that the difference is statistically significant (p < 0.01, paired t-test, 8% gelatine phantoms (n=3), and 14% gelatine phantoms (n=3))......	219
Figure 6.38. The Young's modulus measurements of the remainder (excluding the top 0.5 cm) of 8% and 14% gelatine phantoms with water standoff and probe touching the phantoms. The Young's moduli seemed to decrease slightly in both phantoms when the wat standoff was used but it was not statistically significant. This is the result of the experiments performed using 8% gelatine phantoms (n=3) and 14% gelatine phantoms (n=3). ....	220

Figure 6.39. SWE display for porcine brain scanning with Q-boxes for upper, middle and lower thirds and overall measurements.....	221
Figure 6.40. The graph of mean and plus and minus one standard deviation of overall Young's modulus measured by SWE for the porcine brains (n=3). There is a slow nonlinear increase in the Young's modulus measurements that appears to begin from about 5 mm displacement but becomes significant for displacements greater than about 15 mm.....	221
Figure 6.41. The graph of mean and plus and minus one standard deviation of Young's modulus measured by SWE for the upper third portion of the porcine brain with different compression (n=3). This shows an upward trend with a significantly increasing displacement from 10 mm onwards. ....	222
Figure 6.42. The graph of mean and plus and minus one standard deviation of Young's modulus measurement for middle third portion of the porcine brains with different compression. There was no increase in the Young's modulus until ~15 mm displacement, from which point it starts to rise.....	222
Figure 6.43. The graph of mean and plus and minus one standard deviation of Young's modulus measured by SWE for the lower third portion of the porcine brains with different compression. There seems to be a slower rise in Young's modulus from ~15 mm displacement onwards compared with that in the middle third portion.....	223
Figure 6.44. SWE for a stiff adhered inclusion. Note the small size of the SWE ROI, encompassing little background gel around the inclusion. ....	225
Figure 6.45. Stitched image of SWE for stiff adhered inclusion without any strain. Note the bands in the SWE image, of apparently high Young's modulus, that follow the border of speckle-devoid shadow beneath the inclusion in the B-scan. The acoustic shadow region also gives rise to low Young's modulus values. ....	225
Figure 6.46. Stitched image of SWE for a stiff mobile inclusion. Notice the artefact bands are still present for the B-mode shadow region. However, a new feature is now present, namely the "brackets" of low Young's modulus value on the left and right boundary of the inclusion (white arrows). ....	226
Figure 6.47. Profile plot through the centre of a SWE image of the stiff mobile inclusion. The y-axis is in arbitrary units. Notice there was a dip in the pixel values on either side of the inclusion. ....	226

Figure 6.48. Profile plot for the stiff adhered inclusion. Notice the absence of a dip in the pixel values on either side of the inclusion. ....	227
Figure 6.49. Stitched image of SWE for stiff adhered inclusion with 10% strain applied.....	227
Figure 6.50. Stitched image of SWE for stiff mobile inclusion with 10% strain applied.....	228
Figure 6.51. Profile plot for stiff adhered inclusion with 10% applied strain.....	228
Figure 6.52. Profile plot for stiff mobile inclusion with 10% applied strain.....	229
Figure 6.53. Stitched image of SWE for soft adhered inclusion.....	229
Figure 6.54. Stitched image of SWE for soft mobile inclusion. Notice there is a soft 'bracket' on either side of the inclusion. ....	230
Figure 6.55. Profile plot for soft adhered inclusion.....	230
Figure 6.56. Profile plot for soft mobile inclusion.....	231
Figure 6.57. Stitched image of SWE for soft adhered inclusion with 10% applied strain....	231
Figure 6.58. Stitched image of SWE for soft mobile inclusion with 10% applied strain. Note the soft 'bracket' on either side of the inclusion. ....	232
Figure 6.59. Profile plot for soft adhered inclusion with 10% applied strain.....	232
Figure 6.60. Profile plot for soft mobile inclusion with 10% applied strain. Note the appearance of pixel value dip on either side of the inclusion.....	233
Figure 6.61. SWE for small stiff inclusions in a soft background showing the appearance of 2-mm and 1-mm inclusions (arrows). ....	234
Figure 6.62. Mean and plus and minus one standard deviation of Young's modulus measured by SWE as a function of stiff inclusion size for standard mode and penetration mode. The measurements were made with 6 phantoms (3 phantoms) with 2 different modes. ....	234
Figure 6.63. Young's modulus contrast for stiff inclusions in soft background for standard and penetration modes. ....	235
Figure 6.64. Mean and plus and minus one standard deviation of Young's modulus measurements for soft inclusions using both standard and penetration modes. The measurements were made with 6 phantoms (3 phantoms) with 2 different modes. ....	236
Figure 6.65. Young's modulus contrast for soft inclusions in stiff background for standard and penetration modes. ....	236
Figure 6.66. Mean and plus and minus one standard deviation of Young's modulus measured by SWE as a function of stiff inclusion size for standard mode and penetration mode. The	

measurements were made with 6 phantoms (3 phantoms with small inclusions and 3 phantoms with large inclusions) with 2 different modes.....	237
Figure 6.67. Young's modulus contrast for stiff inclusions in soft background for standard and penetration modes. ....	238
Figure 6.68. Mean and plus and minus one standard deviation of Young's modulus measurements for soft inclusions using both standard and penetration modes. The measurements were made with 6 phantoms (3 phantoms with small inclusions and 3 phantoms with large inclusions) with 2 different modes.....	239
Figure 6.69. Young's modulus contrast for soft inclusions in stiff background for standard and penetration modes.. ....	239
Figure 6.70. Mean and plus and minus one standard deviation of Young's modulus measurements for 3D phantoms with stiff inclusions in a soft background. The measurements were made with 3 different phantoms (n=3). ....	240
Figure 6.71. The graph of contrast transfer efficiency for stiff spherical (3D) inclusions in a soft background. ....	241
Figure 6.72. Mean and plus and minus one standard deviation of Young's modulus measurements for 3D phantoms with soft spherical inclusions in a stiff background. The measurements were made with 3 different phantoms (n=3). ....	242
Figure 6.73. The graph of contrast transfer efficiency for soft spherical (3D) inclusions in a stiff background. ....	242
Figure 6.74. Mean and plus and minus one standard deviation of Young's modulus measured by SWE for 0.5-mm stiff inclusions arranged diagonally at different depths (n=3). The measurements when the phantom is flipped 90° are also plotted (n=3). These measurements were performed in 3 different phantoms for each experimental setup. ....	243
Figure 6.75. Mean and plus and minus one standard deviation of Young's modulus measurements for 0.5-mm soft inclusions arranged diagonally in different depths (n=3). Measurements taken with the phantom flipped 90° were also plotted (n=3). These measurements were performed in 3 different phantoms for each experimental setup. ....	244
Figure 6.76. Mean and plus and minus one standard deviation of Young's modulus measurements for 1-cm stiff inclusions arranged diagonally in different depths (n=3).	

Measurements taken with the phantom flipped 90° were also plotted (n=3). These measurements were performed in 3 different phantoms for each experimental setup.....	244
Figure 6.77. Mean and plus and minus one standard deviation of Young's modulus measurements for 1-cm soft inclusions arranged diagonally in different depths (n=3). Measurements taken with the phantom flipped 90° were also plotted (n=3). These measurements were performed in 3 different phantoms for each experimental setup.....	245
Figure 6.78. SWE acquired with transducer held perpendicular to the spinal cord. ....	246
Figure 6.79. SWE acquired with transducer held parallel to the length of the spinal cord. .	246
Figure 6.80. Mean and plus and minus one standard deviation of the Young's modulus measurements of the 2 spinal cords measured parallel and perpendicular to their lengths (n=2). The difference is not statistically significant (p = 0.202, paired t-test).....	247
Figure 6.81. This is the view from the top of a block gelatine (blue) with a cylindrical inclusion (red). The dashed lines across the inclusion represent the scan plane. Therefore, the inclusion appearing on the B-mode is larger than the actual size of the inclusion. The Young's modulus measurements for the inclusion are taken from the transparent green area, which has contributions from both the background and inclusion. ....	254
Figure 6.82. Magnified volume where Young's modulus measurements are calculated. The cylindrical inclusion is only a part of the total volume, hence resulting in lower values of measured Young's modulus due to contributions from the background. ....	255
Figure 6.83: Plot of "corrected" Young's modulus for small stiff inclusions. The correction seemed to be overcorrecting the Young's modulus, especially the smaller inclusions (1 mm to 3 mm). Overall, the "correction" overcorrected the Young's modulus for the inclusions in this experiment. ....	255
Figure 6.84: Plot of "corrected" Young's modulus for small soft inclusion sizes. The correction seemed to be overcorrecting the Young's modulus, making the soft inclusions appearing with very small Young's modulus or even negative Young's modulus. ....	256
Figure 6.85: Plot of "corrected" Young's modulus for 3D stiff inclusions.....	259
Figure 6.86: Plot of "corrected" CTE for 3D stiff inclusions. The correction seemed to give a positive CTE for stiff inclusions. ....	259
Figure 6.87: Plot of "corrected" Young's modulus for 3D soft inclusions. The correction seemed to overcorrect the smallest inclusion (2.5mm).....	260

Figure 6.88: Plot of “corrected” CTE for 3D soft inclusions. The correction factor seemed to be overcorrecting the CTE for SWE standard mode, with positive CTE for all inclusion sizes. ....	260
Figure 7.1: Box and whiskers plot for Young's modulus measurements according to different stiffness grading (n=37). The upper and lower bounds of the box were the third and first quartiles, respectively while the line within the box was the median. The upper and lower whiskers were maximum and minimum values, respectively. ....	276
Figure 7.2: Box and whiskers plot for Young's modulus contrast according to different stiffness grading (n = 37). The upper and lower bounds of the box were the third and first quartiles, respectively while the line within the box was the median. The upper and lower whiskers were maximum and minimum values, respectively. ....	276
Figure 7.3: SWE of GOSH 72 showing the lack of SWE signal in the hippocampus. This scan was performed in the coronal plane with the left being superior. The stiff region (red) in the sylvian fissure was consistent with the pia effect, described in chapter 6. ....	277
Figure 7.4: SWE for GOSH 6 showing the soft lesion relative to the surrounding brain. As this case was one of the earliest clinical cases, the SWE gain was set to 100%, thereby giving rise to artefactual stiff regions under the lesion. ....	278
Figure 7.5: SWE for GOSH 8 showing the stiff lesion superficially. This case also demonstrated that the lesion was absent on ultrasound B-mode. The areas deeper down which were also stiff were probably due to anisotropy of deep white matter. ....	279
Figure 7.6: SWE for NHNN 3 showing the stiff lesion. This is another case demonstrating that the lesion was absent on ultrasound B-mode. ....	279
Figure 7.7: SWE for NHNN 6 showing the stiff lesion relative to surrounding brain. This case had previously undergone resection of DNT but seizure returned. The resection cavity was shown not to be epileptogenic but the adjacent area was, which appeared normal on MRI scan. ....	280
Figure 7.8: MRI FLAIR sequence for GOSH 41 showing clearly the lesion in the right mesial temporal lobe (arrow). ....	282
Figure 7.9: SWE for GOSH 41 showing a subtle soft lesion, which appeared as hyperechoic region on ultrasound B-mode. ....	282

Figure 7.10: MRI FLAIR scan for GOSH 4 showing subtle lesion near the right motor strip. .....	283
Figure 7.11: SWE for GOSH 4 showing the obvious stiff lesion. ....	283
Figure 7.12: T2-weighted MRI sequence showing the subtle abnormality in the left temporal pole extending into the mesial temporal lobe (arrow). ....	284
Figure 7.13: SWE for GOSH 59 showing a subtle soft lesion. ....	284
Figure 7.14: SWE for GOSH 22 showing an obvious stiff lesion with a non-diagnostic histological appearance. ....	285
Figure 7.15: SWE for GOSH 27 showing an obvious stiff lesion with a non-diagnostic histological appearance. ....	286
Figure 7.16: Box and whiskers plot for Young's modulus for normal brain and epileptogenic lesions. The upper and lower bounds of the box were the third and first quartiles, respectively while the line within the box was the median. The upper and lower whiskers were maximum and minimum values, respectively. *There is statistically significant difference in the Young's modulus between normal brain and epileptogenic lesions ( $p < 0.001$ , Wilcoxon's signed-rank test).....	288
Figure 7.17: Box and whiskers plot of Young's modulus measurements for non-tumoural lesions, tumours, and normal brain. The upper and lower bounds of the box were the third and first quartiles, respectively while the line within the box was the median. The upper and lower whiskers were maximum and minimum values, respectively. *There was a statistically significant difference in the Young's modulus between non-tumoural lesions and normal brain ( $p < 0.001$ ). There was no statistically significant difference between tumours and brain ( $p = 0.064$ ), and between tumour and non-tumour ( $p = 0.467$ ). Wilcoxon's signed-rank test was used for statistical analysis.....	288
Figure 7.18: Box and whiskers plot of Young's modulus for epileptogenic lesions according to the grading of cellularity ( $n=29$ ). The upper and lower bounds of the box were the third and first quartiles, respectively while the line within the box was the median. The upper and lower whiskers were maximum and minimum values, respectively. There was no statistically significant difference ( $p = 0.699$ , Mann Whitney U test). ....	290
Figure 7.19: Box and whiskers plot of Young's modulus for epileptogenic lesions according to the presence of proliferation ( $n=28$ ). 'No' in the horizontal axis indicates low proliferation.	

The upper and lower bounds of the box were the third and first quartiles, respectively while the line within the box was the median. The upper and lower whiskers were maximum and minimum values, respectively. There was only one patient (n=1) with increased proliferation with Young’s modulus of 143.3kPa. Although the Young’s modulus was higher in the patient with higher proliferation compared with those with lower proliferation, there was no statistically significant difference (p = 0.071, Mann Whitney U test). .....290

Figure 7.20: Box and whiskers plot of Young's modulus for epileptogenic lesions according to the presence of calcification (n=28). The upper and lower bounds of the box were the third and first quartiles, respectively while the line within the box was the median. The upper and lower whiskers were maximum and minimum values, respectively. There was only one patient (n=1) with the presence of calcification with Young’s modulus of 13.3kPa. There was no statistically significant difference (p = 0.286, Mann Whitney U test). .....291

Figure 7.21: Box and whiskers plot of Young's modulus for epileptogenic lesions according to the presence of gliosis (n=21). The upper and lower bounds of the box were the third and first quartiles, respectively while the line within the box was the median. The upper and lower whiskers were maximum and minimum values, respectively. There was no statistically significant difference (p = 0.185, Mann Whitney U test).....291

Figure 7.22. SWE of the lesion for GOSH 65 showing that the lesion was stiff (red) with its corresponding Young’s modulus of 143.3 kPa ± 84.8 kPa (mean ± SD). The lesion, which was recurrent ganglioglioma was hyperechoic on US B-mode. ....293

Figure 7.23. SWE of the lesion for NHNN 9 showing that the hyperechoic lesion appeared to have low Young’s modulus (blue). The adjacent isoechoic region appeared to have high Young’s modulus (red) compared to regions further to the right.....294

Figure 7.24: SWE for GOSH 72 showing stiff temporal lobe.....295

Figure 8.1: Box and whiskers plot for Young's modulus measurements according to stiffness grade assessed by independent surgical opinion (n=34). The upper and lower bounds of the box were the third and first quartiles, respectively while the line within the box was the median. The upper and lower whiskers were maximum and minimum values, respectively. ....307

Figure 8.2: Box and whiskers plot for Young's modulus contrast according to stiffness grade assessed by independent surgical opinion (n=32). The upper and lower bounds of the box

were the third and first quartiles, respectively while the line within the box was the median. The upper and lower whiskers were maximum and minimum values, respectively. ....	308
Figure 8.3: Intra-operative SWE for GOSH 25 showing the tumour lying under the ventricles. The adjacent deep grey matter did not have any SWE signal. ....	309
Figure 8.4: Intra-operative SWE for GOSH 29 showing the tumour lying under the ventricles at a depth of 5 cm from the transducer. There was a lack of SWE signal in the adjacent brain. ....	309
Figure 8.5: Intra-operative SWE for NHNN 2 showing a soft 'bracket' sign (white arrow). There was a cleavage plane, identified independently by the surgeon, in the corresponding area. ....	312
Figure 8.6: Intra-operative SWE for NHNN 15 showing a soft 'bracket' sign (white arrow), where there was a slippery boundary identified by the surgeon intra-operatively. ....	313
Figure 8.7: Intra-operative SWE for GOSH 55 showing a soft 'bracket' sign for slip plane (white arrow). Intra-operatively. There was a slippery boundary in the corresponding area. ....	313
Figure 8.8: Intra-operative SWE of NHNN 11 showing insufficient signal generated due to insufficient water standoff. ....	314
Figure 8.9: Box and whiskers plot for Young's modulus measurements of normal brain and tumour. The upper and lower bounds of the box were the third and first quartiles, respectively while the line within the box was the median. The upper and lower whiskers were maximum and minimum values, respectively. *There was a significant difference between the 2 groups ( $p = 0.003$ , Wilcoxon's signed-rank test). ....	315
Figure 8.10: Box and whiskers plot of Young's modulus distributions for various tumour types. The upper and lower bounds of the box were the third and first quartiles, respectively while the line within the box was the median. The upper and lower whiskers were maximum and minimum values, respectively. *There was a significant difference between the Young's modulus values for low grade tumour and normal brain ( $p = 0.036$ ) and between metastases and normal brain ( $p = 0.007$ ) but the differences between high grade and normal brain ( $p = 0.125$ ), high grade and low grade ( $p = 0.220$ ), metastases and high grade ( $p = 0.132$ ), and low grade and metastasis ( $p = 0.288$ ), were not significant. Mann Whitney U test was used to perform statistical analysis. ....	315

- Figure 8.11: Box and whiskers plot for Young's modulus according to cellularity grading on histology (n=29). The upper and lower bounds of the box were the third and first quartiles, respectively while the line within the box was the median. The upper and lower whiskers were maximum and minimum values, respectively. There was no statistically significant difference between the median values of the groups ( $p = 0.647$ , Mann Whitney U test).....316
- Figure 8.12: Box and whiskers plot for Young's modulus according to proliferation grading on histology (n=29). The upper and lower bounds of the box were the third and first quartiles, respectively while the line within the box was the median. 'Yes' indicates high proliferation whereas 'No' indicates low proliferation. The upper and lower whiskers were maximum and minimum values, respectively. There was no statistically significant difference between the median values of the groups ( $p = 0.566$ , Mann Whitney U test).....317
- Figure 8.14: Box and whiskers plot for Young's modulus according to the presence of gliosis on histology (n=5). The upper and lower bounds of the box were the third and first quartiles, respectively while the line within the box was the median. The upper and lower whiskers were maximum and minimum values, respectively. 'Yes' and 'No' indicate the presence and absence of gliosis, respectively. There was no statistically significant difference between the median values of the groups ( $p = 0.400$ , Mann Whitney U test).....318
- Figure 8.15: Box and whiskers plot of Young's modulus and cellularity grading on histology (n=56). The upper and lower bounds of the box were the third and first quartiles, respectively while the line within the box was the median. The upper and lower whiskers were maximum and minimum values, respectively. There was no significant difference between lower and higher cellularity ( $p = 0.816$ , Mann Whitney U test).....319
- Figure 8.16: Box and whiskers plot of Young's modulus according to the presence of proliferation on histology (n=56). 'Yes' indicates high proliferation whereas 'No' indicates low proliferation. The upper and lower bounds of the box were the third and first quartiles, respectively while the line within the box was the median. The upper and lower whiskers were maximum and minimum values, respectively. There was a statistically significance increase in Young's modulus with proliferation ( $p = 0.007$ , Mann Whitney U test). \* $p < 0.05$  .....320
- Figure 8.18: Box and whiskers plot for Young's modulus according to the presence of gliosis on histology (n=25). 'Yes' and 'No' indicate the presence and absence of gliosis. The upper

---

and lower bounds of the box were the third and first quartiles, respectively while the line within the box was the median. The upper and lower whiskers were maximum and minimum values, respectively. There was no significant difference in the Young's modulus with the presence of gliosis ( $p = 0.533$ , Mann Whitney U test).....321

Figure A.1: Frequency dispersion of shear wave speed measured using the Aixplorer® in the livers of 10 healthy volunteers. The shear wave speed is directly proportional to its frequency. (Reproduced from Muller et al. (2009)) .....358

## List of Symbols and Abbreviations

$\alpha$	Ultrasound attenuation coefficient.
$\varepsilon$	Strain.
$\sigma$	Stress.
$\sigma_\varepsilon$	Standard deviation of strain.
$\rho$	Tissue density.
$\nu$	Poisson's ratio.
$\mu$	Shear modulus. Also second Lamé's constant.
$\mu_\varepsilon$	Mean strain.
$\lambda$	First Lamé's constant.
$\phi$	Phase.
$\tau$	Shear stress.
$\gamma$	Shear strain.
$\omega$	Vibrating frequency.
$C_o$	Observed contrast.
$C_t$	True contrast.
$a$	Radius of beam aperture.
$D$	Diffraction dimensionless parameter.
$E$	Young's modulus.

---

$f$	Ultrasound frequency.
$F$	Force. Also used for acoustic radiation force
$G$	Shear modulus.
$G^*$	Complex modulus.
$G'$	Storage modulus.
$G''$	Loss modulus.
$i$	Complex number ( $\sqrt{-1}$ ).
$j$	Complex number ( $\sqrt{-1}$ ).
$I$	Temporal average intensity of acoustic beam.
$K$	Bulk modulus.
$M$	Mach number.
$P$	Compressional pressure.
$t_{max}$	Rising time to maximal axial displacement.
$T$	Time.
$W_{absorbed}$	Acoustic power absorbed by the medium.
cm	centimetre.
$c_{sound}$	Speed of sound in tissue. Usually approximately 1540 m/s.
$c_S$	Shear wave speed.
dB	decibel.
exp	Exponential.
Hz	Hertz.

---

kHz	kilohertz.
MHz	megahertz.
$\mu\text{m}$	micrometre.
mm	millimetre.
ms	millisecond.
s	second.
1D	One dimension.
2D	Two dimensions.
3D	Three dimensions.
5-ALA	5-aminolevulinic acid.
ARF	Acoustic radiation force.
ARFI	Acoustic radiation force impulse.
CNR	Contrast-to-noise ratio.
CNR <sub>e</sub>	Elastographic contrast-to-noise ratio.
CT	Computed tomography.
CTE	Contrast transfer efficiency.
CUSA	Cavitron ultrasonic surgical aspirator.
DNT	Dysembryoplastic neuroepithelial tumour.
EEG	Electroencephalography.
FCD	Focal cortical dysplasia.
iCT	Intra-operative computed tomography.

---

iMRI	Intraoperative magnetic resonance imaging.
MEG	Magnetoencephalography.
MRE	Magnetic resonance elastography.
MRI	Magnetic resonance imaging.
MSI	Magnetic source imaging.
PET	Positron emission tomography.
PSF	Point spread function.
QSE	Quasistatic elastography.
RF	Radiofrequency.
ROI	Region of interest.
SD	Standard deviation.
SNR	Signal-to-noise ratio.
SNR <sub>e</sub>	Elastographic signal-to-noise.
SPECT	Single photon emission computed tomography.
SSI	SuperSonic Shear Imaging.
SWE	Shear wave elastography.
US	Ultrasound.
YM	Young's modulus.
YMC	Young's modulus contrast.

## **Chapter 1**

### **Introduction**

This chapter introduces the theory of medical ultrasound imaging and ultrasound elastography, and describes the motivation behind intra-operative shear wave elastography (SWE) in neurosurgery during resection of brain tumours and epileptogenic foci. Previous work on intra-operative ultrasound elastography in neurosurgery is also described, and the aims and contributions of this thesis outlined. It concludes with the outline of this thesis.

## 1.1 Medical Ultrasound

Ultrasound is sound waves with frequency greater than the upper limit of human hearing range. Although this limit varies from person to person and with age, it is approximately 20 kilohertz (kHz). Diagnostic medical ultrasound devices typically use frequencies of 1 - 20 megahertz (MHz). The frequency will determine the resolution of the image and imaging depth. The imaging depth is limited by the attenuation of ultrasound by tissue, which increases with the frequency. For low frequency waves, the wavelength<sup>1</sup> and the pulse length<sup>2</sup> are relatively long, and the beam is relatively wide<sup>3</sup>, resulting in poorer axial and lateral resolution but better imaging depth. In contrast, high frequency waves have a short wavelength and pulse length, and a narrow beam, resulting in higher resolution images with very limiting depth of penetration.

An ultrasound transducer transmits the ultrasound waves and receives the echoes. It emits ultrasound waves through vibration of piezoelectric elements at a frequency determined by their thickness when an electric voltage is applied, a phenomenon known as the reverse piezoelectric effect. When the ultrasound waves hit an interface between different tissues, specifically tissues where there are compressional elastic modulus changes, part of the sound waves get reflected back to the transducer as echoes. These echoes strike the piezoelectric elements to produce an electrical signal (the piezoelectric effect) that travels back to the ultrasound scanner, which processes and transforms them into a digital image.

A single element transducer transmits and receives a single line of ultrasound waves and echoes, respectively. The magnitude of the echoes is proportional to the magnitude of the reflection modified by attenuation of the ultrasound signal due to acoustic absorption and scattering along the path of travel. The depth is determined by multiplying the speed of sound (1540 m/s +/- 6% in soft tissue) with half the time delay between transmit and

---

<sup>1</sup> Wavelength is inversely proportional to frequency, i.e.  $\lambda = \frac{v}{f}$ , where  $\lambda$  is the wavelength,  $v$  is the sound velocity in tissue and  $f$  is the frequency.

<sup>2</sup> Pulse length is twice the axial distance occupied by one ultrasound echo from a point reflector divided by the speed of sound, and is proportional to the wavelength.

<sup>3</sup> Beam width is the lateral distance occupied by one ultrasound echo from a point reflector and is proportional to the wavelength.

receive of the echoes. By plotting the magnitude of the echoes as a function of depth, an A-line is produced which forms the basis for A-mode (amplitude mode) ultrasound, the simplest type of medical ultrasound display. A one-dimensional image is produced when the signal magnitude is recorded digitally as pixel intensity at its corresponding depth.

Most ultrasound transducers in clinical use have a line of elements, known as an array, where groups of adjacent elements fire together acting like a single element. Transmission and reception happen across the array by sequentially exciting different groups of elements with the resultant 2-dimensional (2D) image formed from a row of A-lines, each A-line formed from a different group excitation pattern; this is known as B-mode ultrasound. To achieve better resolution of a B-mode image, the ultrasound beams are focussed into the centre of the region of interest. This is achieved by firing the elements each with slightly different time delay so that the wave fronts converge to focus at certain depth (focal depth).

The granular appearance on a B-mode ultrasound image is known as speckle. The echoes received by the ultrasound transducer come from very small reflectors present in biological tissues. There are many such reflectors within one resolution cell of the scanner (an area of smallest resolvable detail determined by the pulse length and the beam width). The interference between the echoes reflected results in the degree of brightness within one resolution cell. Therefore, the echoes from these small reflectors form the basis of the image of larger structures that resemble anatomical structure familiar to clinicians. Although speckle behaves like noise in that it is visually distracting, if the scan is repeated without changing any experimental variables the same speckle pattern is generated. This property of speckle is used in elastographic imaging.

## 1.2 Ultrasound Elastography

Ultrasound elastography is an ultrasound-based technique of imaging tissue elasticity to characterise different pathologies. The elastic properties of tissues depend on their molecular building blocks and structural organisation of these blocks (Fung, 1993). Therefore, pathological tissues may be characterised by measuring their elastic moduli.

Medical practice of palpation provides qualitative assessment of soft tissue stiffness, and has been the basis of diagnosis of different pathologies including many cancers. Cancerous tissues are normally a lot stiffer than benign lesions, therefore medical practitioners rely on these properties to make the diagnosis and plan treatments. However, due to its high inter-operator variability and difficulty in assessing small deep-seated lesions, various techniques for elasticity imaging have been developed. Ophir et al. (1991), first used the term elastography, to describe a method of quasistatic ultrasound strain imaging. Prior to this, researchers had largely been employing images of tissue displacement. Nowadays, there are 3 main types of ultrasound elastography, namely: quasistatic strain elastography (QSE) (Ophir et al., 1991), shear wave elastography (SWE) (Bercoff et al., 2004; Catheline et al., 1999; Sandrin et al., 2003; Sarvazyan et al., 1998), and acoustic radiation force impulse (ARFI) imaging (Nightingale et al., 2002). These different types of ultrasound elastography and the physics behind them will be discussed in detail in Chapter 3.

### 1.3 Motivation

Numerous studies have shown that survival outcomes are significantly improved with higher extent of resection of brain tumour (Chapter 2). Similarly, seizure outcomes are dependent on the completeness of resection of epileptogenic foci (Chapter 2). Therefore, neurosurgeons aim to perform resection of brain tumours and epileptogenic foci to the maximal extent possible without causing neurological deficit. In order to achieve this target, neurosurgeons usually employ intra-operative tools, which offer spatial orientation, navigational guidance, and up-to-date imaging. However, as these intra-operative tools do not offer elasticity imaging, to gain information on tissue mechanics neurosurgeons ultimately rely on visual inspection and tactile feedback during surgery. Albert et al. (1994) and Orringer et al. (2012) showed that neurosurgeons tend to overestimate the extent of resection of brain tumours by up to 3 times, as judged by post-operative MRI. This could be due to the similarity in appearance of tumour and brain resulting in the neurosurgeon having difficulty in differentiating tumour from brain. This could also be due to the competitive nature of surgeons, tending to over-estimate the “success” of an operation and degree of

resection of tumour. As shown by studies using ultrasound elastography (Chakraborty et al., 2006; Chakraborty, 2007; Scholz et al., 2007; Scholz et al., 2005; Selbekk et al., 2010; Selbekk et al., 2005; Uff et al., 2009; Uff, 2011), these lesions have different stiffness compared to surrounding brain, and hence can be demonstrated on ultrasound elastography.

As described above, ultrasound elastography employs ultrasound technology to image elasticity. Therefore, not only does this imaging modality offer real-time anatomical imaging, it also provides a more objective method of detecting tissue of different stiffness. Another advantage of this modality is that it does not have ionising radiation and is easy to use, allowing neurosurgeons the freedom to use it as many times as required. Finally, it is relatively cheap compared with some of the newer imaging modalities.

## 1.4 Previous work

Intra-operative QSE in neurosurgery was first shown to be feasible by Chakraborty et al. (2004, 2006), by application of compression to the exposed brain to generate strain. Since then, Selbekk et al. (2005, 2010) showed that intra-operative QSE was possible with strain generated through the natural pulsation of the brain. Selbekk et al. (2012) also showed that intra-operative QSE demonstrated a better contrast than B-mode imaging for some brain tumours. Chakraborty et al. (2007, 2012) showed that intra-operative QSE was able to image slippery boundary between the tumour and the surrounding brain, and determine the force required to produce slip at the boundary, known as “slip elastography”. Slippery boundary is the potential surgical plane between the tumour and the brain, where the neurosurgeon can utilise to resect brain tumours. Although these techniques were employed intra-operatively, the elasticity images or elastograms were processed offline, which means at a later time. Therefore, Scholz et al. (2005, 2007) devised a technique known as “vibrography”, where quasistatic strain was generated through a low-frequency low-amplitude vibrator. This technique used the “phase root seeking algorithm”, which requires less computational cost to implement, and thus allowed for the first time real-time elastography using the computer technology at the time.

However, improvements in computer technology have produced many real-time elastographic systems, thus enabling real-time intra-operative ultrasound elastography in neurosurgery. Uff et al., (2009, 2011) showed the feasibility of implementing real-time intra-operative QSE in neurosurgery, and the ability of QSE in demonstrating slippery boundary as high strain at the tumour-brain boundary as well as a characteristic heterogeneous strain pattern within the tumour. In his thesis, Uff (2011) also showed the effect on strain at the boundaries, in the background medium and within inclusions, of soft and stiff inclusions with both adhered and slippery boundaries. In the last part of his thesis, Uff (2011) showed the feasibility of intra-operative SWE in neurosurgery during brain and spinal tumour resection, and focal cortical dysplasia resection in epilepsy patients. He also provided a preliminary demonstration of the relative elasticity of grey and white matter. However, the artefacts of intra-operative SWE were not studied, nor were reasons for the difference in grey and white matter explained, and no study was performed of the SWE characteristics of brain tumours. Furthermore, the features of SWE for different tumour boundary conditions were not explored. Therefore, the work of this thesis represents an in-depth study of intra-operative SWE in neurosurgery for both brain tumour and epileptogenic foci resection.

## 1.5 Aims

The aims for this project are as follows:

1. As SWE is a quantitative elasticity imaging technique, the validity of the measurements must first be determined. Therefore, the first aim of this thesis is to establish their validity by verifying the measurements against those made using a standard rheometer (Instron 3342 with load-cell 2519-103, Instron, Bucks, UK) using homogeneous gelatine phantoms. To extend the verification of the measurements to living tissue, post-mortem mouse brain measurements are compared with magnetic resonance elastography (MRE). Both the experiments are described in Chapter 4.

2. To establish the artefacts that are created during intra-operative scanning, a preliminary clinical study involving the first 10 patients is performed. Each of the suspected artefacts encountered is documented and investigated in detail in the laboratory using gelatine phantoms. Some artefacts are not easily modelled with gelatine phantoms. For these, post-mortem porcine brains and spinal cords are used to study the artefacts. Through these experiments, recommendations to produce good quality intra-operative SWE images are listed. The preliminary clinical study is described in Chapter 5 and the investigations of the artefacts together with recommendations for intra-operative scanning are described in Chapter 6.
  
3. Having established the validity of SWE measurements and characterised the clinical intra-operative artefacts, clinical studies are performed on patients undergoing craniotomy for brain tumour and epileptogenic focus resection, with the aims as follows.

Epileptogenic foci can be difficult to visualise on MRI scans, and sometimes are even absent. However, it was shown that they can have different elasticity to, in particular be stiffer than, surrounding brain (Uff, 2011). Therefore, for the epileptogenic focus group, the aims of the clinical study are to determine the ability of SWE in visualising epileptogenic foci, and the correlation of Young's modulus measurement with histology. To establish whether the lesions excised under guidance of elastography are responsible for epileptogenicity, the seizure outcomes of these patients were also recorded. This clinical study is described in Chapter 7.

As brain tumours are sometimes difficult to differentiate from surrounding brain, especially during and after resection, it is hypothesised that SWE may identify the tumour residual more accurately through elasticity imaging. Therefore, for the brain tumour group, the aims of the clinical study are to establish the ability of SWE in detecting residual tumour and differentiating between tumour and brain, and the

correlation of Young's modulus measurements with histology. This clinical study is described in Chapter 8.

## 1.6 Thesis outline

This thesis has a total of 9 chapters. This chapter introduces medical ultrasound and the concept of ultrasound elastography, and describes the motivation behind the use of intra-operative ultrasound elastography in neurosurgery.

Chapter 2 reviews the literature on the resection of brain tumours and epileptogenic foci, to establish the evidence to support the practice of maximal extent of resection to achieve better clinical outcomes. It also performs literature reviews on intra-operative application of ultrasound elastography in neurosurgery, and discusses the pros and cons of the different approaches. It concludes with the hypotheses for this thesis.

Chapter 3 describes the theory of elasticity, and the physics behind each of the different ultrasound elastography systems. It concludes with the recommended settings and operating steps for the use of Supersonic Aixplorer® scanner for intra-operative SWE measurements on the brain.

Chapter 4 shows the verification of SWE measurement of Young's modulus by comparison with compressive rheometer measurements using gelatine phantom models. Then, using post-mortem mouse brains, the SWE measurements are compared against MRE measurements to further validate the measurements in living tissue.

Chapter 5 describes the preliminary clinical study involving 10 patients undergoing craniotomy for both brain tumour and epileptogenic foci resection. It documents the artefacts encountered in these patients and which required study in laboratory investigations in Chapter 6.

Chapter 6 describes the laboratory experiments to characterise the artefacts encountered in the first 10 patients. In addition, it also describes the laboratory experiments for characterising the artefacts shown by other literature relevant to SWE. It also reports

---

the characterisation of boundary conditions by SWE. It concludes with recommendations regarding the implementation of intra-operative scan acquisitions for clinical study.

Chapter 7 describes the clinical application of intra-operative SWE during epileptogenic focus resection. It compares the SWE measurements of these lesions with surgical findings. It also compares the visibility of these lesions on intra-operative SWE with magnetic resonance imaging (MRI) scan. It also reports the seizure outcomes from resection of these lesions. It concludes by reporting the correlation between SWE measurements and histological features of these lesions.

Chapter 8 demonstrates the clinical application of intra-operative SWE during brain tumour resection. It reports the comparison between SWE measurements and surgical findings. It also compares SWE findings of residual tumour with post-operative MRI scan. From the SWE characteristics of slip inclusion-background interface in gelatine phantoms shown in Chapter 6, it reports on the SWE appearance of slip tumour-brain interface *in vivo*. It concludes by reporting on the correlation between SWE measurements and histological features of the tumours.

Chapter 9 summarises the main findings of this thesis, and discusses the achievements and limitations of this project. It also reports on its novelty and contribution to knowledge. It concludes by summarising the hypotheses being tested and stating the extent to which the findings are consistent with these hypotheses.

## **Chapter 2**

### **Literature Review**

This chapter discusses the literature relating to the resection of brain tumour and epileptogenic foci. Next, it examines the different types of ultrasound elastography systems and their applications in clinical practice. Finally, it reviews the use of ultrasound elastography intra-operatively in the resection of brain tumour and epileptogenic foci. This chapter concludes with the hypotheses for the project.

## 2.1 Brain tumour resection

The age-standardised incidence rate of brain tumours in the United Kingdom is 12.4 per 100,000 population (“Brain, other CNS and intracranial tumours incidence statistics,” 2013). Brain tumours can be grouped into intrinsic and extrinsic. The intrinsic tumours grow and infiltrate within the brain tissue. The extrinsic tumours grow from the structures surrounding the brain tissue such as meninges, cranial nerves, pituitary gland and the skull.

### 2.1.1 Extrinsic brain tumours

Extrinsic tumours account for less than half of the all brain tumours – 23% meningioma, 11% endocrine glands and 8% other central nervous system (“Brain, other CNS and intracranial tumours incidence statistics,” 2013). These tumours cause symptoms by the following mechanisms:

- 1) Localised pressure effect on cranial nerves or brain, causing focal neurological deficit and seizures.
- 2) Increased generalised pressure within the skull (intracranial pressure) due to size of the tumour and surrounding brain swelling known as oedema.
- 3) Blocking the cerebrospinal fluid (CSF) drainage pathways causing hydrocephalus, which is a condition where there is excessive accumulation of fluid within the skull.

As most of these tumours are benign, the treatment strategy is for complete excision of such tumours resulting in cure for these patients. Incomplete excision of extrinsic tumours can result in 3 possible outcomes: 1) persistence of symptoms requiring additional treatment; 2) growth or malignant transformation of residual tumour to cause symptoms in the future; or 3) additional treatment with other modalities such as radiation in the hope of killing off the residual tumour cells. Therefore, it is clear that the best outcome is with complete excision.

### 2.1.2 Intrinsic brain tumours

In contrast to extrinsic tumours, intrinsic tumours tend to be malignant. In addition to the symptoms such as localised pressure effect, seizures, raised intracranial pressure and hydrocephalus, these tumours are also capable of invading and destroying normal brain tissue, hence causing irreversible damage and making complete excision difficult. Although surgeons rely on visual inspection and tactile feedback during tumour resection to assess completeness of resection, this method is not accurate as it has been shown that surgeons underestimate residual tumour when compared with an early post-operative MRI scan (Albert, et al., 1994; Orringer et al., 2012). Albert et al. (1994) showed that 71% of the cases were deemed to have complete resection by the surgeon while only 18% were evident on early post-operative MRI, indicating a 3-fold overestimation by the surgeon. In the study by Orringer et al. (2012), 50% of the cases were deemed completely resected by the surgeon while only 17.4% were proven radiographically, and of those deemed to have been completely resected by the surgeon, only 30.4% were evident on MRI, indicating an overestimation by a similar magnitude to that estimated by Albert et al. (1994). This is true not only for small residual tumours but also for relatively large tumour remnants. The reason for this is that intrinsic tumours tend to have similar visual and textural characteristics to surrounding brain (Albert et al., 1994). Therefore, this calls for a more improved visualisation or detection of tumour residual. Elastography has been shown previously that tumours may have a different stiffness to surrounding brain. It may therefore be a candidate modality to visualise tumour residual. Furthermore, with SWE, which is said to be quantitative and objective, it may be possible to detect the effect of the presence of residual tumour even though it is not clearly visualised.

#### 2.1.2.1 High grade glioma

Of the primary brain tumours, more than 50% of intrinsic tumours are high-grade glioma (Hervey-Jumper & Berger, 2014). Despite improvement and optimisation in the treatment modalities for high-grade glioma, the median survival rates are still only 12.2 to

18.2 months and 41 months for glioblastoma multiforme (GBM) and anaplastic astrocytoma (AA), respectively (Hegi et al., 2005; Keles et al., 2006).

There have been numerous studies looking at the impact of the extent of resection on the survival of patients with high-grade gliomas. Neurosurgeons may have to balance and trade-off of surgical complications and resection extent. Increased resection extent, especially in eloquent areas<sup>4</sup>, may lead to more handicap. In these cases, the neurosurgeon may consider a more conservative approach to achieve a better quality of life. When the tumour is in non-eloquent areas, the neurosurgeon may want to achieve greater extent of resection as the risk of resulting in functional deficit is low.

There is only one randomised study looking at debulking versus solely biopsy of GBM (Vuorinen et al., 2003). The study randomised 30 patients over the age of 65 years into stereotactic biopsy only and resection groups. Only 23 patients were included (19 GBM and 4 AA) as 6 patients had diagnosis other than high-grade glioma (infarct ( $n = 1$ ), haematoma ( $n = 2$ ), metastasis ( $n = 2$ ) and malignant lymphoma ( $n = 1$ )), and 1 patient withdrew consent. One patient required re-operation due to post-operative haematoma. The median survival time for the debulking group is higher than biopsy group (171 days versus 85 days). The difference was statistically significant ( $p = 0.0346$ ). Tumour grade-adjusted hazard ratio for deterioration was 2.8 suggesting that the patients having biopsy only are 2.8 times higher risk of deterioration compared with those having debulking. The grade-adjusted hazard ratio is statistically significant ( $p = 0.049$ ). However, although there was a shorter time to deterioration of 72 days in the biopsy group compared with 105 days in the debulking group, the difference was not statistically significant ( $p = 0.0566$ ). Two of the drawbacks of this paper are that it is underpowered due to the small number of patients included in the study, and it only looked at a small subgroup of the population, i.e. those above 65 years old. Additionally, in the debulking group, there was heterogeneity of the extent of resection, with 2 total resections, 7 subtotal resections ( $>70\%$ ) and 1 limited resection ( $<70\%$ ). The distribution of patients between the 2 groups was also unequal, with exclusively GBM in the debulking group and mixture of AA and GBM in the biopsy group.

---

<sup>4</sup>important areas if injured will lead to functional deficit.

Thus although there was no significant difference between the time to deterioration for the two groups, if there were truly no benefit from debulking, one would have expected the opposite result, that is, a substantially worse time to deterioration for the debulking group (due to the lower number of GBM in the biopsy only group). This implies that the result could have been improved if the two groups had been composed of only AA or GBM, but this was not possible due to the small sample size.

Table 2.1 summarises the recent studies since 2000 (Lacroix et al., 2001; Laws et al., 2003; McGirt et al., 2009; Nomiya, et al., 2007; Oszvald et al., 2012; Pope et al., 2005; Sanai, et al., 2011; Stummer et al., 2006; Ushio, et al., 2005), which analysed the role of extent of resection on survival time for high-grade glioma, where data were obtained either retrospectively or prospectively but without randomisation. Three out of 9 studies used volumetric analysis to assess the extent of resection. The extent of resection was determined by neuroradiologists (McGirt et al., 2009; Oszvald et al., 2012; Pope et al., 2005; Stummer et al., 2006), by neurosurgeons through the use of segmentation software (Sanai et al., 2011; Lacroix et al., 2001), and by both neuroradiologists and neurosurgeons (Nomiya et al., 2007). Laws et al. (2003) compared patients who underwent biopsy with those who had resection, and did not attempt to determine the radiographic extent of resection in the resection group. Ushio et al. (2005) did not specify who determined the extent of resection. All except one retrospective study (Pope et al., 2005) showed that there is a survival advantage with greater extent of resection with statistical significance. Of the 8 studies that demonstrated advantage of increased extent of resection, 5 were prospective studies.

Hervey-Jumper & Berger (2014) reviewed 31 recent studies, which included the studies reviewed above. Three out of 5 volumetric studies and 13 out of 24 non-volumetric studies supported a significant survival benefit with greater extent of resection. The authors concluded that greater extent of resection improves survival rates for both AA (from 64.9 to 74.2 months) and GBM (from 11.3 to 14.5 months). Using a more stringent criteria, a review by Hart et al. (2014) excluded all non-randomised studies and ended up with only one study with randomisation to biopsy and resection (Vuorinen et al., 2003), which is the same study described above. Hart et al. (2014) concluded that this study was “of insufficient reliability to be used to influence treatment decisions” but showed that

randomised studies are feasible in this area and should be used as building blocks for future randomised studies.

Authors, Year	Volumetric analysis	Number of cases	Histology	Retrospective/prospective	Extent of resection	Mean survival (Months)	Surgery improves survival
Lacroix et al., 2001	Yes	416	GBM	Prospective	<98%	8.8	Yes
					>98%	13	
Laws et al., 2003	No	565	AA & GBM	Prospective	Biopsy (AA)	12	Yes
					Resection (AA)	20	
					Biopsy (GBM)	4.8	
					Resection (GBM)	10.5	
Pope et al., 2005	Yes	151	AA & GBM	Retrospective	<20%	27.4	No
					20 – 89%	11.1	
					90 – 99%	17.1	
					100%	22.1	
Ushio et al., 2005	No	105	GBM	Prospective	Biopsy	8.3	Yes
					Subtotal	14.2	
					Total	20	
Nomiya et al., 2007	No	170	AA	Retrospective	Biopsy & Partial (<75%)	22.9	Yes
					Subtotal (75% - 99%) & Total	62.6	
Stummer et al., 2008	No	243	GBM	Prospective	Subtotal	11.8	Yes
					Total	16.7	
McGirt et al., 2009	No	949	AA & GBM	Retrospective	Subtotal (AA)	34	Yes
					Near total (AA)	46	
					Total (AA)	58	
					Subtotal (GBM)	8	Yes
					Near total (GBM)	11	
					Total (GBM)	13	
Sanai et al., 2011	Yes	500	GBM	Retrospective	≥78%	12.5	Yes
					≥80%	12.8	
					≥90%	13.8	
					100%	16	
Oszvald et al., 2012	No	146 (≥65y) 215 (<65y)	GBM	Prospective	Biopsy (<65y)	7.9	Yes (biopsy vs resection only)
					<96% (<65y)	13.3	
					96-99% (<65y)	15.3	
					Total (<65y)	16.5	
					Biopsy (≥65y)	4	Yes (both biopsy and extent of resection)
					<96% (≥65y)	11.4	
					96-99% (≥65y)	16.1	
					Total (≥65y)	17.7	

Table 2.1. Table summarising the studies since 2000 looking at survival and extent of resection of high-grade glioma. AA = anaplastic astrocytoma; GBM = glioblastoma multiforme.

Even for recurrent GBM, the benefit from greater extent of resection is less clear. Bloch et al. (2012) retrospectively analysed 107 patients who underwent a second operation for recurrence. The authors showed that for patients who underwent gross total resection (GTR) (>95% resection by volume) for initial operation, greater extent of resection did not confer a statistically significant ( $p = 0.2$ ) survival benefit – median survival 11.5 months for GTR versus 8.5 months for subtotal resection (STR), defined as  $\leq 95\%$  resection by volume. However, for patients who underwent STR for initial operation, there is a statistically significant survival benefit with increased extent of resection – median survival 19.0 months for GTR versus 15.9 months for STR.

In summary, the available evidence suggests that there may be survival advantage to the patients with greater extent of surgical resection of high-grade glioma. There is only one randomised controlled study (Vuorinen et al., 2003) showing that debulking improved median survival time and time to deterioration but it was underpowered with small number of subjects recruited. All the other studies (5 prospective and 4 retrospective) showed improvement in mean survival time for greater extent of resection for high grade glioma.

### ***2.1.2.2. Low-grade glioma***

Low-grade glioma is a diffuse neuro-ectodermal tumour, accounting for 15% of all gliomas (Capelle et al., 2013). Median survival times have been reported between 5 and 10 years (Keles, et al., 2001). For WHO grade I glioma, the management is surgical resection, and complete resection confers cure in patients with these tumours. Conversely, the management of WHO grade II glioma is still being debated due to the lack of a randomised trial (Pouratian & Schiff, 2010). However, there is growing evidence favouring more extensive resection in patients with WHO grade II glioma (Keles, et al., 2001).

Keles et al. (2001) identified 30 non-randomised series of patients with low-grade glioma, published between 1970 and 2000. After excluding series with paediatric populations, unless adults were analysed separately, series with low numbers of patients ( $< 75$ ) and series including pilocytic or gemistocytic astrocytoma, only 5 series remained and were evaluated in detail. Table 2.2 is the summary table from the paper showing the 5 series evaluated in

detail. This review found that only 1 series (Leighton et al., 1997) determined the residual tumour by post-operative imaging whereas the rest relied on surgeon's intra-operative perception. This review found extent of resection to be a statistically significant prognostic factor in all 5 series using univariate analysis but only in 4 out of 5 series when multivariate analysis was performed. Table 2.2 shows that in all series, the 5-year survival rates increased from partial resection (PR) / subtotal resection (STR) / bulky residual disease (RD) / <75% resection (res) to gross total resection / minimal RD / >75% res, and in 2 series (Leighton et al., 1997; Soffiatti, et al., 1989), the median survival times increased from 1.6 years for PR through 3.3 years for STR to 5 years for GTR, and 8.4 years for bulky RD to 10.7 years for minimal RD.

Authors & Year	Years of Study	No. of Pts	Groups	No. of Pts	5-Year PFS Rate (%)	5-Year S Rate (%)	10-Year S Rate (%)	MST (yrs)	UV p Value	MV p Value
Soffiatti et al., 1989	1950 – 1982	81	GTR	19	NA	51	11	5	<0.001	<0.01
			STR	49	NA	24	3	3.3		
			PR	13	NA	0	0	1.6		
Phillippon et al., 1993	1978 – 1987	179	GTR	45	NA	80	NA	NA	0.0002	<0.01
			STR	95	NA	50	NA	NA		
			Bx	39	NA	45	NA	NA		
Rajan et al., 1993	1974 – 1990	82	GTR	11	NA	90	68	NA	<0.05	NS
			STR	30	NA	52	36	NA		
			PR	22	NA	50	31	NA		
			Bx	19	NA	42	28	NA		
Leighton et al., 1997	1979 – 1995	167	min RD	82	NA	82	59	10.7	0.008	0.006
			bulky RD	85	NA	64	41	8.4		
van Veelen et al., 1998	1975 – 1989	90	>75% res	13	46	62	NA	NA	0.002	0.04
			<75% res	59	10	18	NA	NA		
			Bx	18	28	33	NA	NA		

Table 2.2: Summary of the series of low grade glioma evaluated in Keles et al. (2001) for the effect of extent of resection on survival. Abbreviations: MST=median survival time; PFS=progression-free survival; res=resection; S=survival. (Adapted from Keles et al., 2001)

There have been 8 more studies since 2000 evaluating the extent of resection of low-grade glioma as a prognostic factor (Capelle et al., 2013; Claus et al., 2005; Johannesen, et al., 2003; McGirt et al., 2008; Nakamura et al., 2000; Shaw et al., 2002; Smith et al., 2008; Yeh et al., 2005). They are summarised in Table 2.3. None of the studies were randomised controlled trials. All except one of the studies (Johannesen et al., 2003) showed a survival

advantage with increased extent of resection with statistical significance. Although Johannesen, et al. (2003) failed to show statistical significance, the result showed improved survival with increased extent of resection. The limitation of this study is that the extent of resection was based purely on surgeon's intra-operative perception, which has been shown to be unreliable (Albert et al., 1994; Orringer et al., 2012).

Authors, Year	Volumetric analysis	Number of cases	Retrospective/prospective	Extent of resection	Mean survival (Years)	5-year survival (%)	Surgery improves survival
Nakamura et al., 2000	No	88	Retrospective	"Non-radical"	4.3	NA	Yes (p < 0.001)
				"Radical"	11.3	NA	
Shaw et al., 2002	No	203	Prospective	Bx	NA	71	Yes (p = 0.0116)
				STR	NA	56	
				GTR	NA	88	
Johannesen et al., 2003	No	993	Retrospective	Bx	6.4	57.8	Not significant (p = 0.59)
				STR	6.8	59	
				GTR	7.6	62.7	
Yeh et al., 2005	No	93	Retrospective	Subtotal	NA	52	Yes (p = 0.0349)
				Total	NA	92	
Claus et al., 2005	Yes	156	Retrospective	STR	NA	92	Yes (p = 0.05)
				GTR	NA	98.2	
Smith et al., 2008	Yes	216	Retrospective	<90%	NA	76	Yes (p < 0.001)
				>90%	NA	97	
				100%	NA	98	
McGirt et al., 2008	No	170	Retrospective	STR	NA	70	Yes (p = 0.017)
				NTR	NA	80	
				GTR	NA	95	
Capelle et al., 2013	Yes	929	Retrospective & prospective	<50%	NA	NA (~76)	Yes (p = 0.0199)
				50-99%	NA	NA (~88)	
				Total	NA	NA (~100)	

Table 2.3. Summary of studies since 2000 looking at extent of resection of low-grade glioma on survival. GTR = gross total resection; NTR = near total resection; STR = subtotal resection; Bx = biopsy; NA = not available. NB. The prefix "~" symbol represent approximate value from interpretation of the graph as value is not available in the text or table.

Hervey-Jumper & Berger (2014) examined 21 studies since 1990 and found 7 of 8 studies and 4 of 5 volumetric studies showed evidence to support extent of resection as a statistically significant prognostic factor for low-grade glioma. The authors concluded from these studies that the mean survival times improved from 61.1 to 90 months with maximal resection.

A population-based study by Jakola et al. (2012) looked at 153 patients treated at 2 different Norwegian hospitals, one favouring "watchful waiting" policy while the other early

resection. This study showed that the median survival time for the “watchful waiting” group was 5.8 years while that of the early resection group was not reached in the median follow-up period of 7 years. The 5-year survival rates were 60% and 74% in the “watchful waiting” and early resection groups, respectively. The difference was statistically significant ( $p = 0.01$ ). Therefore, although this is not a randomised study, it took advantage of differing approach to treating low-grade glioma in these 2 centres, and showed with statistical significance that early resection improves survival outcomes compared with just biopsy and “watchful waiting”.

Another reason for improved outcomes from maximal resection is that 13% to 86% of patients with low-grade glioma will undergo malignant transformation with the time to malignant transformation of 28 to 60 months (Keles et al., 2001). Smith et al. (2008) demonstrated a statistically significant malignant progression-free survival with greater resection ( $p = 0.005$ ).

In summary these studies, despite being not randomised, showed the evidence that earlier and more extensive resection can result in a better overall survival and malignant progression-free survival outcomes in low-grade glioma. The closest to randomised trial is the population study by Jakola et al. (2012), making use of the different approach to low grade glioma in 2 different hospitals (one favouring early resection while the other favouring “watchful wait”), which showed improvement in median survival time in the early resection group.

### 2.1.3 Current techniques to improve extent of resection

As described above, improved surgical outcomes can be achieved by performing function-preserving maximal resection of both extrinsic and intrinsic brain tumours. In order to gain access to the intracranial compartment, neurosurgeons have to perform a craniotomy, i.e. removal of skull bone. The placement and size of a craniotomy plays a vital role in brain tumour resection, as small and precisely placed craniotomy can locate the tumour accurately and minimise iatrogenic injury to the underlying cortex and white matter (Sabin & Whittle, 1990). A larger craniotomy is sometimes required to expose important vascular structures to

facilitate safe resection such as superior sagittal sinus when resecting parafalcine meningioma. Frameless stereotactic neuronavigation allows 3-dimensional (3D) navigation with a pointing device, and has become a routine neurosurgical practice (Golfinos et al., 1995). Dorward et al. (1999) demonstrated that the accuracy of frameless stereotactic neuronavigation in phantom-based *in vitro* testing was 1.1mm for CT-guided and 1.4mm for MRI-guided neuronavigation whereas the accuracy in patients was 2.5mm for CT-guided and 2.6mm for MRI-guided neuronavigation. The lower accuracy in patients compared with phantoms may be due to inexact pre- and post-operative images, brain shift and imaging errors. Therefore, frameless stereotactic neuronavigation is a useful tool in planning neurosurgical exposure for brain tumour resection.

After gaining access into the intracranial compartment, neurosurgeons need to determine the location of the tumour to facilitate removal of such lesion. Intra-operative tools have been developed to help neurosurgeons maximise surgical resection while minimising neurological deficit. These include frameless stereotactic neuronavigation, fluorescence imaging, intra-operative computed tomography (iCT), intra-operative MRI (iMRI), and intra-operative ultrasound (IOUS).

### ***2.1.3.1 Frameless stereotactic neuronavigation***

As pointed out above, frameless stereotactic neuronavigation has become a routine surgical practice (Golfinos et al., 1995) as it helps neurosurgeons in planning craniotomy and surgical approach to the tumour. Once craniotomy is performed, the intracranial pressure changes; if the pressure was higher than atmospheric pressure before craniotomy, then craniotomy will cause the intracranial structures, i.e. brain and the tumour, to bulge; otherwise, craniotomy will result in the sinking of the intracranial structures. In brain tumour resection, it is invariably the former that is encountered as the presence of tumour will cause space occupying effect and therefore result pressure increase. This means that the brain previously compressed by the tumour will re-expand slightly, the extent of which will be limited by the dura, which is the outer covering of the brain. Opening the dura will cause further shift in the intracranial structures due to loss of tight constraints from the dura and

loss of buoyancy effect from CSF outflow and gravity. During tumour resection, further shift will be seen due to tissue removal, brain retraction, re-expansion of the brain and ventricles, and the effects on intracranial structures by the administration of anaesthesia including anaesthetic drugs and mechanical ventilation, and diuretic medication. Using neuronavigation and its software measurement tool, Dorward et al. (1998) showed that the shift increased as the operations proceeded: the mean shifts of the cortex<sup>5</sup> after dural opening and at completion of resection were 4.6mm and 6.7mm, respectively. This was supported by a study using 0.2-Tesla iMRI (Nimsky et al., 2000), which showed that mean cortical and deep tumour margin shift was 8.4mm and 4.4mm, respectively. Another study by Keles et al. (2003), utilising intra-operative ultrasound co-registered with neuronavigation, showed that a cortical shift of 3.5mm was noted.

A prospective randomised controlled trial by Willems et al. (2006) looked at the extent of solitary tumour resection with and without neuronavigation. The authors recruited 45 patients – 23 patients were randomised to neuronavigation group and 22 patients to the standard (without neuronavigation) group. Although this trial showed that the mean residual tumour and contrast-enhancing residual tumour volumes were less in the neuronavigation group (13.8% and 24.4%) compared with the standard group (28.9% and 29.2%) with a non-significant difference ( $p = 0.28$  and  $p = 0.90$ ), more patients in the standard group achieved GTR compared with the neuronavigation group (5 versus 3). There was more neurological deficit noted in the standard group (45.5% versus 18.2%), albeit without a significant difference ( $p = 0.10$ ). This trial failed to show a significant improvement in the extent of resection with neuronavigation. In fact, the GTR rate was higher in the standard group, indicating that whilst neuronavigation may assist in tumour resection, neurosurgeons may still be relying on their visual inspection and tactile feedback when assessing the extent of resection.

---

<sup>5</sup> Cortex refers the outermost layer of the brain.

### **2.1.3.2 Intra-operative CT (iCT)**

In the early 1980s, Lunsford et al. (1984) pioneered the technique of using iCT to improve the extent of glioma resection. Further surgical series by the same group (Engle & Lunsford, 1987) showed that increased extent of tumour resection with iCT. However, iCT is being superseded by iMRI for guiding glioma resection, as the latter offers better soft tissue contrast and does not expose the patient to ionising radiation.

### **2.1.3.3 Intra-operative MRI (iMRI)**

The motivation for the use of iMRI over conventional frameless stereotactic neuronavigation is to overcome the brain shift described above. First introduced in 1994 was a 0.5-Tesla iMRI, which has a ‘double doughnut’ configuration with the surgeon standing in the gap between the 2 halves of the magnet (Black et al., 1997). iMRI has developed in 2 directions: ultra low-field-strength iMRI and high-field-strength iMRI. Ultra-low-field strength refers to systems with 0.5-Tesla or less magnet whereas high-field strength refers to those with 1.5- to 3-Tesla magnet.

A randomised controlled trial performed by Senft et al. (2011) investigated the effect of ultra-low-field strength iMRI on the extent of resection of glioma. The authors randomised 24 patients to iMRI group and 25 patients to conventional group. The study showed that iMRI group achieved significantly higher complete resection rate compared with conventional group (96% versus 68%;  $p = 0.023$ ). At 6 months, significantly fewer patients in the iMRI group had progressive disease compared with conventional group (36% versus 64%;  $p = 0.046$ ).

However, Senft et al. (2011) also showed that iMRI added a mean of 67 minutes to the overall operating time; the mean operating time in the iMRI group was 429 minutes compared with 362 minutes in the conventional group, with a statistically significant difference ( $p = 0.007$ ). This was further supported by a retrospective database analysis (Shah et al., 2012), which showed an increase of 107 minutes in the iMRI operating time (mean 350 minutes versus 243 minutes;  $p < 0.0001$ ). Another drawback of this technique is

the relatively long image acquisition time, i.e. about 13.5 to 73 minutes (Kubben et al., 2011), precluding real-time imaging capability. Furthermore, the high cost of iMRI would limit its use to affluent neurosurgical units.

#### 2.1.3.4 Fluorescence imaging

The fluorescence imaging exploits the fact that there is increased accumulation of fluorescent porphyrins<sup>6</sup> in malignant glioma when 5-aminolevulinic acid (5-ALA) is administered (Stummer et al., 2006). 5-ALA was initially developed as a photosensitising agent for photodynamic therapy for gastrointestinal tract tumours (Regula et al., 1995) and skin conditions (Wolf et al., 1993) because exogenous 5-ALA administration leads to relatively low activity of ferrochelatase, an enzyme responsible for converting protoporphyrin IX to haem, thereby resulting in accumulation of protoporphyrin IX within cells (Regula et al., 1995). Furthermore, 5-ALA is also metabolised at tissue level to protoporphyrin IX, which is responsible for *in vivo* photosensitisation. Therefore, patients who were administered with 5-ALA needed to stay away from direct sunlight as elevated levels of protoporphyrin IX render them photosensitive to direct sunlight for 1-2 days (Regula et al., 1995).

Protoporphyrin IX has an intracellular concentration peak at 6 hours, and remains elevated at 24 hours (Stummer et al., 1998). Using violet-blue light with wavelength of 375 nm to 440 nm will cause porphyrins, which have an absorption band of 405 nm, to emit red fluorescence at 635nm and 704nm in brain tissue (Stummer et al., 1998). Therefore, in practice, patients are given either oral or intravenous solution of 5-ALA 3 hours prior to induction of anaesthesia, aiming to complete tumour removal approximately 4-5 hours after 5-ALA administration. A long-pass filter mounted to the surgical microscope enables the operator to switch between white and violet-blue light to facilitate tumour visualisation.

A randomised controlled trial conducted by Stummer et al. (2006) randomised 322 patients with suspected malignant glioma into conventional white light microsurgery

---

<sup>6</sup> Porphyrins are a group of organic compound, many of which are naturally occurring. Protoporphyrin IX is a specific porphyrin contained in haem B, which is a constituent of haemoglobin and myoglobin.

(conventional) group (n = 161) and fluorescence-guided surgery (5-ALA) group (n = 161). The extent of resection of contrast-enhancing tumours in the 5-ALA group was significantly better than in the conventional group (65% versus 36%,  $p < 0.0001$ ). The 6-month progression free survival also improved in the 5-ALA group (41.0%) compared with conventional group (21.1%) with statistically significant difference ( $p = 0.0003$ ). Therefore, this provides Class 1 evidence supporting that fluorescence-guided surgery improves extent of resection and confers survival benefit.

However, there are some limitations with this technique. During surgery, blood contaminating the tumour cavity completely obscures the fluorescence emitted from tumour (Stummer et al., 1998). In cases where corticotomy is smaller than the tumour, overlying brain tissue can also prevent detection of the fluorescence signal. As low-grade glioma does not fluoresce with 5-ALA administration, this technique is not applicable in patients with this group of tumours. This technique also cannot be used in patients who develop sensitivity to 5-ALA or porphyrin. Lastly, this technique can be cumbersome to implement. Patients will have to ingest 5-ALA 6 hours prior to surgery (or 3 hours prior to anaesthesia) and need to stay away from direct sunlight for 48 hours afterwards, to allow peak levels to be reached during surgery and to avoid photosensitivity side effects. This has an implication for longer hospital stay and higher treatment cost.

### ***2.1.3.5 Intra-operative ultrasound (IOUS)***

Although B-mode IOUS has been used in neurosurgery since the 1980s (Chandler & Rubin, 1987), its application has been limited due to low image quality, unfamiliarity with ultrasound (US) among neurosurgeons, and user-dependent variability in image interpretations, especially with unexplained artefacts (Woydt et al., 1996). Technological advances in IOUS with improved image quality and co-registration capability with neuronavigation system (Gronningsaeter et al., 2000) have revived its use in neurosurgery. The advantages of IOUS over other intra-operative adjuncts are that it is relatively cheap, quick and easy to set up and use, and allows real-time imaging. Le Roux et al. (1992) showed in a prospective study that while some low-grade gliomas are not visible on CT scan,

IOUS successfully visualised all the low-grade gliomas in this study. The authors also reported 85% sensitivity for IOUS in detecting residual tumour with histological confirmation. In another prospective study of 70 patients (Hammoud et al., 1996), IOUS successfully visualised all gliomas and metastatic lesions, with well-defined margin in all 18 gliomas with no previous therapy (primary gliomas) and all 34 metastatic lesions. In contrast, previous surgery and radiation artefacts resulted in poor definition of the tumour margins by IOUS. Using post-operative MRI as the gold standard, IOUS had 67% sensitivity in detecting residual tumour overall, with a non-significant mean tumour volume difference of 0.02 cc ( $p = 0.97$ ). In metastatic lesions, IOUS successfully identified total resection of all of the lesions as confirmed on post-operative MRI. Another prospective study comparing IOUS with post-operative MRI scan (Erdoğan et al., 2005) showed a similar sensitivity of 69% in detecting residual tumour, using post-resection hyperechoic rim of <5mm thick as normal findings. Using histology of biopsy specimens from post-resection hyperechoic rim of <3mm thickness, Woydt et al. (1996) showed that 26% was solid tumour, 35% infiltrative zone<sup>7</sup>, and 39% normal brain, in high-grade tumour resection, while 100% was infiltrative zone in low-grade tumour resection. On intra-operative microscopic assessment by experienced<sup>8</sup> neurosurgeons, post-resection hyperechoic rim was deemed normal, so these cases would have traditionally been considered total resection. Furthermore, post-resection irregular hyperechogenicity with similar appearance to tumour confirmed on histology as solid tumour, 75% and 64% of high-grade and low-grade tumours, respectively, were considered normal by the neurosurgeons, further confirming the difficulty in differentiating tumour from normal brain on visual inspection. In a study comparing IOUS with high-field iMRI (Gerganov et al., 2011), IOUS was able to define pre-resection tumour borders almost as well as iMRI (81.8% versus 90.9%) with the advantage of short acquisition time. Therefore, while having a good sensitivity of 67% to 85% in detecting residual tumour, IOUS still presents the user with the difficulty of interpreting artefacts such as those due to previous surgery, radiation changes and hyperechoic rim. Other artefacts include acoustic

---

<sup>7</sup> Infiltrative zone was defined by the authors (Woydt et al., 1996) as scattered tumour cells in normal brain tissue.

<sup>8</sup> More than 10 years experience.

shadowing from Surgicel®<sup>9</sup> (Erdoğan et al., 2005), hyperechogenicity of peritumoural oedema (van Velthoven & Auer, 1990), and hyperechoic band of blood clot (van Velthoven & Auer, 1990).

To overcome the orientation problem encountered with IOUS, Gronningsaeter et al. (2000) have introduced co-registration of IOUS with neuronavigation. In theory, neuronavigation may provide better orientation with regard to surrounding structures. However, a retrospective clinical analysis by Renovanz et al. (2014) comparing navigated with non-navigated IOUS in the resection of high-grade glioma, showed that although navigated IOUS achieved higher rate of GTR (57% versus 52%), the difference was not statistically significant ( $p > 0.05$ ).

In summary, IOUS has good sensitivity for detecting residual tumour and is comparable to iMRI in defining tumour border but there are problems with interpretation of artefacts and orientation. Co-registration of IOUS with neuronavigation may improve spatial localisation and orientation but has not been shown to improve GTR compared with standalone IOUS.

## 2.2 Epileptogenic foci resection

### 2.2.1 Refractory epilepsy

In the United Kingdom, the prevalence of patients receiving treatment for epilepsy is estimated to be approximately 4.5/1000 (Hart & Shorvon, 1995), and about 60% of these patients suffer from focal epilepsy syndromes (Rosenow & Lüders, 2001). Although refractory epilepsy is loosely defined (Perucca, 1998), anti-epileptic drugs (AEDs) do not adequately control seizures in about 15% of these patients (Rosenow & Lüders, 2001). Refractory epilepsy is multifaceted and characterised by a constellation of disabilities as summarised in Table 2.4 (Kwan & Brodie, 2002). Patients with refractory epilepsy will have, in addition to uncontrolled seizures, drug toxicity from multiple AEDs; cognitive decline from high frequency of seizures; psychosocial dysfunction from prolonged recurrent seizures

---

<sup>9</sup> Surgicel is oxidised regenerated cellulose and used as a haemostatic agent intra-operatively.

leading to dependent behaviour and restricted lifestyle, all resulting in unsatisfactory quality of life; and excess mortality associated with refractory epilepsy from sudden unexpected death from epilepsy.

<b>Dimensions of refractory epilepsy</b>
Intractable seizures
Excessive drug burden
Neurobiochemical plastic changes
Cognitive decline
Psychosocial dysfunction
Dependent behaviour
Restricted lifestyle
Unsatisfactory quality of life
Increased mortality

Table 2.4. Different facets of refractory epilepsy. (Reproduced from Kwan & Brodie, 2002)

### 2.2.2 Temporal lobe epilepsy and surgery

In these patients, it has been shown that epilepsy surgery can improve seizure outcomes in mesial temporal epilepsy (Engel et al., 2012; Wiebe et al., 2001). Engel et al. (2012) conducted a multicentre, randomised controlled trial at 16 United States epilepsy surgery centres, recruiting 38 participants (18 males and 20 females) aged  $\geq 12$  years with refractory temporal lobe epilepsy. In this study, refractory epilepsy was defined as disabling seizures despite adequate trial of 2 AEDs. Participants were randomised to either continued AED treatment (medical) or anteromesial temporal resection and AED (surgical), and followed up at 3-month intervals for 2 years. There were 15 and 23 participants in the surgical and medical groups, respectively. This study showed that 11 of 14 (79%) surgical and none of 23 (0%) medical participants were seizure-free at 2 years with a statistically significant difference ( $p < 0.001$ ). An earlier randomised controlled trial conducted by Wiebe et al. (2001) at a single centre in Canada, recruiting 80 participants with refractory unilateral temporal lobe epilepsy, showed that significantly higher number of surgical participants were free of seizures impairing awareness compared with medical participants (64% versus 8%,  $p < 0.001$ ). This was also true for those achieving seizure-free status: 42% in surgical group versus 3% in medical group, with statistical significant difference ( $p <$

0.001). In the medical group, there was a participant who died (sudden unexplained death) 7.5 months into the study. These 2 randomised controlled trials showed the evidence that anterior mesial temporal resection improves seizure outcomes in those with refractory temporal lobe epilepsy.

### 2.2.3 Extratemporal epilepsy and surgery

While the majority of epilepsy syndrome in adult is comprised of temporal lobe epilepsy, most seizures originate in the extratemporal region in children (Englot et al., 2013). The most common location for extratemporal epileptogenic foci is the frontal lobe, followed by neocortical temporal, parietal and occipital lobes (Frater et al., 2000; Roper, 2009). A high proportion of extratemporal epileptogenic lesions are cortical dysplasia with involvement of multiple lobes (Frater et al., 2000), thus making resection of these foci more tricky and less successful than temporal lobe resection (Ramey et al., 2013). The histological study of resected extratemporal epileptogenic lesions by Frater et al. (2000) demonstrated that neuronal heterotopia represents 44.4% of all lesions, followed by cortical dysplasia (37.6%), tumours (27.8%), ischaemic lesions (18.0%), vascular malformations (3.0%), Sturge-Weber malformations (2.3%) and Rasmussen's encephalitis (1.5%). Table 2.5 summarises the pathological findings of the extratemporal epileptogenic lesions.

**Histopathologic Findings in Extratemporal Lobe Resections From 133 Patients**

<b>Finding</b>	<b>No. (%) of Resection</b>
Cortical dysplasia	50 (37.6)
Tumour	37 (27.8)
Astrocytoma (WHO* grades I and II)	10 (27.0)
Astrocytoma (WHO grade III)	3 (8.1)
Ganglioglioma	7 (18.9)
Dysembryoplastic neuroepithelial tumour	6 (16.2)
Glioneuronal hamartoma	6 (16.2)
Oligodendrogliomas	4 (10.8)
Oligoastrocytoma (mixed glioma)	1 (2.7)
Remote infarct or ischaemic lesion	24 (18.0)
No significant pathologic finding	23 (17.2)
Neuronal heterotopia	59 (44.4)
Vascular malformations	4 (3.0)
Sturge-Weber malformation	3 (2.3)
Rasmussen encephalitis	2 (1.5)

Table 2.5. Summary of histopathological findings of extratemporal lobe epilepsy. \*WHO indicates World Health Organisation. (Reproduced from Frater et al., 2000)

The seizure freedom rates from resection of extratemporal epileptogenic lesions depend on complete resection of the epileptogenic lesion and some adjacent cortex (Cohen-Gadol et al., 2004; Roper, 2009), which in turn depends on the ability of the surgeon to delineate the lesions, which can be challenging in cortical dysplasia due to difficulty in defining the boundaries and involvement of eloquent cortex which cannot be resected (Roper, 2009). Therefore, extratemporal epilepsy is associated with less favourable results compared with temporal epilepsy, with only 14% to 63% achieving seizure-free status (Ramey et al., 2013). This is further complicated by the fact that epileptogenic lesions are not visible on MRI scan in 16% to 43% of cases (Berg et al., 2003; Bien et al., 2009; McGonigal et al., 2007; Scott et al., 1999; Siegel et al., 2001), thereby precluding the surgeon from fully resecting the epileptogenic lesions. Therefore, MRI-defined non-lesional cases, that is, patients who have epilepsy with normal MRI scan, have lower seizure freedom rate from surgery compared with lesional cases, where abnormalities are visible on MRI scan (Jeha et al., 2007; Zentner et al., 1996).

In summary, approximately 15% of patients with focal epilepsy have refractory epilepsy. The majority of these patients are adults with temporal lobe epilepsy, and respond well to anterior mesial temporal resection. In the paediatric population, most seizures originate in the extratemporal region, where surgery is not as well defined anatomically as for temporal lobe epilepsy. In cases where lesions are demonstrated on MRI scans, the boundaries are sometimes not clearly defined. Up to 43% of patients with focal epilepsy are MRI-defined non-lesional, thereby precluding delineation of such lesions. For both MRI-defined lesional and non-lesional cases, complete resection of epileptogenic lesions will likely lead to better seizure outcomes.

### ***2.2.3.1 Cortical zones in epilepsy***

The success rates of epilepsy surgery depend on the extent of resection of epileptogenic zone, which is defined as the cortical area indispensable for generating clinical seizures (Rosenow & Lüders, 2001). Therefore, successful resection of epileptogenic zone is defined by the absence of clinical seizures, regardless of the histology of the resection.

Epileptologists employ different diagnostic techniques to define the location and boundaries of the epileptogenic zone (Rosenow & Lüders, 2001). These diagnostic techniques demonstrate different cortical zones, each of which is an approximation of the exact location of the epileptogenic zone. Table 2.6 summarises the definitions of the cortical zones and their corresponding diagnostic methods.

Cortical Zone	Definition	Diagnostic Methods
Symptomatogenic zone	Area of cortex that produces ictal symptoms.	Video EEG
Irritative zone	Area of cortex that generates interictal electrographic spikes.	Interictal EEG, MEG <sup>§</sup> , fMRI*
Ictal onset zone	Area of cortex from which clinical seizures are generated.	Ictal EEG
Functional deficit zone	Area of cortex that is functionally abnormal in the interictal period.	Neuropsychology, fMRI*
Epileptogenic lesion	Radiographic lesion that is the cause of the epileptic seizures.	MRI, ultrasound

Table 2.6: The definitions of the cortical zones detected by different diagnostic methods. (Adapted from (Rosenow & Lüders, 2001)). \*functional MRI; <sup>§</sup>magnetoencephalogram.

## 2.2.4 Neuroimaging techniques for MRI-defined non-lesional cases

### 2.2.4.1 MRI sequence and image postprocessing

As described above, the seizure freedom rate for MRI-defined non-lesional epilepsy cases depends on complete resection of the epileptogenic lesion. The challenge with MRI-defined non-lesional cases is the detection and delineation of the epileptogenic lesions. Therefore, techniques to improve visualisation of such lesions have been described. MRI is the neuroimaging modality of choice for the preliminary evaluation of patients with refractory epilepsy (Ruggieri et al., 2004). Bergin et al. (1995) found in 36 patients that fluid-attenuated inversion recovery (FLAIR) sequence was superior in visualising epileptogenic lesions, where 8 lesions were only visible on this sequence. FLAIR is thought to be superior to T2-weighted MRI as FLAIR suppresses the high intensity signal from CSF,

which can obscure epileptogenic lesions. High-field 3-Tesla MRI scanning has been shown to improve detection rate of epileptogenic foci by 20% (Strandberg et al., 2008) to 65% (Knake et al., 2005). Wang et al. (2013) showed that voxel-based morphometric MRI postprocessing was able to detect 5 of 6 MRI-negative epilepsy patients. However, the findings from this technique have to be interpreted in conjunction with clinical findings, as false-positive findings have been reported in 25 healthy subjects (Focke et al., 2008).

#### ***2.2.4.2 Fluorodeoxyglucose positron emission tomography (FDG-PET)***

Functional imaging techniques have been exploited to visualise epileptogenic foci, as these foci are usually hypermetabolic during ictal<sup>10</sup> activity and hypometabolic during interictal<sup>11</sup> phase. Fluorodeoxyglucose positron emission tomography (FDG-PET) scan detects gamma rays emitted by a radioactive tracer (Fluorine-18 or <sup>18</sup>F) tagged to a glucose analogue (fluorodeoxyglucose or FDG), which will accumulate in metabolically active regions of the brain. During interictal phase, the epileptogenic foci are hypometabolic and thus emit gamma ray photons at a lower rate than normal brain. Therefore, the cortical zone that is demonstrated by FDG-PET is the irritative zone. Up to 84% of MRI-negative cases can be localised correctly with FDG-PET (Chassoux et al., 2012) but due to its low spatial resolution of 5mm (Spencer, 1994), co-registration to MRI was studied, which proves to be as good as FDG-PET and can improve second interpretation of normal MRI scan from MRI-defined non-lesional to subtle-lesional in 43% of cases (Rubí et al., 2011).

#### ***2.2.4.3 Single photon emission computed tomography (SPECT)***

Another functional imaging technique for mapping cerebral perfusion is single photon emission computed tomography (SPECT), where radioactive tracer (Technetium-99m or <sup>99m</sup>Tc) tagged to hexamethylpropylene amine oxime (HMPAO), which is taken up by

---

<sup>10</sup> seizure

<sup>11</sup> in between seizures

brain tissue proportional to the cerebral blood flow. During ictal activity, the blood flow will increase in the epileptogenic focus, which will show up on ictal SPECT scan whereas during the interictal phase, there may be hypoperfusion in the focus. Therefore, ictal and interictal SPECT scans demonstrate the ictal onset and irritative zones, respectively. Interictal SPECT is less commonly used because it has lower sensitivity than ictal SPECT (60% to 66% versus 81% to 90%) (Spencer, 1994). There are inherent problems with ictal SPECT interpretation (Wetjen et al., 2002). If the epileptogenic focus is hypoperfused during interictal period, then hyperperfusion of the focus might not be visible against the background. The time between injection and image acquisition, and the amount of radioactive tracer injected may affect the overall image intensity. The changes in head position may affect the comparison in the image slices. It has poor spatial resolution (7-8mm) (Spencer, 1994) and anatomical details compared to structural MRI. Therefore, subtracted ictal SPECT co-registered to MRI (SISCOM) was introduced and shown to improve localisation of blood flow changes compared to side-by-side comparison of interictal and ictal SPECT (82.9% versus 31.4%;  $p < 0.00001$ ) (O'Brien et al., 1999). However, the actual spatial resolution of SPECT is still the same and the interpreter is relying on MRI to pinpoint the epileptogenic foci.

#### ***2.2.4.4 Magnetoencephalography (MEG) and Magnetic source imaging (MSI)***

Magnetoencephalography (MEG) is a functional imaging technique for mapping brain activity. Electrical currents, which can be measured by EEG, produce extremely small magnetic fields ( $10^{-12}$  to  $10^{-15}$  Tesla), which can be recorded using extremely sensitive magnetometer<sup>12</sup>, the most commonly used is superconducting quantum interference device (SQUID) (Sato & Smith, 1985). As the ambient magnetic noise in the urban environment is many magnitudes higher ( $10^{-7}$  Tesla), MEG has to be performed in a room shielded from external magnetic signals. MEG has the advantage over EEG in that it does not get

---

<sup>12</sup> Magnetometer is a measurement instrument used to measure the strength and direction of the magnetic field at a point in space.

distorted by the scalp, skull or dura, and are independent of a reference (Rosenow & Lüders, 2001). However, MEG requires synchronous discharge of 6-8 cm<sup>2</sup> of cortex to generate a detectable potential, which is attenuated to the third power of the distance between the signal and detector (Rosenow & Lüders, 2001). As magnetic field is generated in an orthogonal plane to electrical current according to Maxwell's equation, only neurons that are orientated perpendicular to the scalp surface give rise to measurable magnetic field. This means that MEG is only capable of sampling neurons lining the sulci and not the ones from the gyri (Sato & Smith, 1985), therefore MEG is more sensitive to localising discharge foci without interference from noise signals coming from the gyral surface. When MEG is co-registered to MRI using a common set of fiducial points, magnetic source imaging (MSI) is created. Therefore, the cortical zone that is demonstrated by both MEG and MSI is the irritative zone. Wu et al. (2012) showed in a retrospective study of 18 patients that MSI was able to detect epileptic clusters in 94.4% (17 of 18) of MRI-negative patients in the cohort but there were several drawbacks from this study. This study had a small number of subjects in the cohort and was retrospective. There were 5 patients (27.8%) who had non-specific changes and only 10 patients (55.6%) were seizure-free after surgery, indicating that MSI may have inadequately delineated the epileptogenic lesions, as Chassoux et al. (2012) achieved an 88% seizure freedom rate from surgery for MRI-negative cases. However, MSI can only be practically used for detecting interictal discharges. Concordance between MSI and intracranial EEG is associated with improved seizure outcomes (F. Schneider et al., 2013). Therefore, although MSI shows potential for localising epileptogenic foci in MRI-defined non-lesional cases, further research is still necessary to validate the usefulness of MSI in delineating epileptogenic foci in MRI-defined non-lesional cases.

### 2.2.5 Invasive intracranial recording

Scalp EEG is vulnerable to interference from the dura, skull and scalp (Rosenow & Lüders, 2001) and may lack the precision in localising the epileptogenic foci (Sweet et al., 2013). Invasive intracranial recording with electrodes placed on the surface of the brain or inside the brain tissue may offer much more localisation information (Sweet et al., 2013), and

can record the irritative, ictal onset, symptomatogenic and functional deficit zones. Intra-operative electrocorticography pioneered by Foerster in 1930s has given way to the application of subdural strips and grids (Rosenow & Lüders, 2001). Invasive intracranial recording is indicated in MRI-defined non-lesional cases or poorly localised cases (Yuan et al., 2012).

Placement of subdural electrodes involves a generous craniotomy and large dural opening. In some patients where epileptogenic foci are thought to be arising from deeper regions, intracerebral depth electrodes are inserted. After placement of the electrodes, the patient is normally observed on the ward for about a week attached to a telemetry monitor. Following that, once seizure activities have been observed and seizure onset epileptic discharges have been pinpointed, the patient will undergo either resection of the epileptogenic focus if it does not involve an eloquent region, or disconnective surgery if it involves an eloquent region. However, if the epileptogenic focus could not be localised, then the patient only undergoes removal of the electrodes and no surgery is undertaken.

Subdural recordings allow 2-dimensional spatial resolution and are relatively free of artefacts but the effects of anaesthesia and the reaction to subdural electrodes can complicate the recording interpretation (Jayakar et al., 1994). Incorrect placement of subdural electrodes can preclude accurate localisation of epileptogenic foci as the subdural electrodes only detect small areas of electrical discharges and thus may miss electrical discharges a few centimetres away (Jayakar et al., 1994). It may not detect the electrical discharges arising from the depth (Surbeck et al., 2011), which can be better detected with intracerebral depth electrodes. However, the disadvantages of depth electrodes are that it has limited spatial sampling and more invasive than subdural electrodes. The overall complication rate of invasive intracranial recording is up to 48.9% (Blauwblomme et al., 2011). There are potential risks of haemorrhage, infection, cerebral oedema, venous infarction, cerebrospinal fluid leak, transient neurological complications, and death from such procedures (Blauwblomme et al., 2011; Onal et al., 2003; Sweet et al., 2013).

Stereoelectroencephalography (SEEG) is another invasive monitoring technique where multiple intracerebral depth electrodes are inserted under neuronavigation guidance,

to localise the epileptogenic foci. SEEG implantation involves placement of 9 to 15 parallel intracerebral depth electrodes spaced around 1cm apart in a rectangular manner (Sweet et al., 2013). Therefore, SEEG allows 3-dimensional capability for sampling and localisation of epileptogenic foci. However, this technique is very invasive and has been shown to cause intracranial haemorrhage resulting in neurological deficit and infection, with a complication rate of up to 5.6% (Cossu et al., 2005), and mortality of 0.002% (Cossu et al., 2012).

Although invasive intracranial monitoring is still currently the “gold standard” for localising epileptogenic foci in both MRI-defined lesional and non-lesional cases, it is associated with morbidity and mortality.

### 2.3 Motivation for intraoperative ultrasound elastography

As described in Section 2.1, neurosurgeons have employed various intraoperative techniques to improve extent of brain tumour resection and minimise neurological deficit from damage to eloquent areas. Frameless stereotactic neuronavigation is invaluable in assisting neurosurgeons when planning a craniotomy placement. Shift in intracranial structures during resection renders this technique inaccurate in determining extent of resection. Therefore, intraoperative imaging technique has been employed to overcome the inaccuracies caused by this shift. These intraoperative imaging techniques, including iCT, iMRI, fluorescence imaging and IOUS, have been shown to improve the extent of resection. However, none of these techniques actually inform the neurosurgeon regarding the biomechanical properties of the brain tumour being resected or the tumour-brain boundary conditions. As brain tumours usually feel different compared to normal surrounding brain, it is hypothesised that intraoperative ultrasound elastography may assist neurosurgeons in differentiating residual tumour from surrounding brain and characterising tumour-brain boundary.

As described in Section 2.2, MRI remains the mainstay imaging technique for visualising epileptogenic lesions. However, some of these lesions are not clearly seen on MRI. Therefore, additional techniques have been employed to improve identification of these

lesions, such as MRI image postprocessing, SPECT, FDG-PET, MEG and MSI. However, these techniques are not reliable enough to be used independently for localising epileptogenic lesions. The “gold standard” for localising these lesions is still invasive intracranial monitoring. However, this technique is associated with mortality and morbidity. As epileptogenic foci usually feel different to surrounding brain during surgery, it is hypothesised here that ultrasound elastography, which is an ultrasound-based technique capable of imaging biomechanical properties of tissues, may assist the surgeon in identifying the lesion and defining the boundaries.

## 2.4 Ultrasound elastography

Traditionally, physicians used palpation to detect abnormalities in superficial organs such as breasts, skin and liver. However, this is qualitative, has high inter-operator variation depending on their experience and is limited to superficial regions. Tissues of different stiffness may have similar echogenicity on ultrasound B-mode, thereby making them inseparable on such images (Ophir et al., 2002). Ophir, et al. (1991) first coined the term elastography to describe a method of inferring the elastic properties of a tissue using strain imaged with ultrasound. As other methods of imaging elasticity have emerged, it is now more appropriate to term all ultrasound-based methods as ultrasound elastography and this has become the common usage of the term. There have been a number of reviews of the technology for and applications of ultrasound elastography (Bamber et al., 2013; Doyley et al., 2001; Ophir et al., 1991; Parker et al., 1990; Shiina et al., 2015), which demonstrate that there are several main methods: 1) quasistatic strain elastography (QSE) (Ophir et al., 1991) 2) shear wave elastography (SWE) (Bercoff et al., 2004; Catheline et al., 1999; Sandrin et al., 2003; Sarvazyan et al., 1998; Wu et al., 2006) and 3) acoustic radiation force impulse (ARFI) imaging (Nightingale et al., 2002). A variation of QSE by applying strain using vibration termed as “vibrography” has been described (Pesavento et al., 2000). Wu et al. (2006) described crawling wave imaging where the interference patterns of propagating shear waves are imaged. All these ultrasound elastography methods will be described with further details in Chapter 3.

## 2.5 Intra-operative ultrasound elastography in neurosurgery

Although the use of ultrasound elastography in superficial organs has been well described, the intra-operative application of ultrasound elastography is not as common. As mentioned above in the IOUS subsection, this could be due to the fact that neurosurgeons are less familiar with ultrasound imaging and early ultrasound technology with poor image quality has impeded the acceptance of ultrasound in neurosurgery. Three groups, including the author's, have described the use of intra-operative ultrasound elastography. The other 2 groups have only applied it in brain tumour resection while the author's group has also described its use in epilepsy surgery.

### 2.5.1 Intra-operative ultrasound elastography in brain tumour resection

As the extent of brain tumour resection affects the clinical outcomes of patients with brain tumour, surgical intervention is aimed at maximal resection with preservation of neurological function. Neurosurgeons' intra-operative assessment of the extent of resection has been shown to be inaccurate (Albert et al., 1994; Orringer et al., 2012). Although IOUS can generally visualise most solid tumours, radiation changes and previous surgery make visualisation of the tumour challenging (Hammoud et al., 1996). Therefore, Selbekk et al. (2005) proposed that ultrasound elastography can improve visualisation of tumour in such cases. The authors studied 2 patients using a 10 MHz linear array probe to acquire intra-operative images prior to dura opening. The images were acquired by holding the probe static freehand for 3-4 seconds to allow for natural brain pulsations to generate a time-varying strain within the tissue. The ultrasound elastography technique employed by this group is QSE, where strain<sup>13</sup> was measured off-line using a correlation technique for time shift estimation, which is suitable for detecting tissue displacement with low velocities and small amplitudes. The authors showed that brain pulsations caused by arterial pressure are

---

<sup>13</sup> Strain is the extent to which a material deforms in response to applied force.

enough to generate reliable strain images. This study only included 2 patients. Using the same strain imaging technique, the same group carried out a further study involving 16 patients with both low-grade and high-grade gliomas (Selbekk et al., 2010). In this study, the authors showed that lower strain correlated well with hyperechoic areas on US B-mode, which is assumed to be tumour, and may thus complement US B-mode in discriminating tumour from surrounding brain. The drawback from this study is that there was no histology on the isoechoic areas to prove that it did not contain tumour cells. A further study with 15 patients with gliomas was performed by the same group to compare strain imaging and US B-mode contrasts in both low-grade and high-grade gliomas (Selbekk et al., 2012). The authors showed that the strain imaging contrast between gliomas overall and normal brain was significantly higher than US B-mode contrast ( $p < 0.0001$ ). Subgroup analysis comparing low-grade and high-grade gliomas to normal brain also showed significantly higher strain imaging contrast than US B-mode (both  $p < 0.0001$ ). There was no significant difference in either strain imaging or US B-mode contrasts between low-grade and high-grade gliomas. The drawbacks from this study are the subjectivity in the placement of the region of interest (ROI) for contrast analysis in both strain imaging and US B-mode, and the lack of histological confirmation in both hyperechoic and isoechoic regions. The strain image processing was performed off-line and there has been no subsequent study since the development of real-time strain imaging. Therefore the practicality of performing real-time strain imaging with this (passive) technique still needs to be addressed.

Scholz et al. (2005) described a technique called vibrography, where small-amplitude (0.2 mm to 0.5 mm) low-frequency (5 to 10 Hz) mechanical vibration was applied by means of a stepper motor for 60 seconds to induce strain. This technique had been previously described by Pesavento et al. (2000). As described above, like the method of passive strain imaging of Selbekk et al. (2005, 2010, 2012), this technique is also a variation of QSE described by Ophir et al. (1991). It is different from real-time freehand QSE in that, instead of using hand-induced motion (Chakraborty et al., 2006; Uff et al., 2009) or passive physiological motion (Selbekk et al., 2005), which are operator dependent and variable, vibrography is automated and therefore is controlled and reproducible. By using phase root seeking algorithm, vibrography technique is computationally more efficient and could be

performed real-time using a conventional personal computer at the time. In this study (Scholz et al., 2005), the authors showed that there was minimal rise in intracranial pressure of less than 4 mmHg when performing vibrography on pig's brain with 1-mm amplitude of vibration and pre-compression of less than 3 mm. The authors later performed vibrography on 20 human patients with amplitude of 0.3 mm and only slight pre-compression (<1 mm). Intracranial tumours were visualised on 18 of 20 cases; in the 2 cases where tumour was not visualised, one had GBM at 1 cm depth and one did not have vibrography due to a software problem. The authors grouped these tumours into 3 major groups: 1) tumours with identical strain to normal surrounding brain with easily identified peripheral zone of high strain; 2) tumours with high strain which were found to be softer than brain during surgery; and 3) tumours with low strain which were found to be stiffer than brain during surgery. This study showed that real-time vibrography with 30 frames per second was feasible and able to visualise the majority of the brain tumours during resection of these lesions. A further study was performed by the same group with 42 patients with 45 tumours (Scholz et al., 2007). Vibrography was able to detect 41 of 45 tumours; 2 tumours not detected were at depths of 2 cm and 3 cm; and 2 tumours were not visualised due to technical problems. The authors were able to detect tumours with identical strain to normal brain owing to a peripheral zone of high strain. In this larger cohort, the authors identified a further group of patients with heterogeneous tumours with heterogenous appearance on vibrography and inhomogeneous consistency during surgery. Vibrography guided resection at various stages and detected residual tumour, which was absent on US B-mode. One haemorrhagic complication was noted but that did not have any serious sequelae. The drawback of this study is that post-operative CT was performed to look for residual rather than MRI, which offers better soft tissue contrast and has been the "gold standard" for detecting residual disease in various centres. The authors still did not explore the reason for the presence of peripheral high strain in isostrain tumours.

Our group started looking at the application of intra-operative ultrasound elastography in 2004 (Chakraborty et al., 2004; Chakraborty et al., 2006). The early study showed good correlation between intra-operative elastography findings and surgical findings, in terms of stiffness and boundary condition, in 2 patients undergoing brain tumour resection

(1 GBM and 1 metastatic melanoma). This study was the first to apply ultrasound elastography co-registered to neuronavigation and was also the first to apply freehand version of QSE as described by (Doyley et al., 2001) with off-line processing. The authors showed that when there was no compression on the brain surface, i.e. relying on arterial pulsation to generate strain, there was good tumour-brain strain contrast. These findings were later reported by Selbekk et al. (2010, 2005, 2012). However, applied compression on the brain surface generated shear strain at the brain tumour boundary, diminishing the tumour-brain strain contrast but providing high strain contrast for visualising the tumour boundary, and offering potential for characterising the degree of adherence between tumour and brain as well as an explanation for the observations of the peripheral zone of strain made by Scholz et al described above. This study was only a feasibility study involving 2 patients. This led to the investigation of ultrasound elastography in characterising boundary conditions at the tumour-brain interface, a novel method termed slip elastography (Chakraborty et al., 2012). In the study (Chakraborty et al., 2012), the authors created gelatine phantoms with various angles of slip, 5.7°, 7.8°, 9.9° and 13.8°, and compared 4 shear strain estimators using axial and lateral tracking data. The authors showed that axial force required to overcome friction could be quantified using slip elastography and shear strain estimators were superior to US B-mode in identifying slip. Of the different shear strain estimators, a vector based shear strain estimator had the least shear strain artefacts. In his thesis, Chakraborty (2007) described the study investigating the application of slip elastography on 22 patients undergoing craniotomy for brain tumours: 1 underwent biopsy while the remaining underwent resection. The author showed that 19 of 21 patients had good correlation between surgical findings and slip elastography findings. In 1 patient, slip elastography was able to identify the focal areas of slip and quantify the force required to produce the slip, but the surgeon felt that the tumour was adherent to the brain but a cleavage plane was identified. This pilot study showed that slip elastography was feasible during brain tumour resection.

Another study by our group (Uff et al., 2009) involving 31 consecutive patients undergoing brain tumour resection showed that both 2-dimensional (2D) and 3-dimensional (3D) QSE are feasible during brain tumour resection. It also showed the possibility of

performing QSE in spinal cord tumour resection with water standoff. In addition to confirming the finding by Chakraborty (2007) that high shear strain at the tumour boundary is indicative of a slippery boundary, this study also showed that high strain on conventional axial strain imaging was also another sign of slip, confirming the findings of the earlier feasibility study (Chakraborty et al., 2006). In his thesis, Uff (2011) showed that while 3D QSE seemed to be advantageous for characterising the tumour-brain interface compared with 2D QSE albeit not significantly (area under receiver operating curve (AUROC) 0.749 versus 0.624;  $p = 0.0857$ ), the large footprint of 3D probe was disadvantageous in terms accessibility for small intra-operative exposure, especially in the posterior fossa and in paediatric population. Later on in his thesis, Uff (2011) started using SWE intra-operatively to assess its feasibility in neurosurgery in 8 brain tumour and 1 spinal tumour patients. The author showed that SWE was capable of quantifying the elasticity of grey and white matter of normal human brains *in vivo*. However, the author mentioned that SWE was not able to characterise the boundary condition but this was not studied in his thesis.

### 2.5.2 Intra-operative ultrasound elastography in epileptogenic foci resection

In a preliminary study described in his thesis, Uff (2011) showed that in his small series of 10 patients who underwent lesionectomy<sup>14</sup>, ultrasound elastography was able to visualise the lesions absent on MRI scan in 5 cases (2 using QSE and 3 SWE), with all lesions appearing stiff on ultrasound elastography, thus showing the potential for the application of ultrasound elastography during lesionectomy. Furthermore, in a presentation, Chakraborty et al. (2011) showed that SWE was superior to MRI at identifying epileptogenic lesions in 5 patients. Therefore, these preliminary studies have shown the potential for intra-operative elastography in epilepsy surgery.

---

<sup>14</sup> Up to 30% of patients with intractable focal epilepsy have an intra-axial cerebral lesion; removal of such lesion leads to seizure freedom. Lesionectomy refers to removal of the lesion.

### 2.5.3 Shear wave elastography (SWE)

SWE is one of the methods of ultrasound elastography, where ultrasound echoes are tracked to measure the local speed of shear wave propagation. Various ways of generating the shear wave have been described: 1) a impulse piston at the body surface which generates complicated shear waves and having frequency components up to 250 Hz (Catheline et al., 1999) and 50 Hz (Sandrin et al., 2003), 2) two bending piezoelements known as biomorphs that generate simple shear at the body surface (Wu et al., 2006), and 3) acoustic radiation force<sup>15</sup> (ARF) (Sarvazyan et al., 1998) that generates mostly simple shear deep inside the tissue when focused at single or various depths (Catheline et al., 1999; Sarvazyan et al., 1998), and ARF swept over depth to produce a Mach cone and hence a more planar shear wavefront (also known as supersonic shear imaging (SSI)) (Bercoff et al., 2004b). SSI is an ultrasound-based elasticity imaging technique, where acoustic radiation force is emitted by the ultrasound transducer to create micromillimetre displacement at different depths where the depth is varied more quickly than the travel time of the shear wave (Bercoff et al., 2004b). In all of the ARF methods the shear wave propagates most strongly in a direction perpendicular to the ARF-induced displacement, i.e. in the ultrasound lateral direction. The shear wave propagation speed is dependent on the Young's (elastic) modulus<sup>16</sup> of the medium by the following equation:

$$E \approx 3\rho c^2, \quad (2.2)$$

where  $E$  is the Young's modulus,  $\rho$  is the medium density, and  $c$  is the shear wave propagation speed. Assuming that the medium through which the shear waves travel has a density of approximately 1000 kg/m<sup>3</sup>, the equation becomes

$$E \approx 3c^2. \quad (2.3)$$

As the shear wave propagation speed for soft tissue is in the region of a few metres per second (ms<sup>-1</sup>), the ultrasound transducer needs to have a frame rate of several kilohertz

---

<sup>15</sup> ARF results from a focused ultrasound beam capable of causing micromillimetre displacement in the direction of the beam in the medium.

<sup>16</sup> Young's modulus is a measure of stiffness of a particular medium and is characteristic for that particular medium. It is derived from the amount of deformation (strain) of that medium when subjected to a certain amount of stress.

(kHz) (Bercoff et al., 2004b). A typical conventional ultrasound scanner only has a frame rate of 50 Hertz (Hz) or less, so would be unable to track the shear waves. The physics of SWE, in particular the SSI method, will be explained in more detail in Chapter 3.

The application of intra-operative SWE on the human brain has been limited to resection of epileptogenic foci in a preliminary study using SSI (Uff, 2011). A study by Macé et al. (2011) evaluated SWE using SSI system on the brains of 4 trepanated anaesthetised rats, using a motorised arm to achieve a 3D sweep. The authors showed that SSI was able to provide a 3D elasticity map with a resolution of  $0.7 \text{ mm} \times 1 \text{ mm} \times 0.4 \text{ mm}$ , and to characterise the elastic modulus for different parts of the brain. In addition, the study was able to demonstrate anisotropy in the deep white matter by showing a significant difference in elastic modulus on orthogonal scanning of the brains: external capsule 14.9 kPa (sagittal) versus 25.3 kPa (coronal),  $p = 0.005$ ; genu of corpus callosum 21.4 kPa (sagittal) versus 7.8 kPa (coronal),  $p = 0.013$ . Therefore, with high resolution and ability to demonstrate anisotropy, this study showed the potential for using intra-operative SWE on the brain.

Since I (the author) started this project, there were 2 further studies evaluating SWE using the SSI system in assessing elasticity changes after a stroke in mouse models. The first study (Martín et al., 2012) involved 52 rats, of which 46 had occlusions of the right middle cerebral and common carotid arteries for 2 hours to induce right-sided stroke and were subsequently reanaesthetised and had the occlusions removed to allow reperfusion, while 6 did not have occlusions. Of the 52 rats, 20 rats (17 with stroke and 3 without) were scanned with SSI while 32 (29 with stroke and 3 without) were scanned with PET and SPECT. The study showed that infarcted brain was softer on SSI but there was no comparison with another assessment modality, either mechanical rheometer or magnetic resonance elastography (MRE). This study did show the reproducibility in 20 rats that the left-sided normal brain had consistent elastic modulus. Another study performed by Xu et al. (2013) involving 29 mice, of which 13 were controls and 16 had occlusions of the right middle cerebral and common carotid arteries for 45 minutes to induce stroke, after which time the occlusions were removed while still under anaesthesia to allow reperfusion. Nine mice with no evidence of infarct on histopathology were retrospectively excluded. This study showed that there was a significantly lower elastic modulus in the infarcted hemisphere compared to

normal hemisphere at both 24- and 72-hour post-infarction (3.85 kPa versus 4.86 kPa,  $p < 0.01$ ; 3.66 kPa versus 4.23 kPa,  $p < 0.01$ ; respectively). Therefore, this study confirmed the findings from the earlier study by Martín et al. (2012), that infarcted brain was softer than normal brain in considerably smaller brains, i.e. mice rather than rats. Both these studies showed that SWE was capable of identifying pathology in the brain, in this case stroke, adding to the reasons for me to consider whether it could also visualise pathology such as brain tumours and epileptogenic foci intra-operatively.

As this project uses the SSI system to perform SWE, both in the laboratory and intra-operatively, the term SWE will be used to mean the SSI method of obtaining SWE in the rest of the thesis.

## 2.6 Hypotheses

Prior to this project, the use and understanding of ultrasound elastography in the resection of brain tumours and epileptogenic foci was very limited. The predecessors in this group (Chakraborty, 2007; Uff, 2011) had demonstrated the feasibility of 2D and 3D QSE in identifying slippery boundaries of brain tumours and of SWE in visualising brain tumours and epileptogenic foci. In the latter, however, the studies had not been done in a controlled way, the artefacts and optimisation of SWE had not been studied and the clinical experience had been limited to 19 patients (8 brain tumours, 1 spinal tumour and 10 epileptogenic foci). Furthermore, the features of SWE under different tumour boundary conditions had not been investigated. Therefore, the hypotheses of this thesis are as follows:

- 1) SWE can quantify stiffness of normal brain tissue, different epileptogenic lesions and brain tumours.
- 2) SWE measurements are different between epileptogenic lesions and normal brain.
- 3) SWE measurements are different between brain tumours and normal brain.
- 4) SWE appearances are different for mobile and adhered interface.
- 5) SWE can visualise epileptogenic foci better than MRI.

- 6) SWE-quantified elasticity of brain tumours and epileptogenic lesions is correlated with histopathological findings.
- 7) SWE can detect the residual tumour post-resection better than surgeon.
- 8) SWE can detect the residual tumour post-resection better than ultrasound B-mode.

The first 5 hypotheses, if confirmed, would demonstrate that intraoperative SWE is likely to be a valuable intra-operative tool to assist surgeons in improving extent of resection and surgical safety, by providing improved visualisation of epileptogenic foci, quantitative stiffness and characterisation of boundary condition prior to touching the tumour, all in a real-time fashion. In addition, if the sixth hypothesis is also confirmed, then it can provide encouragement that the surgeon could be provided with an intra-operative diagnostic tool to guide biopsy, especially in heterogeneous tumours where diagnostic accuracy heavily relies on the biopsy sites (Chandrasoma et al., 1989; Jackson et al., 2001; McGirt et al., 2003; Woodworth et al., 2005). Lastly, the seventh and eighth hypotheses, if confirmed, would demonstrate that intraoperative SWE could improve detection of residual tumour better than the surgeon and ultrasound B-mode alone.

## **Chapter 3**

# **Physics of Ultrasound Elastography**

This chapter starts off by explaining the theory of elasticity, followed by the physics behind different types of ultrasound elastography, in particular SWE, and subsequently finishes by explaining the functionality of the various controls on the SuperSonic Aixplorer® scanner (SuperSonic, Aix-en-Provence, France) and the methods of optimising the scanner for intra-operative SWE during neurosurgery.

### 3.1 Theory of elasticity

According to Hooke's law, using a spring to illustrate a purely elastic material, there is a linear relationship between the force from a load ( $F$ ) and the amount of spring extension ( $X$ ), that is:

$$F = kX, \quad (3.1)$$

where  $k$  is the measure of stiffness of the spring (Giuliodori et al., 2009). When the force is plotted against the amount of extension, the slope of the plot is  $k$ . Figure 3.1 illustrates spring and load theory according to Hooke's law. Therefore, linear-elastic material is said to follow the Hooke's law.

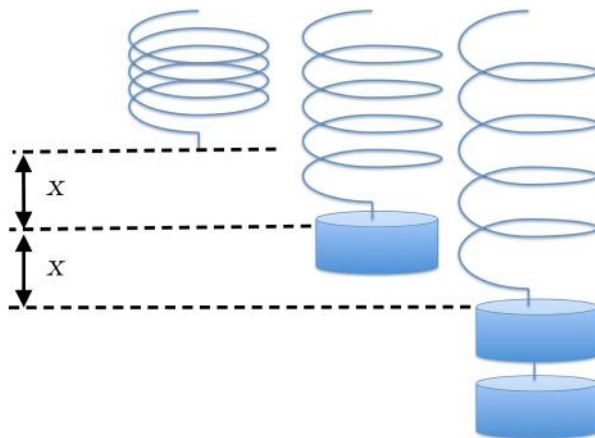


Figure 3.1. The illustration of Hooke's law with spring and load. Each load has the same weight, therefore the same force. With one load, the spring extends by distance  $x$ . By doubling the load, the spring extends twice as much –  $2x$ .

When 2 identical springs are used instead of 1, the amount of extension is halved. In addition, when the spring is twice as long, the length of extension is also doubled. This means that the constant ( $k$ ) in Hooke's law is dependent not only on the material of the spring but also its configuration. Therefore, the terms stress ( $\sigma$ ) and strain ( $\varepsilon$ ) are introduced to define the force ( $F$ ) experienced per unit cross sectional area ( $A$ ), and the amount of extension ( $\Delta L$ ) per the original length ( $L$ ), respectively. The equations for stress and strain are as follows:

$$\sigma = \frac{F}{A} \quad (3.2)$$

$$\varepsilon = \frac{\Delta L}{L} \quad (3.3)$$

Young's modulus ( $E$ ) is a measure of stiffness where a material will exhibit a certain amount of strain when subjected to a certain amount of stress, and is characteristic to that particular material. Therefore, Young's modulus is related to stress and strain by:

$$\sigma = E\varepsilon. \quad (3.4)$$

The Young's modulus is expressed in Newton per square metre ( $\text{N/m}^2$ ) or Pascal (Pa). In a 3D space, each of the components can be expressed in a constitutive equation in tensor notations:

$$\sigma_{kl} = C_{klmn}\varepsilon_{mn}, \quad (3.5)$$

where  $\sigma_{kl}$  is the stress tensor,  $C_{klmn}$  is the elasticity tensor and  $\varepsilon_{mn}$  is the strain tensor. The indices,  $k$ ,  $l$ ,  $m$  and  $n$ , take values of 1, 2 and 3 as it represents the 3 axes in a 3D space. Figure 3.2 illustrates the stress tensor in 3D space.

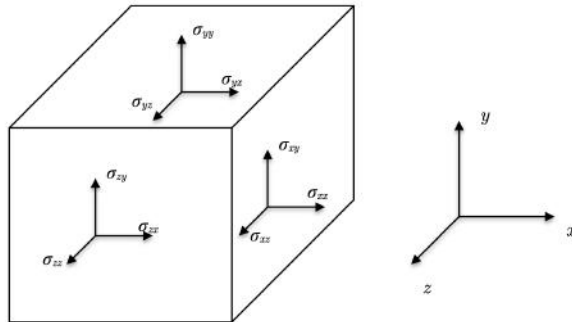


Figure 3.2. Notations of different components of the stress tensor in 3D space. (Adapted from Fung (1993)).

Therefore, the stress and strain tensors have 9 constants each and can be expressed as a matrix as:

$$\sigma_{kl} = \begin{pmatrix} \sigma_{11} & \sigma_{12} & \sigma_{13} \\ \sigma_{21} & \sigma_{22} & \sigma_{23} \\ \sigma_{31} & \sigma_{32} & \sigma_{33} \end{pmatrix}, \text{ and} \quad (3.6)$$

$$\varepsilon_{mn} = \begin{pmatrix} \varepsilon_{11} & \varepsilon_{12} & \varepsilon_{13} \\ \varepsilon_{21} & \varepsilon_{22} & \varepsilon_{23} \\ \varepsilon_{31} & \varepsilon_{32} & \varepsilon_{33} \end{pmatrix}, \text{ respectively,} \quad (3.7)$$

where  $x = 1$ ,  $y = 2$  and  $z = 3$ . As a result,  $C_{klmn}$  is a fourth-order ( $3 \times 3 \times 3 \times 3$ ) matrix having 81 constants, each of which could be an intrinsic elastic property of the material. In reality the situation is even more complicated because the stress-strain relationship is both nonlinear and dependent on the rate of strain. However, assuming linearity (which is equivalent to assuming that the strain is infinitesimal), and that the rate of strain does not alter material behaviour, the material is said to be linearly elastic. In such material,  $C_{klmn}$  can be expressed in Voigt notation as follows:

$$C_{klmn} \Rightarrow C_{\alpha\beta} = \begin{pmatrix} C_{11} & C_{12} & C_{13} & C_{14} & C_{15} & C_{16} \\ C_{12} & C_{22} & C_{23} & C_{24} & C_{25} & C_{26} \\ C_{13} & C_{23} & C_{33} & C_{34} & C_{35} & C_{36} \\ C_{14} & C_{24} & C_{34} & C_{44} & C_{45} & C_{46} \\ C_{15} & C_{25} & C_{35} & C_{45} & C_{55} & C_{56} \\ C_{16} & C_{26} & C_{36} & C_{46} & C_{56} & C_{66} \end{pmatrix}, \quad (3.8)$$

where  $kl \Rightarrow \alpha$ ;  $mn \Rightarrow \beta$ ;  $11 \Rightarrow 1$ ;  $22 \Rightarrow 2$ ;  $33 \Rightarrow 3$ ;  $23,32 \Rightarrow 4$ ;  $13,31 \Rightarrow 5$ ; and  $12,21 \Rightarrow 6$ . As demonstrated, the matrix is symmetrical so the number of constants reduces to 21, assuming the conditions of static equilibrium where all forces acting on the material are summed up to zero, that is  $\sigma_{kl} = \sigma_{lk}$  and thus  $C_{klmn} = C_{mnlk} = C_{lkmn} = C_{klnm}$ . To simplify it further, the number of constants becomes 3 when an isotropic<sup>17</sup> material is assumed, that is:

$$C_{klmn} = \begin{pmatrix} C_{11} & C_{12} & C_{12} & 0 & 0 & 0 \\ C_{12} & C_{11} & C_{12} & 0 & 0 & 0 \\ C_{12} & C_{12} & C_{11} & 0 & 0 & 0 \\ 0 & 0 & 0 & C_{66} & 0 & 0 \\ 0 & 0 & 0 & 0 & C_{66} & 0 \\ 0 & 0 & 0 & 0 & 0 & C_{66} \end{pmatrix}, \quad (3.9)$$

with  $C_{12} = C_{11} - 2C_{66}$ . (3.10)

---

<sup>17</sup> An isotropic material has elastic properties that are independent of the orientation of the axes.

The 3 constants can be expressed in terms of the Lamé constants<sup>18</sup>,  $\lambda$  and  $\mu$ , as follows:

$$C_{12} = \lambda \quad (3.11)$$

$$C_{11} = \lambda + 2\mu \quad (3.12)$$

$$C_{66} = \mu \quad (3.13)$$

The second Lamé constant ( $\mu$ ) is also known as the shear modulus ( $G$ ). The shear modulus is one of the measurements of elasticity of the medium, defined as the ratio of shear stress to the shear strain:

$$G = \frac{\tau_{xy}}{\gamma_{xy}} = \frac{F/A}{\Delta x/L} = \frac{FL}{A\Delta x}, \quad (3.14)$$

$$\tau_{xy} = \frac{F}{A}, \quad (3.15)$$

and

$$\gamma_{xy} = \frac{\Delta x}{L} = \tan \theta, \quad (3.16)$$

where  $\tau_{xy}$  is the shear stress,  $\gamma_{xy}$  is the shear strain,  $F$  is the force,  $A$  is the area on which the force acts,  $\Delta x$  is the transverse displacement,  $L$  is the height of the material and  $\theta$  is the angle determined by  $\Delta x$  and  $L$ . Figure 3.2 illustrates the factors involved in shear modulus using a cube.

---

<sup>18</sup> Lamé constants are independent elastic moduli for an isotropic and homogeneous material.

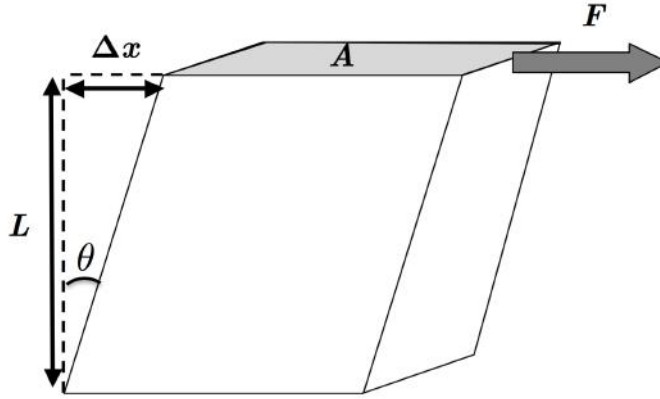


Figure 3.3. Shear modulus is characterised by the amount of force ( $F$ ) required to act on the surface area ( $A$ ) tangentially to create a displacement ( $\Delta x$ ) in a material with a height ( $L$ ).  $\theta$  is the slanting angle of the material subjected to shear stress, and is dependent on  $\Delta x$  and  $L$ .

In Figure 3.2, while the stress tensors that act normal to the surface are known as normal stresses, which are  $\sigma_{xx}$ ,  $\sigma_{yy}$ , and  $\sigma_{zz}$ , those that act tangential to the surface are known as shear stresses, which are  $\sigma_{xy}$ ,  $\sigma_{yx}$ ,  $\sigma_{yz}$ ,  $\sigma_{zy}$ ,  $\sigma_{xz}$  and  $\sigma_{zx}$  (Fung, 1993). Table 3.1 describes the different components of stresses.

	Components of Stresses		
	$x$	$y$	$z$
Surface normal to $x$	<b><math>\sigma_{xx}</math></b>	$\sigma_{xy}$	$\sigma_{xz}$
Surface normal to $y$	$\sigma_{yx}$	<b><math>\sigma_{yy}</math></b>	$\sigma_{yz}$
Surface normal to $z$	$\sigma_{zx}$	$\sigma_{zy}$	<b><math>\sigma_{zz}</math></b>

Table 3.1. Description of different components of stress tensors. Bolded components are normal stresses whereas the rest are shear stresses. (Adapted from Fung (1993))

As the stress tensors are symmetrical, the number of shear stress constants become 3, that is  $\sigma_{xy} = \sigma_{yx}$ ,  $\sigma_{yz} = \sigma_{zy}$ , and  $\sigma_{xz} = \sigma_{zx}$ . Normal stress tensors are related to Lamé constant  $\lambda$ , shear modulus ( $G$ ) and normal strain tensor ( $\varepsilon_{mm}$ ) as follows:

$$\sigma_{kk} = \lambda\varepsilon_{ii} + 2G\varepsilon_{mm}, \text{ with } \varepsilon_{ii} = \varepsilon_{xx} + \varepsilon_{yy} + \varepsilon_{zz}. \quad (3.17)$$

Shear stress tensors only depend on the shear modulus ( $G$ ) and the shear strain tensor ( $\varepsilon_{mn}$ ) as below:

$$\sigma_{kl} = 2G\varepsilon_{mn}. \quad (3.18)$$

Therefore, using the Kronecker delta function,  $\delta_{ij}$ , where its value is 1 if  $i = j$  and 0 if  $i \neq j$ , the above equations can be generalised into one equation, which can be used for both normal and shear stresses:

$$\sigma_{kl} = \lambda\varepsilon_{ii}\delta_{ij} + 2G\varepsilon_{mn}, \text{ or more commonly written as} \quad (3.19)$$

$$\varepsilon_{mn} = \frac{1+\nu}{E}\sigma_{kl} - \frac{\nu}{E}\sigma_{ii}\delta_{ij}, \quad (3.20)$$

where  $\sigma_{ii} = \sigma_{xx} + \sigma_{yy} + \sigma_{zz}$  and  $\nu$  is Poisson's ratio (see below).

According to Cauchy's equation, given infinitesimal displacements ( $u_m$  and  $u_n$ ), the strain tensors are given by the following equation:

$$\varepsilon_{mn} = \frac{1}{2} \left( \frac{\partial u_n}{\partial x_m} + \frac{\partial u_m}{\partial x_n} \right), \quad (3.21)$$

where  $u_m$  and  $u_n$  are displacements, and  $\frac{\partial}{\partial x_m}$  and  $\frac{\partial}{\partial x_n}$  are partial derivatives with respect to  $x_m$  and  $x_n$ . Therefore, the equations for normal strain and shear strain are as follows:

$$\varepsilon_{mm} = \frac{\partial u_m}{\partial x_m}, \text{ and} \quad (3.22)$$

$$\varepsilon_{mn} = \varepsilon_{nm} = \frac{1}{2} \left( \frac{\partial u_n}{\partial x_m} + \frac{\partial u_m}{\partial x_n} \right), \text{ respectively.} \quad (3.23)$$

The shear modulus is related to Young's modulus in the following equation:

$$G = \frac{E}{2(1+\nu)}, \quad (3.24)$$

where  $G$  is the shear modulus,  $E$  is the Young's modulus and  $\nu$  is the Poisson's ratio. The shear modulus is also related to shear wave speed ( $c_s$ ) and tissue density ( $\rho$ ) by:

$$G = \mu = \rho c_s^2. \quad (3.25)$$

This will be explained further in the SWE section below.

Poisson's ratio is the negative ratio of transverse normal strain to normal axial strain. When a material is compressed in one direction, it also has the tendency to expand in the other 2 directions perpendicular to the direction of compression. This phenomenon is known as the Poisson effect, which is illustrated with a cube where all dimensions are the same in Figure 3.4 below.

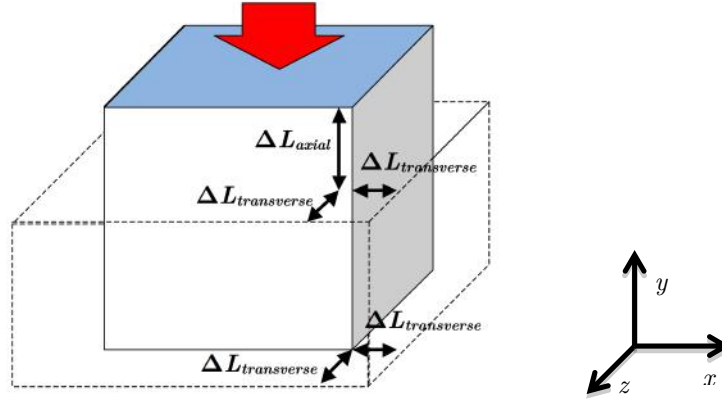


Figure 3.4. When the compressional force (depicted by red arrow) acts on the surface (blue) to produce a displacement of ( $\Delta L_{axial}$ ) there is an expansion of the material in the perpendicular direction ( $\Delta L_{transverse}$ ), resulting in the cuboid depicted by dashed outline.

This effect is measured using Poisson's ratio:

$$\nu = -\frac{d\varepsilon_{transverse}}{d\varepsilon_{axial}} = -\frac{d\varepsilon_x}{d\varepsilon_y} = -\frac{d\varepsilon_z}{d\varepsilon_y}, \quad (3.26)$$

where  $d\varepsilon_x$ ,  $d\varepsilon_y$ , and  $d\varepsilon_z$  are the differentials of strain in the  $x$ ,  $y$ , and  $z$  axes. Therefore,

$d\varepsilon_x = \frac{dx}{x}$ ,  $d\varepsilon_y = \frac{dy}{y}$  and  $d\varepsilon_z = \frac{dz}{z}$ , all of which lead to the following equations:

$$\nu = -\frac{\frac{dx}{x}}{\frac{dy}{y}} \Rightarrow -\nu \frac{dy}{y} = \frac{dx}{x} \quad (3.27)$$

$$-\nu \int_L^{L-\Delta L_{axial}} \frac{dy}{y} = \int_L^{L+\Delta L_{transverse}} \frac{dx}{x}$$

$$\begin{aligned}
-\nu \left( \ln \frac{L - \Delta L_{axial}}{L} \right) &= \ln \frac{L + \Delta L_{transverse}}{L} \\
\left( 1 - \frac{\Delta L_{axial}}{L} \right)^{-\nu} &= 1 + \frac{\Delta L_{transverse}}{L}.
\end{aligned} \tag{3.28}$$

By assuming  $\Delta L_{axial}$  and  $\Delta L_{transverse}$  are very small, first-order approximation yields:

$$\nu \approx \frac{\Delta L_{transverse}}{\Delta L_{axial}}. \tag{3.29}$$

Therefore, for an incompressible material, the  $\Delta L_{axial}$  will be twice  $\Delta L_{transverse}$  to conserve its volume, so the Poisson's ratio equals 0.5. Therefore, in this case, equation (3.12) becomes:

$$G = \frac{E}{2(1 + 0.5)} = \frac{E}{3}. \tag{3.30}$$

This enables estimation of Young's modulus from shear modulus assuming the material is incompressible. However, many soft tissues have been measured *ex vivo* to have a Poisson's ratio ranging from 0.4900 to 0.4999 (Ophir et al., 2002), meaning that this equation is at best a slight overestimate of the true Young's modulus, which we have to bear in mind when estimating Young's modulus with SWE method. However, Poisson's ratio is likely for tissue *in vivo* to be both smaller than this, and strain rate dependent (Berry et al., 2006; Berry et al., 2008; Berry et al., 2006; Konofagou et al., 2001) increasing the more rapidly strain occurs. The latter property is likely to make the incompressible assumption reasonable for SWE because strain using ARF is very rapid.

Another term, bulk modulus ( $K$ ), is defined as the resistance to volume change in response to uniform compression, expressed in the following equation:

$$K = \frac{P}{(\Delta V/V)}, \tag{3.31}$$

where  $P$  is compressional pressure,  $V$  is volume and  $\Delta V$  is volume change. Bulk modulus is also related to the Lamé's constants, Poisson's ratio and Young's modulus by:

$$K = \lambda + \frac{2}{3}\mu, \text{ and} \quad (3.32)$$

$$K = \frac{E}{3(1-2\nu)}, \text{ respectively.} \quad (3.33)$$

Bulk modulus is also related to speed of sound in material ( $c_{sound}$ ) and material density ( $\rho$ ) by:

$$K \cong \rho c_{sound}^2. \quad (3.34)$$

The speed of sound in tissue is assumed to be  $1540 \text{ ms}^{-1}$  by many ultrasound scanners when working in default mode because its range in tissue is very small. The variations in the bulk modulus over the whole range of soft tissue are about 10% whereas the shear modulus varies by a factor of more than  $10^5$  (Sarvazyan & Hill, 2004)

In summary, we assume linearity of the stress-strain relationship, independence of strain rate, and isotropy of the elastic constants in soft tissue to simplify calculations of elastic moduli. The stiffness or elasticity of soft tissue may be estimated from the amount of strain as a response to stress. By knowing the stress, the Young's modulus of the tissue can be calculated from the amount of strain. Where the stress is unknown but the same within the tissue, the relative strain within the soft tissue can be used to differentiate tissue of different stiffness, provided that there are different types of tissue with different stiffness or tumour with differing stiffness. Shear modulus may be estimated from the shear stress and shear strain, or from the shear wave speed. The former requires knowing one parameter and measuring another parameter in order to estimate the shear modulus whereas the latter only requires knowing one parameter, the shear wave speed, assuming most soft tissue has a density of approximately  $1000 \text{ kgm}^{-3}$ . Young's modulus may then be estimated from shear modulus; thus shear wave speed may be used to quantify elasticity.

### 3.2 Types of ultrasound elastography

The general principle of ultrasound elastography is to observe the internal tissue response to the applied force, and display the resultant information in a comprehensible format (Bamber et al., 2013). The ultrasound transducer transmits ultrasound pulse into the tissue and reconstructs the echoes received to generate ultrasound images. The transmitted ultrasound pulse travels at the speed of sound ( $c_{sound}$ ) in soft tissue, which is approximately  $1540 \text{ ms}^{-1}$ , as a longitudinal wave, also known as pressure wave (P-wave). A longitudinal wave moves as a transference of pressure and density differences from one tissue to another, which is illustrated by Figure 3.5.

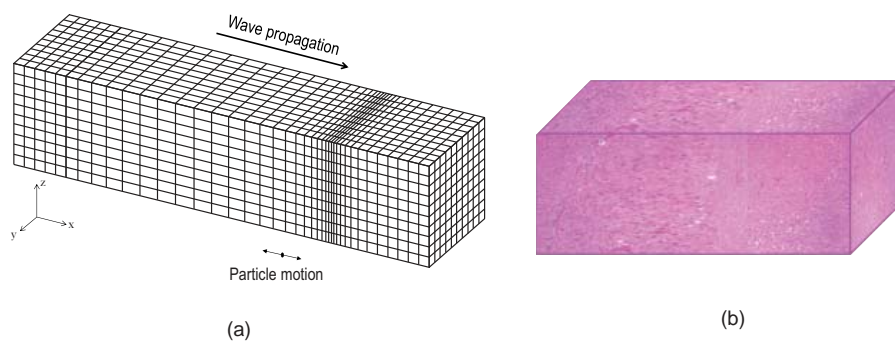


Figure 3.5. The illustration of longitudinal wave propagation. The compressed tissue elements are at maximum pressure whereas the dilated tissue elements just prior to these are at minimum pressure. The left image (a) is the 3D grid representation while the right image (b) is the simulated histological sections from liver tissue. (Reproduced from Bamber et al. (2013))

Ultrasound elastography utilises the properties of ultrasound images to generate elastograms. One of the properties is the speckle, which is the granular appearance on ultrasound images resulting from the interference of reflected echoes and arising from the microscopic variations in bulk modulus ( $K$ ) and tissue density ( $\rho$ ). The speckle provides the imaging markers for tracking tissue deformation (Bamber et al., 2013). To simplify, imagine a soft tissue is being imaged before and after compression as in static one-step elastography. Individual regions of speckle within the B-mode images taken before and after compression are compared. As we are comparing the relative positions of the speckle between the 2 images, this technique is known as speckle tracking.

As mentioned in Chapter 1, an ultrasound transducer utilises a piezoelectric element, which can convert echoes into electrical signal. The electrical signal is measured in voltages and constitutes the radiofrequency (RF) signal. Each A-line consists of a RF signal, which contains the speckle pattern within the tissue. The reference window is a patch of speckle or echo structure in the pre-compression image. The search window is the region over the post-compression image to be searched in order to locate the patch of speckle or echo structure that is the same as that in the reference window. The search window has to be larger than the reference window to allow speckle tracking. While large reference and search windows can result in better tracking (cross-correlation), they can also give rise to more false matches (noise) and higher computational cost. Another technique employed to reduce noise is by increasing the frame rate; this may result in smaller displacement between images, thereby decreasing the chances of false matches. The same technique has also been employed to estimate the time varying displacements associated with shear wave propagation, which are along the ultrasound axis, and hence the speed of the wave, which travels perpendicular to ultrasound axis. Figure 3.6 illustrates the speckle cross-correlation tracking.

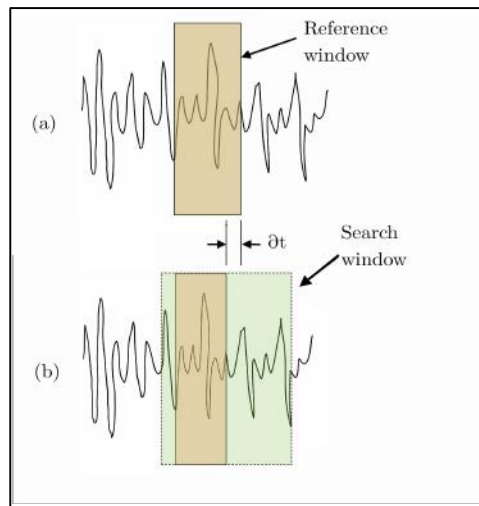


Figure 3.6. Schematic diagram of the cross-correlation technique with the pre-compression (a) and post-compression (b) RF A-line signal. The brown window in (a) is the reference window and the light green window in (b) is the search window. The bottom brown window is the congruent segment with the reference window identifying its location in the compressed RF line.  $\Delta t$  is the infinitesimal time delay detected.

The value of the correlation coefficient at its peak (i.e. when a best match of the reference window in the search region has been located) is the measure of how closely matched the speckle or echo structure is in the RF signals before and after compression. Low correlation coefficient means that the elastogram is not reliable and contains high levels of noise. Therefore, some systems apply thresholding to the correlation coefficient to mask the regions with low correlation coefficient to avoid unreliable interpretation.

Another method of detecting displacement is using the Doppler shift processing technique, whereby a gated region in the RF A-line is correlated with the same region in the same RF line to measure displacement (Bamber et al., 2013).

Resolution of any imaging system is defined as the ability to distinguish two structures that are close together, as separate. The highest potential resolution elastography images (elastograms) can achieve is that of the underlying ultrasound B-mode (Bamber et al., 2013). However, due to signal decorrelation and the consequent need to use a reference window and strain estimating window (see below) larger than a single speckle, the actual resolution of elastograms is worse than that for the B-scan (Bamber et al., 2013). The axial resolution of the B-scan is dictated by the number of cycles in the pulse and the wavelength by the equation:

$$Axial\ resolution = \frac{number\ of\ cycles\ per\ pulse \times wavelength}{2} \quad (3.35)$$

Therefore, transducers having higher frequency (thus shorter wavelength) will have higher axial resolution. Similarly, reducing the number of cycles in the pulse will also improve axial resolution. The product of number of cycles per pulse and wave period (inverse of frequency) is also called pulse length. Equation 3.35 also describes the axial point spread function (PSF), i.e. the image obtained of a point reflector. In a near lossless medium such as water the axial resolution does not depend strongly on the imaging depth. In tissue, the loss of the high frequencies in a pulse due to attenuation with depth causes a progressive lengthening of the pulse and loss of axial resolution with increasing depth. In contrast, the lateral resolution is strongly influenced by the imaging depth even in water, and is

determined by the ultrasound beam width, which in turn depends on the transmitting and receiving apertures of the transducer. Assuming that the transmit and receive foci are coincident on point of interest at the imaging depth, this is given approximately by the equation (Støylen, 2014):

$$\text{Lateral resolution} = \frac{\text{imaging depth} \times \text{wavelength}}{\text{beam aperture}} \quad (3.36)$$

The greater imaging depth will result in worse lateral resolution. In addition, in the region anterior to and beyond the focal depth, the ultrasound beam width tends to be larger than equation (3.36) predicts, thereby deteriorating the lateral resolution further.

The different types of ultrasound elastography are described below.

### 3.2.1 Quasistatic strain elastography (QSE)

First described by Ophir (1991), QSE is a method where the strain in soft tissue is imaged before and after compression is applied to the tissue with the ultrasound transducer. When the compression is applied in the  $y$  direction, the soft tissue shortens by a strain:

$$\varepsilon_{yy} = \frac{1}{E} \sigma_{yy} \quad (3.37)$$

Figure 3.7 illustrates the compression by the ultrasound transducer with a force ( $F$ ) axially on the block of material with soft background and stiff inclusion. The amount of axial strain in the background in response to the compressional force ( $F$ ) is more than that in the inclusion, which can be expressed as below:

$$\frac{Y_{\text{background}} - Y'_{\text{background}}}{Y_{\text{background}}} > \frac{Y_{\text{inclusion}} - Y'_{\text{inclusion}}}{Y_{\text{inclusion}}} \quad .$$

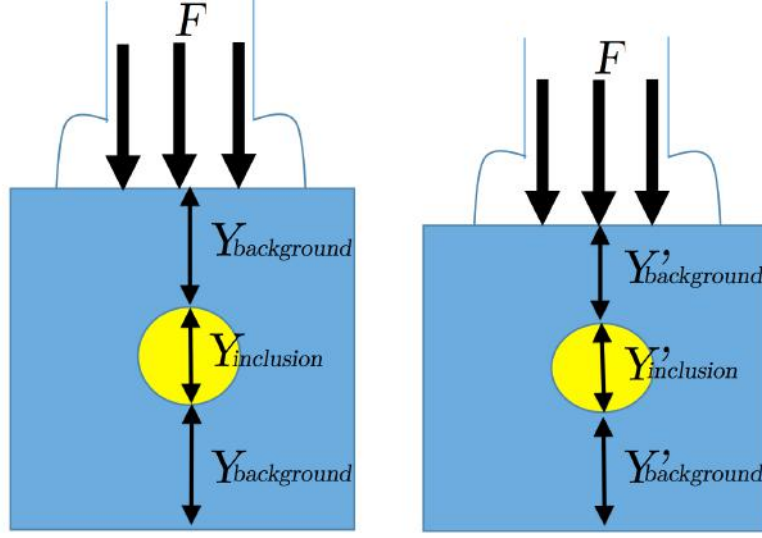


Figure 3.7. Diagrammatic representation of compression with force ( $F$ ) on a soft background (blue) with a stiff inclusion (yellow). The pre-compression image is on the left and post-compression image on the right.

As described above, the tracking algorithm for ultrasound elastography employs the detection of time delay between the pre- and post-compression images. To illustrate the calculation of both displacement and strain, let us take  $P1$  and  $P2$  as positions of point 1 and 2, respectively, and  $D1$  and  $D2$  as displacements of point 1 and 2, respectively. Subscripts pre and post denote pre- and post-compression. Therefore, the displacement is the amount of change in the positions before and after compression:

$$D1 = P1_{post} - P1_{pre}, \text{ and}$$

$$D2 = P2_{post} - P2_{pre}.$$

Relative displacement is given by:

$$D2 - D1 = P2_{post} - P2_{pre} - (P1_{post} - P1_{pre}).$$

Therefore, a strain estimator converts displacement to strain (or gradient of the displacement) by the following equation:

$$\varepsilon = \frac{D2 - D1}{P2_{pre} - P1_{pre}}. \quad (3.38)$$

Figure 3.8 shows the plots of displacement-depth and strain-depth, and Figure 3.9 illustrates the corresponding grey scale images in a simulated model. As demonstrated, the displacement grey scale image does not show the stiff inclusion very well, compared with strain grey scale image, which shows the stiff inclusion clearly.

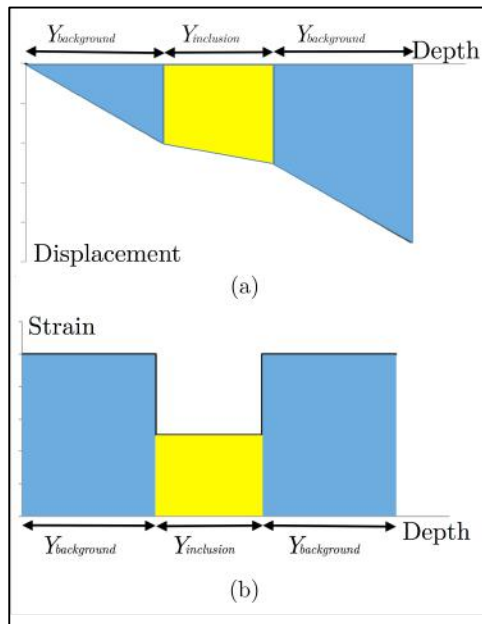


Figure 3.8. Graphs of displacement-depth (a) and strain-depth (b) plots. Note that the displacement was negative because of compression.

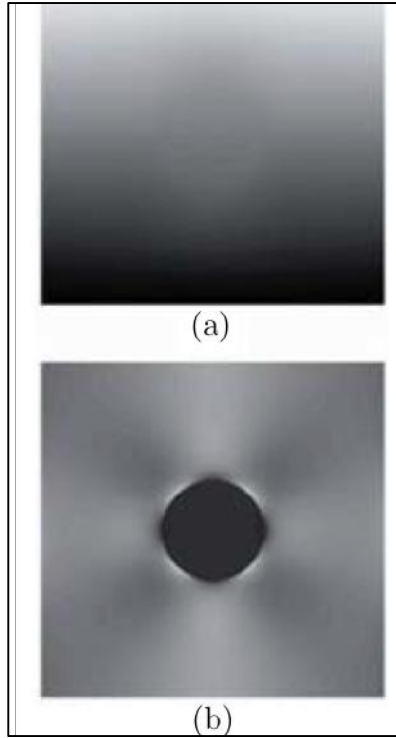


Figure 3.9. The corresponding grey scale image of displacement (a) and strain (b) of simulated soft background with stiff inclusion. (Reproduced from Uff (2011))

According to Poisson's effect, at the same time the lateral sides of the soft tissue will also expand to an extent which is proportional to the stress  $\sigma_{yy}$ . These strains are known as the lateral ( $\varepsilon_{xx}$ ) and elevational strains ( $\varepsilon_{zz}$ ), and from equation (3.20) above, may be expressed as:

$$\varepsilon_{xx} = \varepsilon_{zz} = -\frac{\nu}{E}\sigma_{yy}. \quad (3.39)$$

Due to these lateral and elevational strains (and also displacements), the 1D QSE systems may encounter noise from lateral and elevational decorrelations (Kallel et al., 1997). A weighted interpolation method to account for lateral motions has been shown to improve SNR in axial strain elastograms (Konofagou & Ophir, 1998).

Signal-to-noise ratio (SNR) is the measure to how strong the signal is compared to the background noise. Elastographic SNR ( $\text{SNR}_e$ ) is defined as the mean to standard deviation ratio of strain:

$$SNR_e = \frac{\mu_\varepsilon}{\sigma_\varepsilon}, \quad (3.40)$$

where  $\mu_\varepsilon$  is the mean strain and  $\sigma_\varepsilon$  is the standard deviation of strain. Contrast-to-noise ratio (CNR) is the measure of image quality. Elastographic CNR ( $CNR_e$ ) is defined as (Chaturvedi et al., 1998):

$$CNR_e = \sqrt{\frac{2(\overline{\varepsilon_L} - \overline{\varepsilon_B})^2}{\sigma_L^2 + \sigma_B^2}}, \quad (3.41)$$

where  $\overline{\varepsilon_L}$  and  $\overline{\varepsilon_B}$  are the mean strain in the inclusion and background, respectively, and  $\sigma_L^2$  and  $\sigma_B^2$  are the variances of strain in the corresponding tissues. The highest  $SNR_e$  was shown when axial strain is between 0.5% and 1% while the  $CNR_e$  was highest when the strain is 0.5% (Varghese & Ophir, 1997). When the strain is too low, the SNR is low due to low mean strain value whereas when the strain is too high, the SNR is equally low due to large strain variances (Varghese & Ophir, 1997).

As stated by Bamber et al. (2013), during cyclical axial palpation employed in modern freehand QSE, the tissue strains more during the compression and the release phases than in the periods between these phases. The most useful frames are when the rate of displacement is constant, that is between the maximum and minimum compression. Soft tissue is also susceptible to rate of the applied strain, that is how quickly the compression is applied. Doyley et al. (2001) showed that the optimal strain rate is 2.9% s<sup>-1</sup>.

QSE is only capable of measuring some of the components of the strain tensor in the tissue. It is possible that strain contrast produced by a strain elastogram do not completely represent the true modulus contrast. Contrast transfer efficiency (CTE) is defined as the ratio of the observed strain contrast ( $C_o$ ) measured from the strain elastogram, and the underlying true modulus contrast ( $C_t$ ), and may be expressed in decibels (dB) as (Ponnekanti et al., 1995):

$$CTE(\text{dB}) = |C_o(\text{dB})| - |C_t(\text{dB})|, \quad (3.42)$$

Therefore, the maximum efficiency is achieved when  $CTE = 1$  or  $0$  dB. Kallel et al. (2001) showed that for low elastic modulus contrast, the strain contrast is equivalent to modulus contrast, that is  $CTE \approx 0$  dB. In the case of a hard inclusion, where the true modulus contrast is positive, the CTE is relatively high ( $CTE \approx 0$  dB). As pointed out by Bamber et al. (2013), a soft background strains more when situated next to a hard inclusion, thereby creating a stress-concentration ('Maltese cross') artefact, where there is an exaggeration of the local strain contrast. In contrast, for soft inclusion in hard background, the CTE is low ( $CTE \ll 0$  dB). This is due to the 'egg shell' effect as described by Ponnekanti et al. (1995), where the stiff shell prevents the generation of strain in the egg.

Chakraborty et al. (2012) showed that high strain was observed across the slippery boundary where there is tissue discontinuity. This phenomenon of high strain across slippery boundary has been exploited to demonstrate the cleavage plane for surgical resection of brain tumours. In addition, when applying time varying strain on a slippery boundary created in phantoms by using fluid lubrication, Uff (2011) found that soft inclusions appeared to have low strain contrast when strain of  $\leq 2\%$  was applied and high strain contrast in the inclusion only became apparent when strain of  $> 2\%$  was applied. This phenomenon was due to the presence of mechanical discontinuity (slip) at the upper border of the inclusion initially preventing strain generation in the inclusion. Once the fluid at the inclusion margin had been expelled with sufficient compression, lubrication to reduce friction at the boundary was no longer present and strain was therefore once again generated in the inclusion through the transmitted force from the transducer.

### **3.2.1.1 Vibrography**

Vibrography is a technique proposed by Pesavento et al. (2000), where low-frequency low-amplitude axial vibration is applied to generate strain in the tissue instead of static compression. As this technique replaces manual compression with low-frequency low-amplitude vibration, total compression can be very low and more controlled, and some motion artefacts minimised. Figure 3.10 illustrates the concept of vibrography. The physics

behind this technique are derived from Pesavento et al. (2000) and Pesavento & Emert (1998).

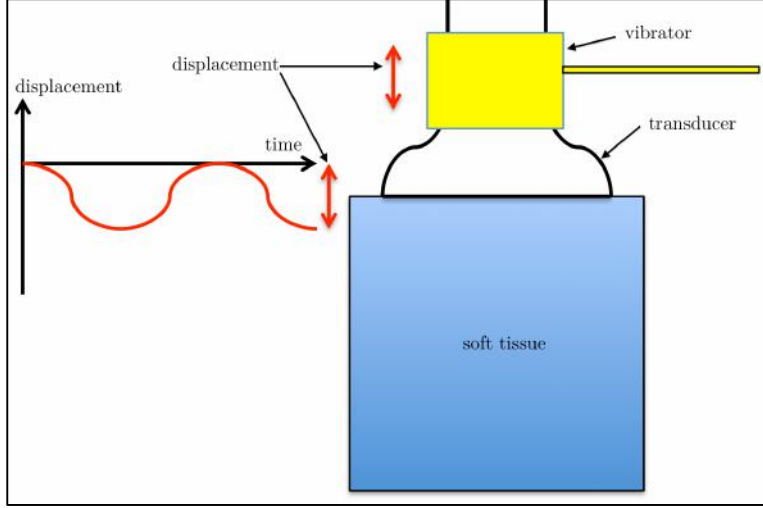


Figure 3.10. The illustration of the concept of vibrography.

For a very low frequency vibration and very slow compression, we can assume the strain being applied is quasistatic. As the vibration is sinusoidal, the compression will also be sinusoidal and can be estimated. Assuming the tissue is linearly elastic and the compression sinusoidal with a frequency ( $\Omega_\nu$ ), the strain ( $\varepsilon_\nu$ ) can be modelled as:

$$\varepsilon_\nu = \varepsilon_E \cos(\Omega_\nu T), \quad (3.43)$$

where  $\varepsilon_\nu$  is estimated strain,  $\varepsilon_E$  is the amplitude of strain,  $T$  is the time,  $\Omega_\nu$  is frequency of vibration and  $\cos(\Omega_\nu T)$  is the phase of vibration. The RF data that are captured at a constant frame rate of  $1/\Delta T$  are given by:

$$x_m = x(m\Delta T), \quad (3.44)$$

where  $m$  is the frame number. Therefore, the RF data at frame  $m$  and  $m - 1$  are denoted by  $x_m$  and  $x_{m-1}$ , respectively, which can be used to estimate axial displacement using phase root seeking algorithm, which will not be discussed here as it is out of the scope of this thesis. The axial displacement obtained can then be used to estimate differential strain ( $\varepsilon_m$ ), which are defined as:

$$\varepsilon_m = \varepsilon(m\Delta T) - \varepsilon((m-1)\Delta T), \quad (3.45)$$

where  $\varepsilon(m\Delta T)$  and  $\varepsilon((m-1)\Delta T)$  are tissue strains at frames  $m$  and  $m-1$ . This technique has been shown to decrease computational cost and improve SNR<sub>e</sub> (Pesavento et al., 2000). There are also options of using this technique with or without lateral compensation or temporal stretching, but the latter significantly increases the computational time (Pesavento & Emert, 1998).

### 3.2.2 Acoustic radiation force impulse (ARFI) imaging

ARFI imaging applies ARF to produce very small displacements in the tissue at a certain focal depth, which are then mapped using a displacement tracking algorithm based on correlation mapping as used in QSE (Nightingale et al., 2002). For a given force induced by ARF, the amount of displacement is inversely proportional to the stiffness of the tissue, as in equation 3.1. Therefore, the relative stiffness between tissues can be estimated.

The force ( $F$ ) induced by ARF at a given spatial location, which is the focal region of the acoustic beam, is given by:

$$F = \frac{W_{absorbed}}{c} = \frac{2\alpha I}{c}, \quad (3.46)$$

where  $F$  is the ARF,  $W_{absorbed}$  is the power absorbed by the medium,  $c$  is the speed of sound in the medium,  $\alpha$  is the absorption coefficient of the medium, and  $I$  is the temporal average intensity (Nightingale et al., 2002).

The implementation described by Nightingale et al. (2002) used a linear array transducer with 194 elements, each element having a dimension of 5mm (height) by 0.2mm (width) with a centre frequency of 7.2 MHz. The ARF employed at each location was 0.7 milliseconds (ms), that is 4 pulses at 5.6 kHz. The shape of the pushing beams, which exerted ARF, was oblong with approximately 4 mm in axially and 0.2 mm laterally. For each ARFI image, there were 19 pushing beams generated, separated laterally by 0.18 mm, giving a lateral region of interest (ROI) of 3.6 mm. At each pushing A-line, the tracking and

pushing beams were alternately fired along the same A-line, which means that the pulse repetition frequency (PRF) for both tracking and pushing beams was 5.6 kHz. The first beam fired was a tracking beam, which served as the initial reference image. The interspersed pushing and tracking beams fired were followed immediately by 21 tracking beams to image tissue response after removal of ARF. The data acquisition for all 19 pushing beams took 90 ms, with time spent on each pushing beam being 4.6 ms.

For each pushing beam, the ARF was estimated to cause an increase of 0.14 °C (Nightingale et al., 2002). The spatial separation of the pushing beams results in minimal accumulation of heat. A temperature rise of less than 1.5 °C is considered safe in humans (WFUMB Symposium on Safety of Ultrasound in Medicine. Kloster-Banz, Germany, 14-16 April 1996, 1998).

The RF data are sampled at 36 MHz, which is then up-sampled to 4.3 GHz giving a minimum measured displacement of 0.18 micrometre ( $\mu\text{m}$ ), assuming the speed of sound in the tissue is 1540  $\text{ms}^{-1}$ . The up-sampling process is performed by adding interpolated data to the original data. One-dimensional cross correlation is then performed in the axial dimension for each up-sampled data in the tracking A-lines. Each tracking line is divided into a series of search windows measuring 0.33 mm in length. The reference window is set at 0.27 mm in length in the preceding tracking line. The cross-correlation function peaks between the reference window and the corresponding search window in the next A-line are used to estimate the axial displacement. A 75% overlap of the windows was used.

The SNR is 40 dB in the focal region, that is 5 to 25 mm in depth, and decreases to 25 dB above and below this region (Nightingale et al., 2002). Assuming a correlation coefficient of 1.0, the errors of axial displacement estimates are  $\pm 0.14 \mu\text{m}$  and  $\pm 0.22 \mu\text{m}$  for 40 dB and 25 dB, respectively. Given the actual axial displacements measured with ARFI imaging are around 5  $\mu\text{m}$ , these errors are very small and should not pose a problem (Nightingale et al., 2002).

As axial displacements can potentially be obscured by physiological pulsations, which can be up to 1.05 mm/s in brain (Selbekk et al., 2010) resulting in 4.83  $\mu\text{m}$  in 4.6 ms,

a simple motion filter is applied. At each location, a linear fit is computed for the displacement data from time-step 0 with no displacement to the last time-step at 4.6 ms, when the tissue is expected to have returned to its original position. The average slopes of these linear fit data are subtracted from temporal displacement data at each location, thereby giving the resultant corrected displacement data, which are assumed to be attributed solely to ARF. The corrected displacement data are used to generate ARFI images, which are subsequently superimposed on the matched B-mode image.

This method has not been implemented in intra-operative neuroimaging, but its high SNR offers potential in this field by possibly providing better tumour-brain boundary characterisation compared to QSE.

### 3.2.3 Shear wave elastography (SWE)

SWE is another type of elasticity imaging technique, which allows quantification of soft tissue elastic modulus. This technique requires generation of shear waves in the tissue either by ARF (Bercoff et al., 2004; Sarvazyan et al., 1998) or mechanically (Catheline et al., 1999; Sandrin et al., 2003; Wu et al., 2006). Shear waves are secondary waves that propagate perpendicular to the direction of displacement, analogous to circular ripples on the water surface that travels outward when a disturbance is introduced (see Figure 3.11). Note that the motion is perpendicular to the direction of propagation.

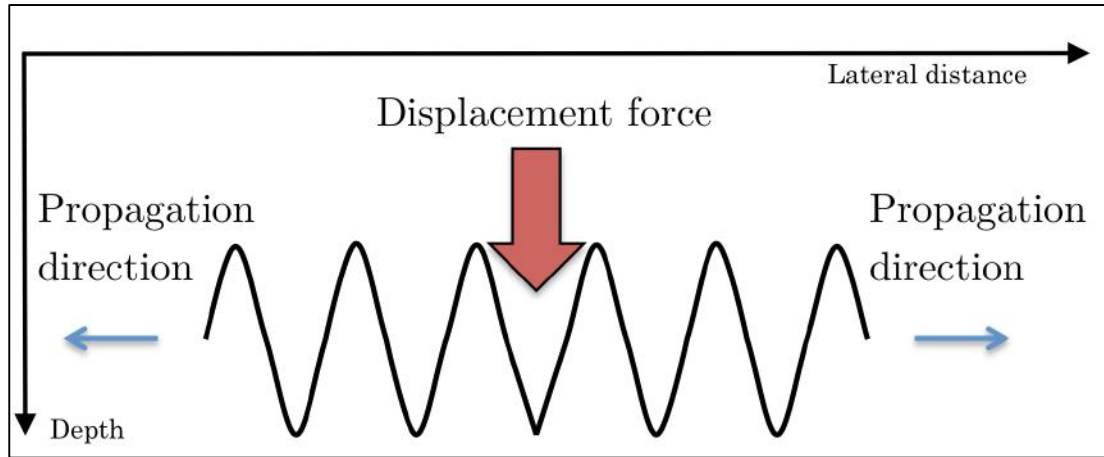


Figure 3.11. Shear waves (black solid line) produced by the displacement force (red arrow), which travels perpendicular to the force (blue arrows).

In a purely elastic material, as shown in equation (3.25) the shear modulus ( $G$  or  $\mu$ ) is given by:

$$\mu = \rho c_s^2,$$

where  $\rho$  is tissue density and  $c_s$  is the shear wave speed. Shear modulus is  $10^6$  smaller than bulk modulus, hence shear wave speed ( $c_s$ ) is approximately 1000 times slower than speed of sound ( $c_{sound}$ ). In addition, the Young's modulus has been shown to have a wide range, that is 18 to 460 kPa depending on the loading frequency and amount of pre-compression (Krouskop et al., 1998).

The Young's modulus ( $E$ ) is given by equation (3.24) that:

$$E = 2(1 + \nu)G, \quad (3.47)$$

where  $G$  is shear modulus and  $\nu$  is Poisson's ratio. Assuming that soft tissue is non-compressible, where the Poisson ratio is approximately 0.5, the Young's modulus ( $E$ ) becomes 3 times shear modulus ( $G$ ), which can be written as:

$$E \approx 3G = 3\rho c_s^2. \quad (3.48)$$

As soft tissue is generally viscoelastic, where the phenomena of stress relaxation and creep occur (Fung, 1993). When strain is applied and then maintained constant, the corresponding stress induced in the viscoelastic soft tissue is reduced; this is called stress relaxation. Similarly, when stress is applied to the soft tissue and maintained constant, the soft tissue continues to deform; this is known as creep. A further consequence is that unlike a purely elastic material, when cyclical loading is applied to a viscoelastic medium, the stress-strain relationship is different during the loading and unloading phase; this is known as hysteresis. In a viscoelastic tissue, the strain in the tissue lags behind the stress applied. If the stress is applied dynamically in a simple harmonic motion, the lag in the strain induced can be quantified in terms of phase shift. Purely elastic tissue does not have lag so the phase shift is  $0^\circ$  whereas purely viscous tissue has maximal lag so the phase shift is  $90^\circ$ . In viscoelastic tissue, the phase shift lies somewhere in between purely elastic and purely viscous. A viscoelastic dynamic modulus is given by:

$$G^* = G' + iG'' , \quad (3.49)$$

where  $G^*$  is the complex modulus,  $G'$  is the storage modulus,  $G''$  is the loss modulus and  $i = \sqrt{-1}$ . The storage and loss moduli are related to the elastic and viscous components of the tissue, respectively. The shear wave speed ( $c_S$ ) is related to  $G'$  and  $G''$  by (Macé et al., 2011):

$$c_S = \sqrt{\frac{2}{\rho} \frac{G'^2 + G''^2}{G' \left(1 + \sqrt{1 + \left(\frac{G''}{G'}\right)^2}\right)}} , \quad (3.50)$$

where  $\rho$  is tissue density. Assuming low viscosity in tissue, that is  $G'' \ll G'$ , the equation becomes:

$$c_S \approx \sqrt{\frac{G'}{\rho}} \quad (3.51)$$

$$G' \approx \rho c_S^2 . \quad (3.52)$$

This equation is similar to equation (3.25) for a purely elastic medium. In Young's modulus ( $E$ ) estimation, the soft tissue is assumed to have low viscosity.

### 3.2.3.1 Transient elastography (Fibroscan®)

Transient elastography is 1D elastographic technique, where a low-frequency mechanical vibrator, typically at 50 Hz, is used to generate shear waves (Sandrin et al., 2003). This type of elastography has been solely applied to liver elasticity measurement, for fibrosis assessment. The technique described here is based on Sandrin et al. (2003). The acquisition is performed using a single element transducer operating at 5 MHz with a focal depth of 35 mm. For a single shear wave (1 mm amplitude with 20 ms duration), a total of 256 RF lines are acquired at a PRF of 4 kHz. The RF lines are segmented in depths into 1-mm segments with 50% overlap. The axial displacement is estimated by comparing with successive RF lines. Parabolic interpolation is used to determine the position of the peak of correlation function. Assuming diffraction and dissipation are negligible, the shear velocity ( $c_s$ ) can be estimated from the phase velocity, through linear regression of the phase delay of the strain as a function of depth and frequency of the shear wave. This is expressed as:

$$c_s = 2\pi f_0 \left[ \frac{\partial \phi(z, f_0)}{\partial z} \right]^{-1}, \quad (3.53)$$

where  $f_0$  is the centre frequency of the shear wave (= 50 Hz),  $\phi(z, f_0)$  is the phase delay of the Fourier transform of the strains induced in the medium  $\varepsilon(z, t)$ , and  $z$  is the depth. A linear regression coefficient of  $r^2 < 0.85$  is rejected while that of  $r^2 \geq 0.85$  are accepted and validated. The median value of validated estimates is used as the patient's liver elasticity value. The Young's modulus is calculated as  $3\rho c_s^2$ , as per equation (3.25).

### 3.2.3.2 Crawling wave imaging

The crawling wave imaging technique uses 2 piezoelectric bending biomorphs as transducers to generate shear waves, which produce 2 low-frequency vibration sources at a slightly different frequency so that the resultant interference pattern can be subsequently imaged with an ultrasound scanner for estimating elastic modulus (Wu Z. et al., 2006). Assuming that the tissue is homogeneous and isotropic, the phase of the vibrating field ( $\phi$ ) is given by:

$$\phi = kd, \quad (3.54)$$

where  $k$  is the shear wave number and  $d$  is the distance of the field from the vibrating source. Assuming the tissue is infinite, an interference pattern can be observed if there are 2 coherent shear wave sources present. The antinode lines correspond to regions of maximum amplitude summation of the sources. If both sources are in phase, then the difference between  $d_1$ , which is the distance between the antinode line and the first wave source, and  $d_2$ , which is the distance between the same antinode line and the second wave source, is equal to integer multiple of wavelength:

$$|kd_1 - kd_2| = 2n\pi \quad (3.55)$$

$$|d_1 - d_2| = n\lambda, \text{ where } n \text{ is an integer.} \quad (3.56)$$

Therefore, the antinode lines can be plotted as hyperbolae. Figure 3.12 illustrates the locations of the antinode lines.

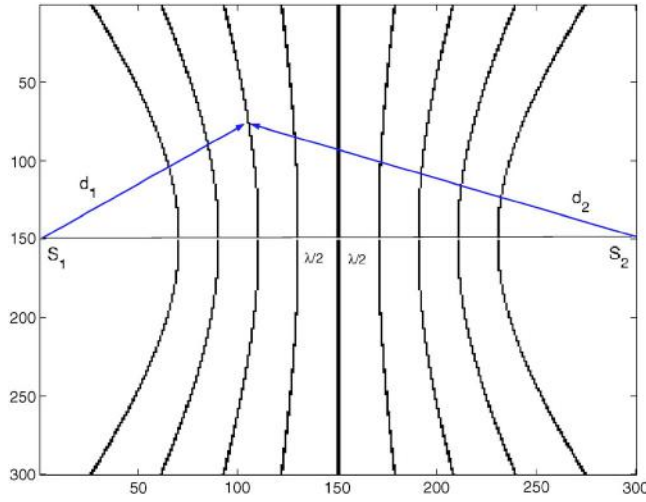


Figure 3.12.  $S_1$  and  $S_2$  are shear wave sources. The antinode lines can be illustrated as hyperbolae. (Adapted from Wu Z. et al. (2006))

The hyperbolae can be expressed as the following equation:

$$\frac{x^2}{a^2} - \frac{y^2}{b^2} = 1, \quad (3.57)$$

$$\text{with } a = \frac{n\lambda}{2}$$

$$\text{and } b^2 = \left(\frac{D}{2}\right)^2 - a^2,$$

where  $\lambda$  is the wavelength, and  $D$  is the distance between the 2 shear wave sources. As the shear wave sources are very far apart, that is distance  $D$  becomes very large, the hyperbolae can be approximated as parallel lines. At  $y = 0$ , from equation (3.57) the antinode lines are half shear wave lengths apart, given by:

$$x = \pm \frac{n\lambda}{2}. \quad (3.58)$$

When one source vibrates at frequency  $\omega$  and another at frequency  $\omega + \Delta\omega$ , with  $\Delta\omega \ll \omega$ , the antinode lines are no longer static but move towards the source with lower

frequency as a wave, which is called crawling wave (Wu Z. et al., 2006). The location of the waves are given by:

$$|kd_1 - (kd_2 + \Delta\omega t)| = 2n\pi \quad (3.59)$$

$$|d_1 - d_2 - \frac{\Delta\omega t}{k}| = n\lambda \quad (3.60)$$

$$|d_1 - d_2| = n\lambda + \frac{\Delta\omega t}{k}. \quad (3.61)$$

Therefore, from equation (3.58) and (3.60), at  $y = 0$ :

$$x = \pm \frac{|d_1 - d_2|}{2}. \quad (3.62)$$

Substituting equation (3.63) into (3.64) with  $y = 0$  yields:

$$\begin{aligned} x &= \pm \frac{n\lambda}{2} + \frac{\Delta\omega \cdot \omega}{2\omega \cdot k} t \\ x &= \pm \frac{n\lambda}{2} + \frac{\Delta\omega}{2\omega} t v_{shear}, \end{aligned} \quad (3.63)$$

where  $\frac{\Delta\omega}{2\omega} v_{shear}$  is the speed of the crawling wave, and  $x$  is the distance between the antinode lines, which is also called the crawling wavelength. The moving antinode lines are known as the crawling wave fronts. As the shear waves from the sources may not move in a straight line, the angle of interference  $\theta$  can influence the crawling speed by:

$$v_{crawling} = \frac{\Delta\omega}{2\omega} \cdot \frac{v_{shear}}{\cos\left(\frac{\theta}{2}\right)}. \quad (3.64)$$

If the distance between the sources are large, then  $\cos\left(\frac{\theta}{2}\right) \approx 1$ , resulting in:

$$v_{crawling} \approx \frac{\Delta\omega}{2\omega} \cdot v_{shear}. \quad (3.65)$$

The method for imaging crawling wave estimates the peak displacement of scatterer motion in the tissue by analysing the power spectral spread of the Doppler ultrasound signal (Lerner et al., 1990). The shear wave speed ( $v_{shear}$ ) is slowed down by a factor of  $\frac{\Delta\omega}{2\omega}$ , thus allowing indirect estimation through crawling wave speed. With the advent of ultrafast imaging (Bercoff et al., 2004b), the shear waves can be tracked and imaged using the supersonic shear imaging (SSI) technique, which is discussed next.

### 3.2.3.3 SuperSonic shear imaging (SSI)

SSI is a method of SWE where ARF is applied to soft tissue to induce displacement to generate perpendicularly propagating shear waves, the speed of which are subsequently estimated with cross-correlation function, thus allowing quantitative real-time mapping of elastic modulus (Bercoff et al., 2004b). The following discussion is based on Bercoff et al. (2004b). As discussed in ARFI imaging section, the ARF is given by the equation:

$$F = \frac{2\alpha I}{c_{sound}}, \quad (3.66)$$

where  $F$  is the ARF,  $I$  is the local intensity of the ultrasound beam,  $c_{sound}$  is the speed of sound in the tissue ( $\sim 1540 \text{ ms}^{-1}$ ), and  $\alpha$  is the ultrasound attenuation coefficient or tissue's absorption coefficient. This system is capable of producing an ARF sweep to successively focus on different depths along the line of excitation in a Mach cone, thus allowing generation of shear waves at multiple depths, known as quasi-plane shear waves (Deffieux et al., 2012). As a result of the Mach cone, the shear waves generated are shaped like a cone, which is at an angle to the axis of excitation travelling in opposite directions to each other (see Figure 3.13). The angle  $\theta$  depends on how fast the ARF focus moves axially and how fast the shear waves travels laterally; this is known as the Mach number ( $M$ ):

$$M = \sin \theta = \frac{c_s}{c_{ARF}} = \frac{c_s}{c_{sound}}, \quad (3.67)$$

where  $c_s$  is the shear wave speed,  $c_{\text{ARF}}$  is the ARF speed, and  $c_{\text{sound}}$  is the sound speed in the tissue. Mach number is defined as the ratio of ARF focusing speed to the shear wave speed. As the former is approximately  $1540 \text{ ms}^{-1}$  in soft tissue and the latter is approximately  $1$  to  $10 \text{ ms}^{-1}$ , the Mach number can potentially reach 1500. This regime is analogous to “sonic boom” created by supersonic aircraft in the air, hence the name SSI for this method of imaging (Bercoff et al., 2004a).

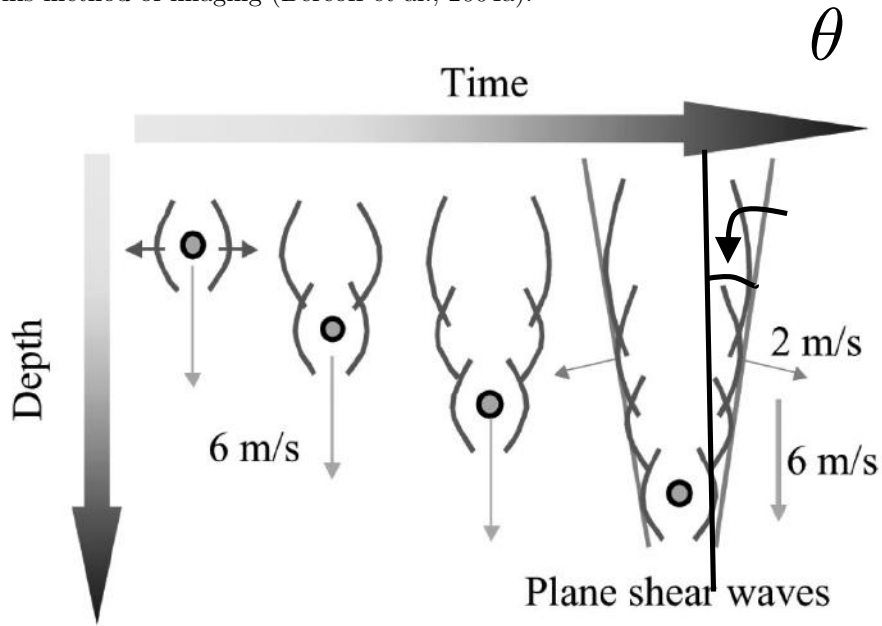


Figure 3.13. The illustration of shear wave generation with ARF sweep focused at different depths. The resultant shear waves have the conical shape travelling in opposite directions. The angle  $\theta$  depends on the speed of focus moving axially and the speed of the propagating shear waves; and is directly linked to the Mach number. (Adapted from Bercoff et al., 2004b).

The shear wave propagation equation is given by:

$$\rho \frac{\partial^2 u}{\partial t^2} = \mu \Delta u, \quad (3.68)$$

where  $\mu$  is the shear modulus,  $u$  is the displacement vector,  $\rho$  is the tissue density, and  $t$  is time. Using the  $z$ -component (axial) of the displacement, the equation becomes:

$$\rho \frac{\partial^2 u_z}{\partial t^2} = \mu \Delta u_z. \quad (3.69)$$

As the image area is on  $(x, z)$  plane, assuming that the out-of-plane displacement (in the  $y$  or elevational direction) is not significant, then:

$$\frac{\partial^2 u_z}{\partial y^2} \ll \frac{\partial^2 u_z}{\partial x^2} + \frac{\partial^2 u_z}{\partial z^2}, \quad (3.70)$$

therefore,

$$\Delta u_z \approx \frac{\partial^2 u_z}{\partial x^2} + \frac{\partial^2 u_z}{\partial z^2}. \quad (3.71)$$

As the displacement is a function of time, by substituting equation (3.71) into equation (3.69), the shear modulus can be re-written in the Cartesian coordinate in the  $(x, z)$  plane domain as:

$$\mu(x, z) = \frac{\rho}{N} \sum_{\omega} \frac{F\left(\frac{\partial^2 u_z(x, z)}{\partial t^2}\right)}{F\left(\frac{\partial^2 u_z(x, z)}{\partial x^2} + \frac{\partial^2 u_z(x, z)}{\partial z^2}\right)}, \quad (3.72)$$

where  $F$  is the Fourier transform in the time domain,  $N$  is the number of frequencies taken into account, and  $\omega$  is the shear wave frequencies. From this equation, local shear modulus can be estimated in the area covered by the shear wave propagation.

Equation (3.72) is only valid in the regions free from ARF, as it does not take into account the interference of ARF on shear wave propagation. Therefore, this may lead to overestimation of the shear wave velocity at the shear source, that is region displaced by ARF to create shear waves.

The duration of ARF “push” at each depth is approximately 100  $\mu\text{s}$  with a PRF of 500 Hz, which is followed by ultrafast imaging sequence at PRF of 3000 Hz (Bercoff et al., 2004b) (see Figure 3.14). These “pushes” create displacements of up to 100  $\mu\text{m}$  in phantoms and up to 40  $\mu\text{m}$  *in vivo* (Bercoff et al., 2004b).

Theoretically, the frame rate achievable by a conventional ultrasound is about 200 Hz, assuming it has 128 elements and the imaging depth is 3 cm. The distance travelled by

the ultrasound beam for an A-line in a B-mode image is twice the depth, as the transmitted beam has to travel to the depth and the reflected echo travel back to the transducer. The subsequent elements are fired in turns, therefore for a 128-element transducer, the total distance travelled by the ultrasound beam and echo is 768 cm ( $6 \times 128$  cm). Therefore, assuming the sound speed in soft tissue is  $1540 \text{ ms}^{-1}$ , the time taken for an image is 0.0049 s. The frame rate is the inverse of that, which is 200 frames per second or Hz.

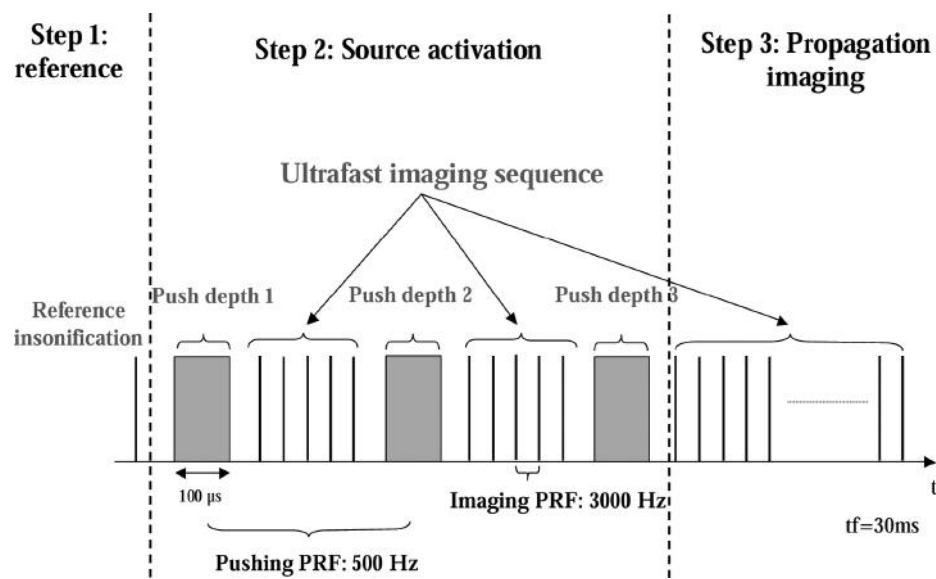


Figure 3.14. The supersonic imaging regime. Initial reference insonification (step 1) is performed to obtain a reference image before any “pushes” are initiated. The pushing sequence (step 2) is performed by applying “pushes” at different depths, each lasting  $\sim 100 \mu\text{s}$ . In between the “pushes”, ultrafast frames can be acquired to monitor the activation of the supersonic ARF. This is followed by imaging of the propagation shear wave (step 3) to estimate the shear wave velocity and elastic modulus. (Adapted from Bercoff et al. (2004))

Assuming shear wave propagation speed is up to  $10 \text{ ms}^{-1}$  in the soft tissue, in order to capture a travelling distance of 1 mm, the time required to capture this distance is 0.00001 s, that is, a frame rate of 10 kHz. This is not possible with conventional ultrasound system. In contrast, ultrafast imaging acquisition is performed using plane wave transmit-receive. This means that the whole 128 elements are fired at the same time, therefore, for a 3-cm imaging depth, the achievable frame rate is  $\sim 25$  kHz, more than 100 times that of

conventional ultrasound. This means that the ultrafast imaging regime can capture up to 3 frames of the shear waves travelling within 1 mm.

In order to improve SNR, SSI is capable of performing shear compounding by tilting the shear waves by the changing the Mach number. As demonstrated above, due to ARF being emitted in a Mach cone fashion, the shear waves generated are conical in shape and thus tilted at an angle. By changing the Mach number, the tilt angle can be changed (see Figure 3.15). The tilt angle seems to be changing for Mach 1 to Mach 5 but for higher Mach number, the shear wave angle becomes parallel to the ARF axis and does not change significantly. The shear wave angle for Mach 10 is illustrated in Figure 3.15(b). Therefore, shear compounding can be performed for 10 tilted waves (from Mach -5 to Mach 5). This technique was shown to reduce the variance from 12% to 4% in the hard inclusion in a heterogeneous phantom, and improve the shape of the inclusion (Bercoff et al., 2004b).

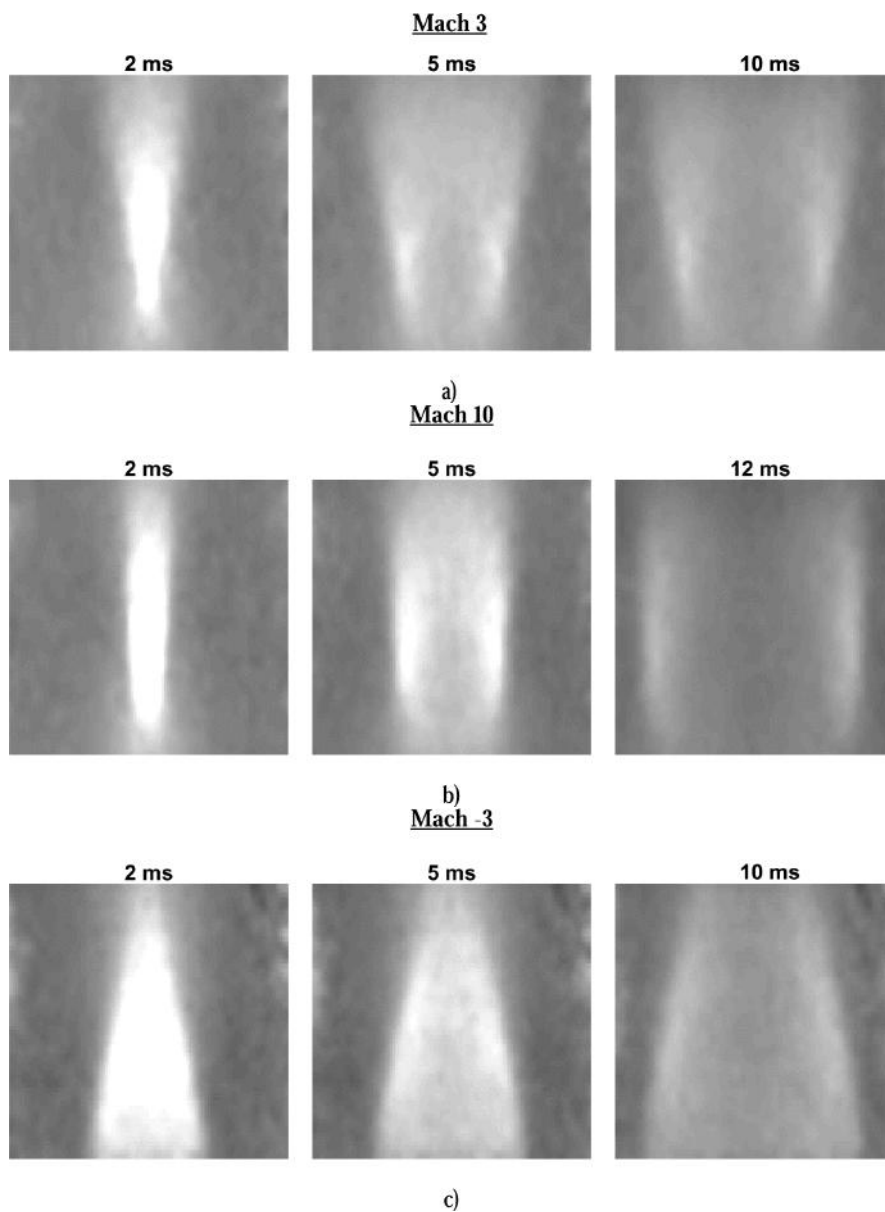


Figure 3.15. The supersonic regime for different Mach number: (a) Mach 3 (b) Mach 10 (c) Mach -3. Note that Mach -3 is the inverse of Mach 3, with the Mach cone converges towards the transducer.

Deffieux et al. (2011) observed a phenomenon with SSI where the shear wave is the reflected from at inclusion boundary. This is important as the estimated shear wave speed can be affected when both incident and reflected shear waves are present, due to the time-of-flight approach in the estimation (see equation (3.73)). Therefore, Deffieux et al. (2011) proposed a directional filter, which was modified from magnetic resonance elastography

directional filter proposed by Manduca et al. (2003) to solve this problem. The sum of 1D waves travelling forward and backward at velocity  $c$  in the temporal domain ( $U(x, t)$ ) is given by:

$$\begin{aligned} U(x, t) &= \iint (U_f(\omega)e^{j(\omega t - kx)} + U_b(\omega)e^{j(\omega t + kx)})d\omega dk \\ &= \int U_f(\omega)e^{j(\omega t - (\omega x)/c)} + U_b(\omega)e^{j(\omega t + (\omega x)/c)}d\omega, \end{aligned} \quad (3.73)$$

where  $U_f$  is the forward travelling wave,  $U_b$  is the backward travelling wave (which is also the reflected wave),  $\omega$  is the angular frequency,  $k$  is the angular wavenumber<sup>19</sup>,  $t$  is time,  $x$  is the lateral coordinate, and  $j$  is a complex number ( $\sqrt{-1}$ ). By Fourier transforming the equation (3.73) into the frequency domain<sup>20</sup> ( $k, \omega$ ), the phase velocity ( $c_{phase}$ ) is given by:

$$c_{phase} = \frac{\omega}{k}, \quad (3.74)$$

where  $\omega$  is the angular frequency, and  $k$  is the angular wavenumber. From equation (3.74), the phase velocity ( $c_{phase}$ ) is negative when  $\omega < 0$  and  $k > 0$  or  $\omega > 0$  and  $k < 0$ , and vice versa. A negative phase velocity implies the wave travelling backwards while a positive phase velocity the wave travelling forwards. Therefore, by multiplying the phase velocity with a mask, one can separate the forward component from the backward component. The borders of the mask are then smoothed out to reduce artefacts.

This thesis describes the application of SSI in neurosurgery during resection of brain tumour and epileptogenic foci, using the SuperSonic Aixplorer® scanner (SuperSonic Imagine, Aix en Provence, France). Therefore, the description and implementation of the scanner for the experimental chapters is discussed next.

<sup>19</sup> The angular wavenumber ( $k$ ) is a constant that represents the proportionality of the angular frequency to the phase velocity.

<sup>20</sup> Also known as k-space representation.

### 3.2.4 SuperSonic Aixplorer® scanner

In this section, a brief description of the SuperSonic Aixplorer® scanner will be presented together with the configuration of the scanner for intra-operative imaging in neurosurgery.

This scanner's basic dimensions are 61 cm (width) by 112 cm (depth) by 168 cm (height) when the monitor is fully raised and 129 cm (height) when the monitor is locked down. These dimensions are relatively normal for an ultrasound scanner, and can fit nicely in the operating room. It is very important to place the scanner so that the monitor is in the direct vision of the operating surgeon, and close enough to the operating field to allow real-time scanning. The setup for the clinical scan at Great Ormond Street Hospital is illustrated in Figure 3.16.

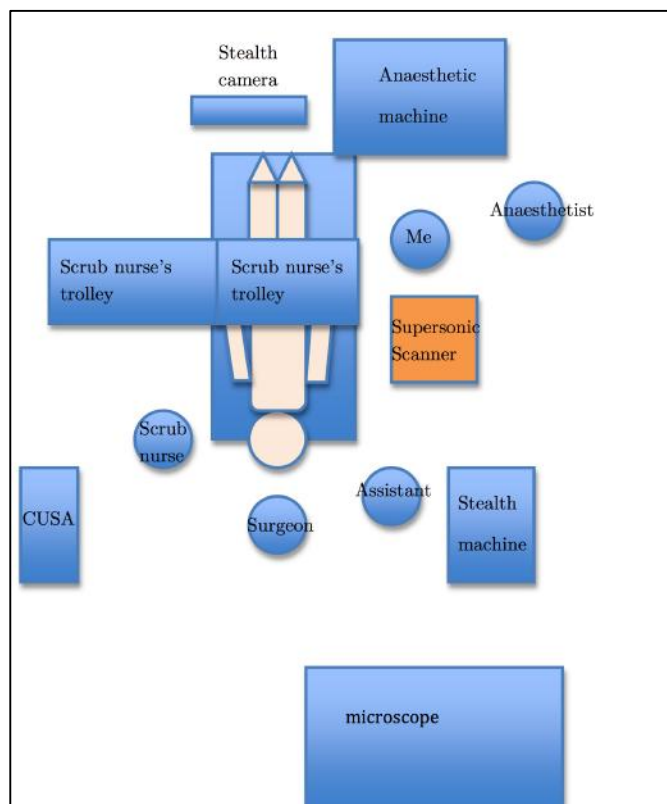


Figure 3.16. The operating room setup at Great Ormond Street Hospital. The SuperSonic Aixplorer® scanner (orange) is placed next to the patient body (beige) with the monitor swivelled to face the surgeon. I stand next to the scanner so that I can optimise the scanner settings as well as acquire images for this thesis.

The ultrasound transducer is placed in a sterile plastic sheath filled with sterile acoustic coupling gel. The surgeon performs the scan by placing the covered ultrasound transducer directly on the brain without applying any pressure on the brain. The surgeon is very experienced with intra-operative ultrasound scanning. As the SSI method does not require application of compression, the elastographic image acquisition is very similar to sonogram acquisition. In order to orientate the sonogram with MRI, the scans are performed in the orthogonal planes whenever possible. When uncertainty arises during ultrasound scanning, the Stealth neuronavigation is used to help with orientation. However, we are aware that the position shown on the neuronavigation is subjected brain shift. Figure 3.17 is a photograph showing the surgeon performing the scan.



Figure 3.17. A photograph showing the surgeon performing the scan.

There are 3 SWE modes in this scanner – resolution, standard and penetration modes denoted by ‘RES’, ‘STD’ and ‘PEN’, respectively. The resolution mode is used for imaging superficial areas of interest whereas the penetration mode is used for imaging deeper or larger areas of interest, which are suspected to be stiff and thus have high shear wave

velocity (SuperSonic Imagine, 2010). The standard mode is the default mode and is balanced between resolution and penetration modes (SuperSonic Imagine, 2010).

Figure 3.18 shows the buttons on the Supersonic Aixplorer® scanner. The sequence for setting up the scanner is as follows:

1. Turn on the scanner in the top left hand corner next to the speaker.
2. Press the ‘PROBE’ button situated leftmost on the second row. This will allow you select the preset configuration for the probe. For clinical scan, I would select GOSH, which has been configured specifically for intra-operative brain scanning.
3. Press on the ‘PATIENT’ button situated on the right of the probe button. This will allow you to enter the patient details.
4. This step is performed after the transducer is draped with sterile sheath and the first scan is about to be acquired. The focus and the depth of the scan can be adjusted with the 2 rightmost grey knobs ‘FOCUS’ and ‘DEPTH’, respectively. To obtain optimal sonogram, the focus needs to be deeper than the area of interest (see Figure 3.19). When the surgeon places the draped transducer on the brain, press the ‘AUTO TGC’ button, which is the fourth button from the bottom on the right. This will allow the sonogram image to be optimised, analogous to auto focus option on a camera. This allows better visualisation of the structures on sonogram but does not affect the SWE mode.
5. Press the ‘SWE’ orange knob, which is the third knob from the left. This will change the display from a single image to 2 images. The top image is the

elastogram superimposed on sonogram while the bottom image is solely the sonogram. Ensure that the SWE gain is set to 70%, which is the preset (see Figure 3.19). But if it is not, then set it to 70% by turning the ‘SWE’ orange knob clockwise or counter-clockwise to increase or decrease the gain, respectively. SWE gain is the threshold mask, which determines the quality of SWE signal that is displayed on the screen. If the SWE gain is set at 100%, then the threshold mask is set at its lowest, thus allowing even very noisy SWE signal to be displayed. This implies that the SWE estimates are not reliable. If the SWE gain is set at 0%, then the threshold mask is set at its highest, thus potentially not displaying any SWE signal. The author has discovered that SWE gain at 70%, which is preset on GOSH configuration, is the optimal setting to use.

When acquiring the SWE images, the surgeon needs to place the transducer lightly on the brain as pressure on the brain can cause artefactually high Young’s modulus, as shown later in this thesis. However, if the region of interest is deeper, these artefacts are no longer significant. Another consideration when performing the scan is to hold the transducer still for about 3 seconds to allow the generation and stabilisation of the SWE signal.

When the region of interest is not on the brain surface, the SWE mode should be set to ‘PEN’ to allow maximal SWE signal, by turning the leftmost grey knob situated just beneath the display clockwise (see Figure 3.20).

6. As the normal brain Young’s modulus is around 30 kPa, as shown in Uff (2011) and later in this thesis, the SWE scale should be set at 0 to 70 kPa (see Figure 3.19) by turning the grey knob on the rightmost situated just beneath the screen (see Figure 3.20).
7. The region-of-interest (ROI) box, which is rectangular, is adjusted to the maximum to allow largest possible elasticity map (see Figure 3.19). This can be adjusted by swiping your finger clockwise on the grey ring circling the trackball. The ROI box can be placed at the desired location by using the trackball.

8. To capture the desired image, press the 'FREEZE' button first, which is situated in the bottom right hand side. Then, using the trackball, you can select the frame(s) you want to save. To save, press the 'SAVE IMAGE' button situated above the 'FREEZE' button.
  
9. If a video clip is required, then press 'SAVE CLIP' button situated on the bottom left above the arrow button. This needs to be pressed before acquiring the clip.
  
10. Once the images are saved, Young's modulus measurement can be performed afterwards. To perform measurements in the same sitting as image acquisition, simply press the 'REVIEW' button, the second button on the second row on the right, and select the image you want to analyse. Press 'MEAS.' button left of the grey ring will display a Q-box (see Figure 3.19). Q-box is a circle that can be placed anywhere within the ROI to give the mean, minimum, maximum, and standard deviation of the Young's modulus measurement and the diameter of the Q-box. Press 'SELECT' button situated just on top of the grey ring to fix the placement of the Q-box. To obtain another Q-box, simply press the 'MEAS.' button once again and repeat the process above. A maximum of 4 Q-box measurements can be displayed at one time. After 4 Q-box's, the 5<sup>th</sup> Q-box measurement will replace the first Q-box measurement on display. Therefore, it is advised to save the image and then reselect the image using 'PREVIEW' button to start measurements of new regions.

To make measurements in a later setting, press the 'PREVIEW' button and select the image set required. Press 'CONTINUE' on the touch screen display to allow Q-box measurements and saving of images.

11. Once the scan acquisition is finished, simply press the 'END EXAM.' button, third button from the left on the second row, and the images including the Q-box measurements will be saved.

These steps have been devised after performing preliminary clinical scans to optimise the performance of SWE mode of Supersonic Aixplorer® scanner for intra-operative brain elasticity imaging. Subsequent clinical scans performed for this thesis, which represent the largest intra-operative SWE in neurosurgery to date, are acquired using the above sequence.



Figure 3.18. The buttons on the Supersonic Aixplorer scanner. (Adapted from SuperSonic Imagine (2010))

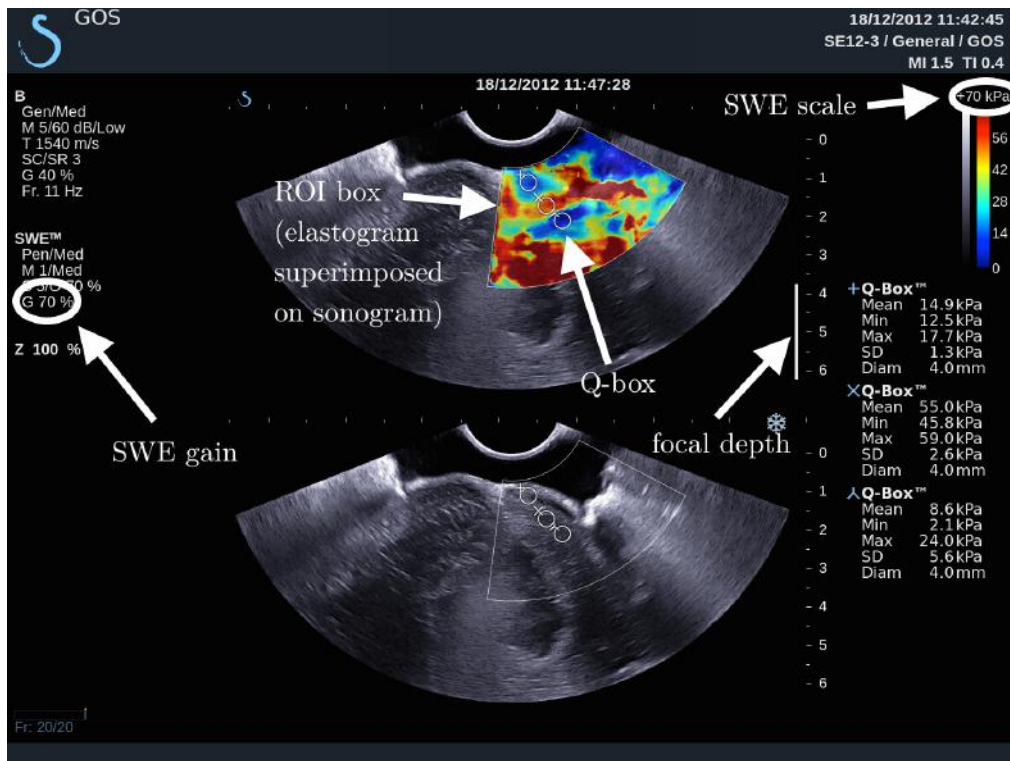


Figure 3.19. The display on Supersonic Aixplorer® scanner on SWE mode, showing SWE gain, SWE scale, focal depth, ROI box and Q-box.



Figure 3.20. This photograph shows the 4 grey knobs just beneath the display. The leftmost knob controls the SWE mode while the rightmost knob controls the SWE scale. (Adapted from SuperSonic Imagine (2010))

## **Chapter 4**

# **Verification of Shear Wave Elastography Measurements**

This chapter describes how shear wave elastography (SWE) measurements with SuperSonic Aixplorer® scanner are verified using gelatine phantoms. The factors affecting the Young's modulus of gelatine phantoms are also demonstrated. The second part of this chapter describes cross validation of SWE with magnetic resonance elastography (MRE) using post-mortem mouse brains

## 4.1 Introduction

Before any measurements made with shear wave elastography can be used reliably in the clinical settings, experiments verifying the measurements need to be performed. Gelatine phantoms were used in these experiments because they are easy to manufacture and possess tissue-like properties, having the speed of sound close to 1540 m/s, mass density close to 1.0 g/cm<sup>3</sup> and elastic properties. However, there are several factors that can affect the stiffness, and hence the Young's modulus, of gelatine phantoms, namely temperature, gelatin concentration, and time.

## 4.2 Nomenclature

Gelatin refers to the precursor protein derived from collagen used for manufacturing gelatine commercially. The term “gelatine”, on the other hand, is the term used for the commercial or laboratory product including inorganic salts and any other impurities (Ward & Saunders, 1958). In this thesis, the phantoms are made using porcine skin gelatin (Sigma-Aldrich, Type A, 300 bloom) combined with either cellulose (Sigmacel® Cellulose Type 20) or polyethylene granules as scatterers. Therefore, these phantoms are referred to as gelatine phantoms.

Bloom is a test used to measure the strength of gelatin (Ward & Saunders, 1958). Gelatin solution of 6.67% concentration needs to be kept at 10 °C for 17 to 18 hours prior to testing. The test determines the weight in grams required by a probe with a diameter of 0.5 inch to deform the gelatin surface by 4 mm without breaking it. The measurement is expressed in bloom.

## 4.3 Gelatine phantom manufacture

Porcine skin gelatin (Sigma-Aldrich, Type A, 300 bloom) was dissolved in water and then heated to 60 °C using the combined heater-mixer apparatus. Cellulose (Sigmacel® Cellulose Type 20) or high density polyethylene granules (HDPE) (119µm mean diameter,

approximately 4000 per cm<sup>3</sup>) were then added as ultrasonic scatterers. When HDPE granules were used, a drop of surfactant (Merck UK, Symperonic N) was added to disperse them in the solution. Cellulose scatterers did not require surfactant. The solution was degassed in a vacuum chamber to remove bubbles in the solution. It was then cooled to 30°C before it was poured into a Perspex or polypropylene mould. During the cooling of the solution, it was constantly stirred to avoid accumulation of polyethylene scatterers on the surface or cellulose scatterers in the bottom of the solution. The solution was finally stored in a refrigerator at 4°C until solidified.

## 4.4 Temperature dependence of gelatine phantoms

### 4.4.1 Introduction

As the rigidity of gelatin gels depends markedly on the temperature of measurements (Ferry, 1948), in this thesis shear wave elastography was used to determine the Young's modulus of gelatine phantoms at different temperatures and the results are compared with that of Ferry (1948).

### 4.4.2 Materials and methods

Cylindrical Perspex moulds with diameter of 53.5 mm and height of 30 mm were used to make the gelatine phantoms with gelatin concentrations of 8%, 10% and 14% and HDPE concentration of 0.25% for all 3 phantoms. An extremely low concentration (0.25%) of ultrasonic scatterers was used to avoid the scatterers contributing to the overall concentration of the gelatine phantoms. The storage time in the refrigerator was approximately 3 hours. The phantoms were scanned with the SuperSonic Aixplorer scanner using the ShearWave Elastography (SWE) mode in the air using ultrasonic gel as the acoustic coupling medium, and their temperature recorded using a digital thermometer (Fluke 52 Series II, Fluke UK Ltd., Norwich, UK). The tip of the thermocouple was placed in the centre of the interior of the gelatine phantoms. The scanning was performed at an interval of every degree Celsius temperature rise.

### 4.4.3 Results

Young's modulus measured with shear wave elastography for all 3 phantoms decreased with increasing temperature, following a pseudo-sigmoid curve (Figure 4.1).

### 4.4.4 Discussion

The trend corresponded well with Ferry's (1948) findings (Figure 4.2). However, Ferry (1948) used complex modulus ( $G$ ) and different gelatin concentrations and molecular weights compared to my experiment. Young's modulus ( $E$ ) for an elastic and incompressible medium is 3 times that of complex modulus ( $G$ ), as dictated by the equation

$$E = 2(1 + \nu) \times G \quad (4.1)$$

where  $\nu$  is the Poisson ratio, which is 0.5 for an elastic and incompressible medium. Therefore, we can infer from Ferry's (1948) findings that the Young's modulus of gelatine phantoms as measured using shear wave elastography broadly followed the expected trend for temperature dependence.

### 4.4.5 Conclusion

This experiment demonstrated that the Young's modulus of the gelatine phantom material measured with SWE is inversely proportional to the temperature. A higher concentration gelatine phantom have a steeper slope with increasing temperature, i.e. a stronger temperature coefficient, and that this behaviour is similar to that found in published literature. As shown in Figure 4.1, for gelatine phantoms with small concentration differences, the desirable temperature at which measurements should be made was between 6 and 17°C. Above 17°C, the difference in Young's modulus measurements between the lower concentration gelatine phantoms was getting smaller to the point that there was no discernable differences at 21°C. Furthermore, above 17°C, the higher concentration gelatine phantom showed steeper drop in the Young's modulus measurements, thereby potentially

causing unreliable measurements. Therefore, in this thesis, the measurements were made at 16°C, with the exception of the experiment on time dependence (Section 4.6) where temperature of 12°C was used. The reason for this is to minimise the exposure time to ambient temperature to avoid excessive water evaporation and fluctuation in the storage temperature.

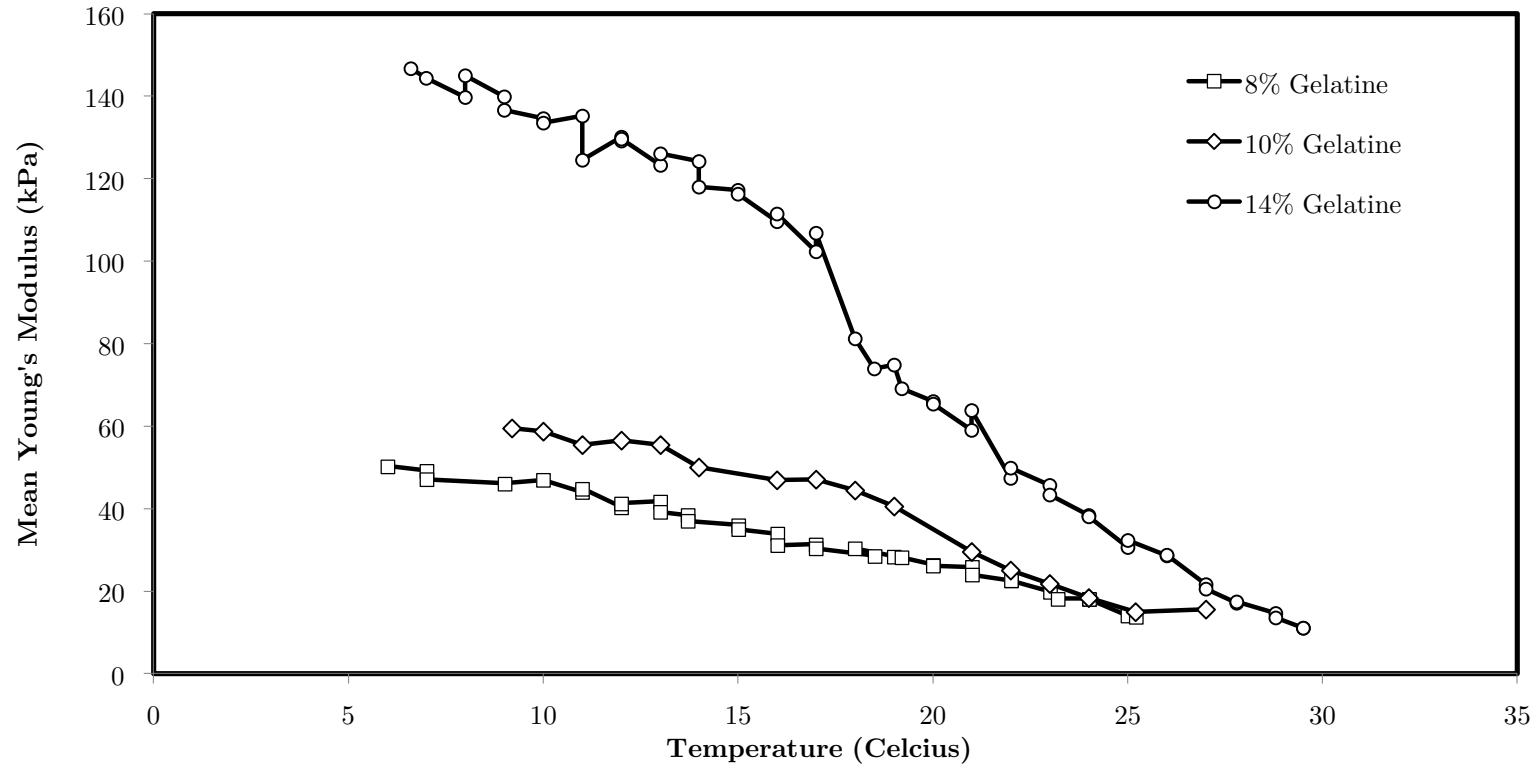


Figure 4.1. Measured Young's modulus for gelatine phantoms with 8%, 10% and 14% gelatin concentrations with respect to temperature.

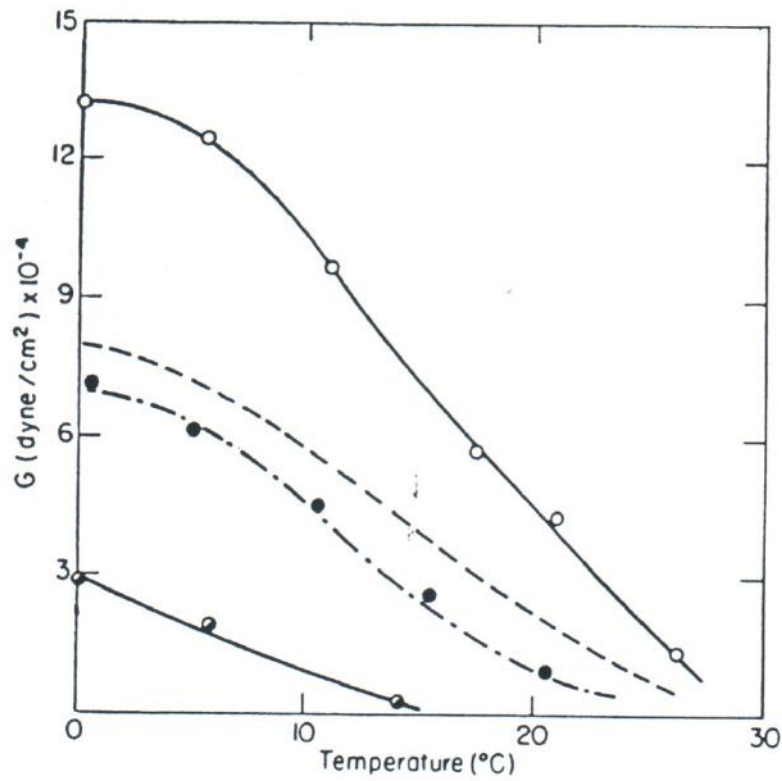


FIG. 13. Comparison of rigidities of a mixed sample and its components at a concentration of 5.75 g./100 ml.:  $\circ$  gelatin 1,  $M_n = 45,000$ ;  $\bullet$  gelatin 2,  $M_n = 22,000$ ;  $\bullet$  mixture of equal parts by weight; —  $\frac{G_1 + G_2}{2}$  (calculated);  
 - - - -  $\left(\frac{\sqrt{G_1} + \sqrt{G_2}}{2}\right)^2$  (calculated).<sup>51</sup>

Figure 4.2. Comparison of rigidities of a mixed sample and its components at concentration of 5.75g/100 ml. (Reproduced from Ferry (1948))

## 4.5 Gelatin concentration dependence of gelatine phantoms

### 4.5.1 Introduction

The shear modulus of undegraded gelatin gels has been shown to be proportional to the square of the gelatin concentration (Ward & Saunders, 1958). Therefore, it is possible to create phantoms with inclusions of different stiffness to mimic tumours. Before any gelatine phantom models were made to mimic clinical situations, measurements of phantoms with various gelatine concentrations using shear wave elastography were verified against compressive rheometer and square concentration law.

### 4.5.2 Materials and methods

Cylindrical Perspex moulds with the same dimensions as described in Section 4.4.2 were used to make the gelatine phantoms with gelatin concentrations of 6%, 8%, 10%, 12%, 14% and 16% and HDPE concentration of 0.25% for all 6 phantoms. The storage time in the refrigerator was approximately 3 hours. The phantoms were warmed in the Perspex moulds until a temperature of 16 °C was reached as measured at their centre using a digital thermometer. The phantoms were scanned with SWE in the air using ultrasonic gel as the acoustic coupling. Then, using a compressive rheometer (Instron 3342 with load-cell 2519-103, Instron, Bucks, UK) as illustrated in Figure 4.3, the Young's modulus of the phantoms were measured from force-displacement data obtained by controlled compression and force measurement. The method for obtaining Young's modulus was described by Crescenti (2009). Samples were pre-compression with just sufficient strain so as to make good contact between the lubricated compressor plate and the phantom. The compressive strain rate was set at 2% per second for 3 seconds and the data were acquired at 20 ms interval. The strain rate was chosen because as shown by Crescenti (2009), this strain rate was fast enough to avoid any significant creep to occur, as any viscous relaxation of the gelatine phantoms happened slower than the time-scale of the compression. It was also verified by Crescenti (2009) that at maximal strain, the stress-strain relationship was still linear and that the gelatine phantoms were intact and repeatable and reproducible compression tests were possible. A total of 10 measurements were made for repeatability and the gelatine phantoms

were removed, repositioned and relubricated between compressions. The Young's moduli determined by compressive rheometer were the slope of force-displacement data. An example of this was shown in Figure 4.4. An average and standard deviations were plotted against the measurements done with SWE.



Figure 4.3: This is a photograph showing the set up for measuring the Young's modulus of the gelatine phantom using the compressive rheometer. Vegetable oil was used to lubricate the top and bottom surface of the phantom to reduce frictional force.

### 4.5.3 Results

There was a significant correlation between Young's moduli measured with SWE and those with compressive rheometry ( $p < 0.001$ ). Figure 4.5 shows the plot of the Young's modulus measurements with SWE and compressive rheometer (Instron) with a least squares linear-fit line forced through the intercept (0,0). Figure 4.6 shows the same data with the fitted straight line allowed to pass through the best-fit intercept. The Young's modulus measured with shear wave elastography obeyed the square concentration law with statistically significant correlation ( $p < 0.001$ ), as illustrated in Figure 4.7.

### 4.5.4 Discussion

Although there was good correlation between the Young's moduli measured using shear wave elastography and compressive rheometry, the actual measurements did not equal each other. The likely reason for the discrepancy is that Young's modulus determined by shear wave propagation speed is frequency dependent in a viscoelastic material such as gelatine phantom. Muller et al. (2009) demonstrated a linear shear wave speed dispersion curve in human liver *in vivo*, with frequency ranging from 60 Hz to 390 Hz. Assuming that the Aixplorer® measures the speed of the shear-wave group from which the ARFI-generated shear wave pulse is composed and that gelatine phantoms exhibit similar viscoelastic properties as liver, the mean frequency of the shear-wave group would be 225 Hz  $((60+390)/2)$  (Muller et al., 2009). Therefore, due to frequency dependence in shear wave propagation through viscoelastic material, the mean Young's moduli measured using SWE would be higher than those measured with compressive rheometer. As 2% strain rate in compressive rheometer was close enough to 0 Hz, we could estimate the measurements obtained compressive rheometer by extrapolating the SWE measurements to 0 Hz. The estimated compressive rheometer measurements were termed as 'corrected SWE measurements' in this thesis. The calculations for applying this correction to the Young's moduli values are shown in Appendix A. Figure 4.8 shows the plot for the corrected SWE Young's modulus measurements against those measured with the compressive rheometer. Figure 4.9 shows the same data with the linear-fit line forced through zero.

On average, the ratio of SWE modulus to Instron modulus before correction seemed to be about 1.3, but the linearity of the relationship between the two seemed to be quite good. After correction, the linearity seemed to be poor. At high moduli the ratio had been reduced by correction to about 1.0, which was the expected result. However, at low moduli, overcorrection seemed to have occurred and a ratio of about 0.7 is obtained. As a result the linear fit in Figure 4.9 was a poor fit to the data. The reason for this is not fully understood. Nevertheless, for some of the measurements the correction brought the data in closer agreement. One of the reasons the correction did not appear to work perfectly could be that gelatine is unlike the liver in its dispersion curve. Another reason could be that SWE has other errors influencing the measurements. Nevertheless, the overall finding was that the two measurements were highly correlated.

#### 4.5.5 Conclusions

This experiment demonstrated that, keeping the temperature constant, the Young's moduli of the gelatine phantoms measured with SWE correlated well with those measured by compressive rheometer (Instron). Applying the correction for frequency dependence of shear wave dispersion brought the ratio of SWE modulus to Instron modulus to about 1.0 for high moduli but seemed to overcorrect the ratio to about 0.7 for low moduli. Nevertheless, the SWE and Instron moduli were highly correlated. This means that when the SWE measurements are higher in one sample than another, you can trust that. Furthermore, the Young's moduli measured with SWE obeyed the square concentration behaviour seen in the literature.

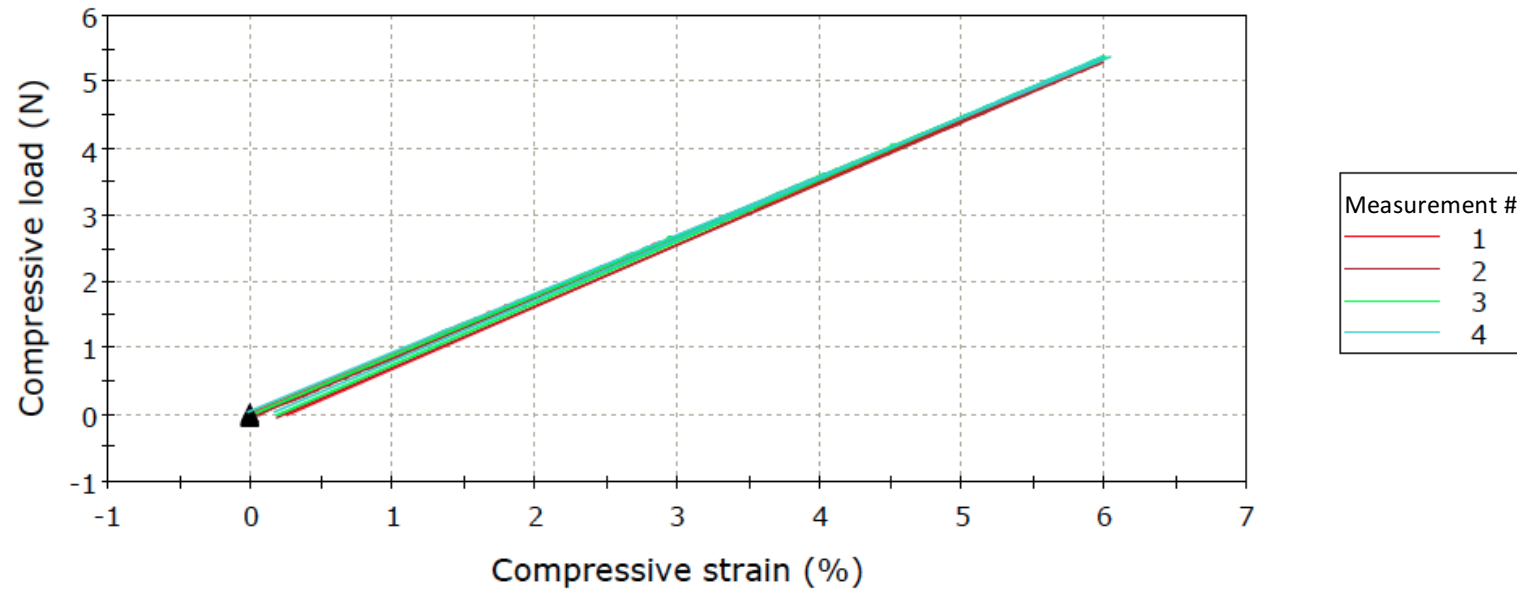


Figure 4.4. The force-displacement data for 10% gelatin concentration phantom for the first 4 measurements. The slope of the graph is the Young's modulus.

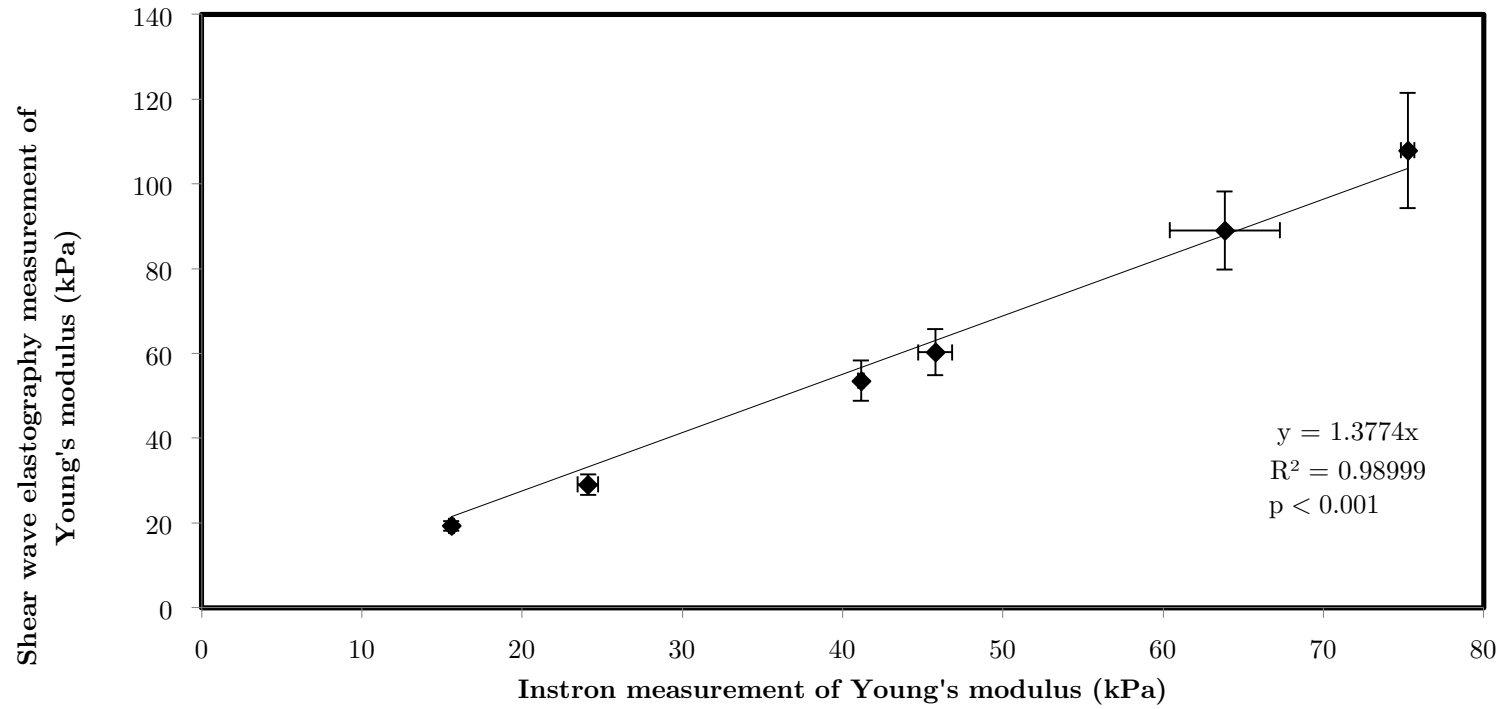


Figure 4.5: Plot of SWE and compressive rheometer (Instron) measurements of Young's modulus in gelatine of different concentrations at 16 °C. The linear-fit line is forced through intercept (0,0). Pearson's correlation was statistically significant ( $p < 0.001$ ).

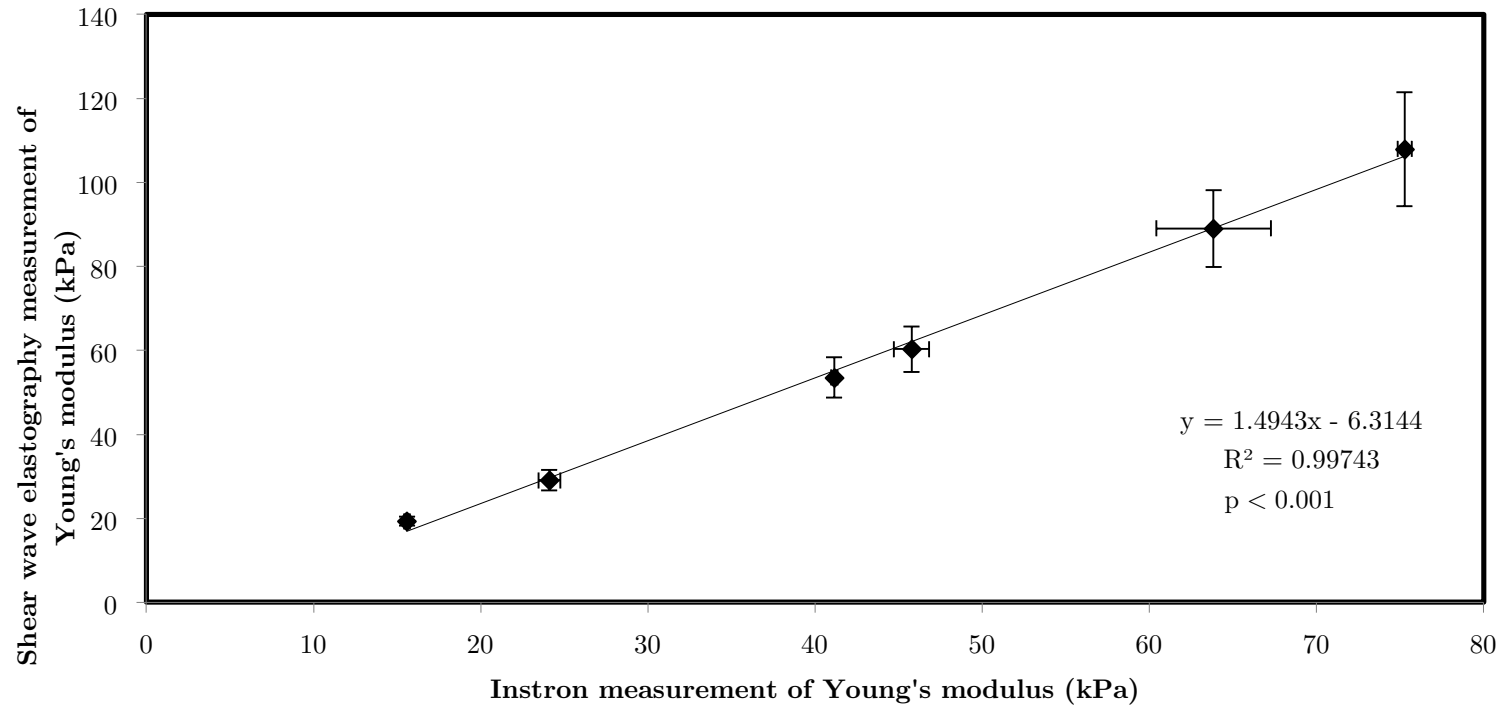


Figure 4.6. Plot of SWE and compressive rheometer (Instron) measurements of Young's modulus in gelatine of different concentrations at 16 °C. The linear-fit line is not forced through intercept (0,0). Pearson's correlation was statistically significant ( $p < 0.001$ ).

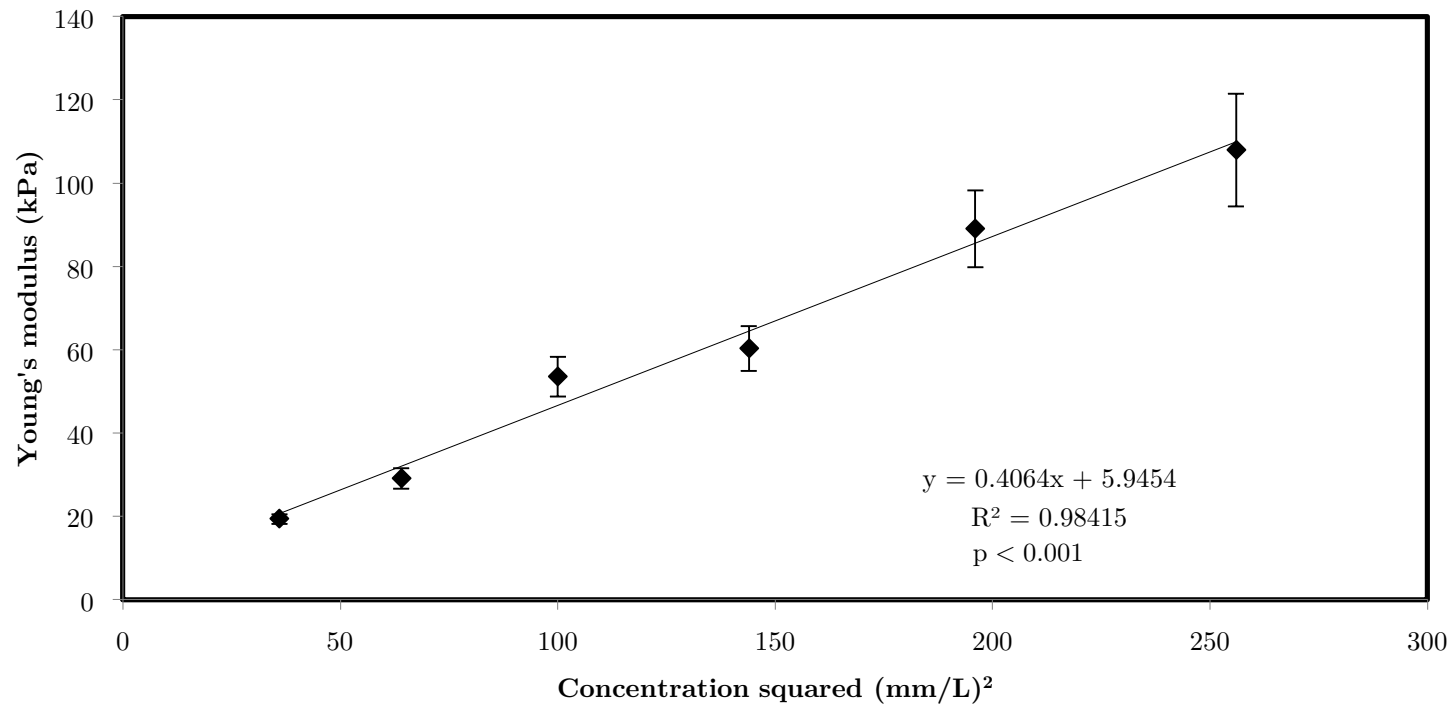


Figure 4.7: Young's modulus as measured with shear wave elastography with respect to square concentration of gelatin. Pearson's correlation was statistically significant ( $p < 0.001$ ).

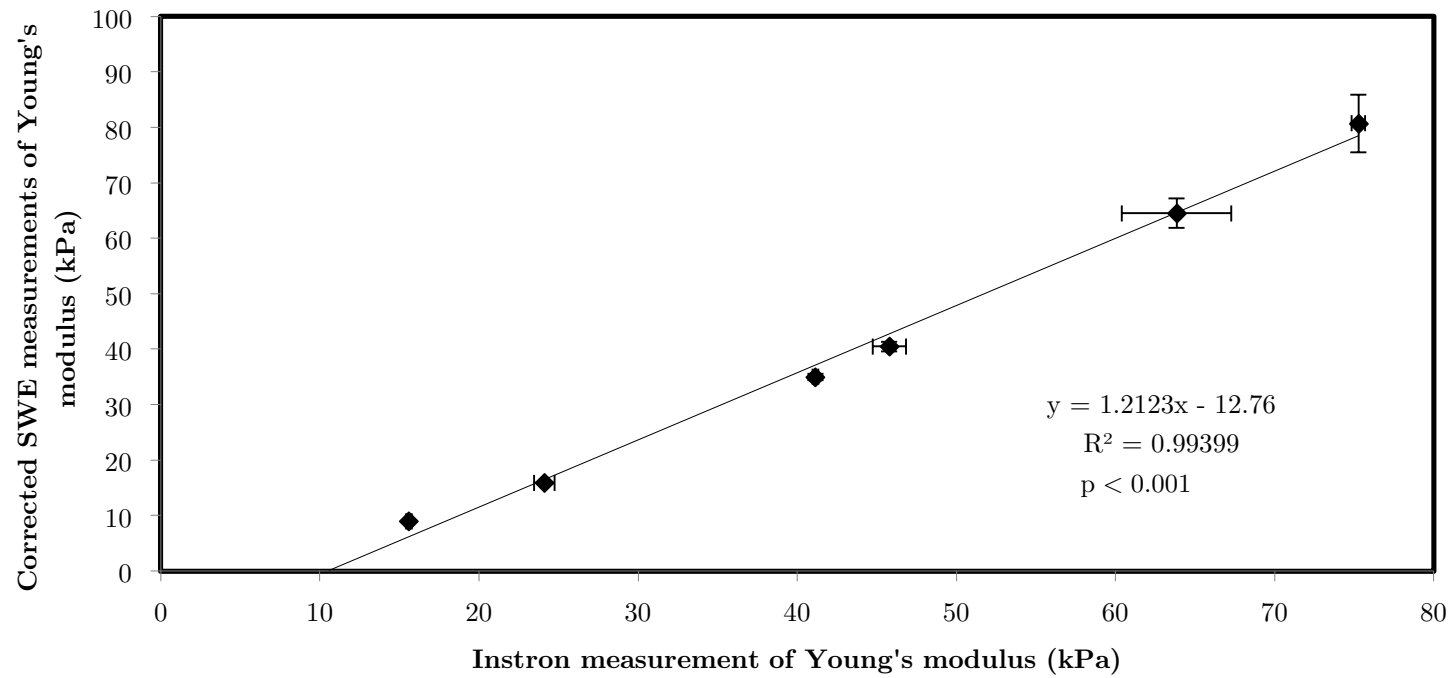


Figure 4.8. The plot of corrected Young's moduli measured using shear wave elastography with respect to those measured with compressive rheometer. The linear-fit line is not forced through intercept (0,0). Pearson's correlation was statistically significant ( $p < 0.001$ ).

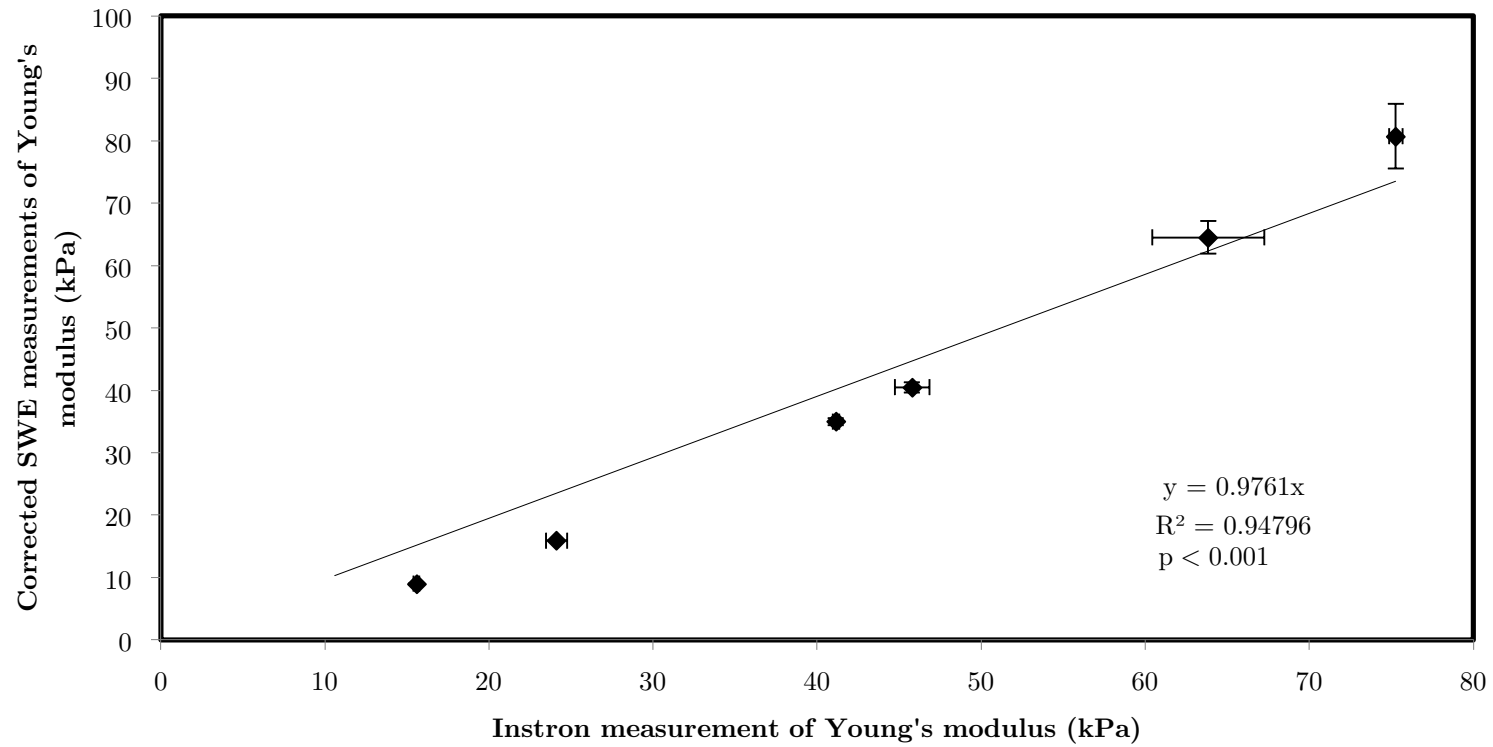


Figure 4.9: The plot of corrected Young's moduli measured using shear wave elastography with respect to those measured with compressive rheometer. The linear fit line is forced through intercept (0,0). Pearson's correlation was statistically significant ( $p < 0.001$ ).

## 4.6 Time dependence of gelatine phantoms

### 4.6.1 Introduction

When a gelatin solution solidifies, it does not assume a constant value of rigidity despite a constant temperature (Ward & Saunders, 1958). According to these authors, the rigidity increases rapidly with time for several hours before settling down to a slow increase, and has never been observed to attain a constant value. However, Ferry (1948) showed that by pre-cooling the gelatin at 0 °C for 24 hours, and then warming it to 15 °C, the rigidity changes rapidly at first but reaches an approximately constant value within about 5 hours. The initial rapid change in the rigidity is possibly due to the effect of temperature change as described above and once the measuring temperature of 15 °C is reached after about 5 hours, the rigidity reaches a constant value. In the present work, shear wave elastography measurements of gelatine phantoms were made over a few days at different time intervals to determine the time to reach a constant stiffness.

### 4.6.2 Materials and methods

Cuboidal polypropylene moulds with dimensions of 90 mm x 65 mm x 55 mm (length x width x depth) were used to make the 6 homogeneous gelatine phantoms with 8% gelatin concentration and 0.25% cellulose concentration. The moulds were numbered and weighed prior to filling with gelatine solution and before incubation in the refrigerator. All 6 moulds were placed in the refrigerator at the same time. The first 3 phantoms were scanned at 12-hour intervals whilst the remaining 3 phantoms were scanned at 24-hour intervals. For the first scan, a thin layer of vegetable oil was poured on top of the phantom to act as acoustic coupling medium and to minimise water evaporation. The phantoms were all warmed to 12 °C and scanned whilst inside the polypropylene moulds to minimise the amount of time of exposure to air. The phantoms with the moulds were all weighed before and after scanning, and any weight loss was assumed to be due to water evaporation.

### 4.6.3 Results

The Young's moduli of all 6 gelatine phantoms as measured by SWE followed a similar sigmoid slope (Figure 4.10). The Young's moduli seemed to be quite stable between 12 and 24 hours and then between 36 to 72 hours of incubation but rose very quickly between 24 to 36 hours of incubation. The weights of the gelatine phantoms including the mould were also plotted against time (Figure 4.11). The phantoms scanned at 12-hour interval lost more weight than those scanned at 24-hour interval. Assuming that the overall weight loss of the phantoms was due to water evaporation, a plot of the expected Young's moduli for corrected gelatin concentrations was calculated (Figure 4.12). The corrected Young's moduli were calculated from the graph in Figure 4.9. Figure 4.12 illustrates the changes in the Young's modulus as expected from weight loss and as measured with SWE.

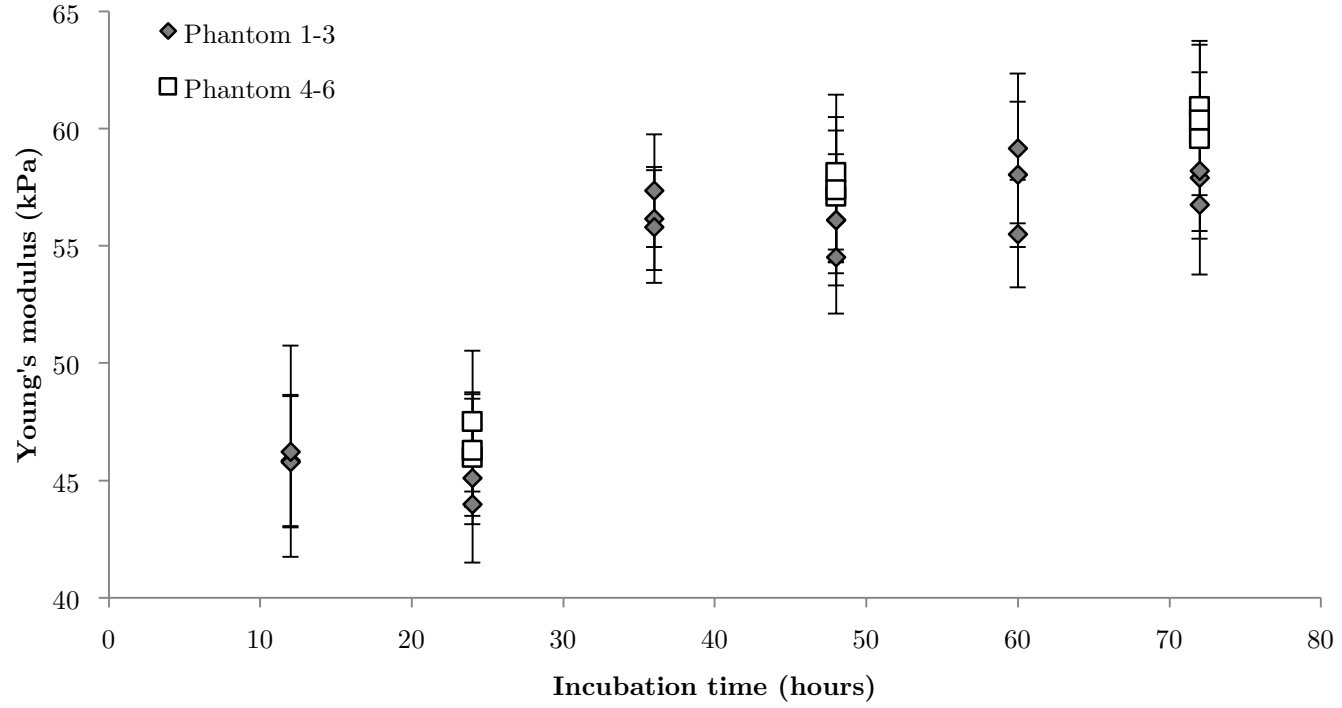


Figure 4.10. Young's moduli of gelatine phantoms with respect to time held at 4 °C.

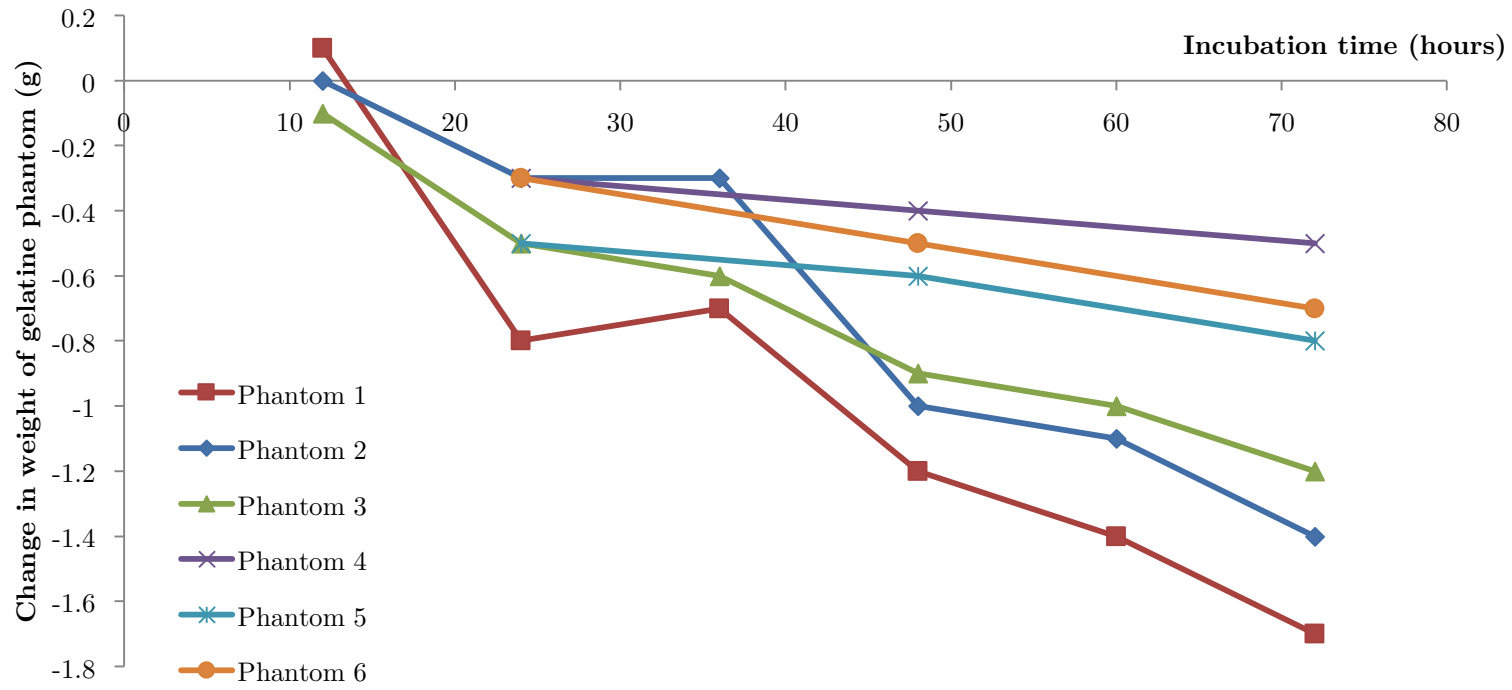


Figure 4.11. This is a plot of the change in weight of gelatine phantoms with polypropylene mould with respect to incubation time. The phantoms scanned at 12-hour interval lost more weight overall than those scanned at 24-hour interval.

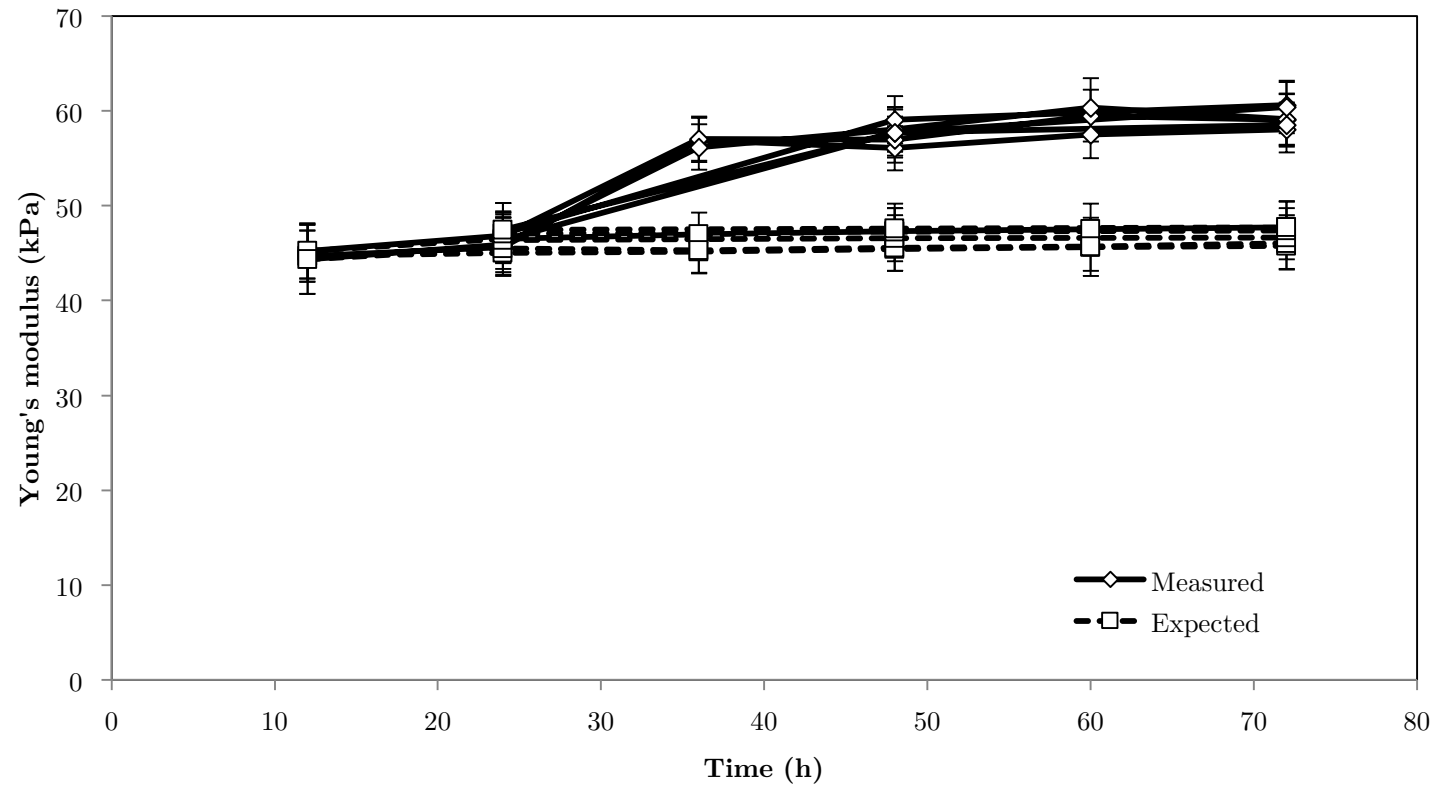


Figure 4.12. This graph shows the Young's modulus expected from weight loss and Young's modulus measured with SWE. The Young's modulus rise from 36 hours onwards was higher than expected rise from just weight loss.

#### 4.6.4 Discussion

The gelatine phantoms in this experiment were prepared in one batch to ensure consistent gelatin and scatterer concentrations throughout all 6 phantoms. The change in the Young's moduli of the gelatine phantoms was very marked between 24 and 36 hours, indicating there might be some cross-linking process happening during this period. Although there was weight loss in the phantoms during the scanning, assuming this was due to water evaporative loss, the expected increase in Young's moduli due to weight loss shown in Figure 4.12 could not account for the measured increase in the Young's moduli, further supporting the cross-linking theory. However, this project did not explore the process behind the observed increase in stiffness, as this was not related to one of the aims.

#### 4.6.5 Conclusion

This experiment demonstrated that the incubation time affects the Young's moduli of the gelatine phantoms, so it is important that the incubation time is standardized for future gelatine phantom manufacture. In order to make sure that the changes in the Young's moduli of the gelatine phantoms were kept to the minimum, the gelatine phantoms were either scanned within 24 hours of storage in the refrigerator. In addition to minimising the effect of water evaporation, the effect of osmosis could also be minimised for heterogeneous phantoms.

### 4.7 Cross validation of SWE with MRE in post-mortem mouse brains

#### 4.7.1 Introduction

In Section 4.5, SWE measurements were validated against compressive rheometer measurements using gelatine phantoms. However, measurements in brain have not been validated. Attempts had been made by the author to compare SWE measurements of excised porcine brains with Instron measurements (not reported in this thesis). However,

Instron measurements of the brain failed to yield any meaningful result. Therefore, it was not possible to validate SWE measurements with Instron measurements for excised porcine brain.

Magnetic resonance elastography (MRE) is a technique of mapping of elasticity using MRI. This technique involves some sort of vibration to introduce shear waves in the tissue when MRI images are being acquired. In the case of brain MRE, vibration is usually in the form of a vibrating head cradle for humans or a vibrating rod for mice. Using computer software, the images are then processed and converted into elasticity maps.

MRE has the advantage of imaging through the skull, thereby enabling non-invasive ‘palpation’ of the brain *in vivo* (Kruse et al., 2008). Murphy et al. (2013) reported a good correlation between MRE measurements and surgical findings. The opportunity arose to perform this study when there was another student in the same team carrying out MRE studies on mouse brains. Mouse brains may have different stiffness *in vivo* and post-mortem. As MRE acquisition is relatively long and there is a limit to how long mice are allowed to be kept anaesthetised, it was decided to perform the MRE and SWE acquisition post-mortem. Although MRE is not regarded as a gold standard for validation, I was comparing one unknown (SWE) against another (MRE). If 2 independent non-validated methods were to give the same results, this would lend confidence that both were giving the correct results. However, it does not prove that the results were correct, since both methods might be incorrect in the same way. Nevertheless, such information helps with overall knowledge, as it is better than nothing, in the absence of a good reference method for measuring Young’s modulus in brain with intact skull.

## 4.7.2 Methods

### 4.7.2.1 Mouse studies

A total of 6 mice were recruited and scanned in this study. The MRE data acquisition was performed with the skull intact while the SWE images were acquired after exposing the brain through a craniectomy performed by the author (see Figure 4.13).



Figure 4.13. A photograph showing the craniectomy for exposure prior to scanning with SWE.

#### 4.7.2.2 MRE acquisition

Another PhD student, Jin Li, performed the MRE acquisition. The methods employed are those originally developed by Juge et al. (2012) can be found in her PhD thesis (Li, 2015) and in papers by Li et al. (2014) and Jamin et al. (2015) but a brief explanation will be given here. A continuous 1 kHz sinusoidal wave was generated by an electromagnetic shaker (Brüel and Kjaer, Nærum, Denmark), applied directly through a carbon fibre rod to a square piston positioned onto the top of the scalp. Three-dimensional MRE data were acquired using a 7-Tesla small animal MRI scanner (Bruker Instruments, Ettlingen, Germany). A total of 10 contiguous coronal slices with 300- $\mu\text{m}$  thick were acquired for each mouse. Figure 4.14 illustrates the MRE setup.

Isotropic pixel size of 300  $\mu\text{m}$  were used to reconstruct maps of the absolute value of complex shear modulus ( $G^*$ ), that is  $|G^*|$ . The mean  $|G^*|$  and standard deviations were determined from the whole brain volume scanned. Figure 4.15 shows an example of a coronal slice obtained with MRE for  $|G^*|$  calculation.

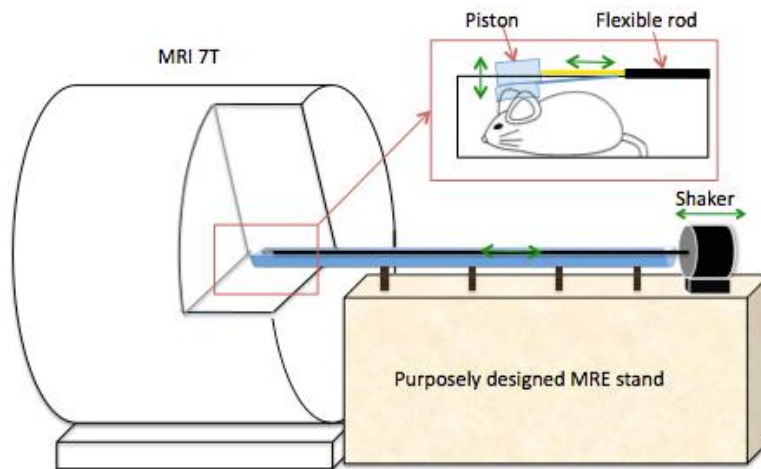


Figure 4.14. Diagrammatic representation of the MRE setup. (Reproduced from Li (2015))

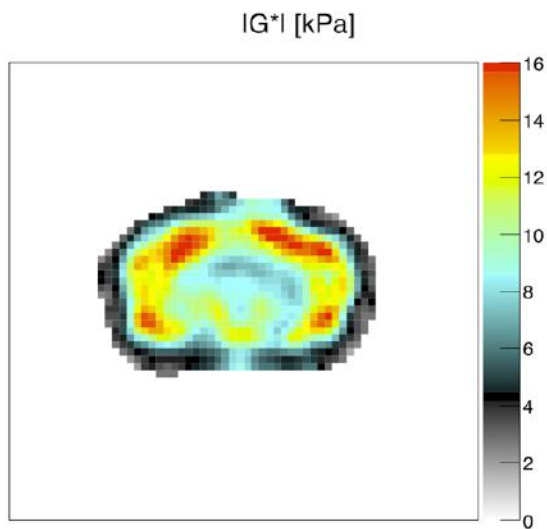


Figure 4.15. A coronal slice of the MRE data.

#### 4.7.2.3 SWE acquisition

SWE images were acquired after craniectomy. The mouse was placed on a heated positioning platform so that small manual movements could be performed. The ultrasound transducer was held with a clamp and a foam pad to protect the transducer above the mouse

brain with plenty of acoustic coupling gel applied to the brain surface. Figure 4.16 shows the setup for SWE acquisition. As it was difficult to measure the entire brain with the circular Q-boxes, the images acquired were exported to MATLAB® for more flexible analysis of the whole mouse brain cross-section images. Figure 4.17 is an example of a region of analysis drawn free-hand to enable better calculation of the mean Young's modulus than would have been obtained using the Q-box facility on the scanner. The hand-drawn ROI was drawn using the B-mode to avoid overlapping with non-brain anatomy. The ROI was then transposed to the SWE to obtain the corresponding Young's modulus.

The MATLAB® program used was written by a post-doctoral fellow (Dr Erwin Alles), the Young's modulus measurements may not be as accurate as the in-built Qbox. However, when we compared the measurements with both our in-house MATLAB® program and the Qbox, the measurements were the same down to 3 significant figures.



Figure 4.16. A photograph of the setup for SWE acquisition in the brain of a dead mouse.

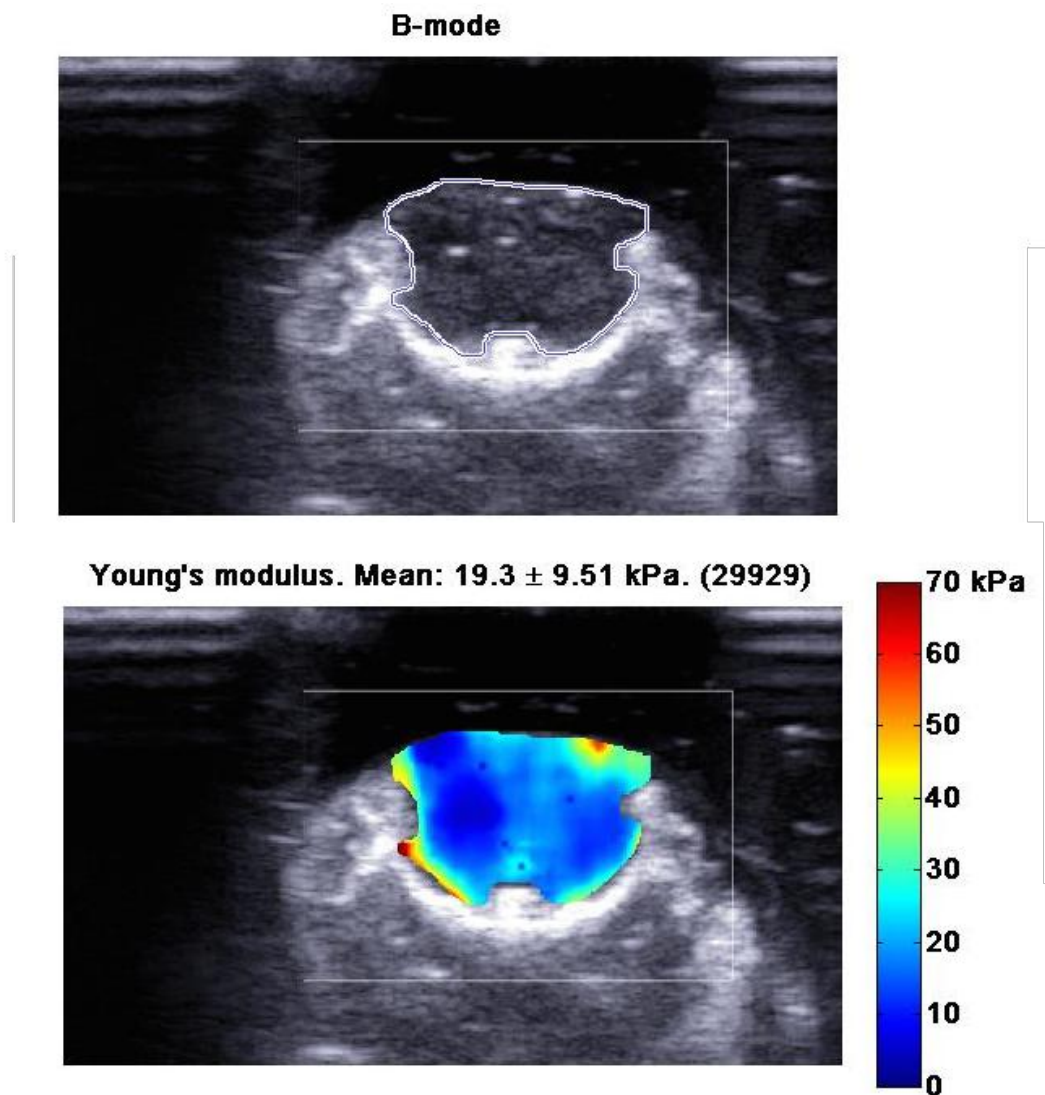


Figure 4.17. An example of the SWE image exported to MATLAB® and a region of interest drawn by hand (white outline) based on B-mode on the upper pane, which corresponds to the region on SWE in the lower pane. The Young's modulus measurements are given as mean  $\pm$  SD, with the number of pixel in the region of interest in brackets.

### 4.7.3 Results

Of the 6 mice, 1 mouse was excluded as its tail vein cannula for barbiturate injection extravasated into the interstitial space in the subcutaneous tissue. Therefore, the

exact time of death was not known. Figure 4.18 shows the graph of Young's modulus measured with SWE plotted against complex shear modulus measured with MRE for 5 mice. There was a significant correlation between the 2 modalities ( $R^2 = 0.9148$ ;  $p = 0.002$ ). As shown in equation (4.1), the Young's modulus of any given medium is exactly 3 times the shear modulus, if that the material is incompressible (Poisson ratio of 0.5). The data obtained in the present study are consistent with this expectation, as demonstrated by the slope of  $3.02 \pm 0.53$  of the linear regression equation in Figure 4.18.

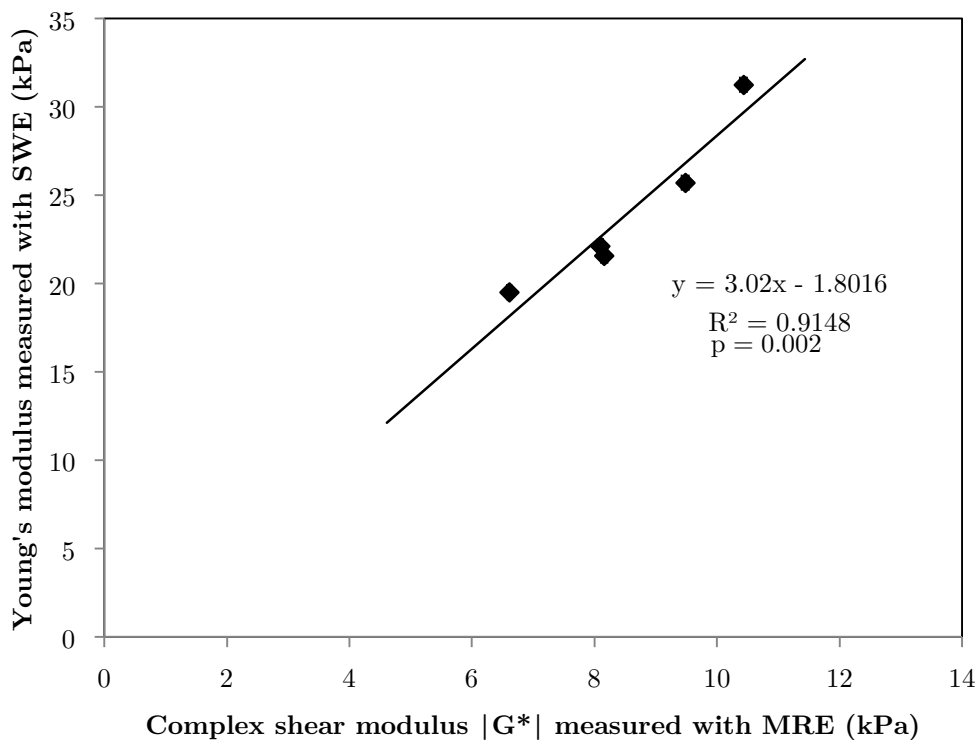


Figure 4.18. Graph of SWE measurements plotted against MRE measurements. The standard errors were within the markers.

#### 4.7.4 Discussion

This study showed that the SWE measurements were significantly correlated with MRE measurements in post-mortem mouse brains. There was a small delay between the finish of MRE acquisition and SWE scanning due to the need to perform craniectomy prior

to the latter. To minimise this delay, the SWE platform was setup and ready to go even when the MRE acquisition was still ongoing. This varied between 3 minutes and 8 minutes.

The linear regression slope agreed within estimated error on the slope with the relationship between Young's modulus and shear modulus for an incompressible material. However, there was a constant offset between the two (see figure 4.18), which indicated a need for a correction factor of about -1.8 kPa, because the Young's modulus was in fact slightly less than 3 times the shear modulus. This may be due to the fact that the frequency of shear wave generation was different for both MRE and SWE (a pure sinusoid of 1 kHz and a pulse with centre frequency 225 Hz, respectively). As brain is viscoelastic (Donnelly & Medige, 1997; Fallenstein et al., 1969), there may be frequency dependent shear wave dispersion in the brain. From the result, it was noted that the shear modulus from MRE was slightly higher than Young's modulus divided by 3, which was expected given that both moduli increase with frequency in a viscoelastic medium and shear modulus was measured at a higher frequency than Young's modulus. Whether the offset was consistent with expectations required an estimated correction factor based on the 5 times ratio of the frequencies. As there is no data on dispersion in brain, I used the dispersion equation in liver (Muller et al., 2009) for the correction. However, the ratio of Young's modulus to shear modulus was  $5.96 \pm 0.99$ , which was almost double the original ratio. This could be due to the fact that the shear wave dispersion is different in brain from liver, leading to inaccurate correction. Another reason could be that the SWE measurements were susceptible to reflected wave phenomena from the base of the skull (Defieux et al., 2011; Manduca et al., 2003), which is explained in the next paragraph. Another possible reason might be that SWE is subject to guided shear wave in brain (Macé et al., 2011), thereby leading to higher shear wave estimates (see below).

In SWE, there would have been reflected wave phenomena from the skull leading to higher shear wave speed estimates unless a directional filter was in place (Defieux et al., 2011; Manduca et al., 2003). However, as MRE does not measure the shear wave speed but apparent wavelength and it is model based, it is not subject to such errors. Therefore, this might lead to higher than expected SWE to MRE moduli ratio of 3.

There is anisotropy of the white matter in the brain, which can lead to directional dependence of shear wave speed in SWE (Macé et al., 2011) as the SWE estimate of Young's modulus comes from measurement of speed of a shear wave propagating in a particular direction. For MRE, the shear waves propagate in all directions, reaching a steady state interference pattern. The MRE estimate of shear modulus comes from an average of shear waves propagating in all directions. Therefore, this might be another reason higher than expected SWE to MRE moduli ratio of 3.

#### 4.7.5 Conclusion

The SWE measurements seemed to be correlated well with MRE measurements in post-mortem mouse brains.

### 4.8 Conclusions

In section 4.4, I have shown that the Young's modulus of the gelatine phantoms of different gelatin concentrations measured with SWE was inversely proportional to temperature, the trend of which follows that in known literature about the behaviour of gelatine phantoms.

In section 4.5, by keeping the temperature constant, SWE measurement of Young's modulus was validated against compressive rheometer measurements. SWE measurements were also shown to be consistent with the expected linear dependence on concentration squared.

In section 4.6, by keeping the gelatin concentration and temperature constant, SWE measurements showed that the gelatine phantoms' Young's modulus stayed almost constant in the first 24 hours and again after 36 hours. Between 24 and 36 hours, the Young's modulus was noted to rise very rapidly, and could not be accounted for by just pure water loss. Therefore, it should be borne in mind that SWE measurements on these phantoms

should be made either within the first 24 hours or after 36 hours of incubation. Ideally, gelatine phantoms should be incubated for at least 36 hours prior to SWE scanning. However, in some circumstances, such as gelatine phantoms with inclusions, there is potential for water diffusion causing undesired alteration of Young's modulus, in which case the gelatine phantoms will be measured within the first 24 hours.

In section 4.7, it was shown that SWE measurements of Young's modulus were validated against MRE measurements of shear modulus in post-mortem mouse brains. The good agreement is suggestive that both measurements are likely to be correct, since these are independent methods, although the possibility that they suffered from the same source of error has not been eliminated.

The work reported in this chapter provides overall confidence in the SWE estimates of Young's modulus provided by the Aixplorer<sup>TM</sup>. It confirms and extends SWE validation studies reported in the literature for phantoms. The comparison with MRE is the first to be reported.

## **Chapter 5**

### **Early Clinical Experience**

This chapter describes the experience from the first 10 clinical scans acquired at Great Ormond Street Hospital, where some unexpected findings and suboptimal images were encountered. This highlighted some of the difficulties with this technique in the clinical setting, which led to additional gelatine phantom experiments (reported in chapter 6) to help understand the findings, and subsequent optimisation of the scanning protocol for the work reported in chapters 7 and 8.

## 5.1 Introduction

Having verified the Young's modulus measurements with SWE using gelatine phantoms as described in previous chapter, clinical scans were performed to evaluate the quality of intra-operative SWE.

## 5.2 Methods

### 5.2.1 Ethics Approval

Full ethical approval for all patients recruited from Great Ormond Street Hospital and The National Hospital for Neurology and Neurosurgery was obtained from the National Research Ethics Service (NRES) Committee London - Queen Square (REC reference: 08/H0716/92; amendment number: AM04).

### 5.2.2 Patient selection

The first 10 consecutive patients were recruited into this study from the department of neurosurgery at Great Ormond Street Hospital. They were due to undergo craniotomy for resection of brain tumours and epileptogenic foci. As these patients were aged between 1 and 13 years old, the consent for research was obtained from their parents. Only 10 patients were selected because the main aim of this study is to identify any technical issues and artefacts associated with the use of intra-operative shear wave elastography.

### 5.2.3 Scanning protocol

The patients were placed in 3-pin Mayfield head fixation. Neuronavigation was used in all cases routinely to plan craniotomy placement and guide resection. The ultrasound probe was placed in a sterile plastic sheath filled with acoustic coupling gel. Following craniotomy and dural opening, using a freehand ultrasound scanning technique, the area of exposed brain was scanned by the author and the operating surgeon (Mr William Harkness),

who had had scanning experience since 2011 and had also been involved in the feasibility study of intra-operative SWE (Uff, 2011). During the scanning, when the author was not the person doing the scanning, the author was adjusting the settings on the scanner for both the B-mode and the SWE and saving the images of interest. The area scanned, including any abnormality, was compared to corresponding region on the pre-operative MRI images using the neuronavigation system. Areas of normal brain were also scanned to obtain the Young's modulus of these areas.

#### 5.2.4 Settings on the scanner

Before the acquisition of the scans, the endocavity sector array probe (SuperEndocavity SE12-3™) was selected. This probe is not designed for intraoperative use in neurosurgery, but was the most suitable available for this scanner, and thus part of the purpose this period of initial clinical experience was to determine whether the probe is adequate for this purpose. During scanning, the SWE mode was activated. Firstly, the 'Auto TGC' button was pressed to optimise the B-mode image. Time gain compensation (TGC) is a technique where deeper signals are amplified to allow visualisation of shallow and deeper structures with equal brightness, compensating for the reduction of strength of the echo signals with depth that is due to attenuation of the ultrasound beam. The 'Auto TGC' button allows rapid and automated correction of the B-mode image for attenuation without having to manually adjust the depth-dependent amplification. After optimising the B-mode image, the SWE region-of-interest (ROI) was placed onto the area of interest. The probe was held still when the desired anatomical location had been found and images were saved once the colour SWE image in the ROI had become stable (about 3 s). For both brain tumour and epileptogenic foci resection, the images were obtained pre- and post-resection.

#### 5.2.5 Grading of surgical findings

During resection, the surgeon was asked to grade the stiffness of the lesions from 1 to 5. The grading system used was:

1. The lesion is very soft like cyst.
2. The lesion is softer than surrounding brain.
3. The lesion has similar stiffness to surrounding brain.
4. The lesion is stiffer than surrounding brain.
5. The lesion is very stiff like cartilage.

In order to limit bias, the surgeon was not informed of the SWE findings. Although the surgeon had scanning experience and could interpret B-mode images, he did not have the knowledge on how to interpret SWE images. The surgical findings were then compared with the Young's modulus measured using the Q-box function on the scanner.

### **5.3 Results**

There was no complication from performing intra-operative SWE in these patients. However, there were some problems identified with the images acquired during scanning, which will be illustrated and described below.

#### **5.3.1 Summary of cases**

Please see Table 5.1 for the summary of cases scanned.

Research No.	Age	Sex	Diagnosis	Location	Stiffness grading	Correlation with SWE?	Problems identified
GOSH 1	12y	M	Low grade astrocytoma	Right temporal	2	Y	Lack of shear wave signal. Softening of brain post-resection. Stiffer cortex at probe contact.
GOSH 2	13y	F	DNT*	Right medial temporal	4	Y	Lack of shear wave signal. Stiffer cortex at probe contact.
GOSH 3	11y	F	PNET <sup>†</sup>	Corpus callosum	2	Y	Lack of shear wave signal. Softening of brain post-resection.
GOSH 4	1y	F	FCD <sup>§</sup>	Right motor strip	4	Y	Lack of shear wave signal.
GOSH 5	1y	F	Choroid plexus papilloma	Left trigone (ventricle)	2	Y	Lack of shear wave signal in the periphery of ROI box. Bands of increased stiffness within ROI box.
GOSH 6	13y	F	FCD <sup>§</sup>	Left insular	4	N	Very stiff areas below the lesion when SWE gain is increased to 100%. Post-resection, very stiff brain throughout with 100% SWE gain.
GOSH 7	11y	F	DNT*	Left frontal parafalcine	2	Y	Softening of brain and lack of shear wave signal post-resection. Stiffer cortex at probe contact.
GOSH 8	7y	M	FCD <sup>§</sup>	Right frontal	4	Y	Lack of shear wave signal in deeper regions.
GOSH 10	6y	F	Epidermoid cyst	Left medial temporal	4	Y	Lack of shear wave signal. Softening of brain post-resection.
GOSH 11	7y	M	Ganglioglioma	Left temporo-occipital	4	Y	Stiff areas superficial to lesion. Softening of brain and lack of shear wave signal post-resection.

Table 5.1: Summary of the initial 10 cases scanned at Great Ormond Street Hospital. \*Dysembryoplastic neuroepithelial tumour. <sup>§</sup>Focal cortical dysplasia. <sup>†</sup>Primitive neuroectodermal tumour.

### 5.3.2 Lack of shear wave signal

There were 9 cases where lack of shear wave signal in soft tissue was noted, as illustrated in Figure 5.1. One case (GOSH 6) did not demonstrate lack of shear wave signal because the SWE gain was increased and a different artefact was noted.

### 5.3.3 Areas of increased Young's modulus by increasing SWE gain

Because of the artefact described in 5.3.2, there was a case (GOSH 6) where the SWE gain was maximised to 100% to see if this artefact could be eliminated. In this particular case, the areas where there was lack of shear wave signal were filled with artefactually high stiffness (Figure 5.2).

### 5.3.4 Decreased Young's modulus of tumour after manipulation and dissection and during resection

In all cases, the scans performed during resection demonstrated softening of the lesion. The case of GOSH 3 is used for illustration. Figure 5.3 shows the lesion before manipulation or dissection, where the Young's modulus was  $65.54 \pm 5.45$  kPa (mean  $\pm$  SD). Figure 5.4 illustrates the lesion after dissection was performed medial to the tumour with placement of patty, where its Young's modulus was  $56.57 \pm 10.59$  kPa (mean  $\pm$  SD). Figure 5.5 illustrates the lesion after partial resection, where its Young's modulus was  $36.10 \pm 11.00$  kPa (mean  $\pm$  SD).

### 5.3.5 Decreased Young's modulus of surrounding brain after manipulation and dissection

In all cases, the brain was noted to be softer during and after resection. This is illustrated in the case of GOSH 1. Figure 5.1 demonstrates the pre-manipulation and dissection image of the surrounding brain, which provided a measurable Young's modulus value at depths of about 3 cm despite the lack of signal of deeper regions. Figure 5.6

illustrates the softening of the cortex during resection while Figure 5.7 shows the appearance of the brain after resection.

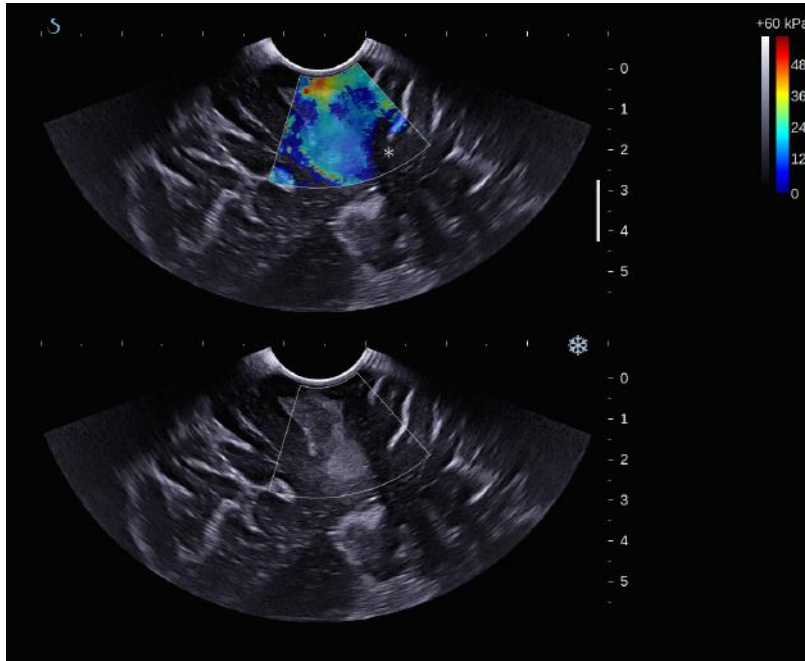


Figure 5.1: There was lack of shear wave signal in deeper areas, especially the region to the right of the tumour (asterisk). This particular case was an image taken from GOSH 1.

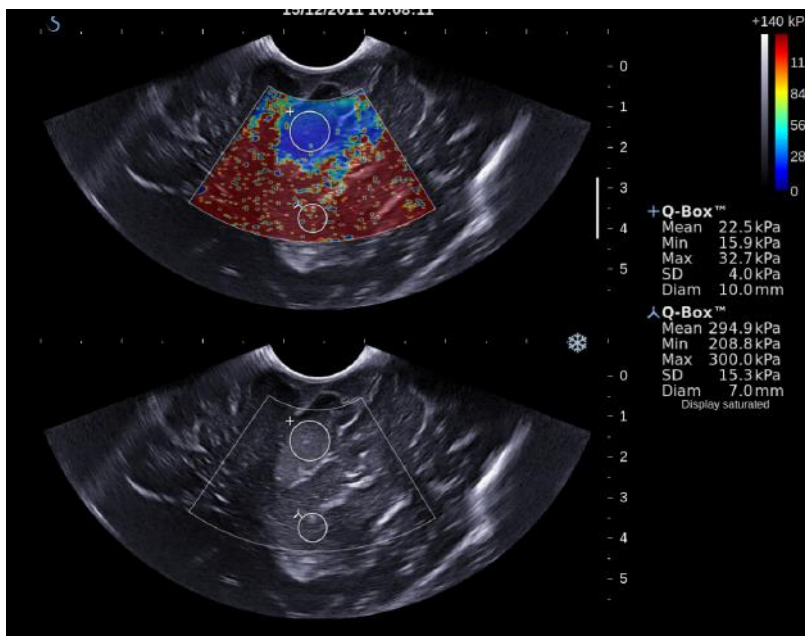


Figure 5.2: The areas surrounding the lesion were artefactually stiff, with a mean of 294 kPa. These areas did not display any elasticity information prior to increasing the SWE gain. The lesion in this case had a Young's modulus of  $22.5 \pm 4.0$  kPa (mean  $\pm$  SD).

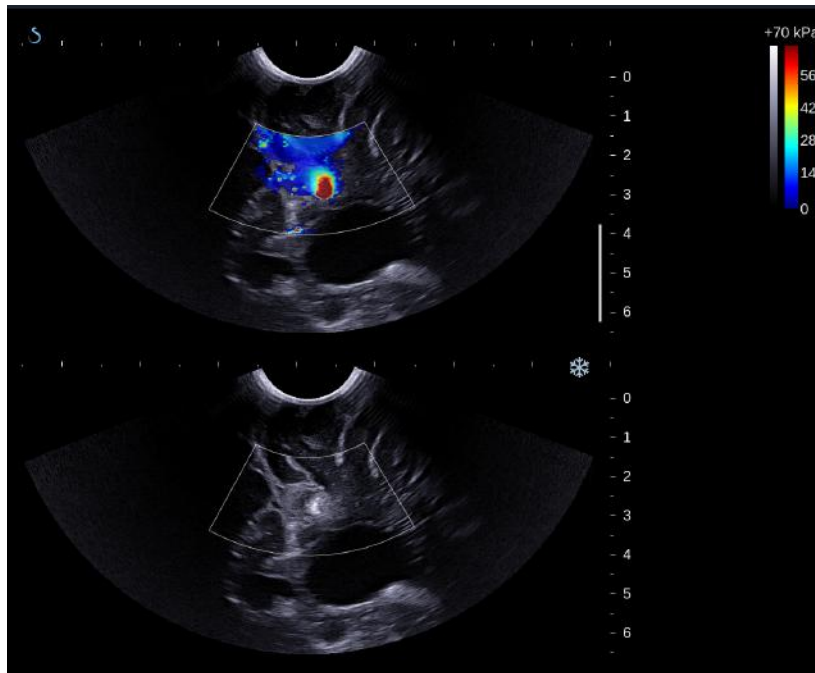


Figure 5.3: This image was acquired before any manipulation or dissection into the tumour. The Young's modulus was  $65.54 \pm 5.45$  kPa (mean  $\pm$  SD).

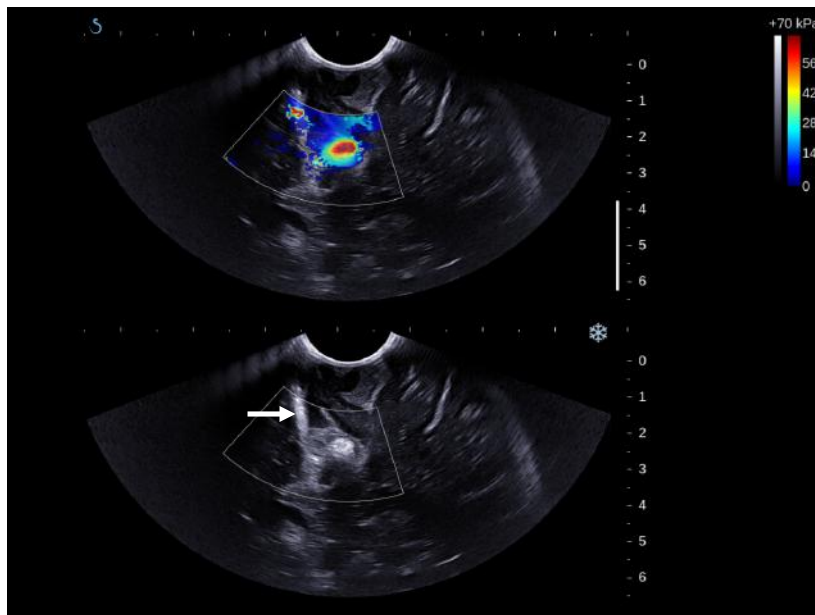


Figure 5.4: This image was acquired after slight manipulation of the tumour and dissection around the medial aspect of the tumour. The Young's modulus was  $56.57 \pm 10.59$  kPa (mean  $\pm$  SD). The surgical patty (arrow) was placed medial to the tumour, which was where the dissection had been performed.

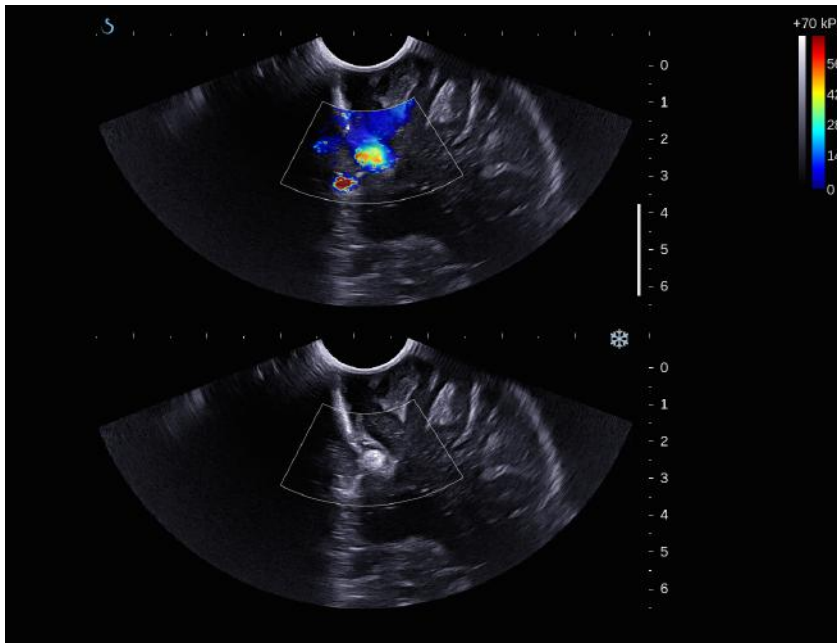


Figure 5.5: This image was taken after partial resection of the tumour. The Young's modulus was  $36.10 \pm 11.00$  kPa (mean  $\pm$  SD).

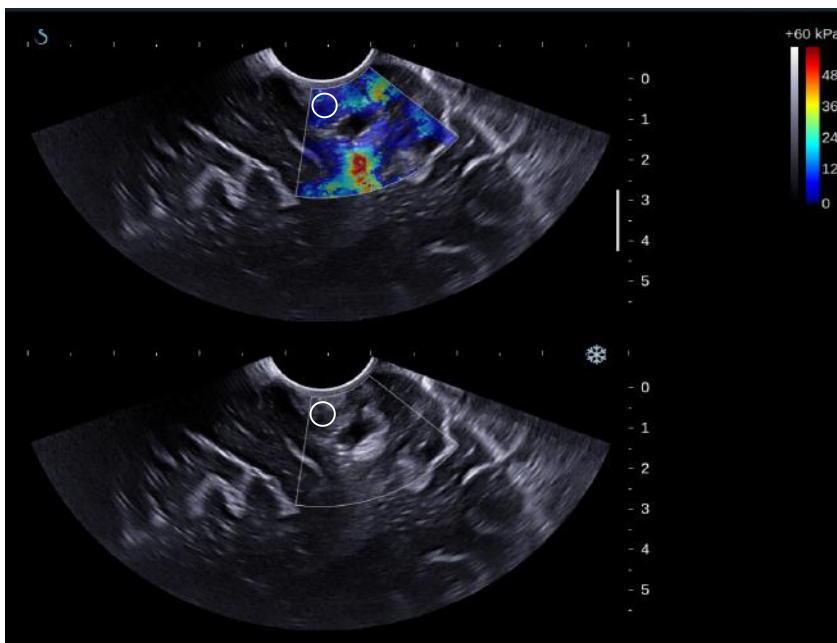


Figure 5.6: Compared to pre-resection scan, the brain surface had a lower Young's modulus during resection of astrocytoma in GOSH 1. The dark blue region superficially within the white circle had a Young's modulus of  $6.49 \pm 8.47$  kPa (mean  $\pm$  SD), compared to Young's modulus of  $39.39 \pm 12.64$  kPa (mean  $\pm$  SD) pre-manipulation or dissection.

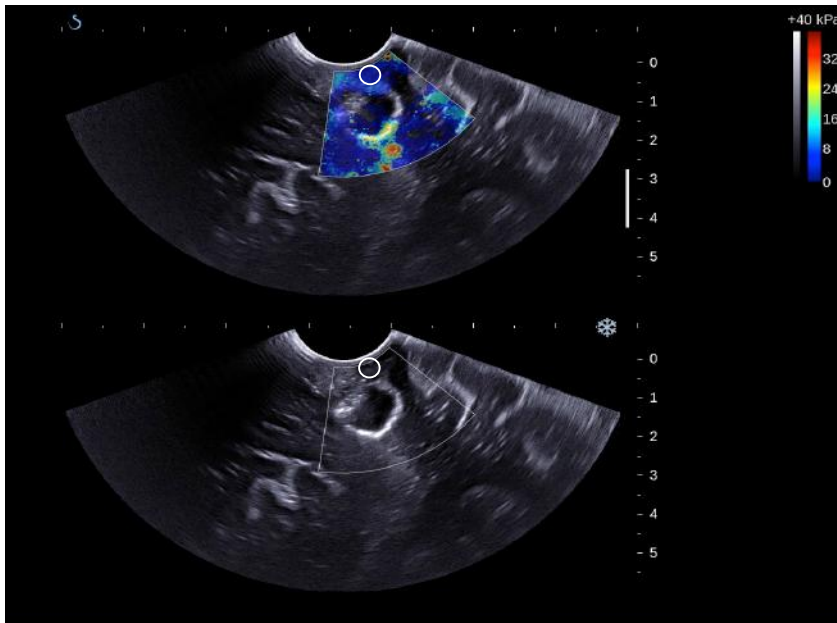


Figure 5.7: There was a further decrease of the Young's modulus of the surrounding brain after complete resection of the lesion. The Young's modulus within the white circle was  $1.33 \pm 1.83$  kPa (mean  $\pm$  SD).

### 5.3.6 Increased Young's modulus of cortex in contact with ultrasound transducer

In 2 cases, the cortex in contact with the ultrasound transducer was noted to have a higher Young's modulus measurement than expected, contrary to the surgeon's perception. The cortex not in contact with the transducer had an expected Young's modulus. Figure 5.8 illustrates the appearance of the cortex with higher and normal Young's modulus; the former was in contact with the transducer. The Young's moduli of the cortex measured were  $51.62 \pm 16.28$  kPa (mean  $\pm$  SD) and  $28.55 \pm 8.97$  kPa (mean  $\pm$  SD) for the cortex in contact with the transducer and not in contact with the transducer (deeper cortex away from the transducer), respectively. The other case is illustrated in Figure 5.9, where the Young's modulus of the cortex in contact with transducer was  $59.70 \pm 2.50$  kPa (mean  $\pm$  SD) whereas that of the cortex deeper and away from the transducer was  $16.51 \pm 14.30$  kPa (mean  $\pm$  SD).

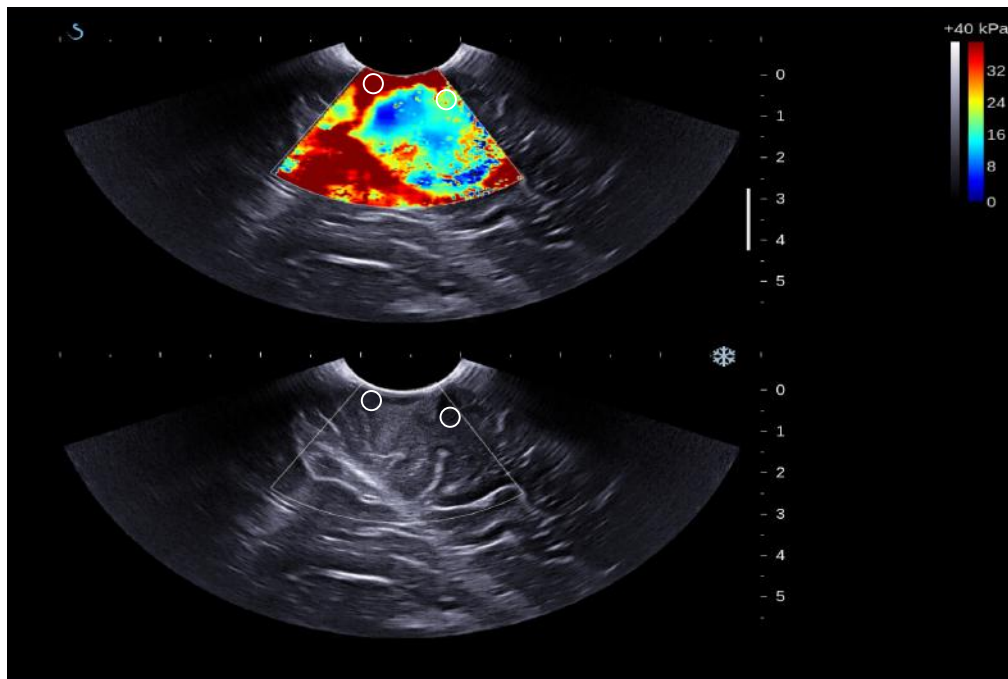


Figure 5.8: This is an image acquired for GOSH 7. The cortex in contact with the transducer appeared stiff with a Young's modulus of  $51.62 \pm 16.28$  kPa (mean  $\pm$  SD), compared to the adjacent cortex away from the transducer with a Young's modulus of  $28.55 \pm 8.97$  kPa (mean  $\pm$  SD).

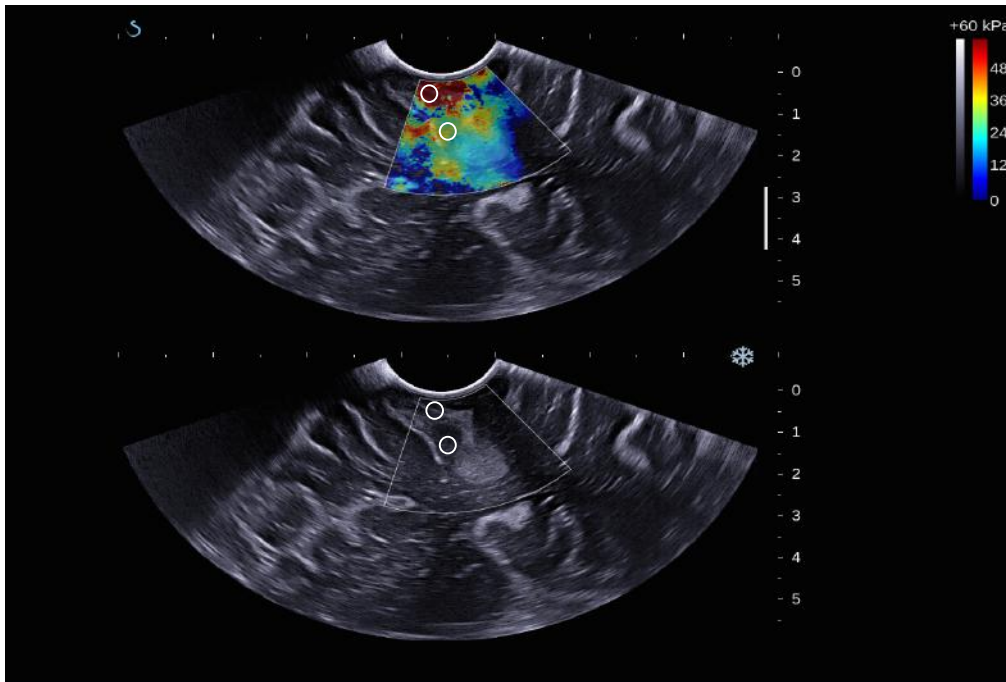


Figure 5.9: This is the image acquired for GOSH 1. The cortex in contact with the transducer appeared stiff with Young's modulus of  $59.7 \pm 2.50$  kPa (mean  $\pm$  SD), compared to the cortex away from the transducer with a Young's modulus of  $16.51 \pm 14.30$  kPa (mean  $\pm$  SD).

### 5.3.7 Young's moduli of grey and white matter

In 9 cases, when SWE acquisition was performed, measurements were also made of the normal brain adjacent to the lesion. The B-mode images were adequate for distinguishing between cortical grey matter and subcortical white matter of the normal brain as illustrated in Figure 5.10. The mean values for the mean Young's moduli were  $31.0 \pm 4.9$  kPa and  $18.8 \pm 6.1$  kPa (mean  $\pm$  SD) for the normal brain for cortical grey matter and subcortical white matter, respectively (Figure 5.11). Using the Wilcoxon's signed-ranks test, these values were shown to be significantly different from each other ( $p = 0.008$ ). Wilcoxon's signed-ranks test was used as the data for white matter was not normally distributed and we were comparing paired data.

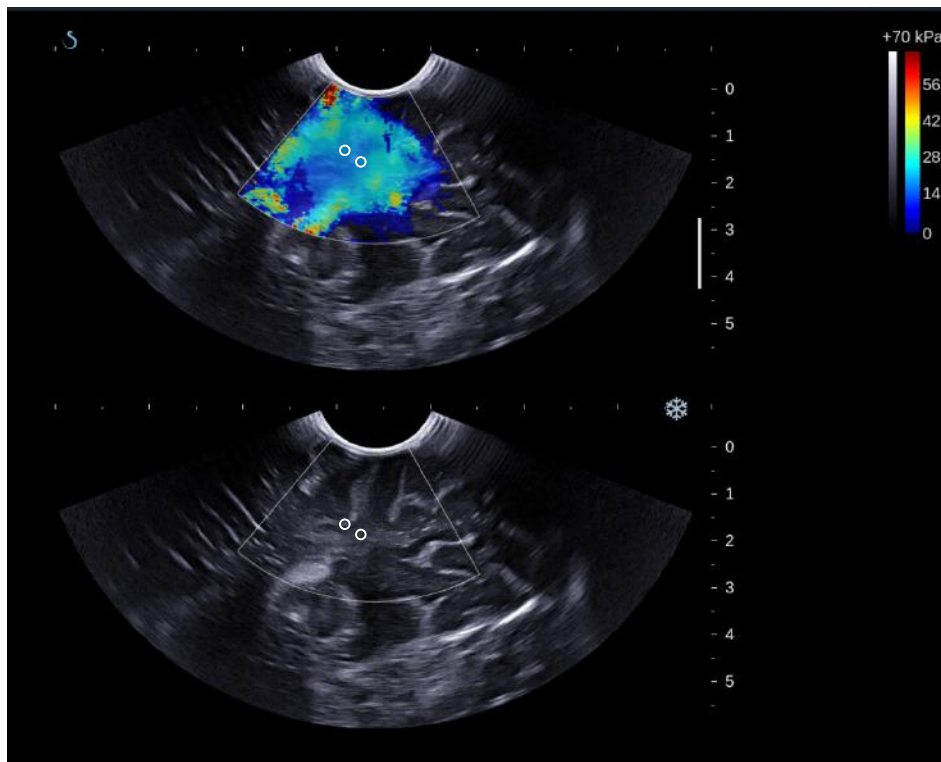


Figure 5.10: SWE image from GOSH 10. The area scanned is frontal lobe where the brain appears normal. Circular ROIs indicate the grey and white matter where the measurements were made.

### 5.3.8 Correlation between surgical findings and measured Young's modulus

There were no cases of grades 1, 3 or 5 in this early clinical series. In 9 cases, the surgical findings concurred with the Young's modulus measurements. However, there was one case (GOSH 6), whose lesion measured a relatively low Young's modulus of  $22.5 \pm 4.0$  kPa (mean  $\pm$  SD), where the surgeon felt the lesion to be stiff.

Figure 5.12 illustrates the distribution of the mean Young's moduli for these 10 cases according to the subjective stiffness grading scored by the surgeon. There was a weak but significant correlation between stiffness grading and Young's modulus measurements (Spearman's rank correlation coefficient ( $\rho$ ) = 0.532;  $p$  = 0.004).

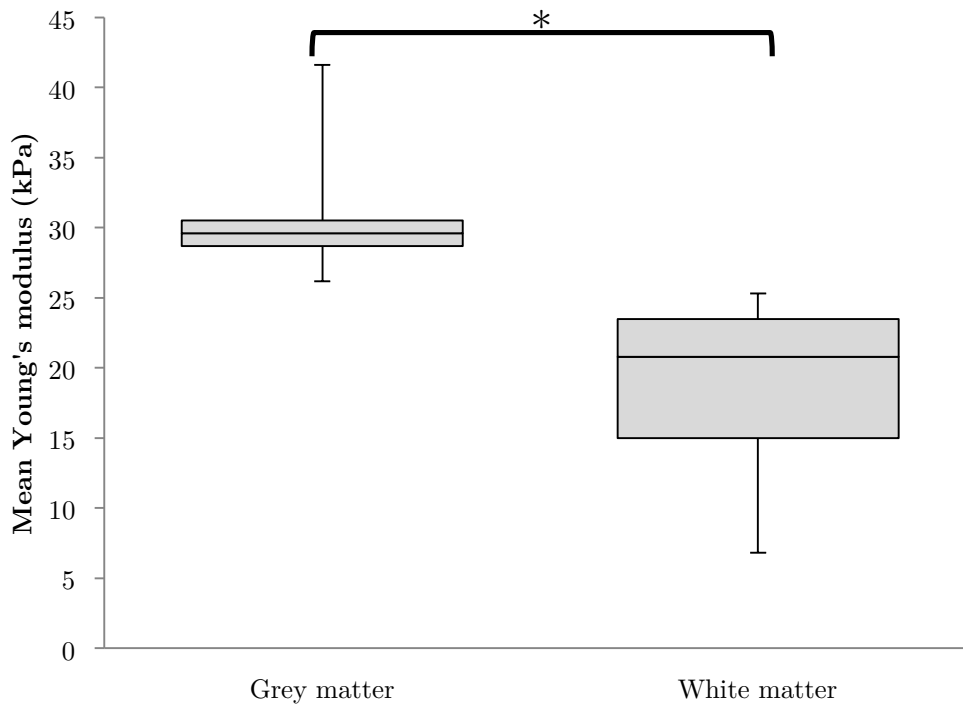


Figure 5.11: The whisker box plot for the mean Young's moduli of normal cortical grey matter and subcortical white matter. The upper and lower bounds of the box were the third and first quartiles, respectively, while the line within the box was the median. The upper and lower whiskers were maximum and minimum, respectively. \*Wilcoxon's signed ranks test showed the difference in the mean Young's moduli between the two regions of the normal brain were statistically significant ( $p$  = 0.008).

## 5.4 Discussion

From these 10 clinical cases, several features have been highlighted that were not apparent when scanning gelatine phantoms. These features could be due to the properties possessed by brain, which are different from gelatine. Human brains have been found to be viscoelastic (Donnelly & Medige, 1997; Fallenstein et al., 1969) and anisotropic (Arbogast & Margulies, 1998). In addition, Levine (1999) also pointed out that the brain is poroelastic<sup>21</sup> due to its high water content and the presence of the ventricular system in which fluid can be pushed out via a narrow outflow through the aqueduct of Sylvius and ultimately out of the ventricular system through foramina of Lushka and Magendie. This effect will be more pronounced when there is tumour or hydrocephalus presence due to increased interstitial fluid from CSF seeping into the subarachnoid space or from increased permeability of the blood vessels around the tumour leading to vasogenic oedema, respectively.

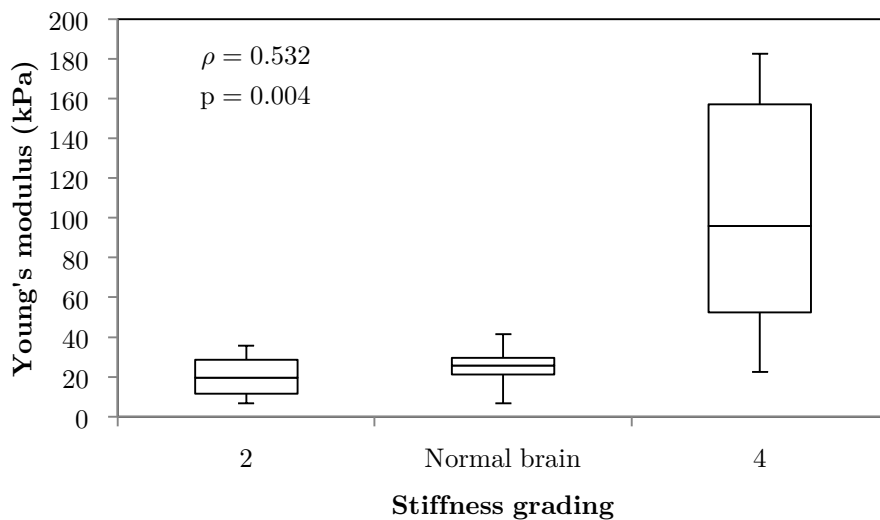


Figure 5.12: The distribution of measured Young's modulus for lesions grouped according to subjective surgical opinion of stiffness relative to brain. The upper and lower bounds of the box were the third and first quartiles, respectively while the line within the box was the median. The upper and lower whiskers were maximum and minimum values, respectively. There was a significant correlation between stiffness grading and Young's modulus measurements ( $\rho = 0.532$ ;  $p = 0.004$ ).

<sup>21</sup> Poroelastic medium is one that has an elastic solid matrix where the matrix pores are filled with fluid.

### 5.4.1 Lack of shear wave signal

There appeared to be no reason for a lack of shear wave signal in soft tissue regions, nor one that could be found in the SWE literature. There were no obvious differences on the B-mode image for regions of brain which produced a shear wave signal and those that did not. As explained in chapter 3, the propagation speed of the shear waves generated by ARFI pushes are estimated and mapped to produce SWE. As brain is viscoelastic, there will be a damping effect on the ARFI pushes which may result in poor generation of shear waves (greater absorption of the ARFI push energy and more rapid decay of the resulting displacement oscillation at the push focus than would occur in a less damped situation). It is also likely that the damping effect applies to the propagation of the shear waves, resulting in rapidly diminishing shear waves propagating in the tissue. Poroelasticity in the brain could also affect the shear wave generation and propagation. The presence of small pockets of fluid might result in weak shear wave generated due to low ultrasonic absorption coefficient, which may not be measurable above noise. Shear waves do not propagate large distances through pure low viscosity fluids. Therefore, the fluid content of poroelastic brain might attenuate the propagation of shear waves, or even result in possible abrupt termination or intermittent discontinuation of shear waves if there are clear fluid pockets, resulting in inaccurate and even impossible estimation of shear wave speed. The presence of ventricles overlying tumours, such as intraventricular tumours might make the estimation of shear wave speed inaccurate or impossible. The pulsations of brain could generate their own shear waves, which may interfere with the SWE measurements and result in inaccurate estimation of shear wave speed. Another possible mechanism could be due to high fluid content in brain would decrease the ultrasonic absorption coefficient. For a given ARFI push intensity, the ARFI displacement and hence strength of the shear wave generated, depends on the absorption coefficient. If the latter is too low, insufficient ARFI displacement may occur and only a very weak shear wave generated, which may not be measurable above noise. This phenomenon remains unexplained, although the present discussion suggests directions for future study.

### **5.4.2 Artefactually increased Young's modulus when increasing SWE gain**

As lack of shear wave signal was noted in many of the images acquired, SWE gain was increased to 100% for GOSH 6 image acquisition. As noted above, there was an artefactually increased Young's modulus noted in the images. It appeared that the surrounding normal brain had a Young's modulus nearly reaching 300 kPa, which is the maximum of the scanner. As noted in Chapter 3, the SWE gain is not strictly a gain control but actually applies a quality mask to the areas of speckle decorrelation or background motion (Deffieux et al., 2012), to remove the noisy areas from the displayed elasticity map. Therefore, the areas of increased Young's modulus in GOSH 6 images were due to noisy artefacts and not true representations of the elastic modulus for the surrounding tissue. Because of this, we did not include the measurements of the surrounding tissue from this patient for calculation of normal brain Young's modulus, and for future studies no attempt was made to overcome lack of signal by increasing shear wave gain; rather, the gain control was kept at the default value of 70%.

### **5.4.3 Decreased Young's modulus of tissue after manipulation and dissection**

Manipulation and dissection of both tumour and brain tissue resulted in a decrease of the Young's moduli of these tissue. This has not previously been reported in any literature as far as the author is aware. The explanation is unknown, although there are several possible factors that could contribute to the effect. Firstly, brain tissue has high water content so pulling the brain tissue aside in order to expose deeper regions of the brain (i.e. retraction) can displace the water compartment which could leave the solid matrix, which might lead to a decrease in hydrostatic pressure, and ultimately the elastic modulus. Secondly, the stiffness in the brain can be influenced by vascular pressure, which will be reduced when measures to achieve haemostasis, such as diathermy, are performed. Thirdly, irrigation with normal saline solution in the resection cavity might result in water seeping into the brain tissue by osmosis, leading to reduced stiffness. Fourthly, tissue swelling due

to increased permeability of the vascular structures from inflammatory response could also contribute to the reduced stiffness. Fifthly, it is possible that a breach in pia mater can result in lower Young's modulus measurements. Finally, during dissection, fluid leakage particularly from the blood vessels would result in a loss of pressure. If brain tissue is a non-linear elastic medium, then loss of pressure represents loss of pre-stress, and this could result in a reduction in Young's modulus. Although these mechanisms are described here for brain tissue, the same phenomena could also apply to brain tumour. As manipulation and resection of tumour will involve more disruption of blood supply and more use of diathermy, the reduction in the stiffness would be more pronounced than for brain.

#### 5.4.4 Increased Young's modulus of brain in contact with ultrasound transducer

In the 2 cases where Young's modulus of brain was noted to be increased where it was in contact with the probe, there is a possibility that probe pressure was applied during the SWE acquisition. Many tissues are non-linear in their stress-strain response, getting stiffer with increased pre-stress. Therefore, pre-stress with the probe may be expected to increase the Young's modulus, as has been reported in images of breast tumours with SWE (Barr & Zhang, 2012).

#### 5.4.5 Young's moduli of normal brain

As ultrasound cannot penetrate the skull, most of the elastographic techniques to measure brain mechanical properties *in vivo* are performed using MRE. Whilst Kruse et al. (2008) and Uffmann et al. (2004) found that white matter was significantly stiffer than grey matter *in vivo*, Green et al. (2008) showed that the grey matter was significantly stiffer than white matter *in vivo*. Using a dynamic viscoelastometer at 3 to 35 Hz to test post-mortem human brains at 3 to 36 °C, Hirakawa et al. (1981) showed that after head injury impact of 5 milliseconds (ms), the complex Young's moduli ( $E^*$ ) for both grey and white matter were  $3.6 \times 10^5$  dyne/cm<sup>2</sup> and  $4.47 \times 10^5$  dyne/cm<sup>2</sup>, respectively (36 kPa and 44.7 kPa,

respectively), also showing the higher stiffness in white matter compared with grey matter. Conversely, Uff (2011) showed that grey matter has a higher Young's modulus than white matter. Uff (2011) provided an explanation for why some authors might artefactually have measured white matter as stiffer than grey matter. However, no clear explanation has been provided for why grey matter should be stiffer than white matter. It may be hypothesised that the greater Young's modulus in grey matter can be attributed to the presence of pia mater, which could contribute the overall stiffness of the tissue. Experiments to test this hypothesis are reported in chapter 6.

White matter fibres have different orientations and therefore exhibit anisotropy with regards to shear wave propagation. In rat brains *in vivo*, shear wave speed has been shown to increase when the transducer is parallel to the white matter fibres, and to decrease when the transducer is perpendicular to the fibres (Macé et al., 2011). The authors showed that the effect of anisotropy could result in an increase of shear modulus up to 3 times by changing the orientation of the transducer. This means the ratio could be 3 times as high in Young's modulus measurements. Therefore, depending on the orientation of the fibres with respect to the transducer, the Young's modulus measurement of the white matter fibres can be higher than normal brain tissue, potentially confusing it with stiff lesions such as focal cortical dysplasia.

#### 5.4.6 Correlation between surgical findings and SWE measurement

This early clinical series demonstrated that there was a significant correlation between the surgical findings and Young's modulus of the various tumours or lesions, which is encouraging. There was one lesion (GOSH 6), which did not have concordance between stiffness grading and Young's modulus measurement. This could be due to the incorrect SWE settings (see Section 5.3.3) which will be investigated in detail in Chapter 6. Future studies looking at brain tumours and epileptogenic lesions may help determine if such abnormal tissues have Young's moduli that are sufficiently different from the normal surrounding brain to make SWE useful for detecting residual for various brain tumours, or

the presence of epileptogenic lesions that are not clearly visible on MRI. Such potential was investigated in this project and the findings are described in chapters 6, 7 and 8 of this thesis.

## 5.5 Conclusions

In this chapter, these early clinical results demonstrated that, although there was good correlation between surgical findings and SWE measurements, a number of artefacts have been noted and illustrated. These artefacts were:

1. Lack of shear wave signal.
2. Areas of increased Young's moduli when increasing the SWE gain.
3. Decreased Young's moduli of both brain and tumour after manipulation.
4. Increased Young's modulus of cortex when in contact with the ultrasound transducer.

Prior to conduction more extensive clinical studies, experiments were conducted to investigate these artefacts using gelatine phantoms and porcine brain. The results of these investigations are reported in Chapter 6.

## **Chapter 6**

# **Characterisation of Shear Wave Elastography Appearance**

This chapter discusses the laboratory experiments that were performed for two purposes: a) to investigate the problems encountered during early clinical scans (see Chapter 5), and b) to assess various aspects of performance of the Aixplorer® scanner in SWE mode so as to assist expectations and interpretation of clinical scans. For each of the problems described in Chapter 5, gelatine phantoms were used as the tissue mimicking models because they are easy to manufacture and modify to simulate the clinical situations. While the gelatine phantoms are useful for gaining an understanding of many of the problems encountered, post-mortem porcine brain and spinal cord are more realistic media. Therefore, the latter were also used to further understand the limitations of the SuperSonic Aixplorer® system. This chapter concludes with recommendations to improve the acquisition of clinical scans.

## 6.1 Introduction

The previous chapter highlighted several problems with using SWE in the clinical settings. The main problems highlighted were:

1. Lack of shear wave signal
2. Areas of increased Young's moduli when increasing SWE gain
3. Decreased Young's moduli of tissue after manipulation
4. Increased Young's modulus of cortex in contact with the ultrasound transducer

## 6.2 Aims

Therefore, this chapter aims to address these problems individually by experimentally simulating different clinical scenarios using gelatine phantoms and porcine brain. Demonstrating the problems in gelatine phantoms should improve understanding of the artefacts seen in clinical scans, and therefore, it should be possible to optimise SWE settings to minimise the artefacts encountered. This was done and, with the resulting recommended settings, experiments were carried out on porcine brains to investigate the effect of changing the settings so as to further optimise them for imaging brain tissue. In addition, aspects of SWE imaging performance, such as resolution and Young's modulus tissue-contrast to display-contrast transfer efficiency, were measured using phantoms, with the aim of providing information that would help both the management of expectations of this new imaging mode and the interpretation of clinical scans. However, since there were surprising and unexplained observations from the preliminary experience reported in Chapter 5, it was decided to also check a number of basic (generally software) operational features, to ensure that the behaviour of the Aixplorer® scanner was as expected. An example of this is the checking of the lack of dependence of the results on ROI size, described in 6.3.1 below.

## 6.3 Methods

### 6.3.1 Effect of changing the region-of-interest (ROI) size

During intra-operative scanning, it was noted that the ROI size needed to be adjusted to include the tumour and the surrounding brain. As frame rate decreases with increasing size, so using a small ROI is helpful. However, it needs to be large enough to include tumour and brain.

It should be expected that changing the ROI size would not change the Young's modulus measurements. A homogeneous gelatine phantom with 8% w/w gelatin concentration was manufactured. Scanning was performed with the ultrasound transducer clamped, with water standoff and the gelatine phantom fully immersed in a water bath at 16°C. Young's modulus measurements were made with ROI sizes ranging from 1.19 cm<sup>2</sup> to 5.29 cm<sup>2</sup>. The measurements were repeated 3 times. The schematic diagram for the experimental set up is illustrated in Figure 6.1.



Figure 6.1. This is the top half of the display on the ultrasound scanner where it shows the B-mode image with superimposed colour SWE image within the ROI.

### 6.3.2 Effect of varying the water standoff

Depending on the location of the craniotomy, the amount of water standoff can differ. Sometimes, it was necessary to scan the brain with the transducer touching the brain, as it was impossible to create a water standoff. It was postulated that changing the water standoff should not influence the Young's modulus measurement (except when the transducer touches the brain, which is investigated in section 6.3.6 below). Therefore, an experiment using 3 homogeneous gelatine phantoms composed of 8% w/w gelatin concentration was performed. Young's modulus was measured with the transducer touching the phantom and with increasing depth of water standoff. The experimental setup is illustrated in Figure 6.2.

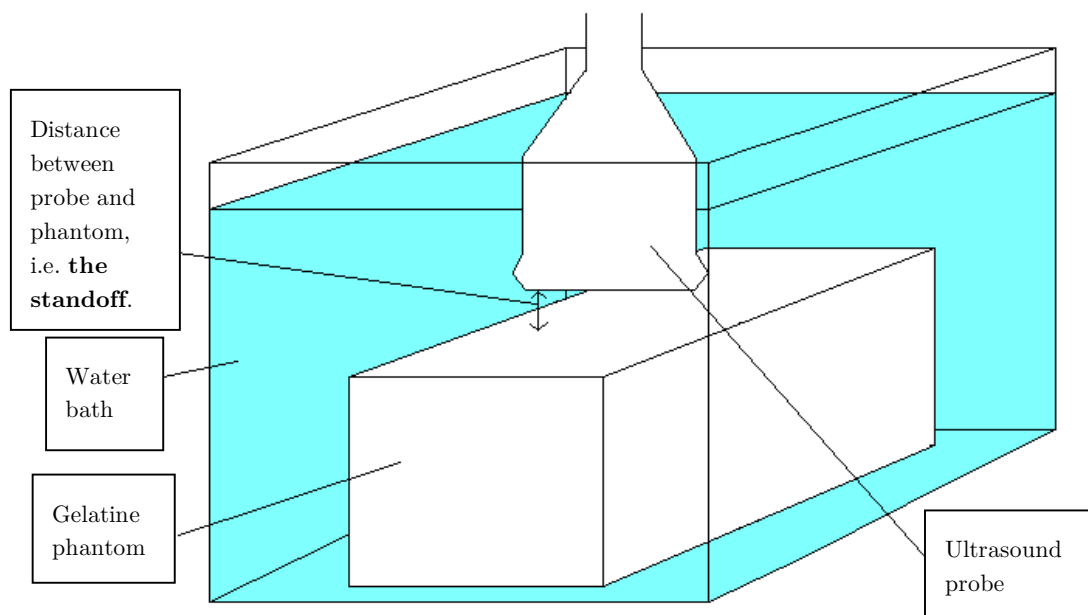


Figure 6.2. The experimental setup to investigate the effect of water standoff on the Young's modulus measurements.

### 6.3.3 Lack of shear wave signals

The Aixplorer® scanner induces a near conical shear wave centred on the acoustic beam axis by emitting acoustic “pushes” that are successively focused on various depths, taking advantage of the fact that the acoustic “push” beams are many times faster (potentially up to 1500 times) than the shear wave speed. Bercoff et al. (2004) demonstrated that this enables generation of shear displacements of up to 100  $\mu\text{m}$  in phantoms and 40  $\mu\text{m}$  in vivo, and it should increase distance of propagation and penetration depth of shear waves in the whole ROI relative to a pushing beam focused at a single depth. However, as seen in clinical images, there were areas that were deficient in shear wave signals. Lacking other explanations, this could mean that brain possesses different acoustic or shear wave properties compared to the agar-gelatin phantoms that were previously tested, as described in chapter 5. Various experiments were conducted to investigate a number of possible explanations, as described below.

#### 6.3.3.1 Attenuation in superficial tissue

It is possible that attenuation of the pushing beam in the tissue anterior to the push locations played a role in contributing to shear wave signal dropout. The factors that determine the ARF ( $F$ ) are described in equation 3.25, repeated here for convenience:

$$F = \frac{2\alpha I}{c_{\text{sound}}}, \quad (6.1)$$

where  $c_{\text{sound}}$  is the sound speed in the tissue,  $\alpha$  is the ultrasound attenuation coefficient at the pushing focus, and  $I$  is the local intensity of the ultrasonic beam. The attenuation coefficient at the pushing focus, particularly the absorption coefficient could have an effect. This equation shows that if it were very low, the force would be correspondingly low. Therefore, strong attenuation of the sound beam in overlying tissue could, in principle, cause shear wave signal dropout due to insufficient excitation to generate shear waves. Although evidence for this ought to have existed in the brightness of the B-scans in regions where

shear wave drop-out occurred (since the imaging beam would have been attenuated by the same tissues as the pushing beam), and no such evidence was noticed, a brief study of SWE with attenuating overlying layers was conducted for completeness and educational purposes.

Three gelatine phantoms with stiff rod inclusions, manufactured using 8% and 14% w/w gelatin concentrations for background and inclusion, respectively, were manufactured. Using these gelatine phantoms, attenuating layers of 14% w/w gelatin concentration with thickness of 1 cm, 2 cm, 3 cm and 4 cm, were employed to assess the depth of shear wave penetration and the degree of signal dropout, and to quantify the change in measured Young's modulus of the region deep to the attenuating layer. Surgicel® and duragen® were also used as attenuating layers. Figure 6.3 illustrates the experimental set-up.

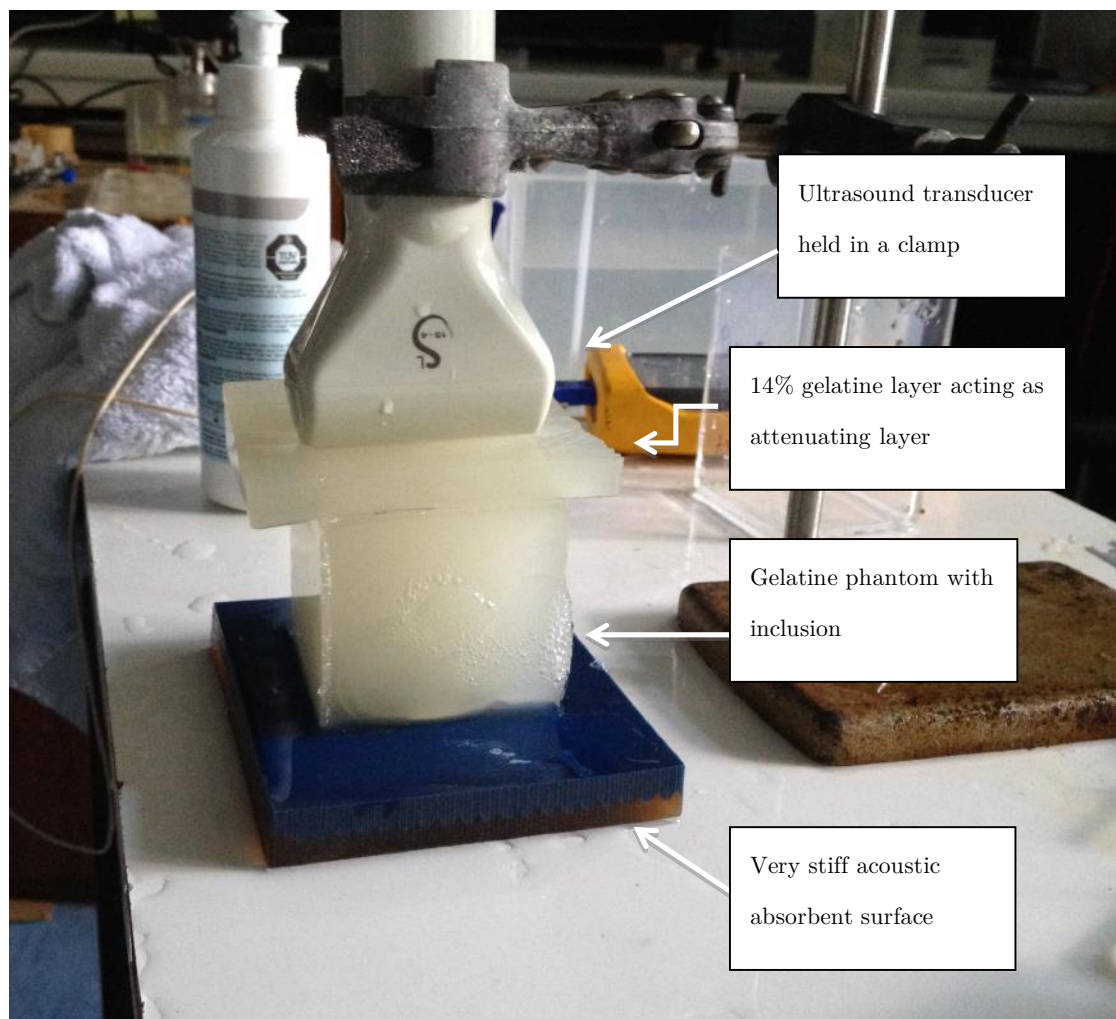


Figure 6.3. The experimental set-up for investigating the effect of attenuating layers on shear wave signal.

### 6.3.4 Effect of adjusting SWE gain

As demonstrated in the previous chapter, when increasing the SWE gain the areas lacking shear wave signal showed artefactually very high Young's modulus. In the Aixplorer® user manual (SuperSonic Imagine, 2010), it is recommended that the SWE gain is used to adjust the quality of image. However, it did not specify the exact function of the gain. Therefore, in this chapter, using one porcine brain where SWE signal dropouts were observed, SWE gain settings from 70% to 100% were assessed to determine the optimal setting for brain imaging. For each SWE gain setting, the scans were repeated 3 times.

### 6.3.5 Effects of manipulations on SWE measurements

Most of the published studies of shear wave elastography have been concentrated on pre- or post-surgical conditions where the lesion and the surrounding tissue are not subjected to direct invasive manipulation. For example, in breast imaging, the ultrasound probe is on the skin surface and not directly in contact with the breast parenchyma or the tumour. Therefore, there is no disruption of tissue margins. From the early intra-operative imaging described in the previous chapter, it was noted that manipulation appeared to affect the Young's modulus of the lesion and surrounding brain. It was postulated that the decreased Young's modulus measurements could be due to an osmosis effect, a breach of pia mater, or retraction of brain tissue (pulling the brain edges apart). These hypotheses were tested using both gelatine phantoms and *ex vivo* porcine brains.

Using 3 gelatine phantoms with a central stiff rod-shaped inclusion, the intra-operative conditions – pre-resection, during resection and post-resection – were simulated to determine the magnitude of change in the Young's modulus. The measurements were compared and statistical analysis performed with paired t-test.

For *ex vivo* experiments, 3 porcine brains were scanned in  $37 \pm 1$  °C bath. To test the effect of pia mater on the Young's modulus measurements, the pia mater on one hemisphere was removed while the other remained intact (Figure 6.4). SWE images were acquired in the coronal plane for all the brains. For each brain, 3 Q-box measurements were made for grey and white matter. The measurements were then compared and statistical analysis performed with Wilcoxon's signed-ranks test.

Intraoperatively neurosurgeons pull the edges of the brain apart to expose the part that is to be resected. This manoeuvre is known to surgeons as retraction. To test the effect of retraction, the porcine brains were subjected to 2-cm displacement using the portable compressive rheometer (InSpec) to simulate retraction intra-operatively. Figure 6.5 illustrates the experimental setup. The Young's modulus measurements of the whole brains

before and after compression were performed and statistical analysis was performed with Wilcoxon's signed-ranks test.



Figure 6.4: *Ex vivo* porcine brain with pia mater removed on the left and preserved on the right.

### 6.3.6 Effect of strain on SWE measurements

In the Aixplorer® manual (SuperSonic Imagine, 2010), it was recommended that when acquiring SWE images one should scan softly, smoothly and slowly. However, as was hypothesised in the previous chapter, the effect of increased pressure on the surface of the scanned tissue was not clear. Using 3 homogeneous gelatine phantoms initially, the transducer was used with different water standoffs, eventually touching the phantoms to determine the effect on the measured Young's modulus (see above). Then, using 3 gelatine phantoms with both adhered and mobile stiff rod inclusions, the change in Young's modulus of both background and inclusion was measured for different values of applied strain. The set-up of the experiment is demonstrated in Figure 6.6. Finally, using 3 porcine brains, the

Young's modulus was measured with increasing displacement 1 cm increment. The experimental set-up is shown in Figure 6.5. The statistical analysis was performed using paired t-test.

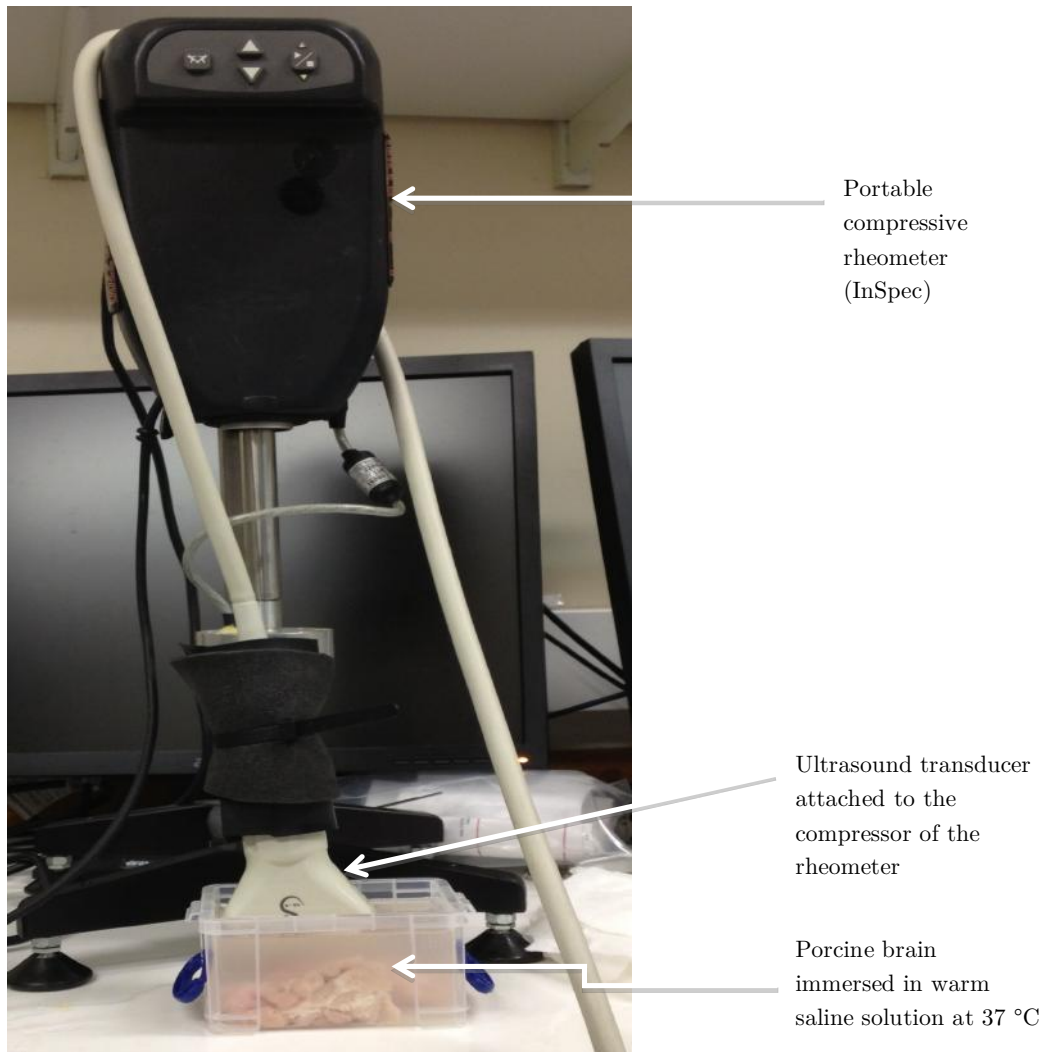


Figure 6.5 Experimental set up for the porcine brain to investigate the effect of strain on the Young's modulus measurements. The ultrasound probe is attached to the compressive rheometer to enable controlled application of strain.

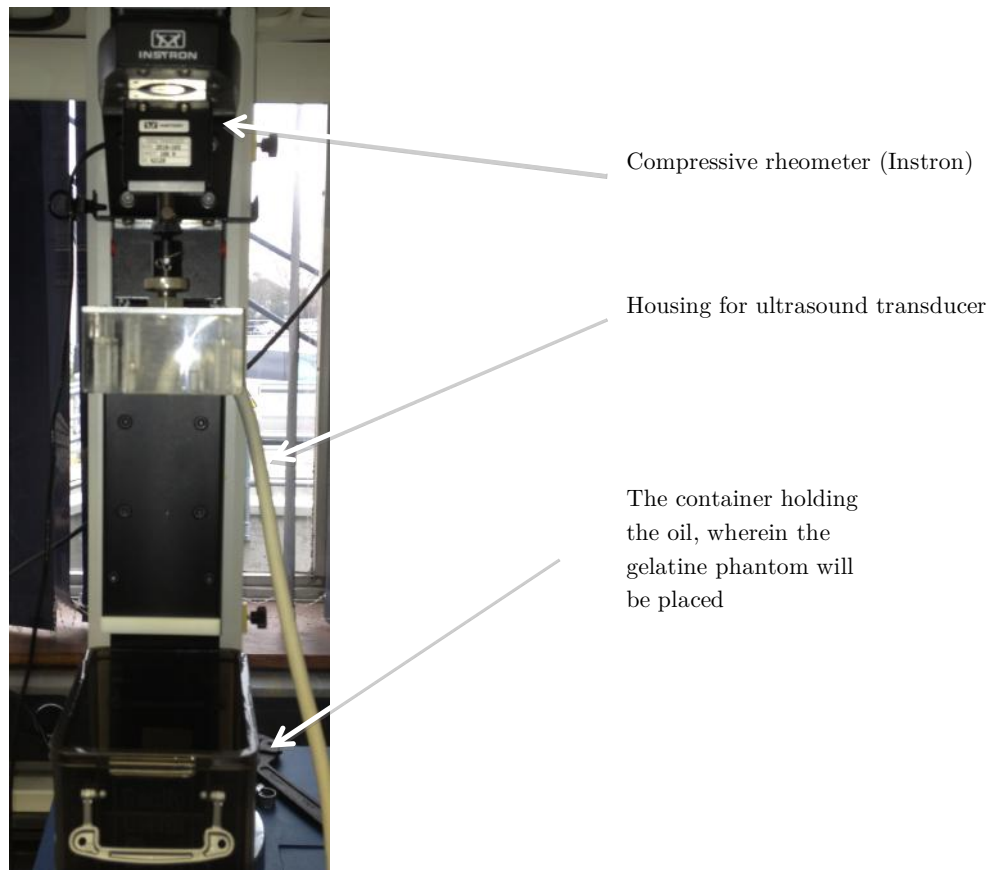


Figure 6.6 The experimental set up for investigating the effect of strain on the gelatine phantoms. The housing for the ultrasound probe extends the footplate of the ultrasound probe to exert a uniform strain in the phantom.

### 6.3.7 Varying the tumour-brain interface conditions

As demonstrated by the previous researchers in this research group (Chakraborty, 2007; Uff, 2011), quasistatic elastography can characterise tumour-brain interface conditions. As quasistatic elastography requires the use of external pressure to generate the elastograms, it is able to detect the difference in the movements between the tumour and background, i.e. slip at the tumour-brain boundary. A slippery tumour-brain boundary may represent a potential surgical plane of cleavage for initiating safe resection. Using axial shear strain in what they called slip elastography, Chakraborty, et al. (2012, 2007) were able to determine the force required to initiate slip in gelatine phantoms with different slippery boundary angles, and applied the method to *in vivo* tumour-brain boundaries intra-operatively. Uff

(2011) showed that slippery boundaries were also visualised by observing a characteristic type of axial normal strain heterogeneity as opposed to axial shear strain. The aim of the present experiments was to determine whether the existence of a slippery boundary influences the appearance of an inclusion on SWE.

Gelatine phantoms were manufactured using 8% and 14% w/w gelatin concentration solution as stiff and soft phantoms, respectively. Using these phantoms, adhered and mobile boundaries were also created to determine appearances on SWE. In order to create the phantoms, background gelatine mixture was poured into a cuboidal mould with sides measuring 6 mm. A 15-mm-diameter rod was suspended in the gelatine mixture to create a rod-shaped well in the gelatine when the gelatine solidified. To make adhered inclusions, the gelatine mixture for the inclusion was poured in at 35°C and allowed to set in the refrigerator at 4°C. To make mobile inclusions, the gelatine mixture for the inclusion was poured in at 28°C and allowed to set in the refrigerator. Once set, a thin metal rod was used to develop the mobile plane between the inclusion and the background with the phantom immersed in vegetable oil bath to prevent effect of osmosis. Both mobile and adhered phantoms were scanned immersed in vegetable oil bath. A total of 12 gelatine phantoms were manufactured, 6 with a soft background and a stiff inclusion (3 mobile and 3 adhered), and 6 with a stiff background and a soft inclusion (3 mobile and 3 adhered). The experimental set-up is illustrated in Figure 6.6.

### 6.3.8 Resolution of shear wave elastography

It has been shown that in glioblastoma resection, survival rates improve with increased extent of resection (Lacroix et al., 2001; Laws et al., 2003; McGirt et al., 2009; Nomiya et al., 2007; Oszvald et al., 2012; Sanai et al., 2011; Stummer et al., 2006; Ushio et al., 2005; Vuorinen et al., 2003). In low-grade glioma, gross total resection has been shown to delay tumour progression (McGirt et al., 2008) and malignant transformation (McGirt et al., 2008), and also improve overall survival (McGirt et al., 2008) and reduce seizure rates (Smits & Duffau, 2011). Therefore, it is essential that any intra-operative imaging technique

should be able to detect residual tumour reliably in order to achieve better extent of resection, especially in high-grade glioma.

Ultrasound B-mode has been used by neurosurgeons as an intra-operative imaging adjunct since 1980's (Chandler & Rubin, 1987). With higher frame rate and central frequency, and 3D functionality of the transducers, intra-operative ultrasound has been shown to guide glioma resection, with (Gronningsaeter et al., 2000) and without (Wang J. et al., 2012) neuronavigation. Whilst ultrasound B-mode illustrates excellent anatomical details, it does not demonstrate the mechanical properties of the tissue. Therefore, during tumour resection, it can sometimes be challenging to differentiate between oedematous tissues and blood on the ultrasound B-mode. By combining SWE with ultrasound B-mode, it was hypothesised that this can improve rates of detecting residual tumour as tissue swelling and blood have different mechanical properties. The sensitivity of IOUS in detecting residual tumour is between 67% and 85% (Hammoud et al., 1996; Le Roux et al., 1994), which could potentially be improved by combining SWE and ultrasound B-mode. Detection of residual tumour by SWE will depend on both SWE resolution and the elastic contrast between tumour and brain. The latter will only be discovered by further clinical studies. However, in order to assess the potential usefulness of SWE in this context, it was felt that the resolution of SWE should be assessed. Macé et al. (2011) demonstrated that SWE has a good resolution of 0.7 mm x 1 mm x 0.4 mm using rat brains, which was estimated from the resolution of ultrasound B-mode images. As direct measurement of SWE resolution was not performed in this study, I propose an experiment to assess the SWE resolution using gelatine phantoms.

To investigate the resolution of the SuperSonic Aixplorer® SWE mode, three 2D phantoms with soft background (8% gelatine concentration) and stiff inclusions (14% gelatine concentration) of diameters of 1 mm, 1.8 mm, 3 mm, 4 mm, and 5 mm, were manufactured. The phantom is illustrated in Figure 6.7. All scans were performed at 16 °C to ensure consistent Young's modulus measurement, because temperature can affect the Young's modulus of gelatine, as shown in Chapter 4. The experiment was also repeated with a gelatine phantom having a stiff background (14% gelatine concentration) and another with soft inclusions (8% gelatine concentration).

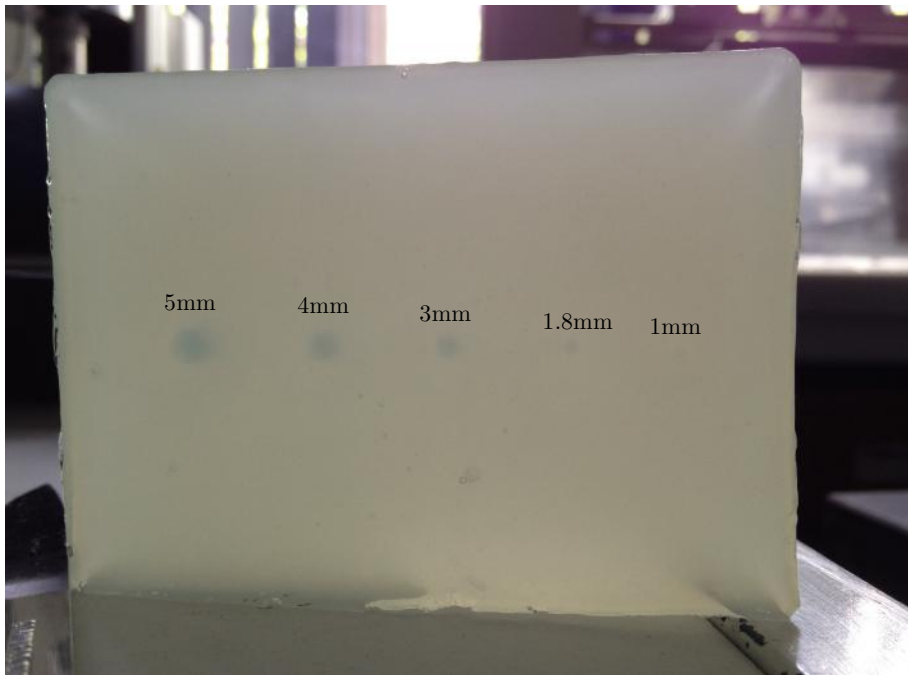


Figure 6.7. The gelatine phantom with small cylindrical inclusions (1mm, 1.8mm, 3mm, 4mm and 5mm diameter).

### 6.3.9 Other factors affecting SWE measurements

As reported by Yoon, et al. (2013), the false-negative and false-positive rates for detecting malignant and benign breast lesions, respectively, are affected by the sizes of the lesions, their depth from the surface and the breast thickness. Similar behaviour might be expected in the present studies.

#### 6.3.9.1 Inclusion size

For the first factor, using SWE and applying a maximum Young's modulus ( $E_{\max}$ ) cut-off value of 82.3 kPa, which was the optimal cut-off value as calculated by using the receiver-operating curve (ROC) analysis in a preliminary study at their institution, Yoon et al. (2013) demonstrated that false-negative  $E_{\max}$  for malignant lesions had significantly more lesions less than 10 mm compared with true-positive  $E_{\max}$  for malignant lesions of the similar size (66.6% versus 4.4%,  $p < 0.001$ ). The same authors also showed that false-positive  $E_{\max}$

for benign lesions had significantly more lesions larger than 20 mm compared with true-negative  $E_{\max}$  for benign lesions of similar sizes (36.1% versus 12.2%,  $p = 0.004$ ). This means that SWE may have underestimated the Young's modulus of the smaller lesions whilst overestimating the larger lesions.

To investigate whether lesion size influences the measured value for Young's modulus, 2D phantoms with different sized inclusions (1 mm, 1.8 mm, 3 mm, 4 mm, 5 mm, 10 mm, 15 mm and 20 mm diameter) were initially manufactured. The phantoms are illustrated in Figure 6.7 above for small inclusions (1 mm to 5 mm), and in Figure 6.8 for large inclusions (10 mm to 20 mm). To assess the effect of inclusion stiffness on the Young's modulus measurements, three replicates of two versions of both phantoms were manufactured, one with a soft background and stiff inclusions, the other with a stiff background and soft inclusions. Thus 12 phantoms with cylindrical inclusions were made. The soft and stiff gels were made with 8% and 14% gelatin concentrations, respectively.

However, any relationship between the measured Young's modulus and lesion size may not be fully explored using 2D phantoms, as the effect could be due to the contribution from the background gelatine through a partial volume effect. Figure 6.9 shows the ultrasound transducer scanning a 3D phantom, i.e. containing a spherical inclusion, (a) with the scan plane shown in transparent green colour (b). Figure 6.10 shows the 3D phantom from the top with a dashed outline of the SWE image slice thickness and the width of the inclusion displayed on ultrasound B-mode. The transparent green rectangle in this figure shows the area produced by a projection of the volume that is included in the Young's modulus measurement. In this case, the inclusion size is larger than the SWE slice thickness, so the volume included for the Young's modulus measurement contains mostly the inclusion, with perhaps small volumes at the edges of the slice containing the background. Therefore, the measured Young's modulus should almost equal the true Young's modulus of inclusion. However, if the inclusion is smaller than the SWE image slice thickness, then the Young's modulus measurement may not equal the true Young's modulus due to the effect from the background. Figure 6.11 illustrates this effect. Therefore, in addition to the 2D phantoms, 3D phantoms were also manufactured to test this hypothesis. The 3D phantoms consisted of 4 small spheres measuring 12 mm, 8.5 mm, 6 mm and 2.5 mm in diameter as inclusions in a

background of gelatine (Figure 6.12). A total of 6 3D gelatine phantoms were manufactured – 3 phantoms with a soft background and stiff inclusions, and 3 phantoms with a stiff background and soft inclusions.

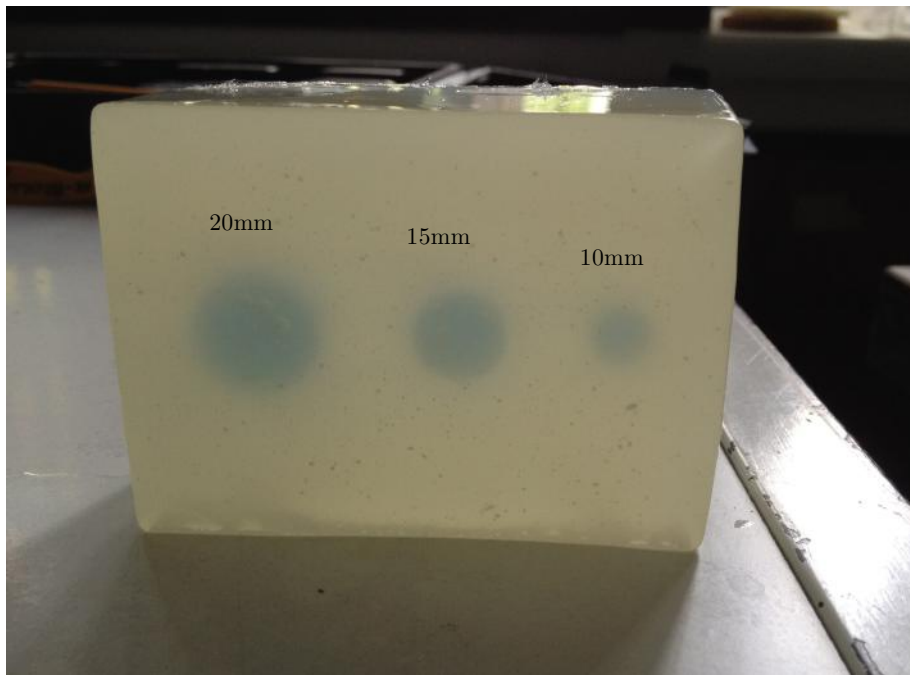


Figure 6.8. Gelatine phantom with large cylindrical inclusions (10mm, 15mm and 20mm diameter).

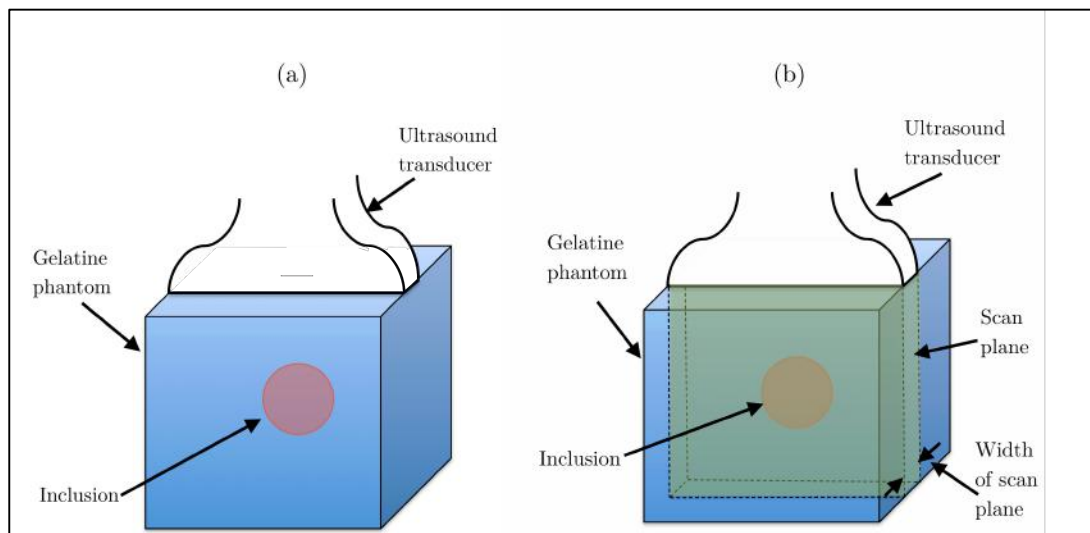


Figure 6.9. The setup for ultrasound scanning of a 3D phantom (a), and repeated but with scan plane coloured transparent green (b).

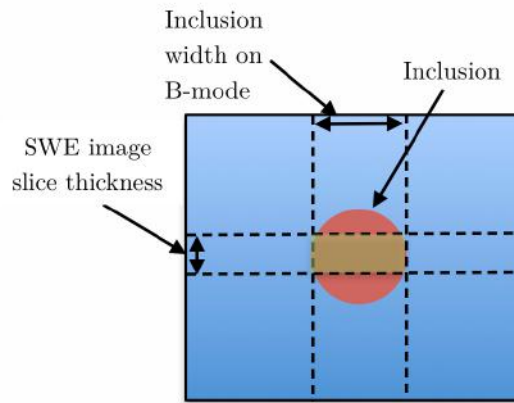


Figure 6.10. The view of the 3D phantom from the top when the inclusion is large. The horizontal dashed lines indicate the outline of the SWE image slice thickness while the vertical dashed lines show the width of the inclusion on ultrasound B-mode image. The transparent green rectangle indicates the area of the projected volume included in the calculation of Young's modulus.

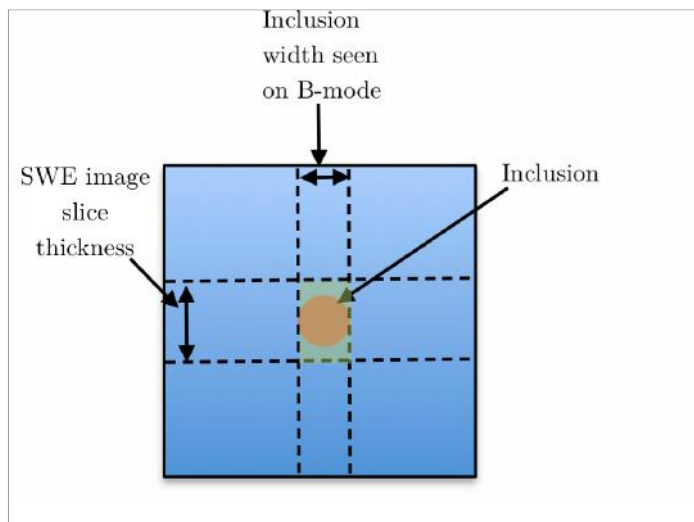


Figure 6.11. The view from the top of the 3D phantom for a small inclusion. The horizontal dashed lines indicate the outline of the SWE image slice thickness while the vertical dashed lines show the width of the inclusion on ultrasound B-mode image. The transparent green rectangle indicates the area of the projected volume included in the calculation of Young's modulus.



Figure 6.12. Three-dimensional (3D) phantom with small spheres measuring 12 mm, 8.5 mm, 6 mm and 2.5 mm in diameter, from the left, placed on a partially solidified background gelatine. More gelatine will be poured over it to make the phantom.

### 6.3.9.2 Inclusions at different depths

Using QSE, Chang et al. (2011) showed that, compared with lesions located 15 mm or shallower, the lesions located deeper than 15 mm led to low quality images. The same authors also demonstrated that sensitivity of detecting malignant lesions was lower in the low quality image group compared with high quality image group (56.8% versus 87%,  $p = 0.015$ ). This is further supported by Raza et al., (2010), who showed that false-positive and false-negative lesions were found to be located deeper than 12 mm with QSE. Using SSI, Yoon et al. (2013) demonstrated that false-negative  $E_{\max}$  for malignant lesions had significantly more lesions located in the deep portion of the breast than those located in the superficial or mid portion of the breast ( $p = 0.027$ ). It was postulated that there could be an attenuating effect of the tissue on elastic and ultrasound waves from the thickness of the breast tissue (Chang et al., 2011; Yoon et al., 2013a; Yoon et al., 2013). To investigate the effect of depth from the surface on the Young's modulus measurement, gelatine phantoms with inclusions positioned at varying depths but laterally offset in a diagonal fashion were manufactured, keeping the size of the inclusions constant at 5 mm diameter (Figure 6.13) and 1 cm (Figure 6.14). A total of 12 gelatine phantoms were manufactured – 3 gelatine

phantoms with a soft background and stiff 5-mm inclusions, 3 gelatine phantoms with a soft background and stiff 1-cm inclusions, 3 gelatine phantoms with a stiff background and soft 5-mm inclusions, and 3 gelatine phantoms with a stiff background and soft 1-cm inclusions.

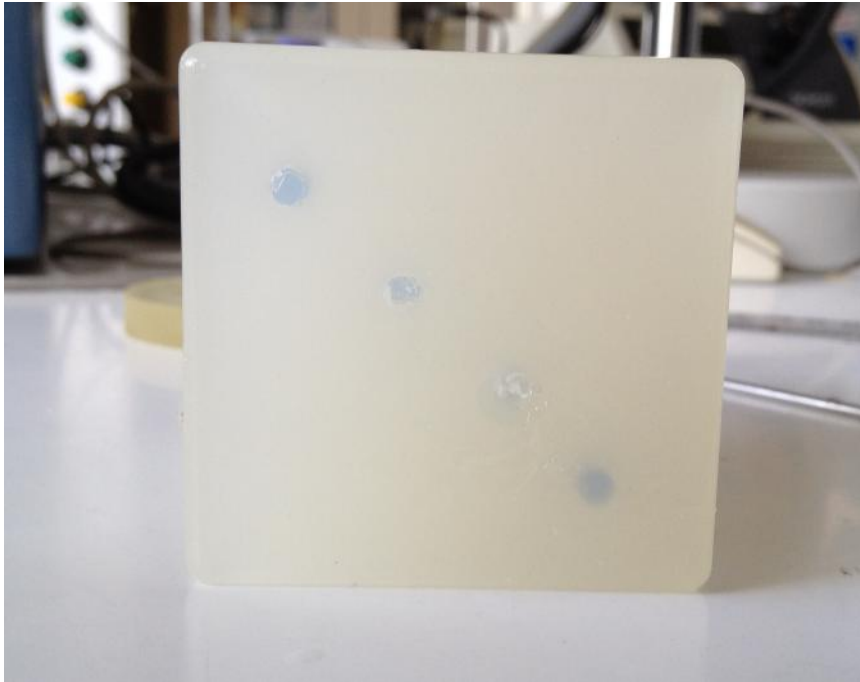


Figure 6.13. Gelatine phantom with cylindrical inclusions of 5 mm in diameter arranged at various depths.



Figure 6.14. Gelatine phantom with 1-cm diameter cylindrical inclusions arranged in diagonal fashion.

For all these experiments, the measured Young's moduli were plotted against the true Young's modulus to assess for any correlations and effects of these factors.

### 6.3.9.3 Anisotropy of tissue

In anisotropic tissues the shear wave speed has been shown to be direction dependent, and therefore the Young's modulus derived from it (Gennisson et al., 2010; Gennisson et al., 2003; Macé et al., 2011). Using bovine muscle in vitro and human muscle in vivo, Gennisson et al. (2010, 2003) showed that shear wave velocity parallel to the fibres is faster than that perpendicular to the fibres. Similarly, Macé et al. (2011) showed that there is white matter anisotropy in rat brains in vivo using SSI. Therefore, to validate this finding, 2 pieces of *ex vivo* porcine spinal cord from different pigs were scanned with the Aixplorer™, with the transducer parallel and perpendicular to the length of the spinal cord, to determine if the former produces higher Young's modulus than the latter.

## 6.4 Results

### 6.4.1 Effect of changing the region-of-interest (ROI) size

During clinical scanning, there is always a need to adjust the ROI size to include the lesion or lesion-brain interface. As shown in Figure 6.15, there was no change in the Young's modulus measurements with ROI size.

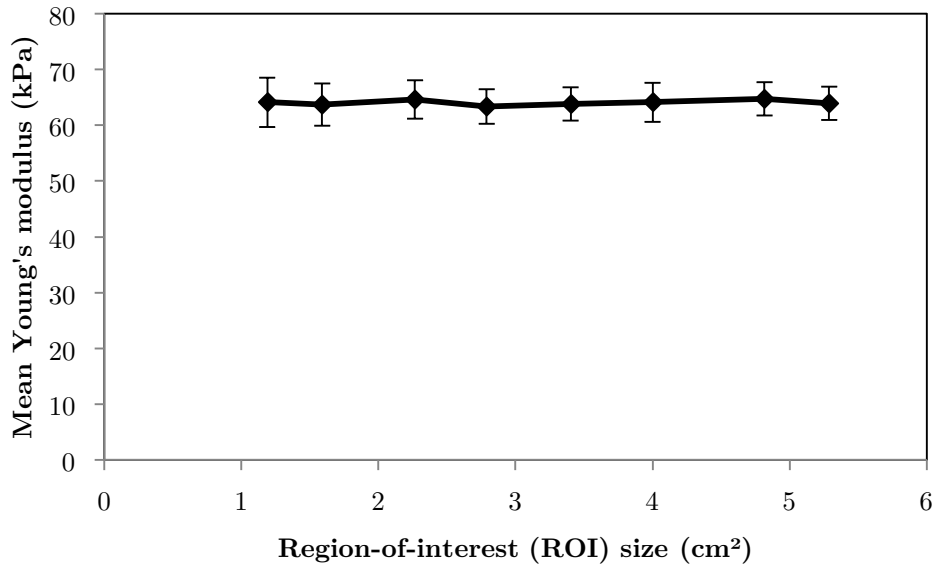


Figure 6.15. Mean Young's modulus measured with varying sizes of the ROI with 3 different phantoms ( $n=3$ ). The error bars are plus and minus one standard deviation.

### 6.4.2 Effect of varying the water standoff

As illustrated in Figure 6.16, the Young's modulus remained almost constant when the water standoff was varied, for both standard and penetration modes. With a water standoff of 5 cm, the Young's modulus measurement was lower in the standard mode compared with the penetration mode. However, the difference is well within the standard deviations.

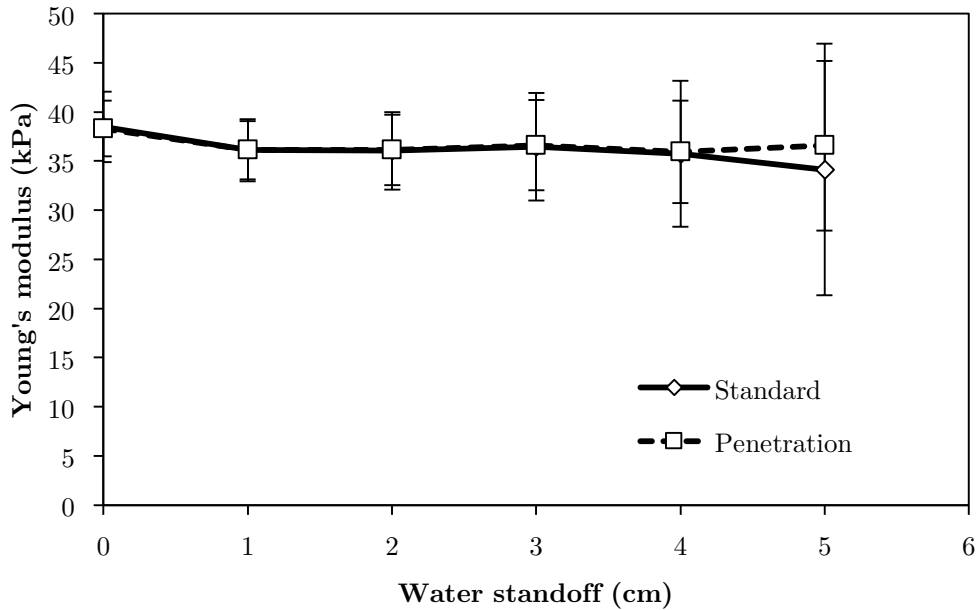


Figure 6.16. Mean Young's modulus measured as a function of water standoff height for 3 different phantoms ( $n=3$ ). The continuous and dashed lines represent 'standard' and 'penetration' modes, respectively. The error bars are plus and minus one standard deviation.

### 6.4.3 Attenuation in superficial tissue

Figure 6.17 shows that the background gelatine Young's modulus measurements remained constant with increasing attenuating layer thickness, where the attenuating layer was composed of 14% gelatine concentration phantom. This gelatine concentration was the same concentration used for stiff inclusions in the experiments in this thesis.

For stiffer inclusion gelatine, the Young's modulus measurements seemed to be decreasing with thickness of the layer; the effect is more obvious for standard mode than for penetration mode, and for thickness of 3 cm or more. Each measurement was made at a constant depth at 5 cm, across different configurations and phantoms. Using surgical as the attenuating layer, the Young's modulus measurements at a depth of 2.5 cm did not seem to be affected – the inclusion and background Young's moduli (mean  $\pm$  SD) were  $111.94 \pm 4.3$  kPa and  $65.3 \pm 6.7$  kPa, respectively. However, the shear wave signal is lacking in the inclusion for the standard mode (Figure 6.18), and lacking deeper down in the penetration

mode (Figure 6.19). Using duragen as an attenuating layer, there was a complete absence of shear wave signal in the phantom, even with penetration mode (Figure 6.20).

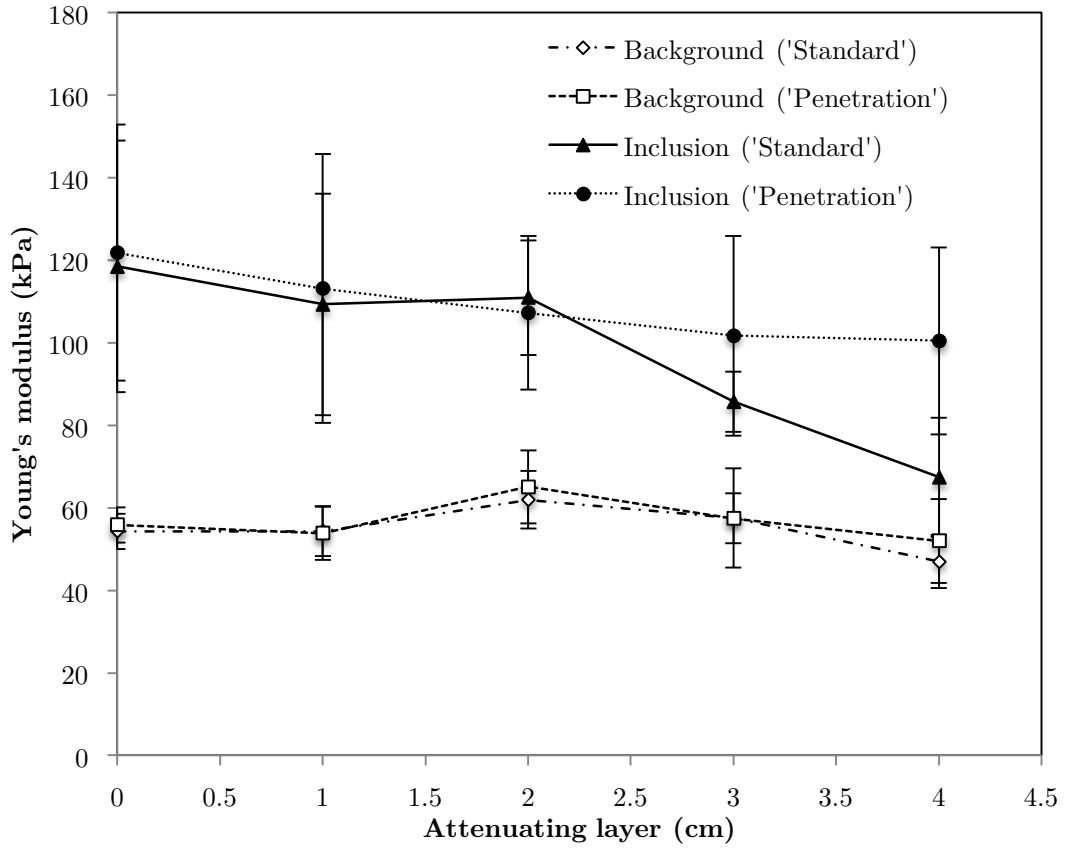


Figure 6.17. Young's modulus measured for inclusion and background, for standard and penetration mode, as a function of the thickness of the overlying attenuating layer composed of 14% gelatine concentration phantom ( $n=3$ ).

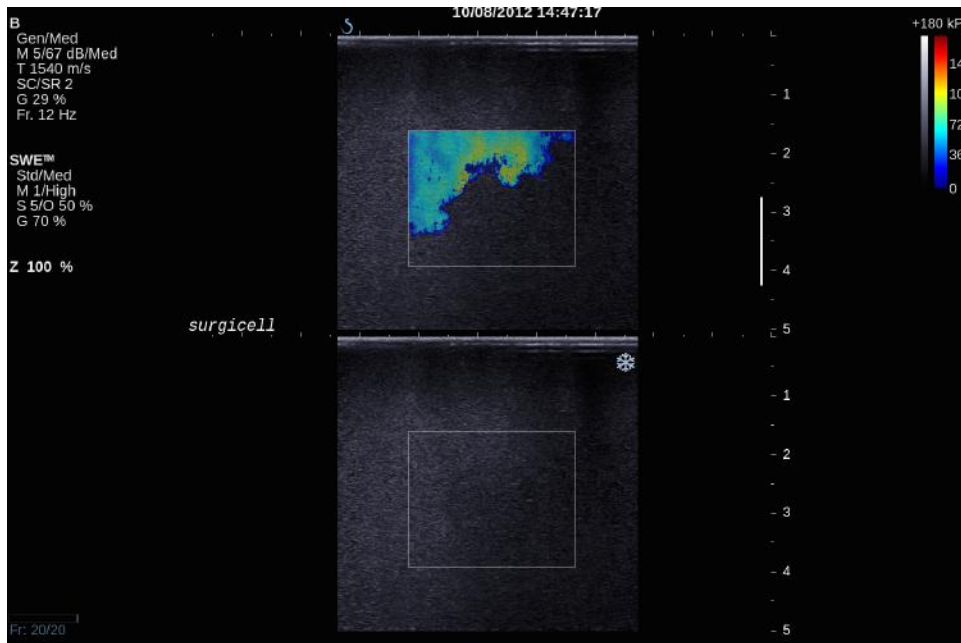


Figure 6.18. SWE appearance with surgicel as an attenuating layer, using standard mode.

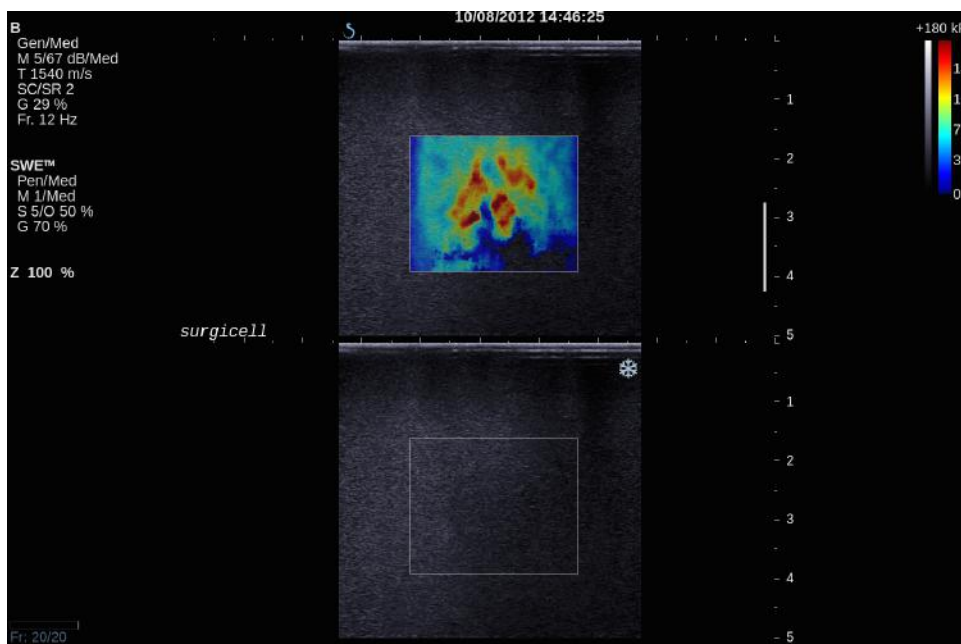


Figure 6.19. SWE appearance with surgicel as an attenuating layer, using the penetration mode.

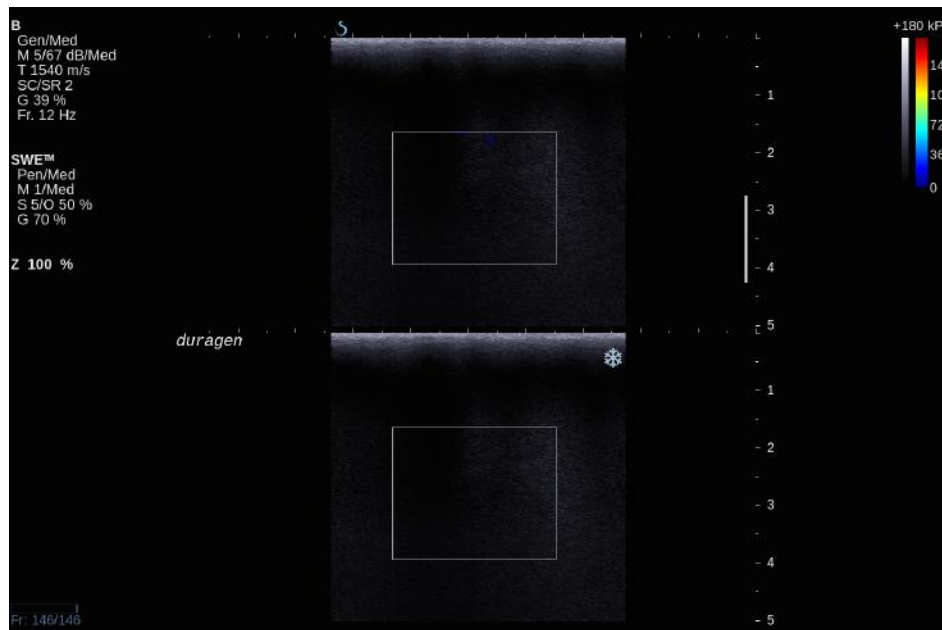


Figure 6.20. SWE appearance with duragen as an additional attenuating layer, using penetration mode.

#### 6.4.4 Effect of adjusting SWE gain

As the SWE gain is increased, the areas devoid of SWE signal on SWE gain of 70% appeared with artefactually high Young's modulus values, rather than simply being displayed with greater variance. This is illustrated in Figure 6.21, Figure 6.22, Figure 6.23, and Figure 6.24, which show the display on the Aixplorer® for SWE gains of 70% through to 100% at 10% increments, respectively.

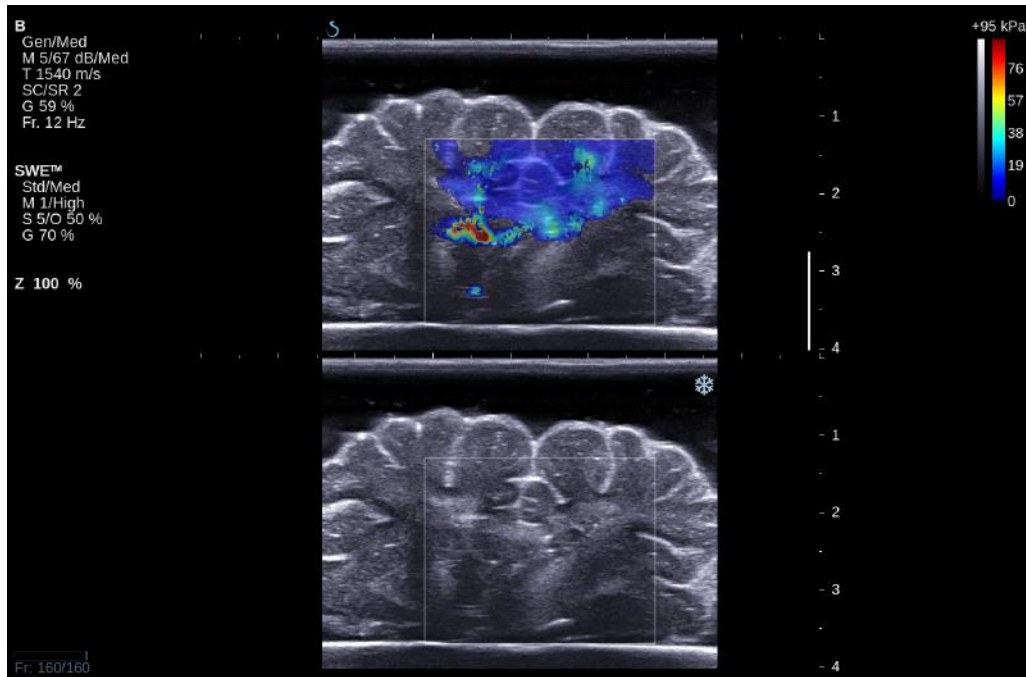


Figure 6.21. Display on Supersonic Aixplorer® for SWE gain of 70%.

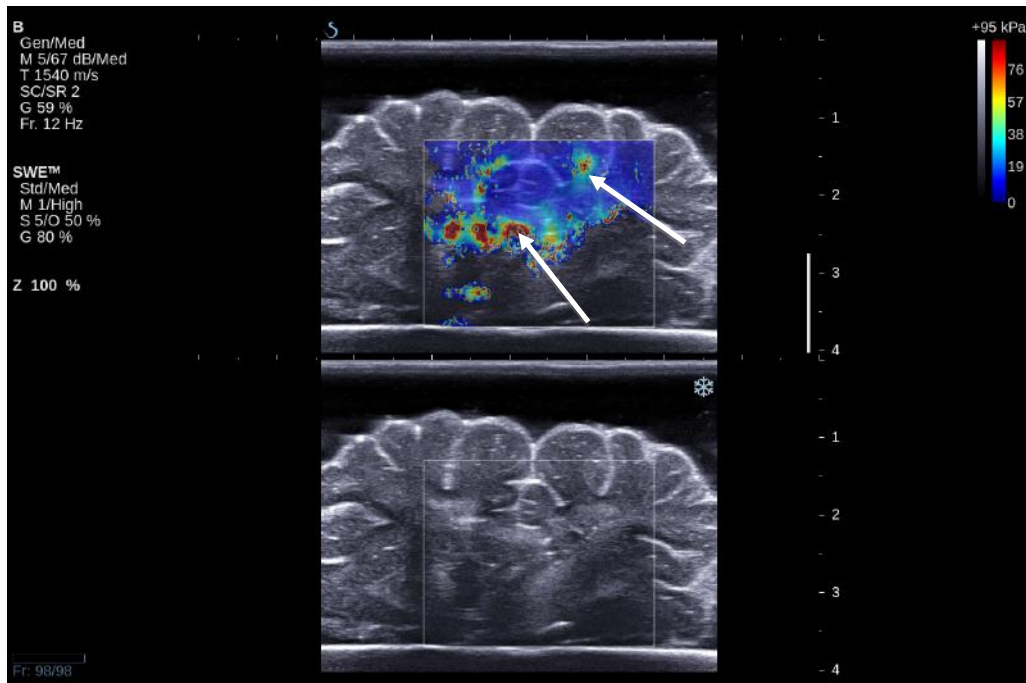


Figure 6.22. Display on Supersonic Aixplorer for SWE gain of 80%. Note the previously areas void of SWE signal are now filled with artefactually high Young's modulus values (white arrows).

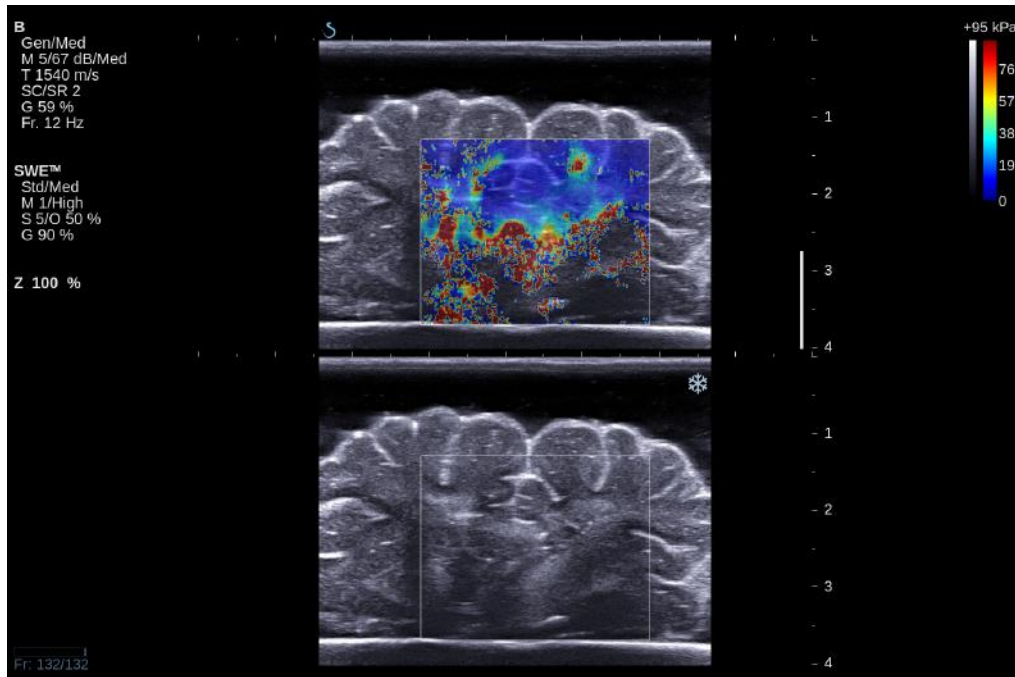


Figure 6.23. Display on Supersonic Aixplorer for SWE gain of 90%. Note more areas of previously void of SWE signal are appearing as artefactually stiff regions.

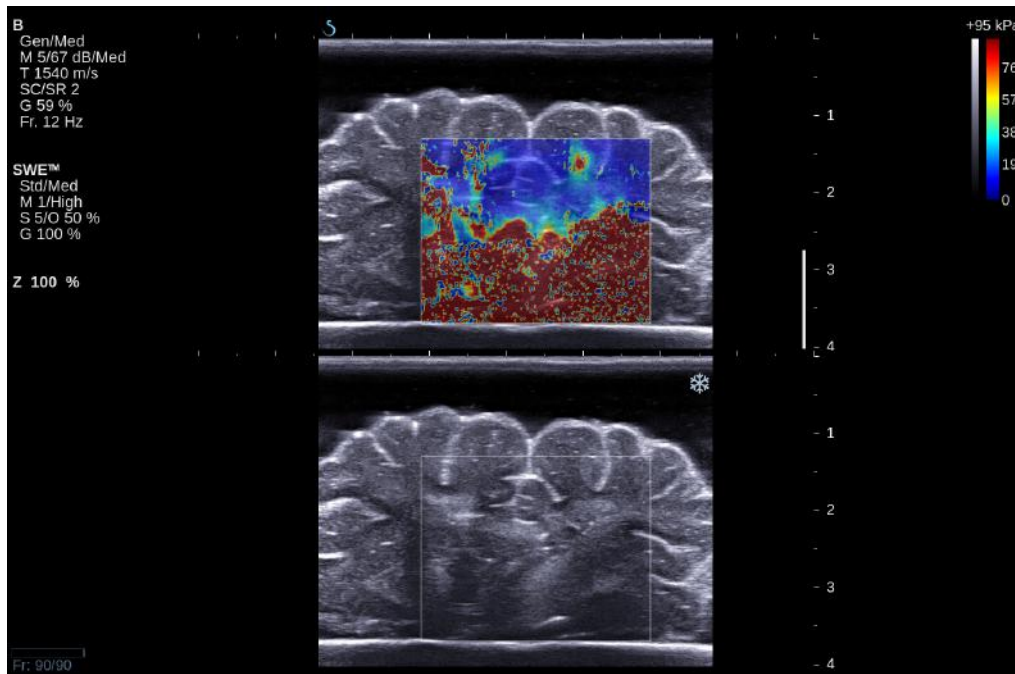


Figure 6.24. Display on Supersonic Aixplorer for SWE gain of 100%. Note the areas previously void of SWE signal are filled with artefactually high Young's modulus values.

### 6.4.5 Effects of manipulations on SWE measurements

Using gelatine phantoms simulating tumour resection, both the background and inclusion demonstrated a decrease in the Young's modulus measurements with manipulation. Figure 6.25 is the SWE for the gelatine phantom before manipulation of the inclusion. Figure 6.26 is the SWE for the same phantom during resection of the inclusion. Figure 6.27 shows the SWE after complete removal of the inclusion. Comparing SWE for post complete removal of the inclusion with that during and before removal, there was a decrease in the Young's modulus measurements in the background where it was exposed to the water bath. These areas were also those subjected to manipulation by the instruments used for the removal. The Young's modulus measurements are shown in Figure 6.28 and Figure 6.29.

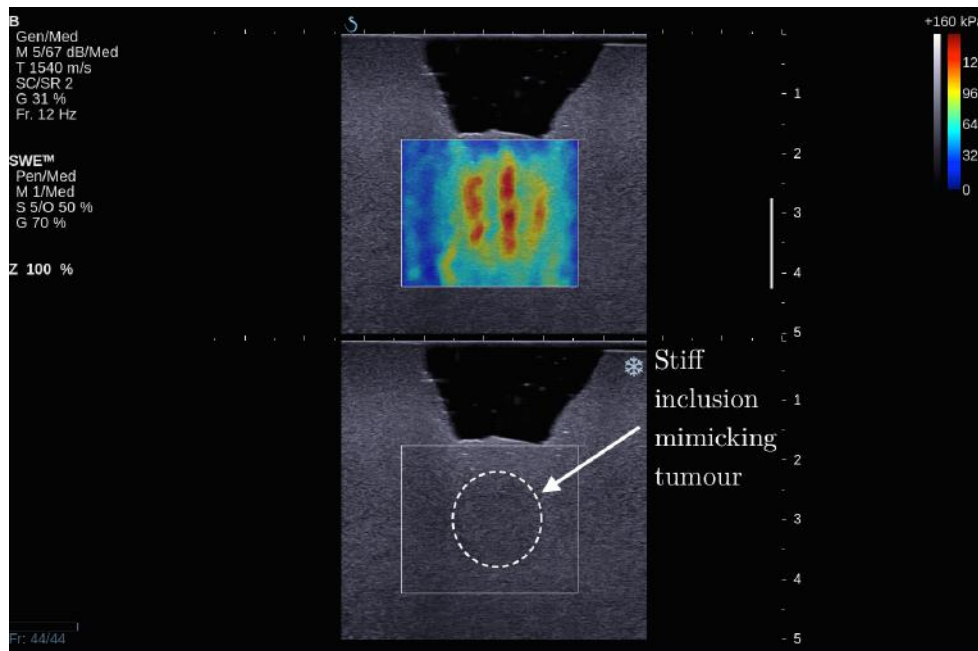


Figure 6.25. SWE of the phantom with stiff inclusion simulating a tumour before resection.

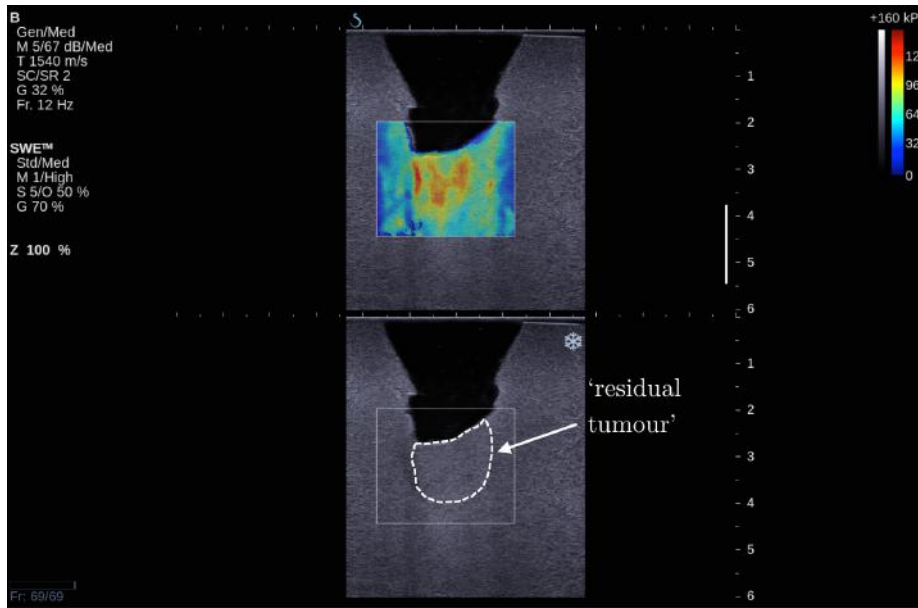


Figure 6.26. SWE during resection of the inclusion.

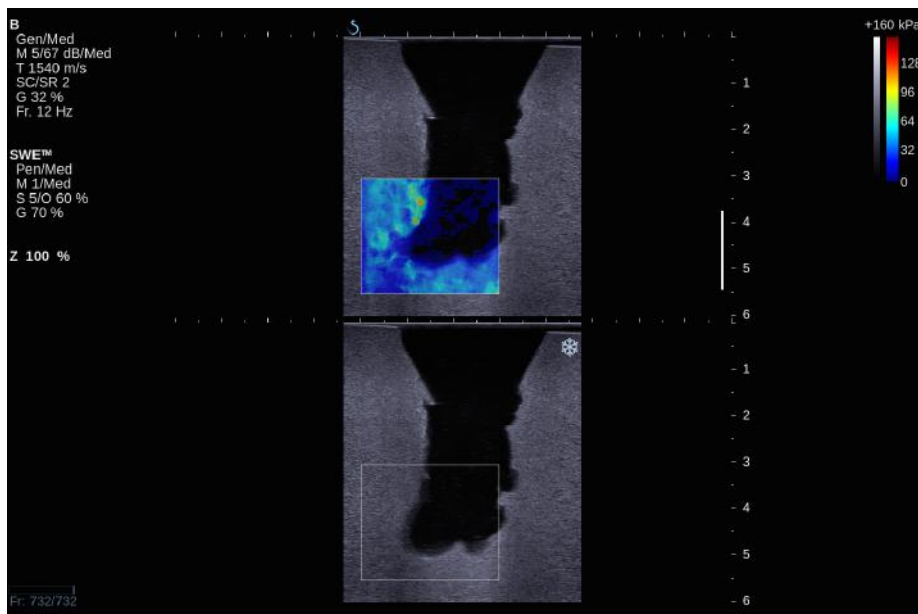


Figure 6.27. SWE after complete removal of the stiff inclusion. Notice the decrease in the Young's modulus in the surrounding tissue compared with previous 3 images.

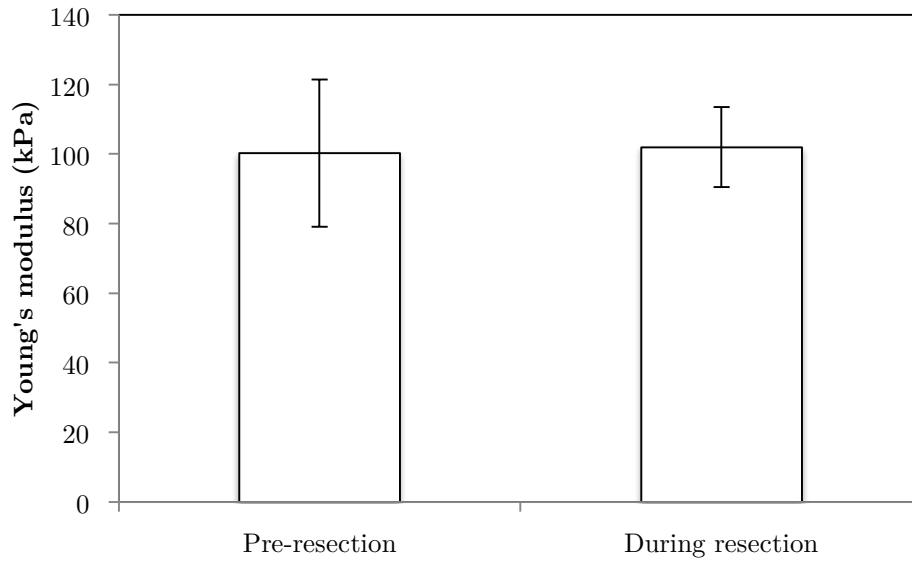


Figure 6.28. Mean and plus and minus one standard deviation of Young's modulus measured by SWE before and during resection of the stiff inclusion for inclusion (n=3). There is no statistically significant difference ( $p = 0.802$ , paired t-test).

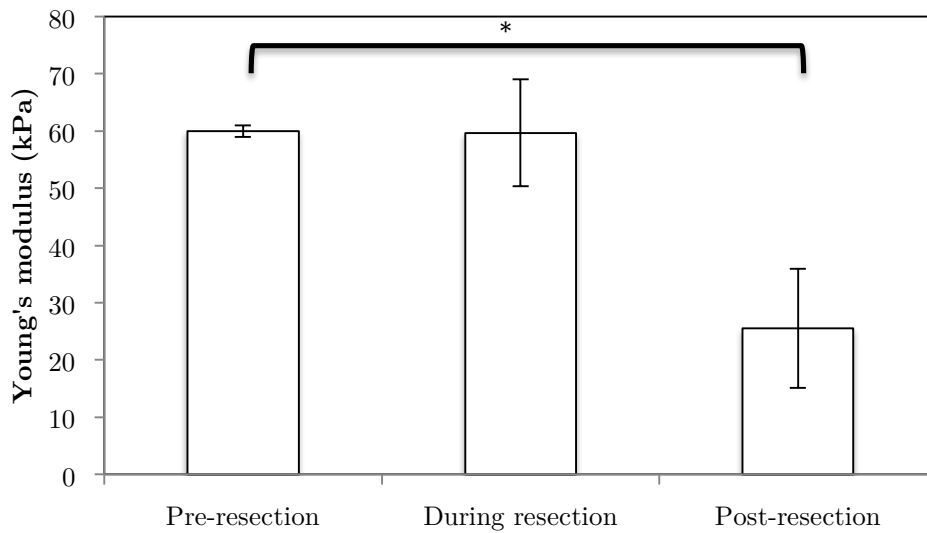


Figure 6.29. Mean and plus and minus one standard deviation of Young's modulus measured by SWE of the background gelatine for different stages of inclusion removal (n=3). \* denotes a statistically significant difference between pre-resection and post-resection ( $p < 0.001$ , paired t-test). However, the difference between during resection and post-resection is not statistically significant ( $p = 0.087$ , paired t-test).

For the experiments on pig brains, Figure 6.30 is the SWE image of porcine brain scanned in coronal plane with pia mater removed on the right and pia mater intact on the left. Figure 6.31 demonstrates the Young's modulus measurements for grey and white matter with pia mater intact and removed. There was a significant decrease in the values for grey matter when the pia mater is removed ( $p = 0.011$ , Wilcoxon's signed-ranks test). However, there was no significant difference between measured Young's modulus values for the grey and white matter, in either situation – whether the pia was intact ( $p = 0.374$ , Wilcoxon's signed-ranks test) or it was removed ( $p = 0.314$ , Wilcoxon's signed-ranks test). There was also no significant difference between the values for the white matter with and without pia mater ( $p = 0.314$ , Wilcoxon's signed-ranks test).

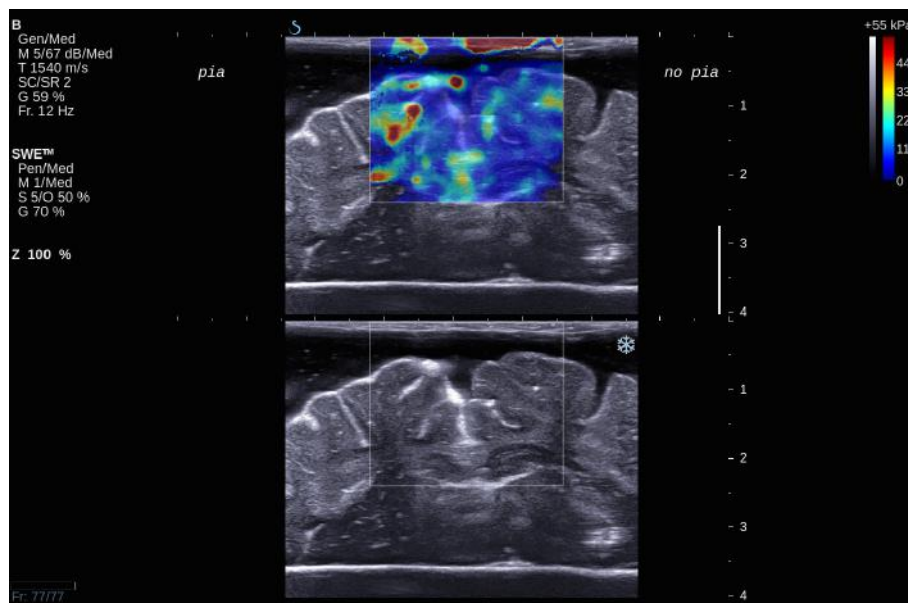


Figure 6.30: The SWE images for porcine brain scanned in coronal section with the pia mater removed on the right side of the image. The pia mater on the left side of the image was intact.

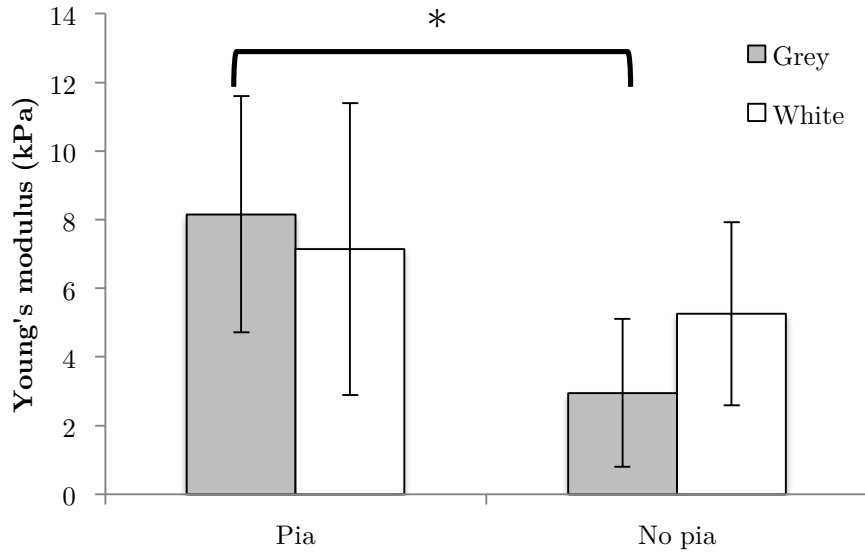


Figure 6.31: Mean and plus and minus one standard deviation of Young's modulus measured by SWE for grey and white matter with pia mater intact and removed ( $n=3$ ). \*There was a statistically significant difference between the grey matter with and without pia mater ( $p = 0.011$ , Wilcoxon's signed-ranks test). However, there was no statistically significant difference between the white matter with and without pia mater ( $p = 0.314$ , Wilcoxon's signed-ranks test).

The Young's modulus measurements were noted to decrease from the pre- to the post-compression state. The graph of Young's modulus measurements is shown in Figure 6.32. The difference between pre- and post-compression states was not statistically significant ( $p = 0.485$ , Wilcoxon's signed-ranks test). The heights of the porcine brains were also noted to decrease from the pre- to the post-compression state. As the brains were noted to expand sideways, the change in height cannot be attributed to the change in volume. The heights are shown in Figure 6.33. The difference between pre- and post-compression states was statistically significant ( $p = 0.036$ , Wilcoxon's signed-ranks test).

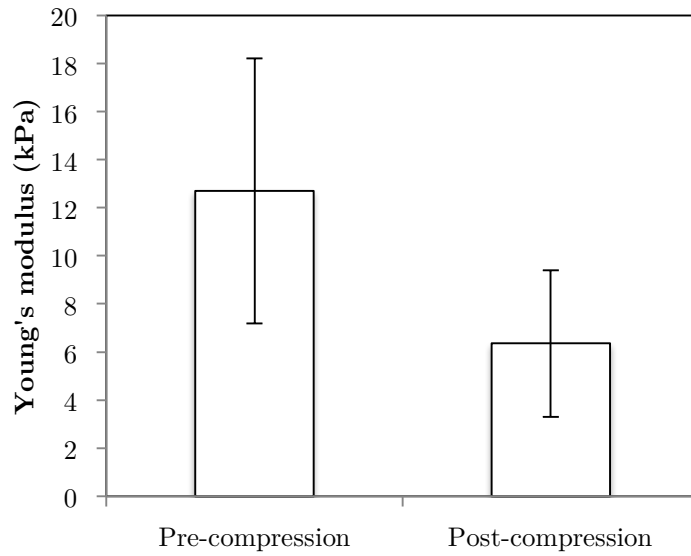


Figure 6.32. Mean and plus and minus one standard deviation of Young's modulus measurements of porcine brains before and after compression ( $n=3$ ). The difference was not statistically significant ( $p = 0.485$ , Wilcoxon's signed-ranks test).

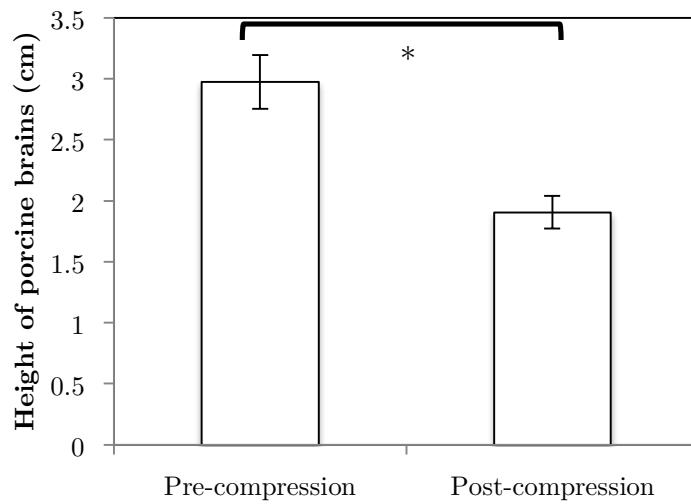


Figure 6.33. Mean and plus and minus one standard deviation of the Young's modulus of porcine brain heights before and after compression. \* There was a statistically significant difference ( $p < 0.05$ , Wilcoxon's signed-ranks test).

### 6.4.6 Effect of strain on SWE measurements

With homogeneous gelatine phantoms, the overall Young's modulus did not change between using a water standoff and with the transducer touching the phantom, but when using the water standoff there appeared to be a reduced Young's modulus for about the first 0.5 cm of the phantom, compared to the remainder of the phantom and when the transducer was touching the phantom. Figure 6.34 and Figure 6.35 are SWE displays with Q-boxes for the same homogeneous 8% gelatine phantom with the probe imaging from above through a water standoff and touching the phantom, respectively. Figure 6.36 demonstrates the Young's modulus measurements of the top layer (the upper Q-box) for 8% and 14% gelatine phantoms ( $n=3$ , respectively) when the probe had a water standoff and was touching the phantoms. There was an increase between the measurements with the probe touching the phantoms compared to with water standoff and the difference was statistically significant ( $p < 0.01$ , paired t-test). Figure 6.37 shows the Young's modulus measurements of the whole (the largest Q-box) for both 8% and 14% gelatine phantoms. The effect of the top layer was to slightly decrease the Young's modulus when a water standoff was used, but the difference was only significant ( $p < 0.01$ , paired t-test) in the 14% gelatine phantom. This is consistent with the observation in figure 6.35 that there was a larger difference in the top layer measurements for the 14% gelatine phantoms than for the 8% gelatine phantoms. Figure 6.38 shows that in the lower layer, without contribution from the top layer, there was no noticeable difference between the measurements with and without water standoff.

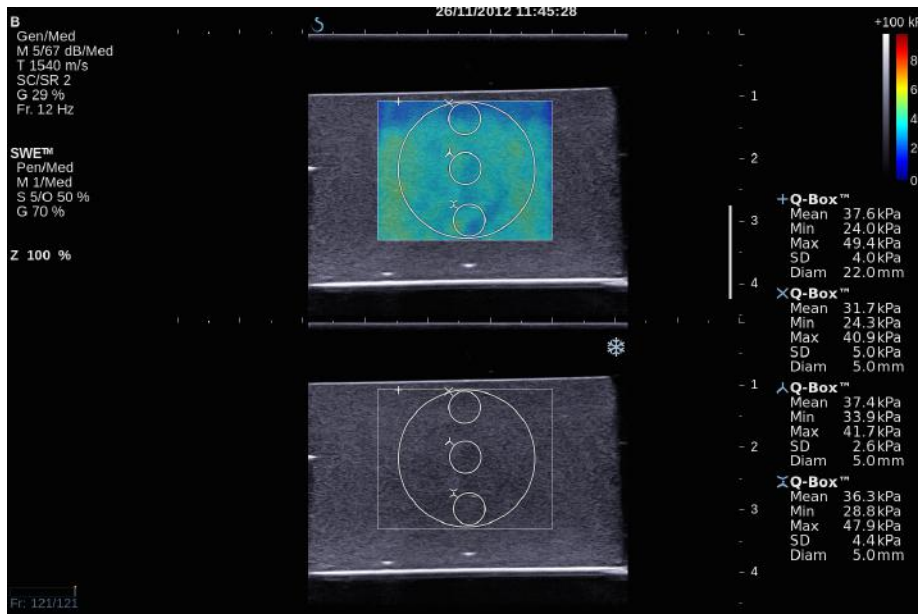


Figure 6.34. SWE display showing the apparently softer top layer of the homogeneous gelatine phantom compared to the rest of the phantom when the probe is used with water standoff.

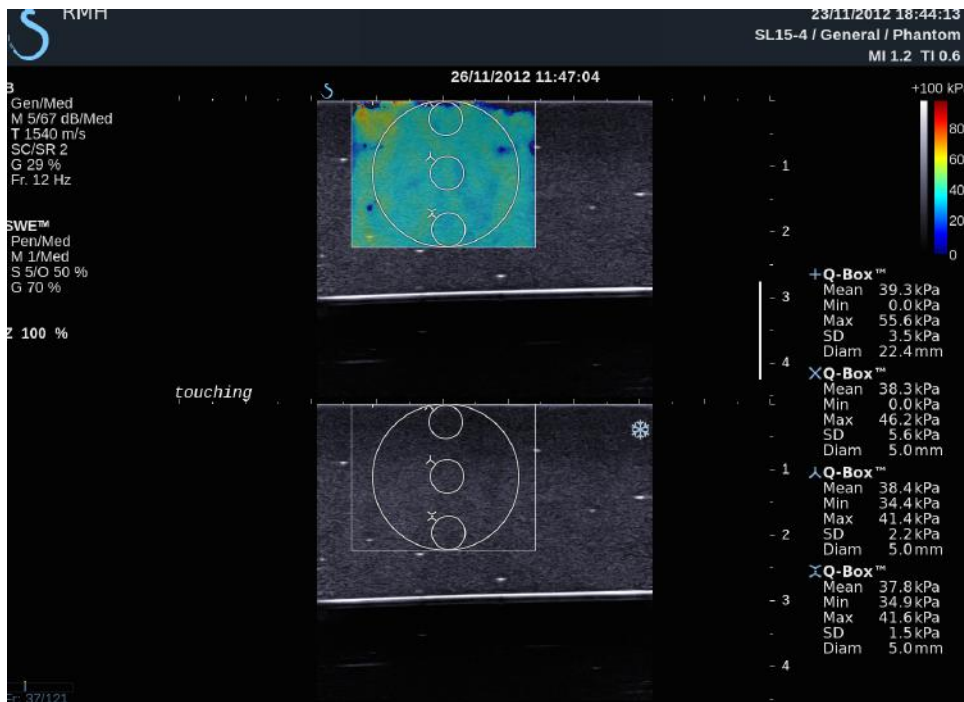


Figure 6.35. SWE display showing the homogeneous Young's modulus measurement when the probe is touching the phantom.

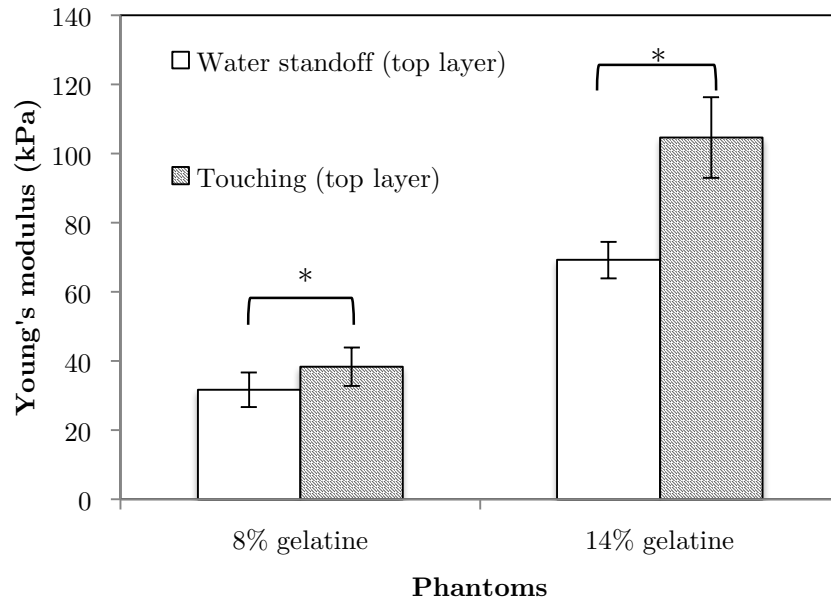


Figure 6.36. The SWE Young's modulus measurements of the top layer of 8% and 14% gelatine phantoms using a water standoff and with the probe touching the phantoms. The Young's modulus seemed to decrease when a water standoff was used. \* denotes that the difference is statistically significant ( $p < 0.01$ , paired t-test, 8% gelatine phantoms ( $n=3$ ), and 14% gelatine phantoms ( $n=3$ )).

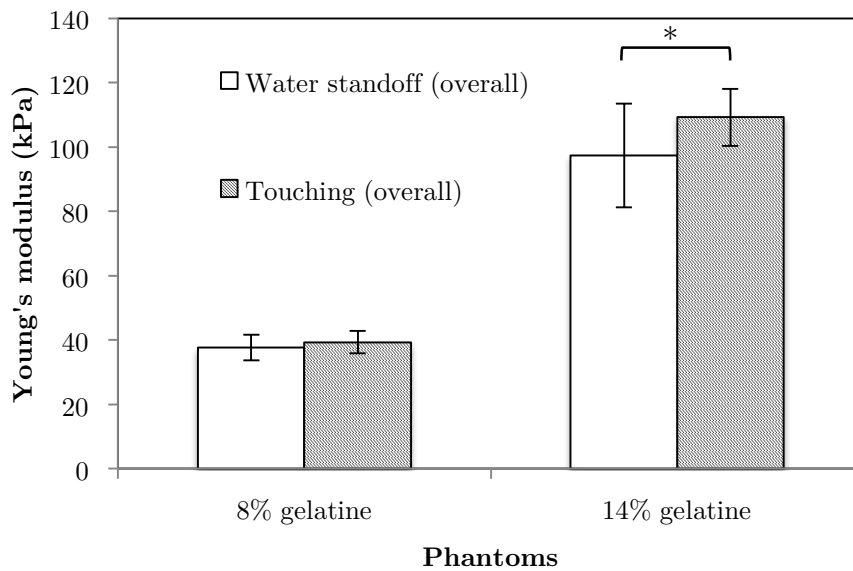


Figure 6.37. The Young's modulus measurements of the whole of 8% and 14% gelatine phantoms with water standoff and probe touching the phantoms. The Young's modulus seemed to decrease significantly in 14% gelatine phantom but not in 8% gelatine phantom, when the water standoff was used. \* denotes that the difference is statistically significant ( $p < 0.01$ , paired t-test, 8% gelatine phantoms ( $n=3$ ), and 14% gelatine phantoms ( $n=3$ )).

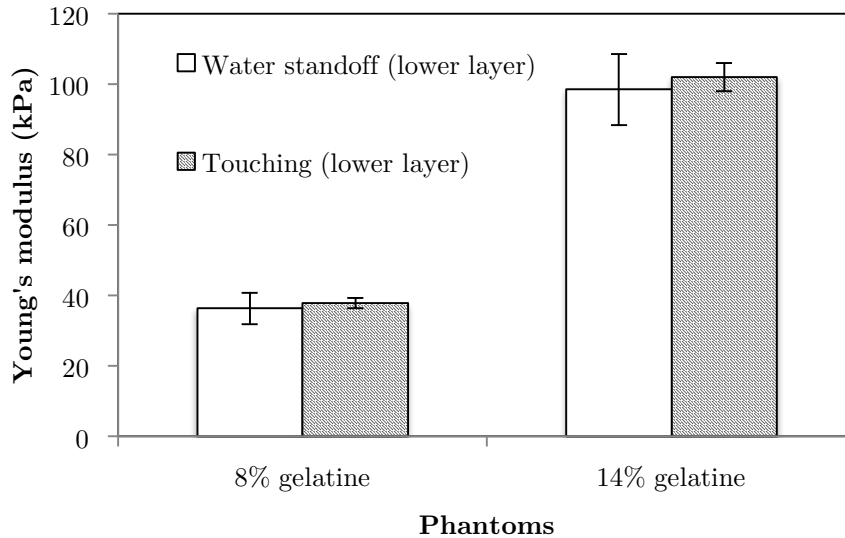


Figure 6.38. The Young's modulus measurements of the remainder (excluding the top 0.5 cm) of 8% and 14% gelatine phantoms with water standoff and probe touching the phantoms. The Young's moduli seemed to decrease slightly in both phantoms when the water standoff was used but it was not statistically significant. This is the result of the experiments performed using 8% gelatine phantoms ( $n=3$ ) and 14% gelatine phantoms ( $n=3$ ).

Figure 6.39 shows the SWE display for porcine brain scanning with the Q-boxes used for Young's modulus measurements. With porcine brain, it was demonstrated that the Young's modulus measurements for the whole brain did not change until the brain was subjected to more than 15 mm displacement at its surface. However, as shown in Figure 6.40, Figure 6.41, Figure 6.42 and Figure 6.43, when the brain SWE was analysed in 3 different regions – upper, middle and lower third – it was noted that the Young's modulus of the upper third portion rose the fastest starting to display an increased Young's modulus at ~10 mm displacement, followed by that of the middle third and lower third, both of which rose at ~15 mm displacement onwards.

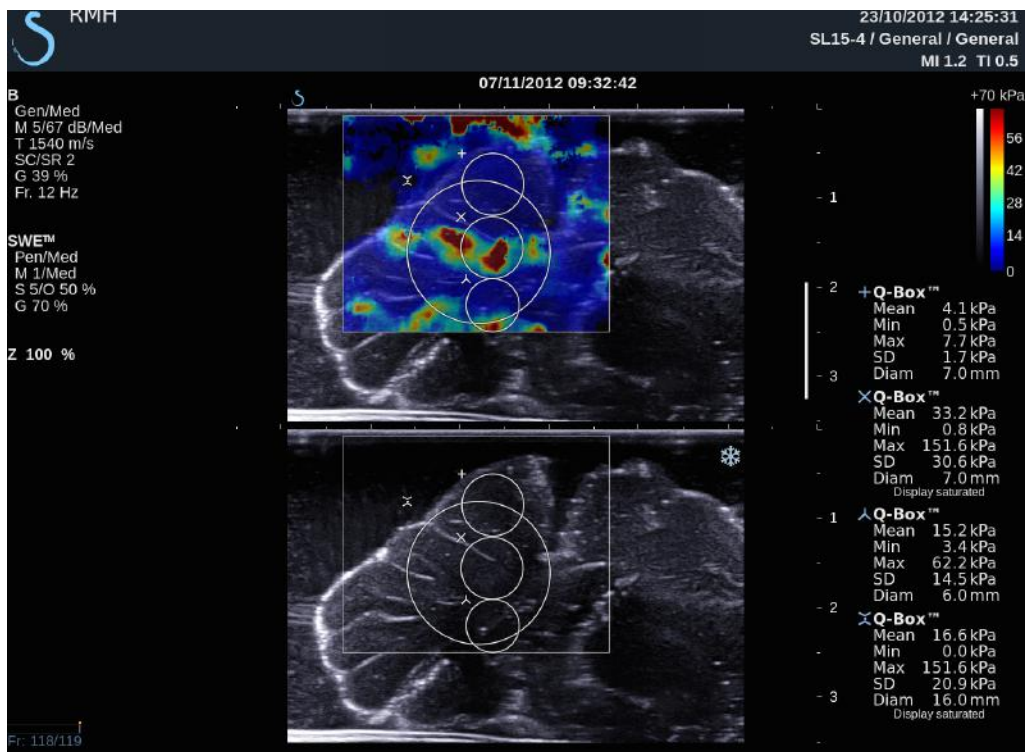


Figure 6.39. SWE display for porcine brain scanning with Q-boxes for upper, middle and lower thirds and overall measurements.

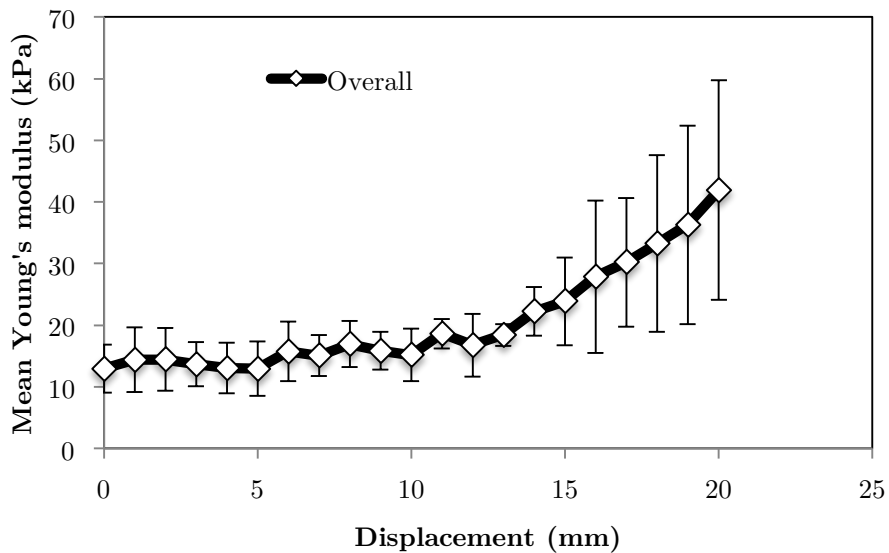


Figure 6.40. The graph of mean and plus and minus one standard deviation of overall Young's modulus measured by SWE for the porcine brains (n=3). There is a slow nonlinear increase in the Young's modulus measurements that appears to begin from about 5 mm displacement but becomes significant for displacements greater than about 15 mm.

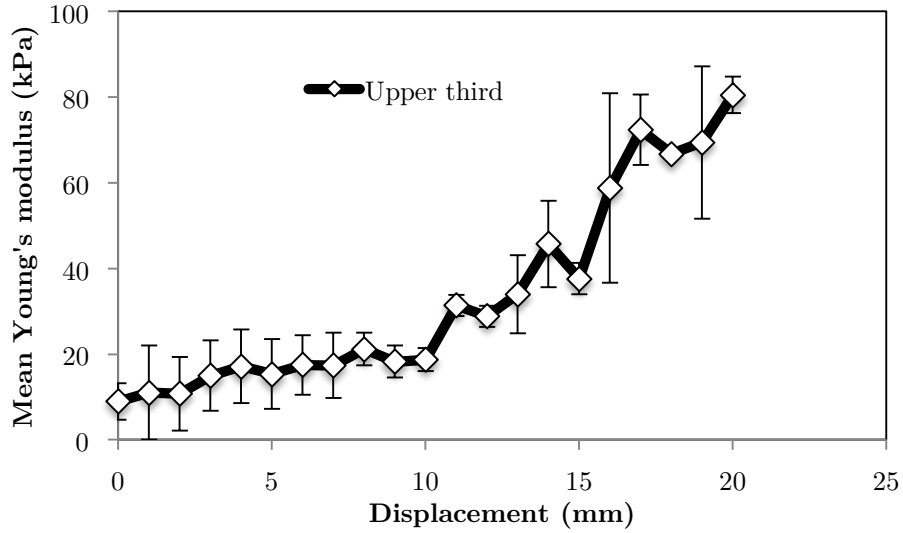


Figure 6.41. The graph of mean and plus and minus one standard deviation of Young's modulus measured by SWE for the upper third portion of the porcine brain with different compression ( $n=3$ ). This shows an upward trend with a significantly increasing displacement from 10 mm onwards.

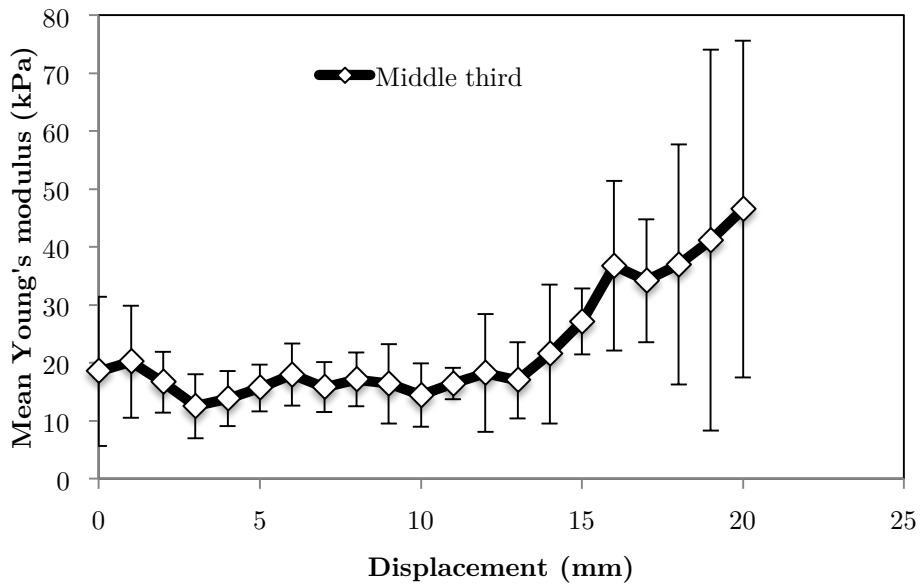


Figure 6.42. The graph of mean and plus and minus one standard deviation of Young's modulus measurement for middle third portion of the porcine brains with different compression. There was no increase in the Young's modulus until ~15 mm displacement, from which point it starts to rise.

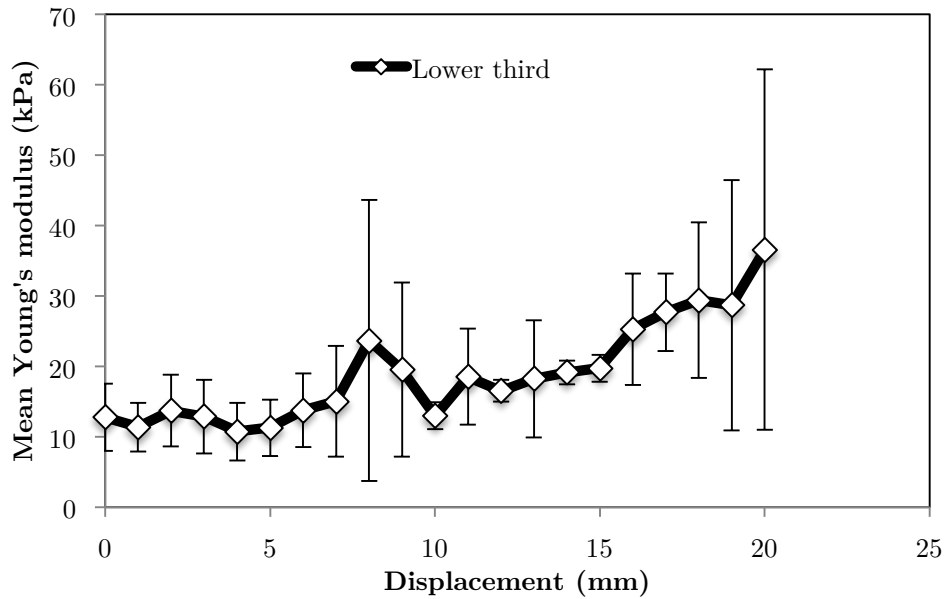


Figure 6.43. The graph of mean and plus and minus one standard deviation of Young's modulus measured by SWE for the lower third portion of the porcine brains with different compression. There seems to be a slower rise in Young's modulus from  $\sim 15$  mm displacement onwards compared with that in the middle third portion.

#### 6.4.7 Varying the tumour-brain interface conditions

The maximum ROI for SWE on the Aixplorer® is about 3 cm laterally and 2.5 cm axially, which was insufficient to study the SWE image properties in the background gel containing a 2 cm diameter inclusion (see Figure 6.44). For this experiment therefore, images with multiple ROIs were captured and subsequently stitched together with ImageJ (Schneider et al., 2012), which is a Java-based image processing programme freely available online.

Figure 6.45 illustrates the stitched image of SWE for an adhered stiff inclusion in a soft background. Notice the apparently stiff bands that follow the borders of the acoustic shadow seen inferior to the inclusion on the B-scan, shown by the white arrows in the figure, and the low Young's modulus, that is very dark blue colour, in acoustic shadow. When the

transducer was tilted to view the inclusion from a different angle, the region of low Young's modulus along with the stiff bands rotated to follow the acoustic shadow, and hence the same angle, always showing the same appearance as that in Figure 6.44. This behaviour implies that these SWE image characteristics are artefacts rather than being inherent features of the phantom. Figure 6.46 is the stitched SWE image for a stiff mobile inclusion in a soft background. The same stiff band artefacts are visible, possibly with greater emphasis than for the adhered case. However, there is also a soft 'bracket' that can be seen on both left and right sides of the inclusion, which was not visible in the image. In Figure 6.47 a horizontal profile of the SWE Young's modulus image (obtained using MATLAB® (MATLAB, 2010)) through the centre of the inclusion shows a noticeable dip in the values on either side of the inclusion. The dip was not present on the equivalent profile plot for the stiff adhered inclusion (see Figure 6.48). Strain was applied to both the stiff adhered and mobile inclusion phantoms to assess the effect of strain on the appearance of SWE for these cases. There was no noticeable difference between the results without (Figure 6.45 to Figure 6.48) and with 10% strain (Figure 6.49 to Figure 6.52), for either the image appearances or the profile plots.

A soft inclusion in a stiff background displayed similar characteristics to those described above; there was no noticeable 'bracket' of lower Young's modulus, or dip in the profile, on either side of the inclusion for the adhered case (Figure 6.53 and Figure 6.55) but these features were present (Figure 6.54 and Figure 6.56) for a soft mobile inclusion. As with the stiff inclusion in a soft background, the application of strain did not affect the SWE or profile appearances of either the adhered or the mobile soft inclusion (see Figure 6.57 to Figure 6.60).

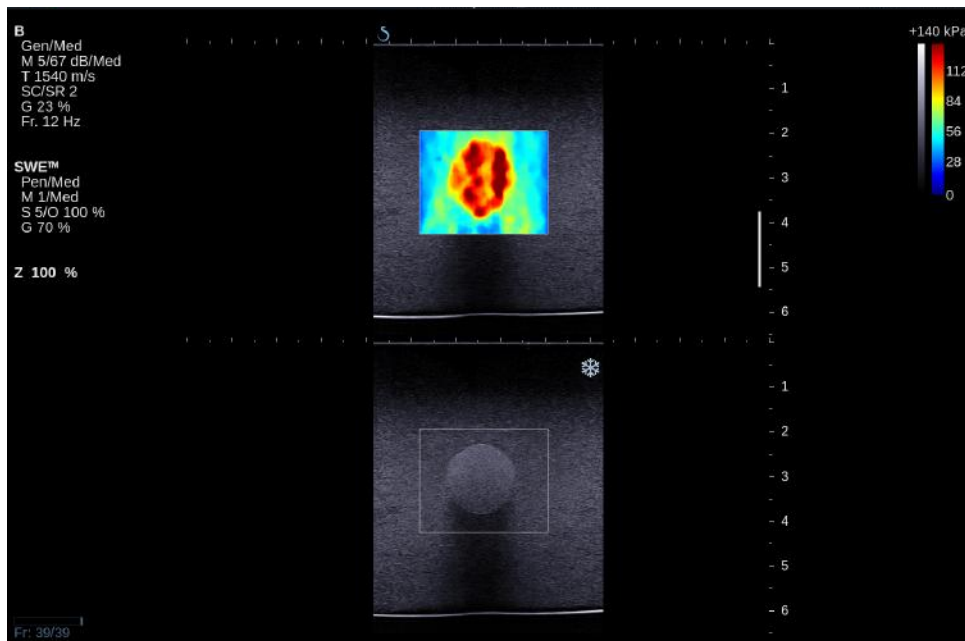


Figure 6.44. SWE for a stiff adhered inclusion. Note the small size of the SWE ROI, encompassing little background gel around the inclusion.

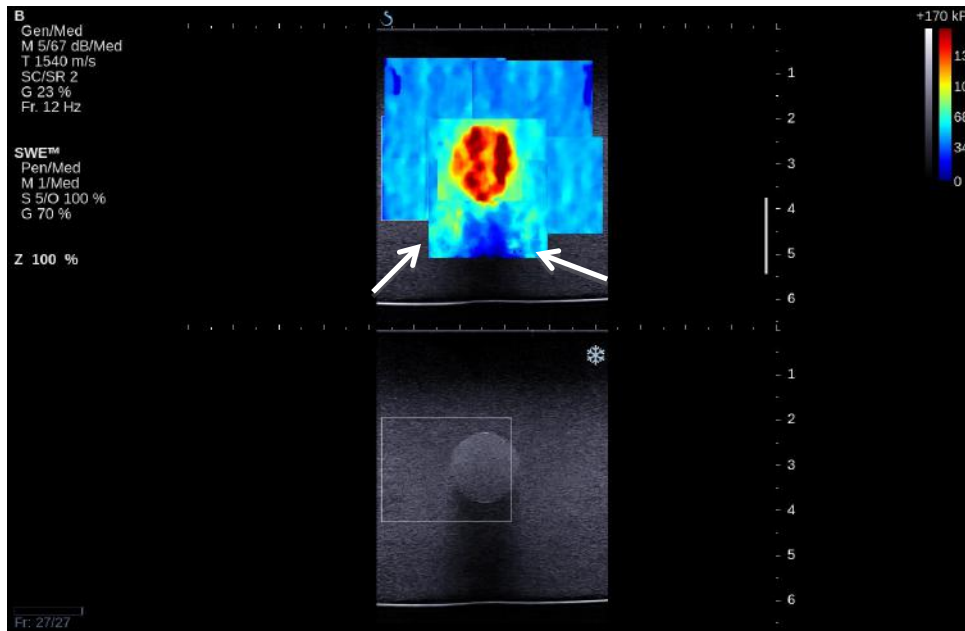


Figure 6.45. Stitched image of SWE for stiff adhered inclusion without any strain. Note the bands in the SWE image, of apparently high Young's modulus, that follow the border of speckle-devoid shadow beneath the inclusion in the B-scan. The acoustic shadow region also gives rise to low Young's modulus values.

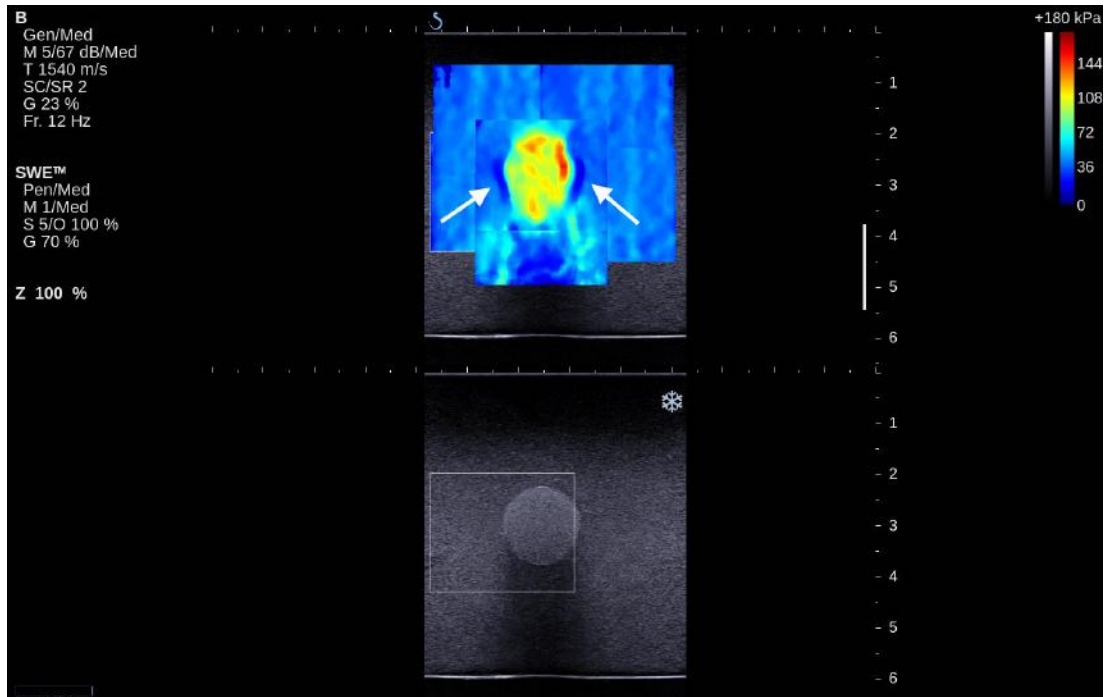


Figure 6.46. Stitched image of SWE for a stiff mobile inclusion. Notice the artefact bands are still present for the B-mode shadow region. However, a new feature is now present, namely the “brackets” of low Young’s modulus value on the left and right boundary of the inclusion (white arrows).

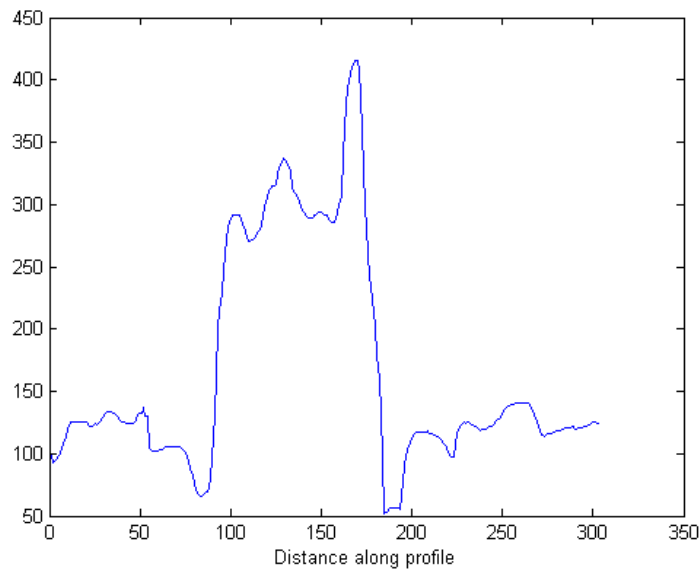


Figure 6.47. Profile plot through the centre of a SWE image of the stiff mobile inclusion. The y-axis is in arbitrary units. Notice there was a dip in the pixel values on either side of the inclusion.

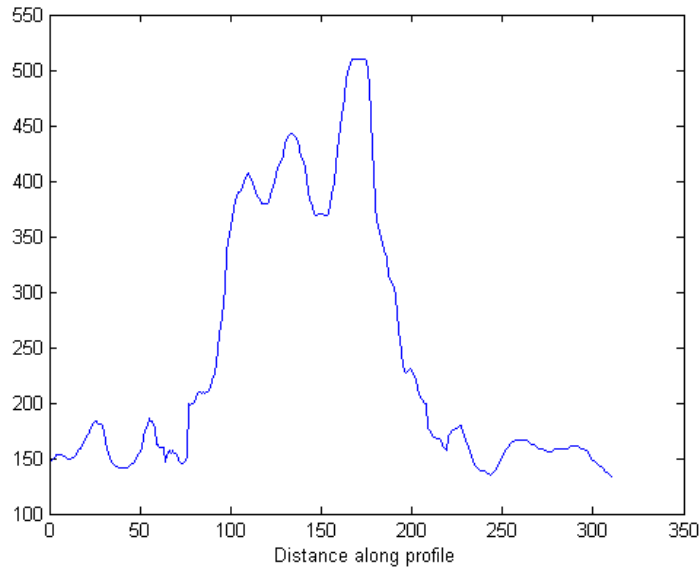


Figure 6.48. Profile plot for the stiff adhered inclusion. Notice the absence of a dip in the pixel values on either side of the inclusion.

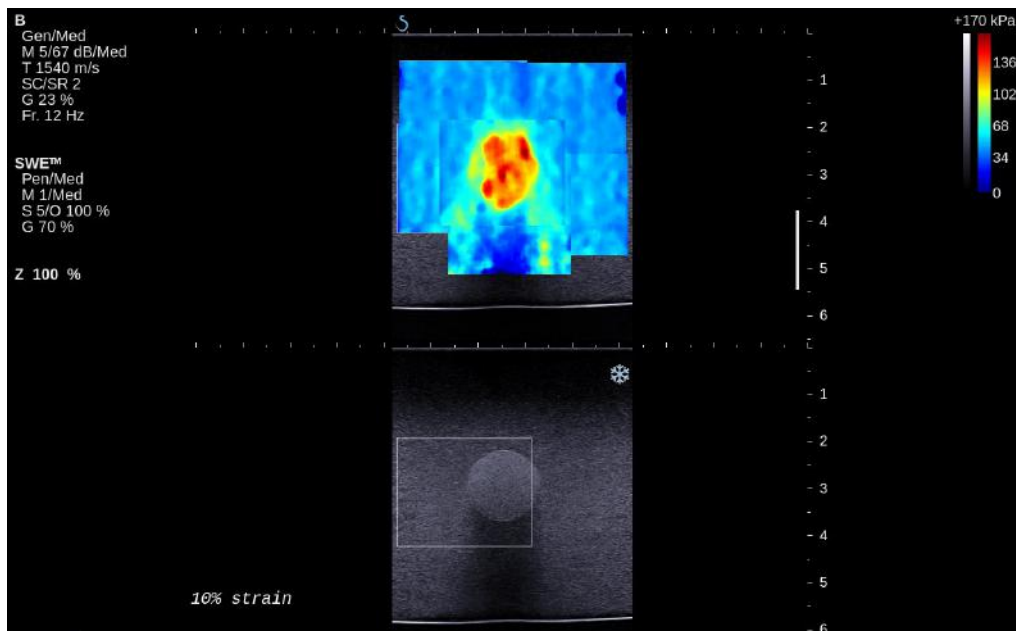


Figure 6.49. Stitched image of SWE for stiff adhered inclusion with 10% strain applied.

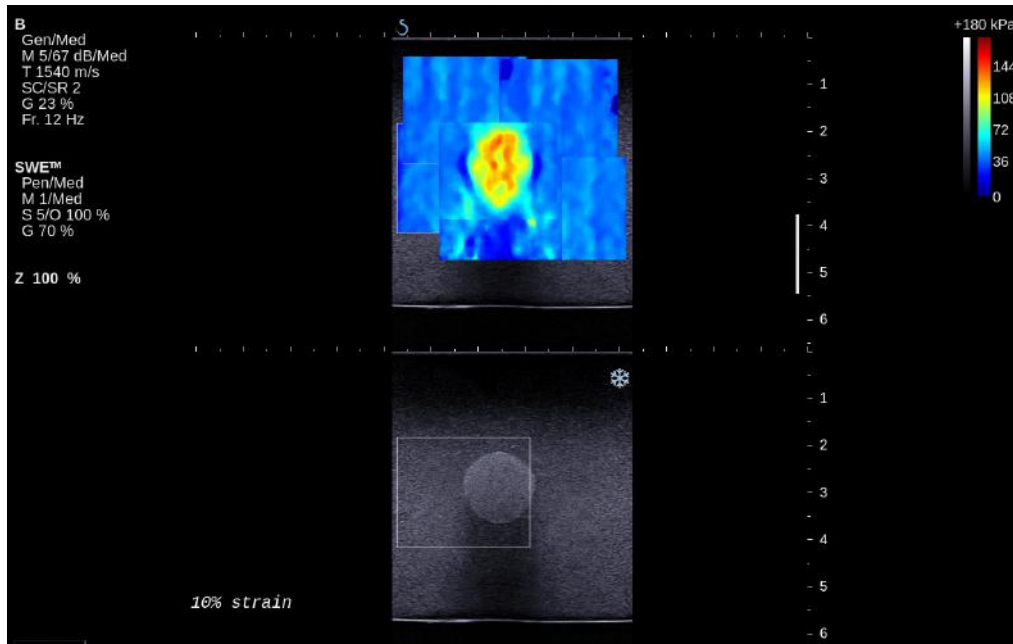


Figure 6.50. Stitched image of SWE for stiff mobile inclusion with 10% strain applied.

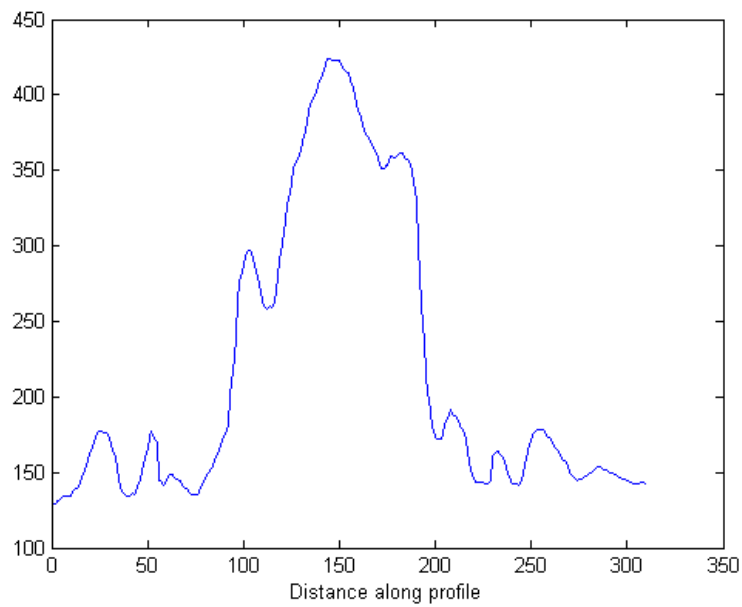


Figure 6.51. Profile plot for stiff adhered inclusion with 10% applied strain.

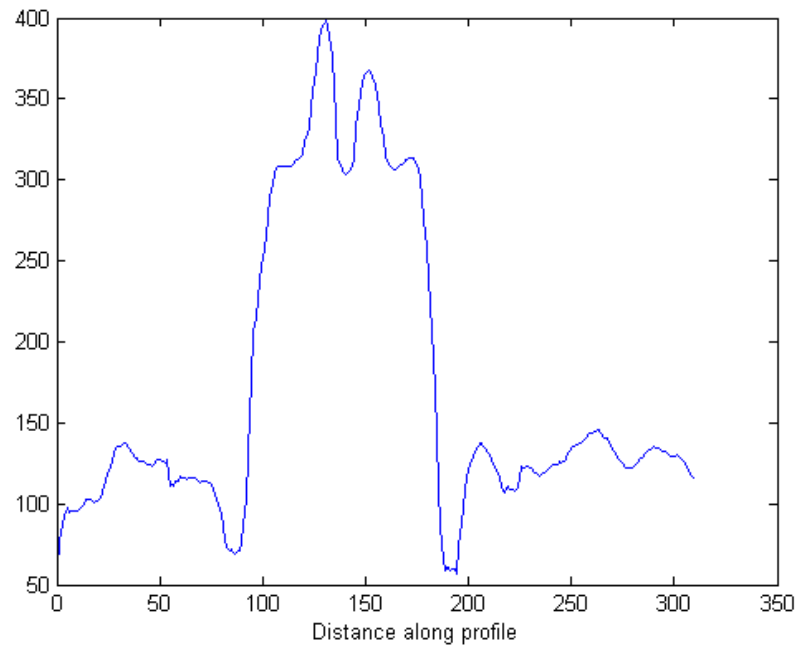


Figure 6.52. Profile plot for stiff mobile inclusion with 10% applied strain.

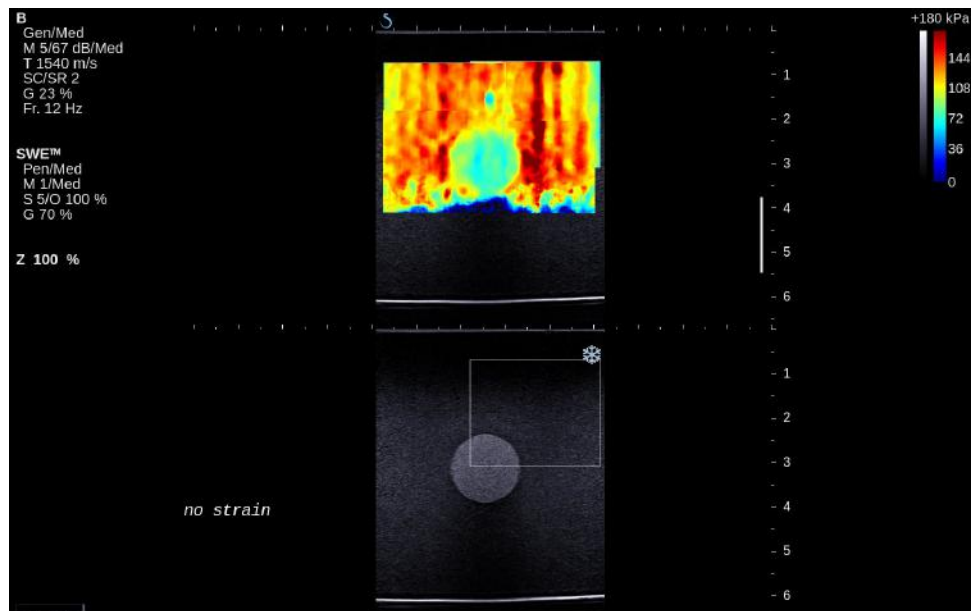


Figure 6.53. Stitched image of SWE for soft adhered inclusion.

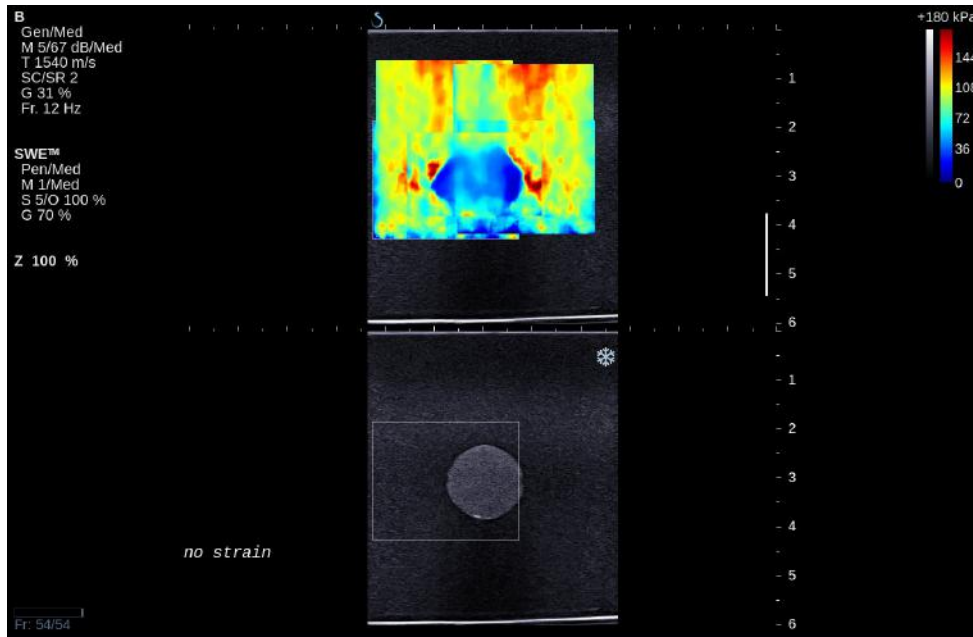


Figure 6.54. Stitched image of SWE for soft mobile inclusion. Notice there is a soft 'bracket' on either side of the inclusion.

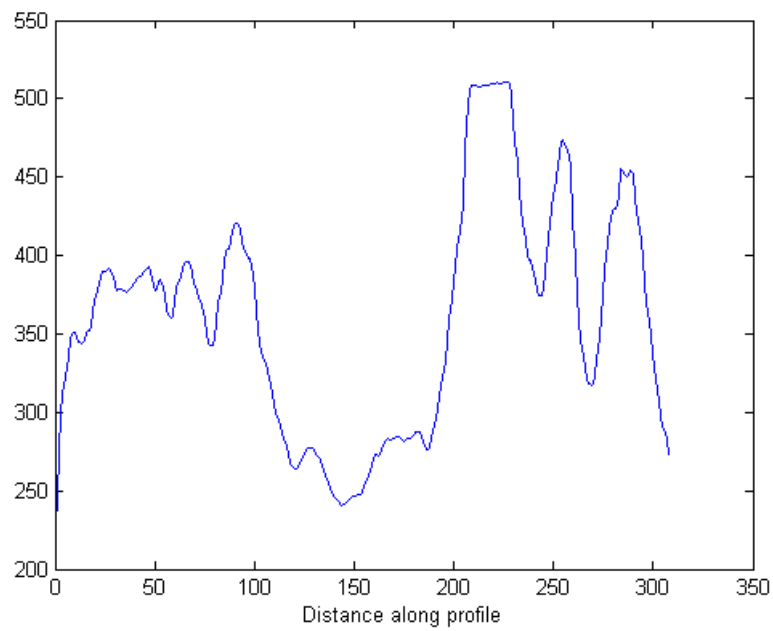


Figure 6.55. Profile plot for soft adhered inclusion.

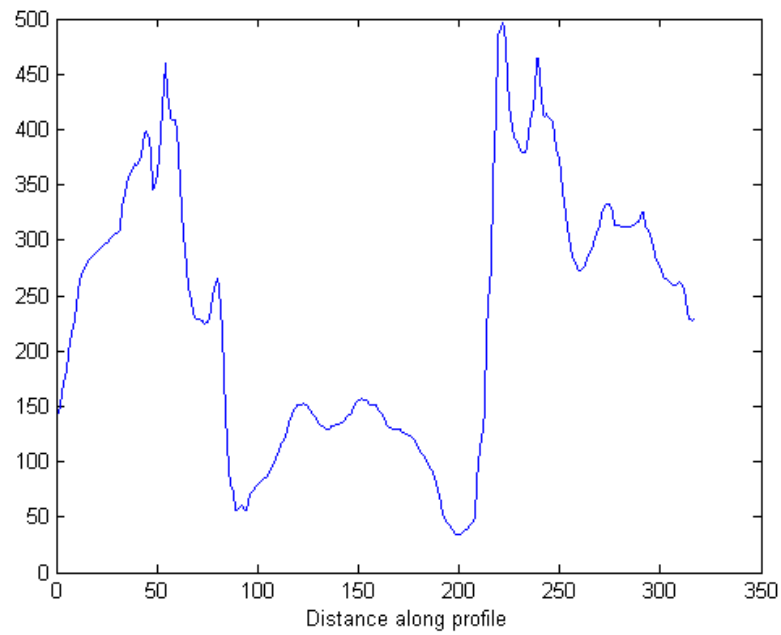


Figure 6.56. Profile plot for soft mobile inclusion.

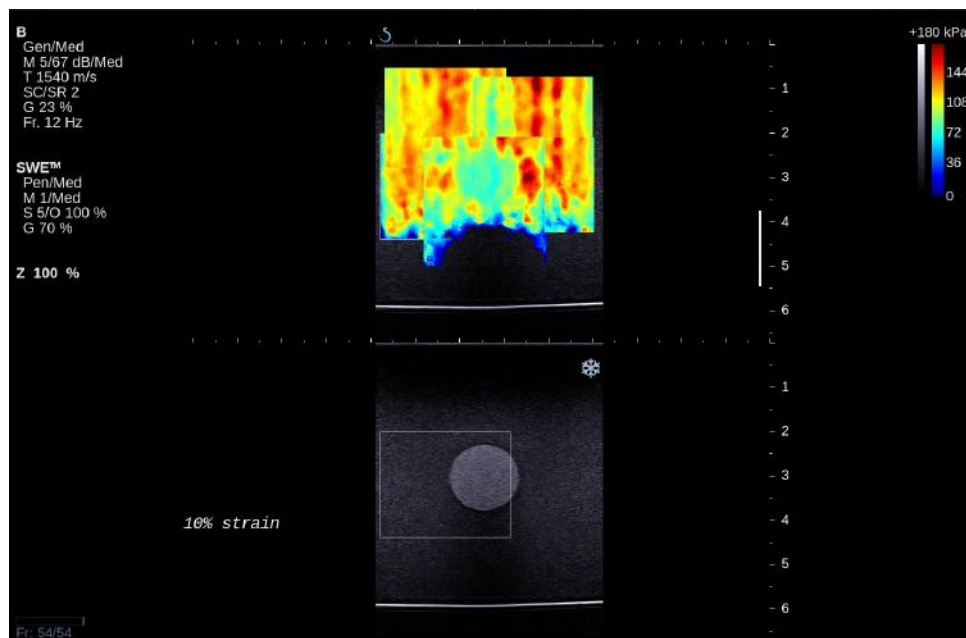


Figure 6.57. Stitched image of SWE for soft adhered inclusion with 10% applied strain.

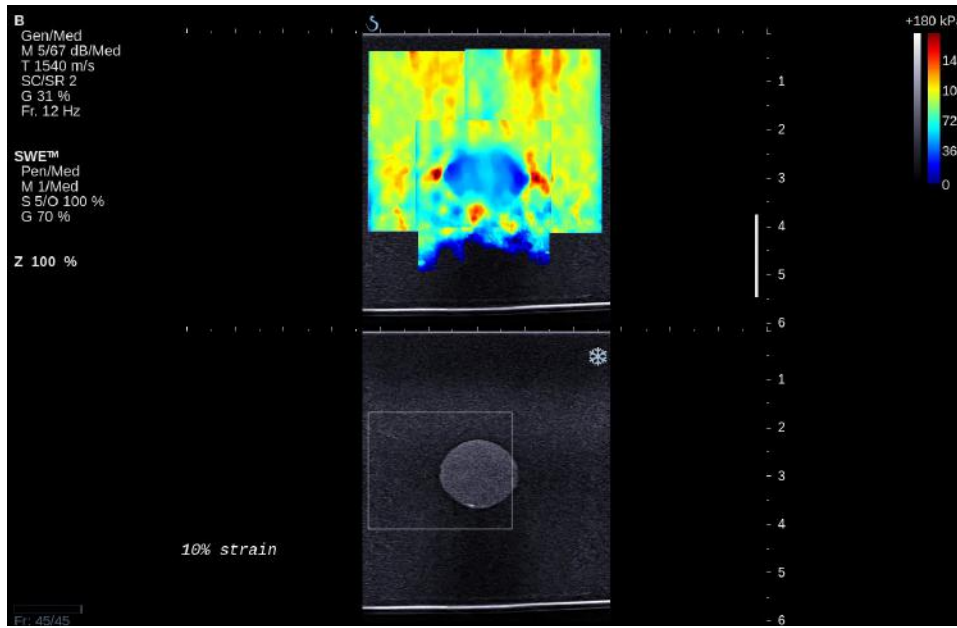


Figure 6.58. Stitched image of SWE for soft mobile inclusion with 10% applied strain. Note the soft 'bracket' on either side of the inclusion.

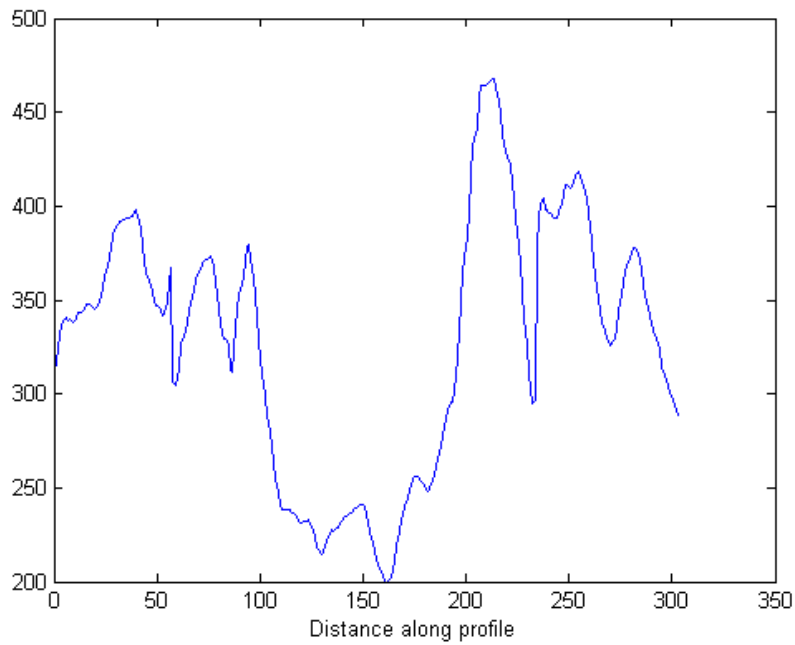


Figure 6.59. Profile plot for soft adhered inclusion with 10% applied strain.

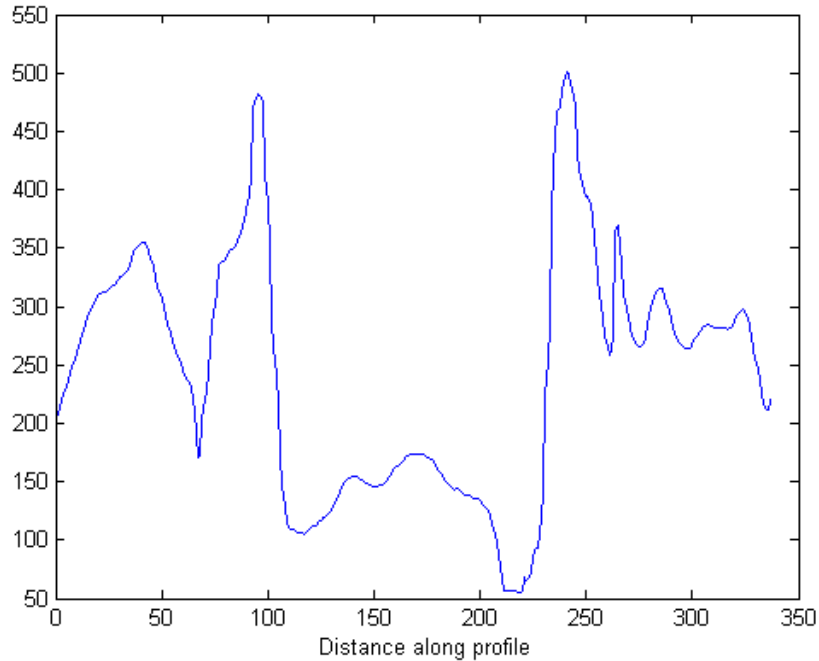


Figure 6.60. Profile plot for soft mobile inclusion with 10% applied strain. Note the appearance of pixel value dip on either side of the inclusion.

#### 6.4.8 Resolution of SWE

In phantoms with a soft background, SWE was able to detect cylindrical stiff inclusions down to the smallest, which was 1 mm in diameter, as shown in Figure 6.61. Notice the Young's modulus measurement was lower in the 1-mm inclusion compared to the 2-mm. Young's modulus measured by SWE as a function of inclusion size is shown in Figure 6.62. Notice there is a small trend of increasing Young's modulus with increasing size, regardless of the SWE mode used. When plotting Young's modulus contrast against different inclusion sizes, there is a more obvious upward trend (see Figure 6.63). Young's modulus contrast is defined as:

$$\text{Young's modulus contrast} = \frac{E_i - E_b}{E_b}, \quad (6.2)$$

where  $E_i$  is the Young's modulus of the inclusion and  $E_b$  is that of the background.

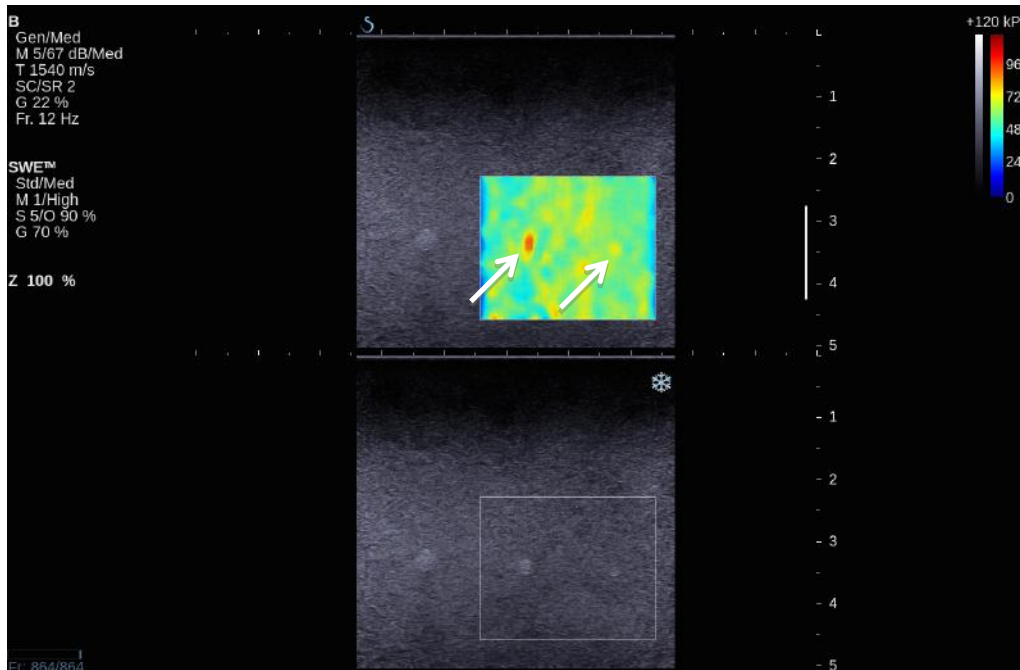


Figure 6.61. SWE for small stiff inclusions in a soft background showing the appearance of 2-mm and 1-mm inclusions (arrows).

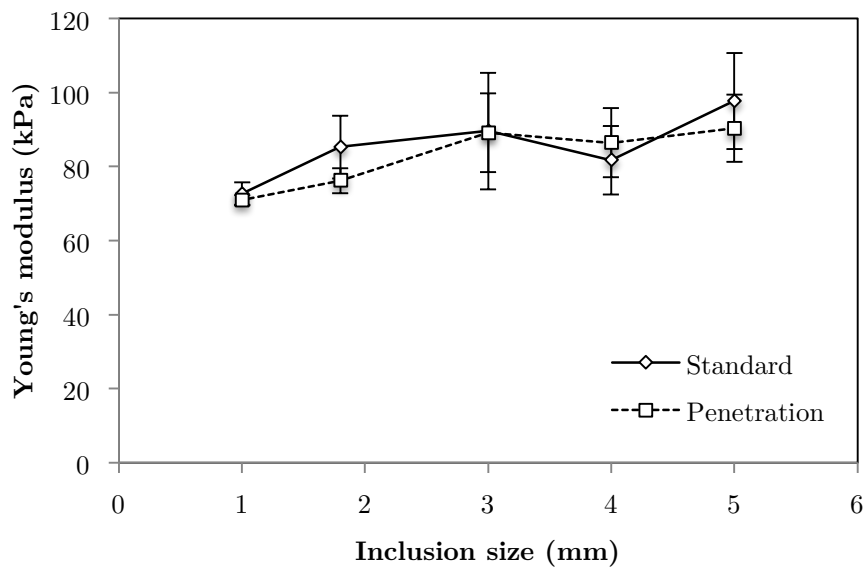


Figure 6.62. Mean and plus and minus one standard deviation of Young's modulus measured by SWE as a function of stiff inclusion size for standard mode and penetration mode. The measurements were made with 6 phantoms (3 phantoms) with 2 different modes.

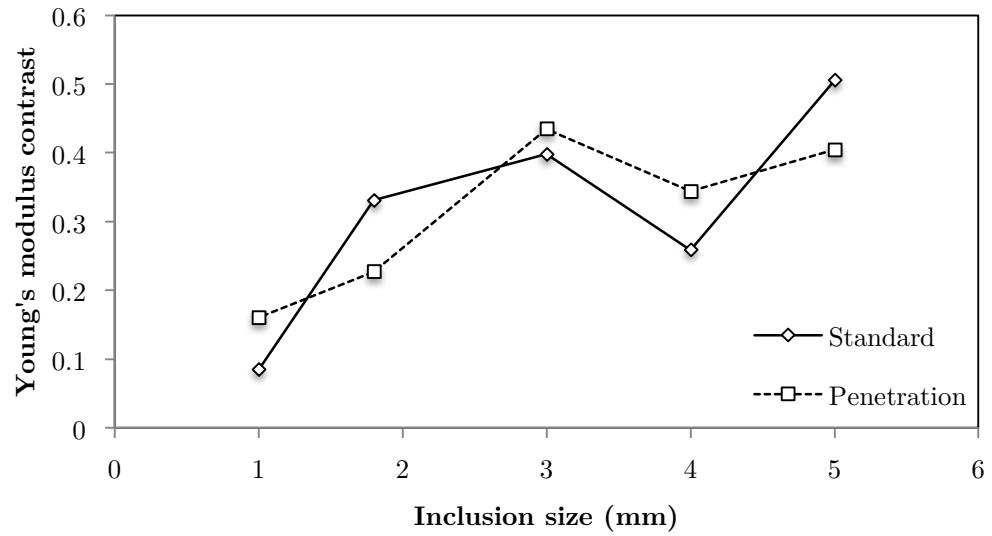


Figure 6.63. Young's modulus contrast for stiff inclusions in soft background for standard and penetration modes.

In phantoms with a stiff background, soft cylindrical inclusions smaller than 3 mm were not detectable by SWE. However, there was little variation in the measured Young's modulus with inclusion size, for both standard and penetration modes (see Figure 6.63). Young's modulus contrast, however, decreased with inclusion size, for both penetration and standard modes, more marked in the former (see Figure 6.64).

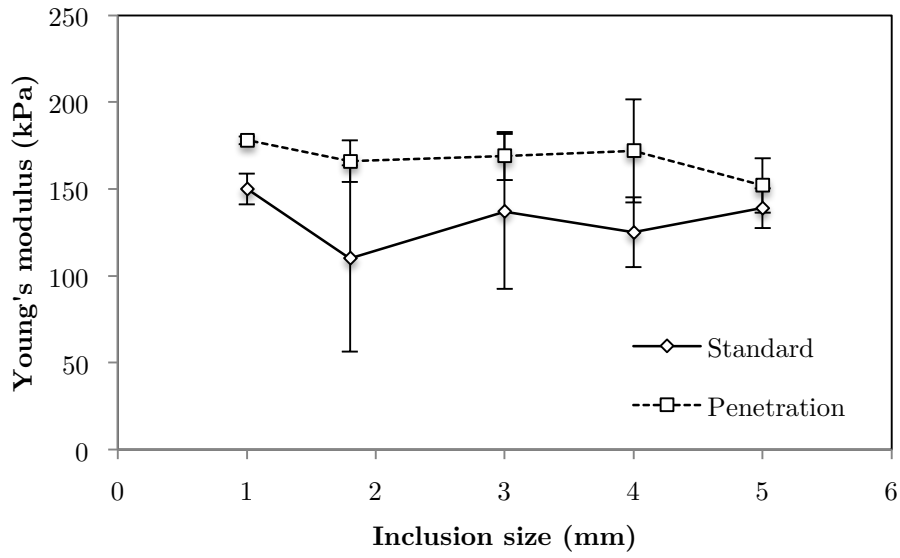


Figure 6.64. Mean and plus and minus one standard deviation of Young's modulus measurements for soft inclusions using both standard and penetration modes. The measurements were made with 6 phantoms (3 phantoms) with 2 different modes.

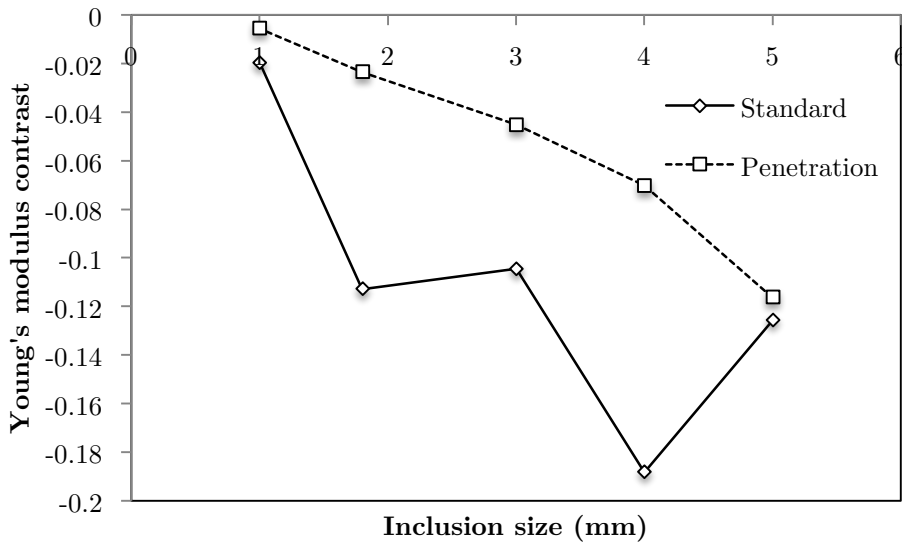


Figure 6.65. Young's modulus contrast for soft inclusions in stiff background for standard and penetration modes.

### 6.4.9 Other factors affecting SWE measurements

#### 6.4.9.1 Inclusion sizes

Section 6.4.8 demonstrated that for small inclusions, ranging from 1 mm to 5 mm in diameter, the Young's modulus measurements and contrast increased with size for stiff inclusions. Conversely, the Young's modulus measurements and contrast decreased with size for soft inclusions. This section extends the experiment to include the large soft and stiff inclusions, which are 1 cm, 1.5 cm and 2 cm in diameter.

Young's modulus measured by SWE as a function of inclusion size for stiff inclusions in a soft background is shown in Figure 6.66. Notice there is a small trend of increasing Young's modulus with increasing size, regardless of the SWE mode used. When plotting Young's modulus contrast against different inclusion sizes, there is a more obvious upward trend (see Figure 6.67).

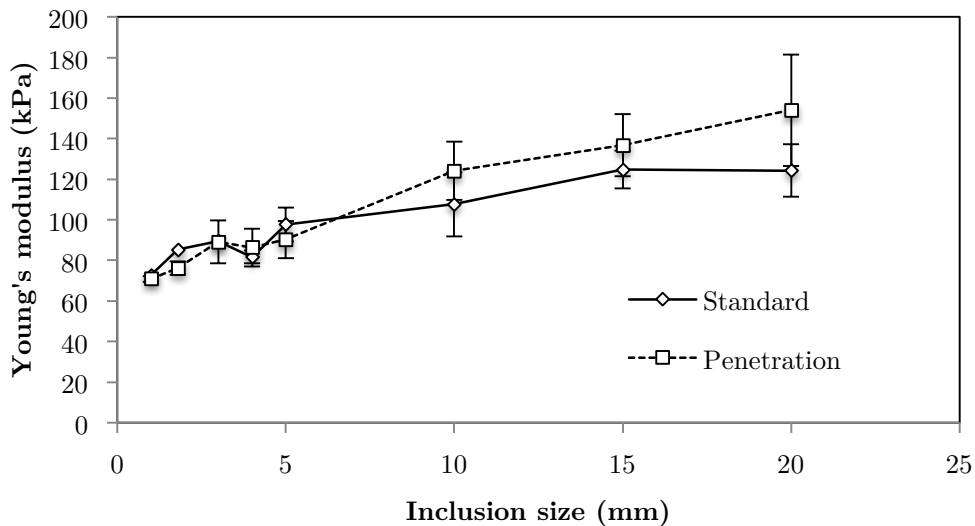


Figure 6.66. Mean and plus and minus one standard deviation of Young's modulus measured by SWE as a function of stiff inclusion size for standard mode and penetration mode. The measurements were made with 6 phantoms (3 phantoms with small inclusions and 3 phantoms with large inclusions) with 2 different modes.

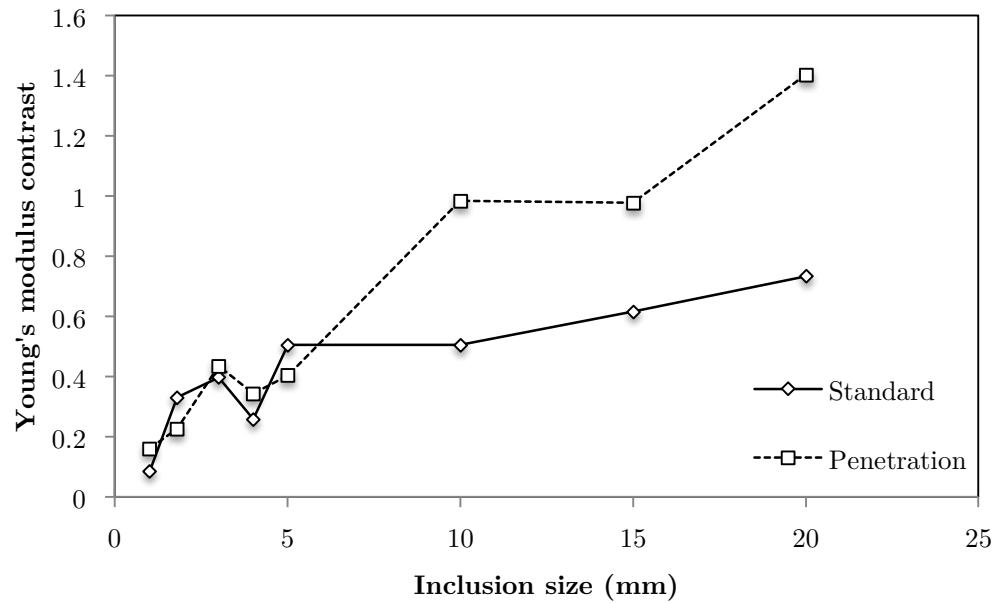


Figure 6.67. Young's modulus contrast for stiff inclusions in soft background for standard and penetration modes.

Young's modulus measured by SWE as a function of inclusion size for soft inclusions in a stiff background is shown in Figure 6.68. Notice there is a small trend of decreasing Young's modulus with increasing size, regardless of the SWE mode used. When plotting Young's modulus contrast against different inclusion sizes, there is a more obvious downward trend (see Figure 6.69).

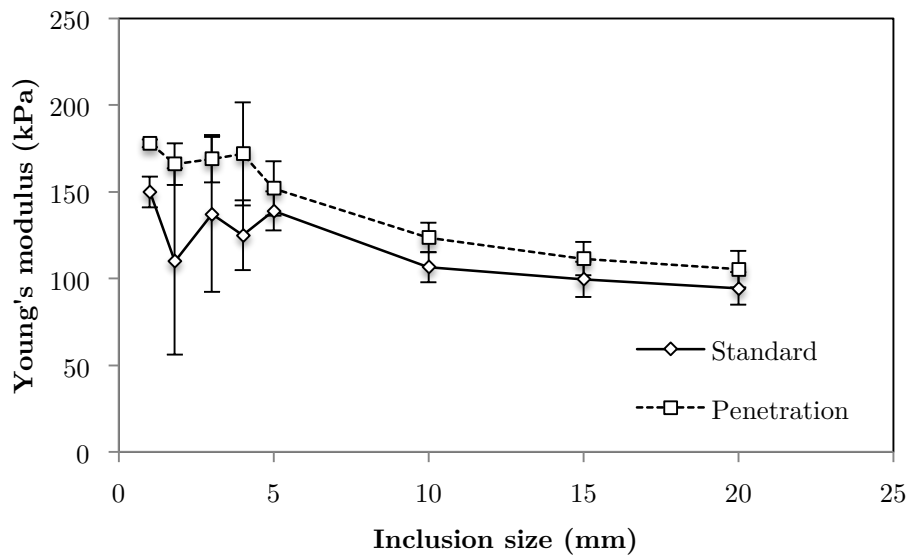


Figure 6.68. Mean and plus and minus one standard deviation of Young's modulus measurements for soft inclusions using both standard and penetration modes. The measurements were made with 6 phantoms (3 phantoms with small inclusions and 3 phantoms with large inclusions) with 2 different modes.

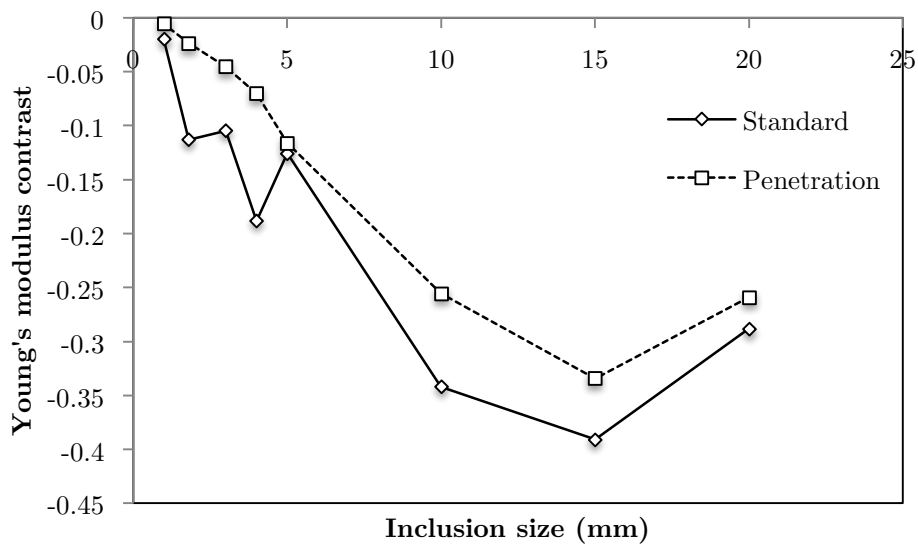


Figure 6.69. Young's modulus contrast for soft inclusions in stiff background for standard and penetration modes..

For 3D phantoms with stiff spherical inclusions, the Young's modulus measured by SWE increased with inclusion size (Figure 6.70). Contrast transfer efficiency (CTE) is defined by the ratio of the Young's modulus contrast displayed by the elastographic system, to that of true Young's modulus contrast (Ponnekanti et al., 1995), and is expressed as:

$$\text{CTE} = \frac{C_{measured}}{C_{true}}, \quad (6.3)$$

where  $C_{measured}$  and  $C_{true}$  are measured and true Young's modulus contrasts, respectively. CTE is normally expressed in decibel (dB):

$$\text{CTE(dB)} = \log_{10} |C_{measured}| - \log_{10} |C_{true}| \quad (6.4)$$

Figure 6.71 shows CTE as a function of inclusion diameter for stiff spherical inclusions, demonstrating that the CTE reaches 0 dB when the inclusion size is 6 mm and 7 mm, for penetration and standard modes, respectively.

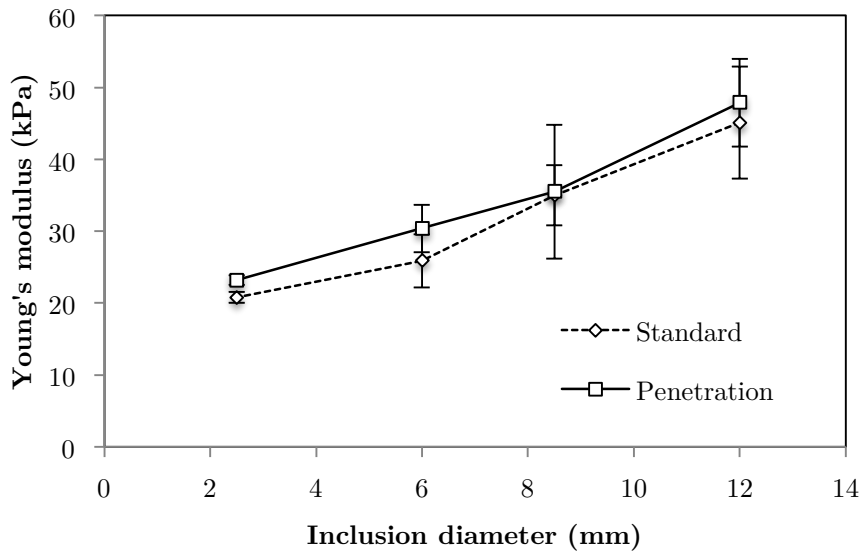


Figure 6.70. Mean and plus and minus one standard deviation of Young's modulus measurements for 3D phantoms with stiff inclusions in a soft background. The measurements were made with 3 different phantoms ( $n=3$ ).

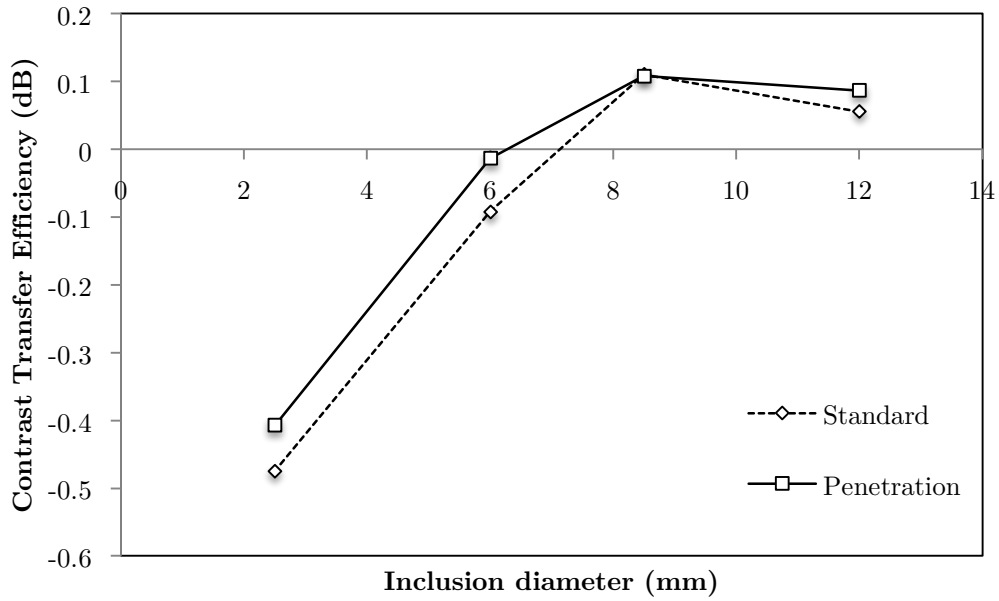


Figure 6.71. The graph of contrast transfer efficiency for stiff spherical (3D) inclusions in a soft background.

For soft spherical inclusions, the measured Young's modulus decreased with size (Figure 6.72). A graph of CTE for soft 3D inclusions is shown in Figure 6.73, where there was an upward trend toward 0 dB. However, even for an inclusion size of 12 mm, the CTE is only  $-0.23$  dB and  $-0.44$  dB for standard and penetration modes, respectively.

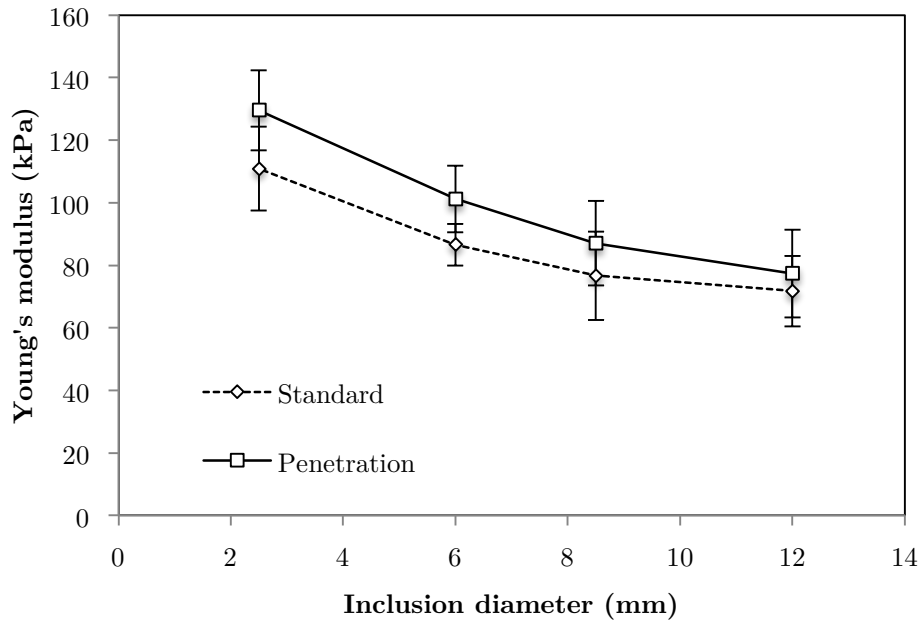


Figure 6.72. Mean and plus and minus one standard deviation of Young's modulus measurements for 3D phantoms with soft spherical inclusions in a stiff background. The measurements were made with 3 different phantoms ( $n=3$ ).

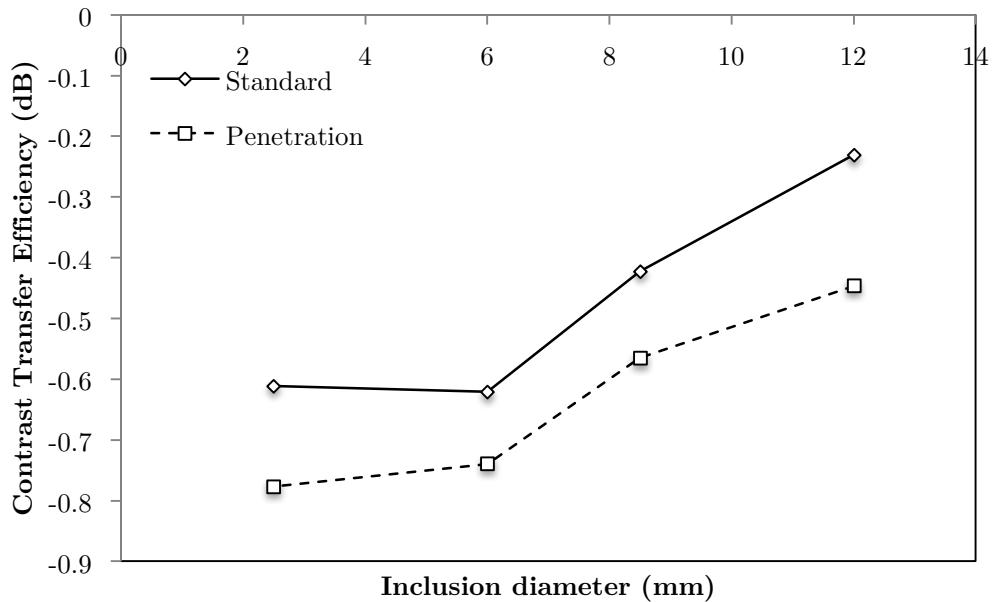


Figure 6.73. The graph of contrast transfer efficiency for soft spherical (3D) inclusions in a stiff background.

### 6.4.9.2 Inclusions at different depths

Figure 6.74 shows that the measured Young's modulus of 0.5-cm stiff cylindrical inclusions did not vary significantly with depth. This was confirmed with the phantom flipped 90° so that the bottom inclusion became the top inclusion, and vice versa. Figure 6.75 shows that the Young's modulus measured by SWE for 0.5-cm soft inclusions seemed to decrease with depth, even when the phantom was flipped 90°.

Figure 6.76 showed that the Young's modulus measurements seemed to increase slightly with depth but when the phantom was flipped 90°, the trend was reversed. This means that the inclusions actually had different Young's modulus. Figure 6.77 shows that there was a slight increase in the Young's modulus measurements with depth for soft 1-cm inclusions, but when the phantom was flipped 90°, the trend was reversed.

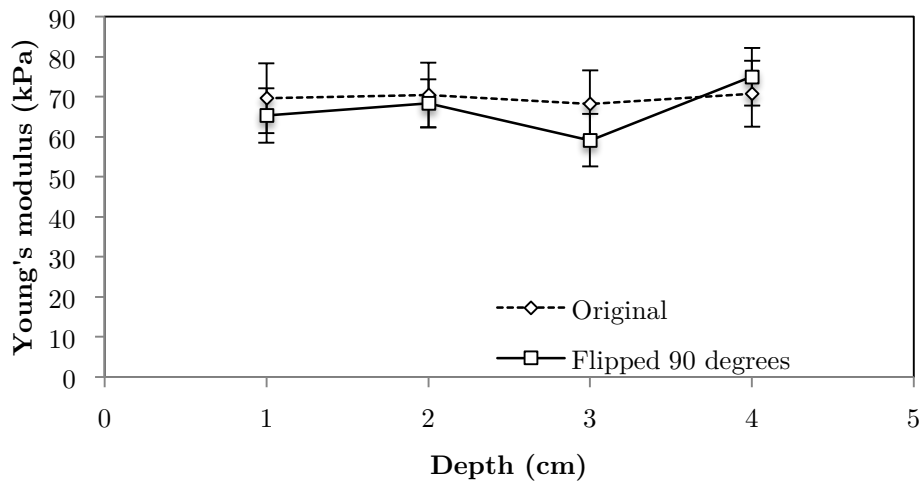


Figure 6.74. Mean and plus and minus one standard deviation of Young's modulus measured by SWE for 0.5-cm stiff inclusions arranged diagonally at different depths ( $n=3$ ). The measurements when the phantom is flipped 90° are also plotted ( $n=3$ ). These measurements were performed in 3 different phantoms for each experimental setup.

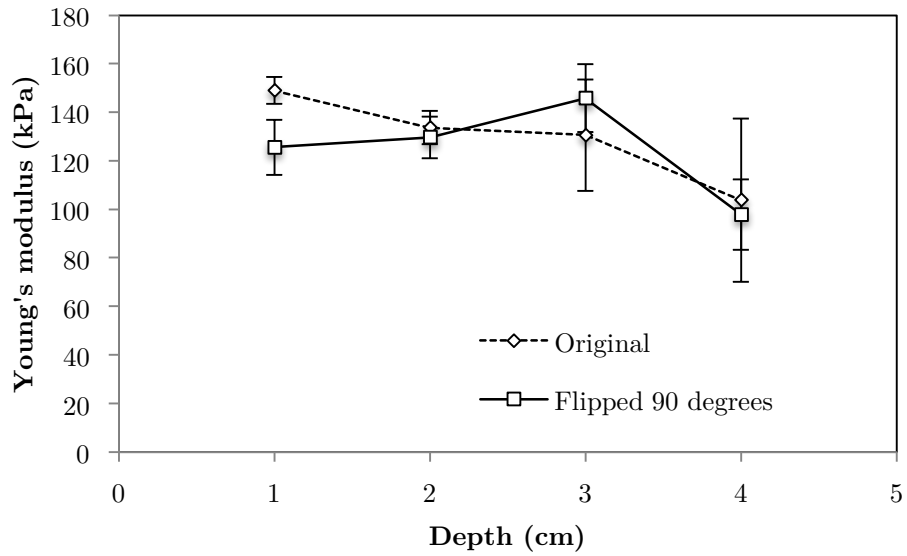


Figure 6.75. Mean and plus and minus one standard deviation of Young's modulus measurements for 0.5-mm soft inclusions arranged diagonally in different depths ( $n=3$ ). Measurements taken with the phantom flipped 90° were also plotted ( $n=3$ ). These measurements were performed in 3 different phantoms for each experimental setup.

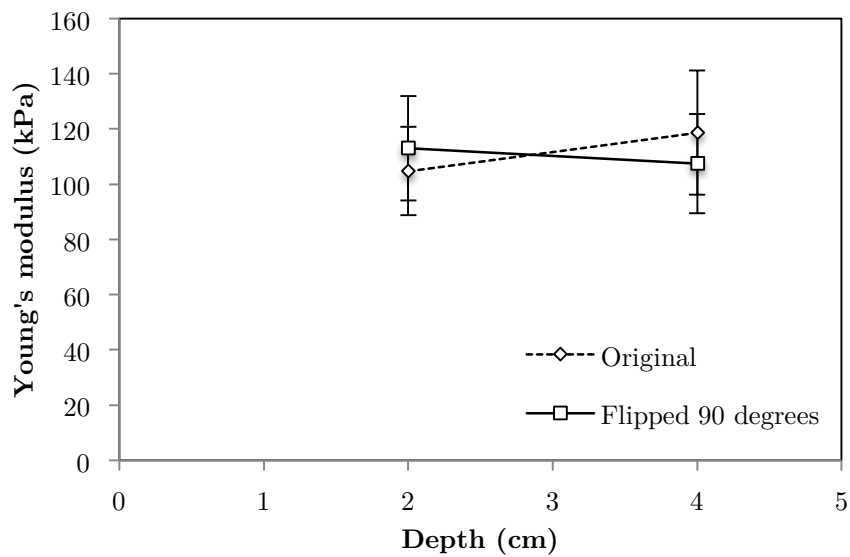


Figure 6.76. Mean and plus and minus one standard deviation of Young's modulus measurements for 1-cm stiff inclusions arranged diagonally in different depths ( $n=3$ ). Measurements taken with the phantom flipped 90° were also plotted ( $n=3$ ). These measurements were performed in 3 different phantoms for each experimental setup.

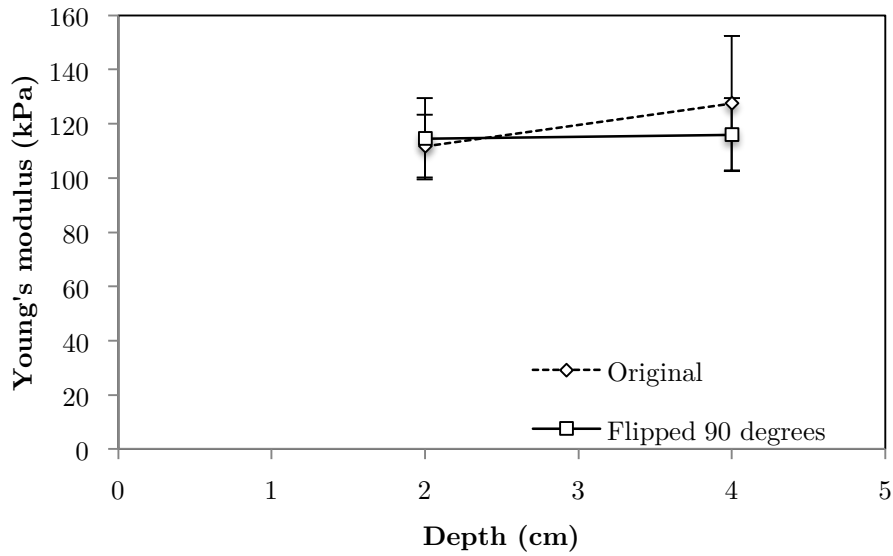


Figure 6.77. Mean and plus and minus one standard deviation of Young's modulus measurements for 1-cm soft inclusions arranged diagonally in different depths ( $n=3$ ). Measurements taken with the phantom flipped 90° were also plotted ( $n=3$ ). These measurements were performed in 3 different phantoms for each experimental setup.

#### 6.4.9.3 Anisotropy of tissue

Figure 6.78 and Figure 6.79 are SWE acquisitions performed with the transducer held perpendicular and parallel to the lengths of the porcine spinal cords. The Young's modulus values, plotted in Figure 6.80, are seen to be higher when the transducer is parallel to the length of the spinal cord than when it is perpendicular. However, using paired t-test, the difference is not statistically significant ( $p = 0.202$ ).

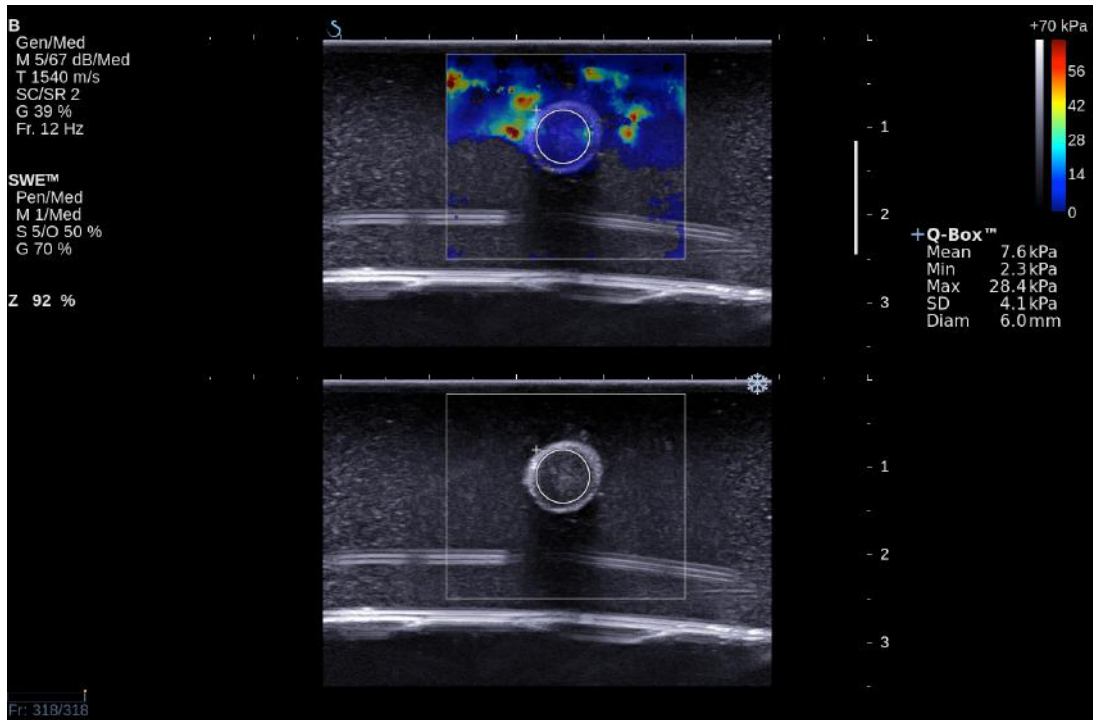


Figure 6.78. SWE acquired with transducer held perpendicular to the spinal cord.

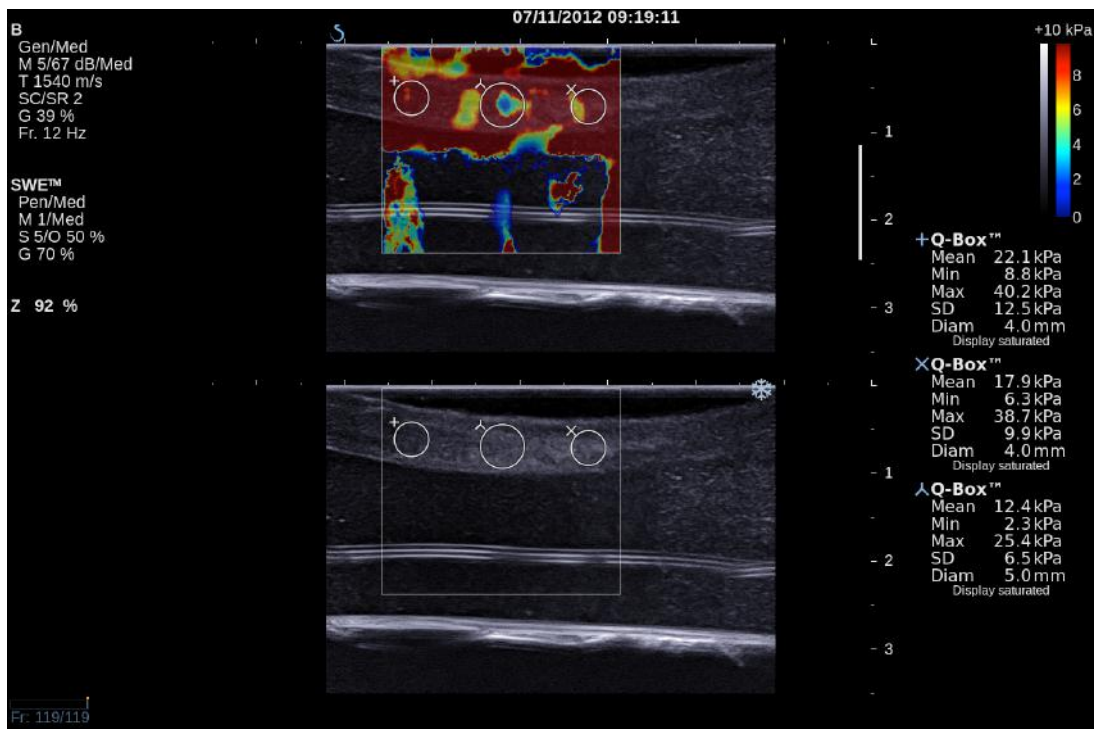


Figure 6.79. SWE acquired with transducer held parallel to the length of the spinal cord.

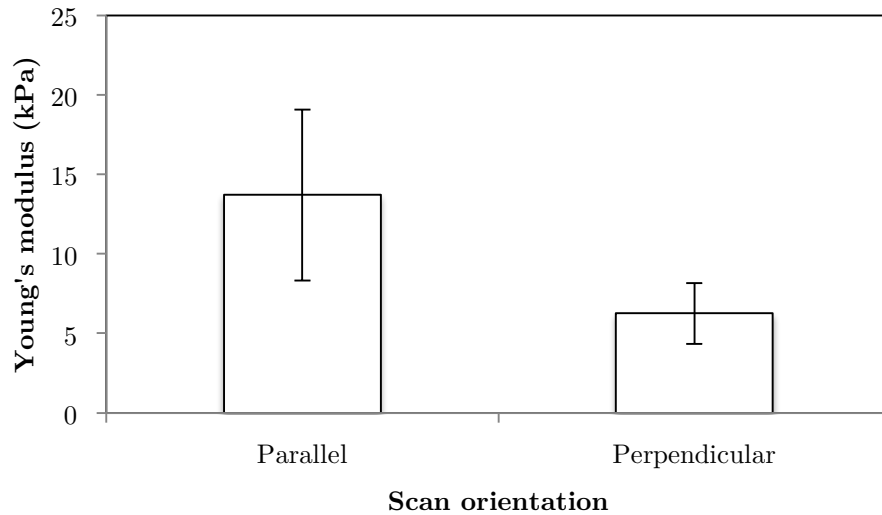


Figure 6.80. Mean and plus and minus one standard deviation of the Young's modulus measurements of the 2 spinal cords measured parallel and perpendicular to their lengths ( $n=2$ ). The difference is not statistically significant ( $p = 0.202$ , paired t-test).

## 6.5 Discussion

This chapter attempts to study the artefacts encountered in the preliminary clinical study (Chapter 5) through laboratory experiments with gelatine phantoms and *ex vivo* porcine brains and spinal cords. In addition, the potential factors that may affect SWE measurements were also investigated and reported in this chapter. The experiments involving gelatine phantoms were all performed at 16 °C. All the experiments reported here were performed with more than 2 phantoms or specimens, and measurements were taken from at least 2 planes, to show reproducibility of the results.

### 6.5.1 Effect of changing the region-of-interest (ROI) size

The ROI size did not affect the SWE measurements. A (small) water standoff was used, with the transducer held by a clamp, to avoid the confounding factor of applying strain to the phantom. The impact of osmosis, which can potentially affect the stiffness of gelatine, was minimised by taking measurements from the centre of the phantom, avoiding the edges.

### 6.5.2 Effect of varying the water standoff

The SWE measurements were not significantly affected by a water standoff in either standard or penetration mode.

### 6.5.3 Attenuation in superficial tissue

When scanning intraoperatively, the superficial cortex might be abnormally stiff and therefore might attenuate the echo signal and pushing beam. In order to test this hypothesis, an attenuating layer composed of 14% gelatine concentration was used, which was stiffer than the background gelatine phantom used to obtain SWE measurements. Although the gelatine composition would not have the same ultrasonic attenuation coefficient as the brain, it had similar properties to tissue and had been used in laboratory experiments to mimic tissue. The attenuating layer did not affect the SWE measurements of Young's modulus in the softer background gelatine. However, in the stiffer inclusion gelatine, the SWE measurements seemed to decrease with increasing thickness of the attenuating layer, especially with standard mode. Therefore, this result showed that, in the presence of an attenuating layer, the SWE measurements with penetration mode are more reliable than with standard mode. However, the reason why the measured Young's modulus decreases with thickness of overlying gelatine is not clear. In the presence of a strongly attenuating overlying medium, a low echo SNR will occur due to attenuation of the imaging ultrasound beam, and a low amplitude shear wave will be generated due to attenuation of the pushing beam. Either or both of these could result poor SNR in detection of shear wave arrival times, and therefore in measurement of shear wave speed. The reason why poorer SNR should produce a bias rather than simply increased variance in Young's modulus estimation is not known, and must be related to the algorithm that the scanner uses for shear wave speed estimation. Reduction of echo image SNR is a mechanism that would be consistent with the low Young's modulus estimates observed in the shadow regions posterior to attenuating inclusions in Section 6.4.7. However, the difference between penetration mode and standard mode is unknown; it was thought to be related to the strength of the pushing beam but this would not influence the echo SNR.

Although imaging through surgical resulted in a shear wave image that has large variance with patches of drop out, the SWE measurements of Young's modulus were similar to those obtained when imaging through a 2-cm attenuating layer composed of 14% gelatine concentration. Duragen seemed to show lack of shear wave speed display altogether, which could be explained by the attenuation of the pushing beam as the echo signal was attenuated and not detectable.

#### **6.5.4 Effect of adjusting SWE gain**

This experiment confirmed that the SWE gain function on the Supersonic Imagine Aixplorer® scanner changes the threshold for masking the shear wave speed display. Therefore, by increasing the SWE gain, more estimates of Young's modulus, with higher variance, are being displayed. These estimates, as shown by this experiment, have very low SNR, and thus can lead to erroneous measurements. In the Aixplorer® scanner, it seems that by increasing the SWE gain, the resulting display of the shear wave signals were artefactually high. The reason why low SNR is associated with an overestimation of Young's modulus remains unexplained. Nevertheless, this experiment showed that it is important to set the SWE gain so as to not try to fill-in regions of drop out. It seems that the company-recommended and default SWE-gain value of 70% is the best for obtaining reliable measurements.

#### **6.5.5 Effects of manipulations on SWE measurements**

In the gelatine experiment, it was shown that there was a significant decrease in the Young's modulus measurement between pre-resection and post-resection in the background gelatine. There was no significant difference between the pre-resection and during resection phase for both the inclusion and background. There was also no significant difference between during resection and post-resection for background gelatine. The possible explanation for the decrease in Young's modulus is that because the gelatine is immersed in a water bath, manipulation involved in removing the inclusion might have created cracks

and pores which accelerated the water absorption, and this is at least could be similar to what is happening with tissue.

The Young's modulus measurements were shown to decrease significantly in the grey matter through the removal of pia mater. Therefore, this experiment proved that the higher Young's modulus in the grey matter than white matter (Chapter 5; Uff, 2011) was due to the presence of pia mater. During resection, it is inevitable that the pia mater will have to be breached in order to perform corticotomy. In this way, the Young's modulus measurements of both the grey and white matter would be comparable to those without pia mater post-resection. Although the Young's modulus of white matter was shown to decrease with the removal of pia mater, the decrease was not significant. This could partially be due to the osmosis effect as removal of pia mater could have facilitated the movement of saline solution into both the grey and white matter.

In the compression experiment, the Young's modulus measurements decreased from pre- to post-compression states but the difference was not significant. This experiment showed that the brains do not return to their original height immediately after release of the compression, possibly due to their viscoelastic and poroelastic properties. The Poisson's ratio could not be calculated as there was a sideways expansion in the brains thereby precluding the assumption of equivalence of height change to volume change.

The limitation of this study is that it has not studied the effect of denaturation of tissue through diathermy, which would require an *in vivo* animal experiment, as *ex vivo* brain might not exhibit the same reaction towards diathermy. It also has not provided evidence to test the hypothesis that osmosis was responsible for the decrease of Young's modulus post-surgical manipulation. To elucidate this phenomenon, an elaborate experiment would be required involving dyed saline solution and porcine brain, with microscopic examination looking at the brain specimen, and using image analysis to quantify the amount of dye in the tissue. Unfortunately, due to the time constraints of this PhD, it was not possible to test these 2 other theories.

### 6.5.6 Effect of strain on SWE measurements

Because the placement of craniotomies is such that they do not allow the use of a water standoff, the only way to obtain a sonogram or elastogram is by applying a small amount of pressure on the brain. In the gelatine experiments, the Young's modulus measurements were significantly higher in the upper layer for both 8% and 14% gelatine phantoms with the probe touching compared to when a water standoff was in place. However, the Young's modulus measurements for the lower layer for both the phantoms did not seem to be affected. This means that when the transducer touches the gelatine, there was a non-linear stress concentration locally, resulting in higher Young's modulus measurements. In the overall Young's modulus measurements, there seemed to be a significant difference in the 14% gelatine phantoms and not the 8% gelatine phantoms. The possible explanation could be due to the higher overall stiffness in the 14% gelatine phantoms, thereby the non-linear stress concentration effect was higher.

In the porcine brain experiment, the Young's modulus measurements did not rise in the upper third until 10 mm displacement was applied while they did not rise in the middle and lower third until 15 mm displacement was applied. This experiment showed that in clinical scans, the application of pressure of up to 10 mm may not affect the Young's modulus measurements. If the area of interest is deeper down, then a displacement of up to 15 mm may not affect the Young's modulus measurements.

### 6.5.7 Varying the tumour-brain interface conditions

This experiment showed that SWE displayed a characteristic artefact of soft 'brackets' on either side of the mobile inclusions, which were absent on the adhered inclusions, and therefore showed the potential for detecting a slippery plane between the inclusion and the background. As shear waves generated by the Aixplorer® propagate in the horizontal direction, the artefact was only displayed on either side of the inclusion instead of around it. With a single elastogram centred on the inclusion, it was impossible to determine if the soft 'bracket' was because of the relatively higher stiffness surrounding the inclusion. Therefore, stitched images were used to determine this artefact. For stiff inclusions, there

was no increase in stiffness surrounding the artefact for both with and without strain. However, for soft inclusions, there was an increase in stiffness adjacent to the artefact for both with and without strain. Therefore, this characteristic artefact could be exploited intraoperatively to detect slip plane in clinical cases.

In the stiff inclusion phantoms, there was another artefact noted beneath the inclusion. Corresponding to the acoustic shadow on the B-mode image, there was a soft shadow bounded by stiff bands on either side. This could not be demonstrated in the soft inclusion as there was lack of shear wave signal in the deeper region. The acoustic shadow is due to the increased attenuation of imaging beam resulting in lower intensity speckle deeper down. However, the explanation for the corresponding lower Young's modulus measurements is unknown.

### 6.5.8 Resolution of SWE

This experiment showed that the Young's modulus measurements increase with inclusion size for small stiff inclusions and decrease with size for small soft inclusions, where small is defined as less than 5-mm diameter. This observation is consistent with the partial volume effect. As explained in Section 6.3.9.1, the Young's modulus measurements of the inclusion might be affected by the contribution from the background, therefore, reducing the Young's modulus contrast. This was explained for a 3D inclusion. However, for a 2D cylindrical inclusion, the same effect might also be present. Imagine viewing the phantom from the top and the scan plane is not exactly perpendicular to the inclusion, resulting in a larger inclusion displayed on B-mode and larger area of Young's modulus measurements (Figure 6.81). The Young's modulus measurement for the inclusion is actually 3D, which is illustrated in Figure 6.82. The actual volume occupied by the inclusion is only a fraction of the total volume. The volume of inclusion is given, to a first approximation, by:

$$Volume_{inclusion} = \frac{\pi d^2 l}{4}, \quad (6.5)$$

where  $d$  is the diameter of the inclusion and  $l$  is the length of the inclusion within the slice thickness of the shear wave elastogram. Imagine the angle of the cylinder is  $45^\circ$ , then the maximum contribution of the background to the measured YM would be achieved. The total volume of the cube is given by:

$$Volume_{inc+back} = w^3, \quad (6.6)$$

where  $w$  is the SWE slice thickness. The Young's modulus measurement of the cube,  $E_{inc+back}$ , (assuming that a simple volumetric mixture rule can approximate the result when attempts use the machine to calculate the average speed of a shear wave that propagates partly through the inclusion and partly through the background) is given by: (6.7)

$$E_{inc+back} = \frac{Volume_{inclusion}}{Volume_{inc+back}} E_{inclusion} + \frac{Volume_{inc+back} - Volume_{inclusion}}{Volume_{inc+back}} E_{background} \quad (6.7)$$

where  $E_{inclusion}$  and  $E_{background}$  are the Young's modulus for the inclusion and background, respectively. Therefore, substituting the equation:

$$E_{inc+back} = \frac{\pi d^2 l}{4w^3} E_{inclusion} + \left(1 - \frac{\pi d^2 l}{4w^3}\right) E_{background} \quad (6.8)$$

As the angle of the cylinder is  $45^\circ$ , then:

$$l = \cos 45^\circ \times \sqrt{2w^2} = w \quad (6.9)$$

The overall equation is then:

$$E_{inc+back} = \frac{\pi d^2}{4w^2} E_{inclusion} + \left(1 - \frac{\pi d^2}{4w^2}\right) E_{background} \quad (6.10)$$

From this equation, the smaller the diameter of the inclusion, the higher the contribution from the background Young's modulus. If the diameter of the inclusion is larger than  $\sqrt{\frac{4w^2}{\pi}}$ , then there will be no contribution from the background. As this correction assumed that the cylindrical inclusion was lying at  $45^\circ$  to the scan plane, the equation would be expected to overcorrect the vast majority of Young's modulus measurements. Figure 6.83 and Figure 6.84 show the plot for "corrected" Young's modulus for small stiff and soft

inclusions, respectively. As demonstrated, the Young's modulus for both conditions was overcorrected. In Section 6.5.9.1, the correction for 3D spherical inclusions based on the partial volume effect will be demonstrated.

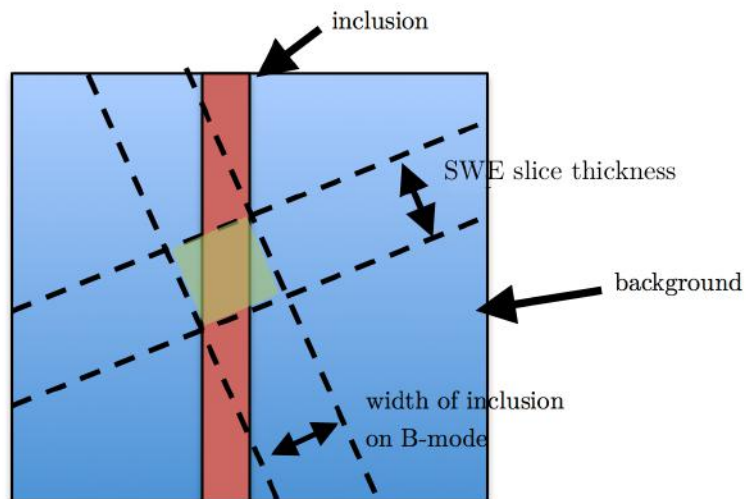


Figure 6.81. This is the view from the top of a block gelatine (blue) with a cylindrical inclusion (red). The dashed lines across the inclusion represent the scan plane. Therefore, the inclusion appearing on the B-mode is larger than the actual size of the inclusion. The Young's modulus measurements for the inclusion are taken from the transparent green area, which has contributions from both the background and inclusion.

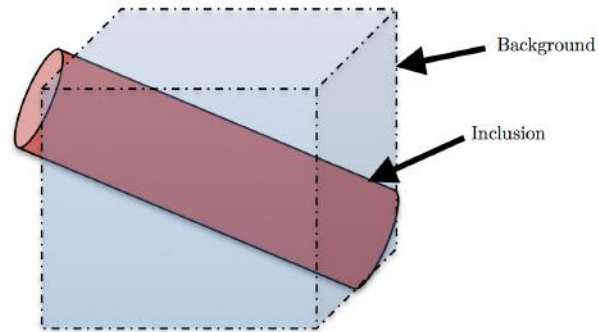


Figure 6.82. Magnified volume where Young's modulus measurements are calculated. The cylindrical inclusion is only a part of the total volume, hence resulting in lower values of measured Young's modulus due to contributions from the background.

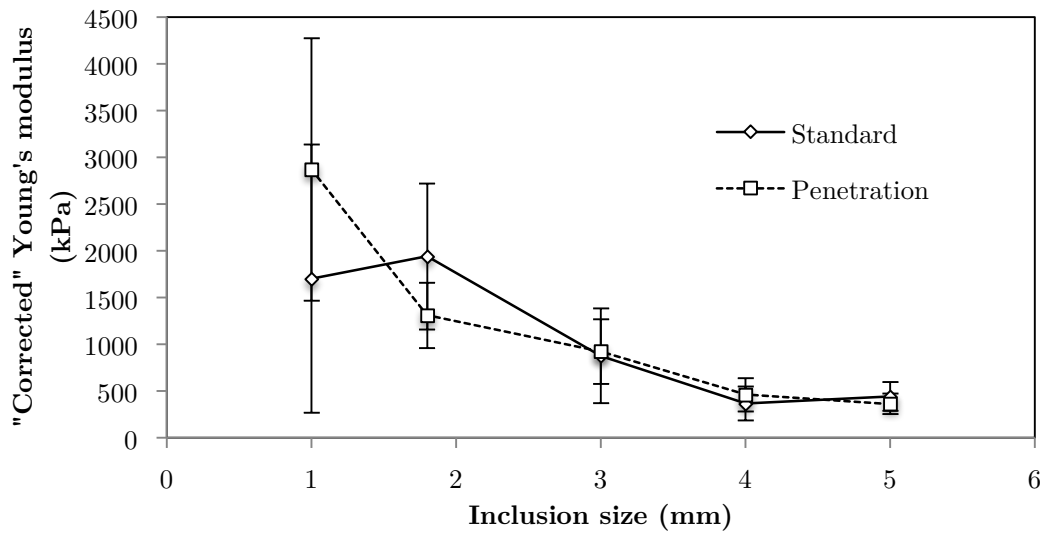


Figure 6.83: Plot of "corrected" Young's modulus for small stiff inclusions. The correction seemed to be overcorrecting the Young's modulus, especially the smaller inclusions (1 mm to 3 mm). Overall, the "correction" overcorrected the Young's modulus for the inclusions in this experiment.

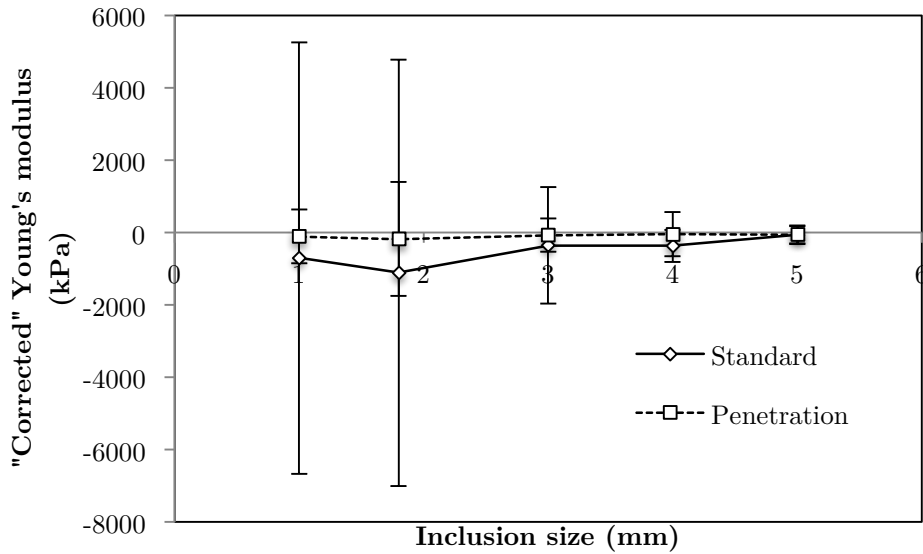


Figure 6.84: Plot of “corrected” Young’s modulus for small soft inclusion sizes. The correction seemed to be overcorrecting the Young’s modulus, making the soft inclusions appearing with very small Young’s modulus or even negative Young’s modulus.

The size limit of detectability of SWE, in detecting an inclusion in a homogeneous background, for a Young’s modulus contrast of  $\pm 0.10$ , was 1 mm for stiff inclusion and 3 mm for soft inclusion by visual observation under normal (darkened) radiology room lighting conditions and a normal viewing distance from the scanner’s monitor. From the Young’s modulus contrast versus inclusion size plot, it was apparent that a Young’s modulus contrast of  $> 0.10$  or  $< -0.10$  should be used as the threshold for detecting the inclusions. Note that for penetration mode, the size threshold for detection of a soft inclusion of contrast  $\pm 0.10$ , is 5 mm compared with 3mm for standard mode.

## 6.5.9 Other factors affecting shear wave measurements

### 6.5.9.1 Inclusion sizes

This experiment showed that the Young’s modulus measurements for larger inclusions are less affected by the size. This is explained in Section 6.5.8. However, as the width of the transducer is approximately 1.5 cm, the minimum inclusion size needs to be at least  $\sim 1.7$  cm to eliminate the partial volume effect. The correction factor was overcorrecting the Young’s modulus in Section 6.5.8, which was not surprising as the

correction was based on the worst case scenario where the cylindrical inclusions were lying at the worst possible angle.

For spherical inclusions, there was an increase in the CTE with increasing size. Therefore, this experiment demonstrated that partial volume effect plays a role in the contribution to CTE-versus-inclusion size graph. The CTE was higher in positive modulus contrast compared with negative modulus contrast, which was shown by Ponnekanti et al. (1995). To correct the Young's modulus for spherical inclusions, it would assumed that the Young's modulus measured would be the contribution of the cuboid containing the inclusion. The volume of the cuboid ( $Volume_{inc+back}$ ) is given by:

$$Volume_{inc+back} = wd^2 \quad (6.11)$$

where  $w$  is the SWE slice thickness and  $d$  is the diameter of the inclusion. The volume of the sphere is given by:

$$Volume_{inclusion} = \frac{4}{3}\pi r^3 = \frac{\pi d^3}{6}, \quad (6.12)$$

where  $r$  is radius of the inclusion. Assuming the partial volume effect and the mixture rule described for cylindrical inclusions above:

$$E_{inc+back} = \frac{Volume_{inclusion}}{Volume_{inc+back}} E_{inclusion} + \frac{Volume_{inc+back} - Volume_{inclusion}}{Volume_{inc+back}} E_{background}, \quad (6.13)$$

where  $E_{inclusion}$  and  $E_{background}$  are the Young's modulus for the inclusion and background, respectively. Therefore, substituting the equation (6.11) and (6.12) into (6.13):

$$E_{inc+back} = \frac{\pi d^3}{6wd^2} E_{inclusion} + \left(1 - \frac{\pi d^3}{6wd^2}\right) E_{background}$$

$$E_{inc+back} = \frac{\pi d}{6w} E_{inclusion} + \left(1 - \frac{\pi d}{6w}\right) E_{background}. \quad (6.14)$$

Rearranging the equation gives:

$$E_{inclusion} = \frac{6w}{\pi d} E_{inc+back} - \frac{6w}{\pi d} \left(1 - \frac{\pi d}{6w}\right) E_{background}$$

$$E_{inclusion} = \frac{6w}{\pi d} E_{inc+back} - \left( \frac{6w}{\pi d} - 1 \right) E_{background}. \quad (6.15)$$

By applying this as a partial volume effect correction equation, the Young's modulus for spherical stiff inclusions seemed to be corrected, demonstrating similar "corrected" Young's modulus throughout different inclusion sizes (Figure 6.85). Similarly, the CTE also showed no demonstrable trend, although the CTE was positive indicating that the correction is over compensating (Figure 6.86). However, the correction equation seemed to work less well for spherical soft inclusions (Figure 6.87). The "corrected" Young's modulus was inaccurate for 2.5-mm soft inclusions and was higher than before correction. As indicated in Section 6.5.8, the smallest soft inclusions detectable by SWE, at a contrast of -0.10, is 3 mm and 5 mm for standard and penetration mode, respectively. The inaccurate "correction" of the Young's modulus for 2.5-mm soft inclusions may therefore be due to the detectability limit of the system. The correction for soft inclusions of 6 mm diameter and larger seemed to demonstrate stable measurements of Young's modulus. As with "corrected" CTE, the penetration mode seemed to show a consistent but negative CTE (Figure 6.88). With standard mode, the correction seemed to be overcorrecting the CTE for soft inclusions, with all the inclusions showing a positive CTE. The correction equation based on partial volume effect seemed to be capable of producing reasonably reliable "corrected" Young's modulus, with better performance in stiff inclusions. The correction for soft inclusions acceptable for larger inclusions with penetration mode, but the correction for smaller inclusions and with standard mode still needs further work to clarify the mechanism behind the inaccuracies in the SWE measurements.

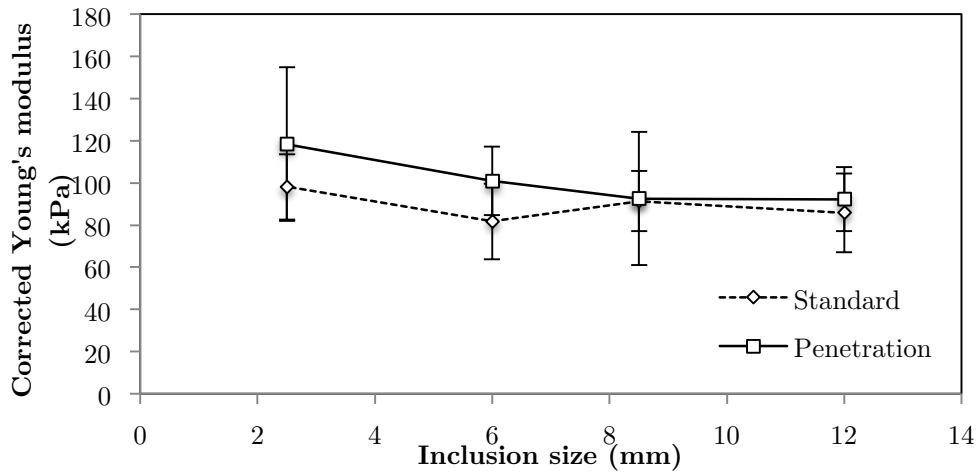


Figure 6.85: Plot of “corrected” Young’s modulus for 3D stiff inclusions.

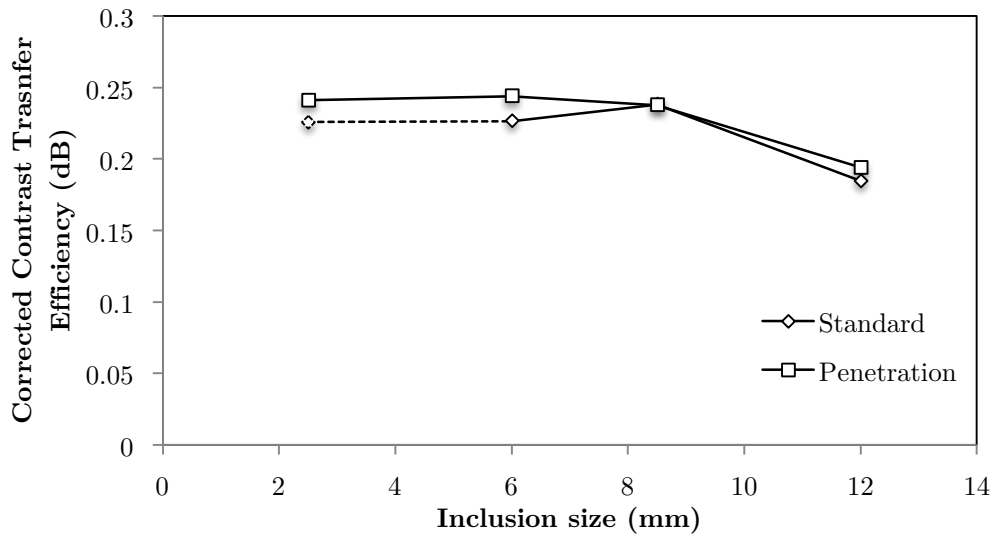


Figure 6.86: Plot of “corrected” CTE for 3D stiff inclusions. The correction seemed to give a positive CTE for stiff inclusions.

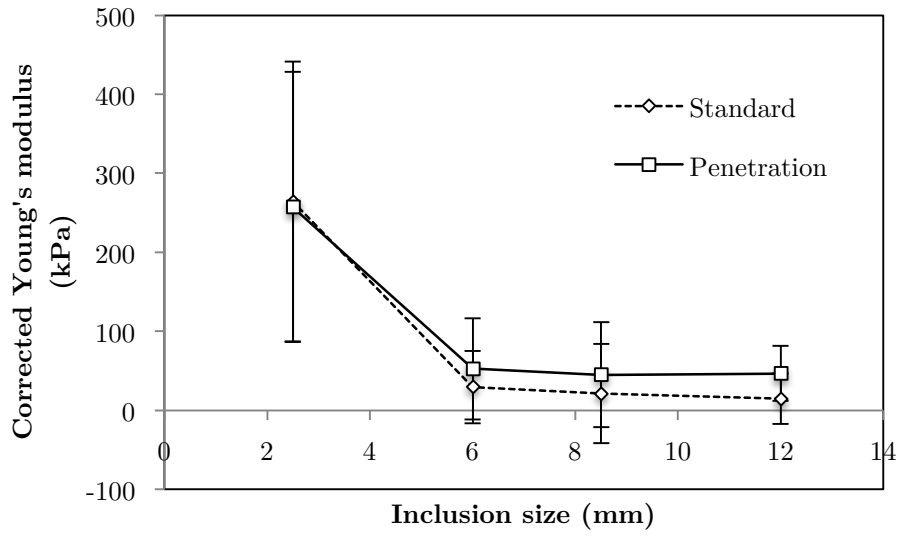


Figure 6.87: Plot of “corrected” Young’s modulus for 3D soft inclusions. The correction seemed to overcorrect the smallest inclusion (2.5mm).

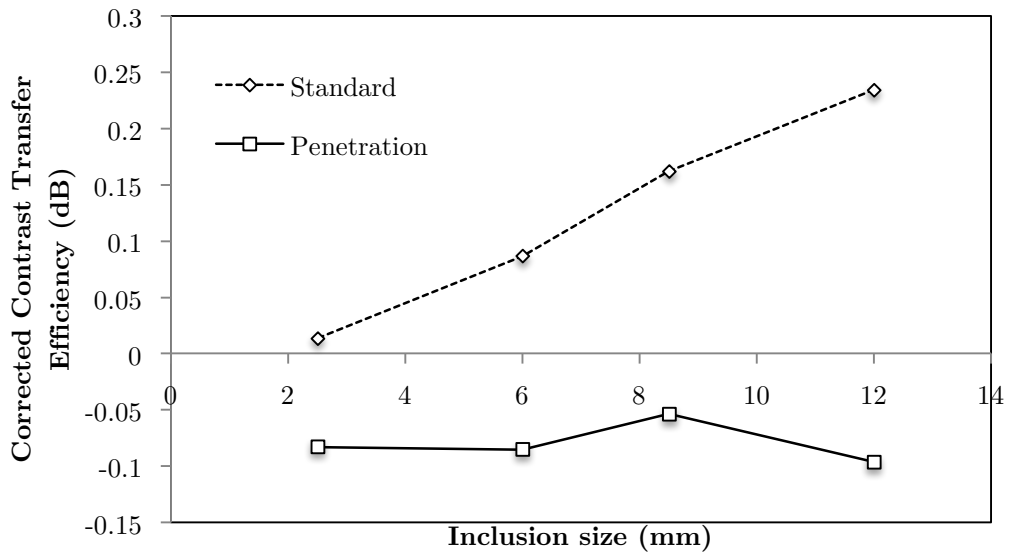


Figure 6.88: Plot of “corrected” CTE for 3D soft inclusions. The correction factor seemed to be overcorrecting the CTE for SWE standard mode, with positive CTE for all inclusion sizes.

### ***6.5.9.2 Inclusions at different depths***

This experiment showed that the Young's modulus measurements within inclusions seemed to be minimally affected by the depth of the inclusion. However, for 0.5-mm soft inclusions, the Young's modulus measurements seemed to be decreasing with depth, despite changing the position of the inclusion. Therefore, the Young's modulus measurements in this case were not due to difference in the inclusion stiffness. A possible explanation is that the deeper the inclusion, the higher likelihood for partial volume effect to manifest, thereby resulting in higher error in Young's modulus measurements. This is because the further away the inclusion from the transducer, the higher the "malalignment" of the scan plane in regard to the inclusion.

### ***6.5.9.3 Anisotropy of tissue***

This experiment showed that SWE has the potential to detect anisotropy in tissue but the result did not reach statistical significance because of the small number of specimens. This result is in line with Macé et al. (2011), who showed that SWE successfully demonstrated anisotropy in white matter fibres in rat brains.

## **6.5 Conclusions**

This results reported in this chapter and the ensuing discussion demonstrated the following:

1. The Young's modulus measurements are not affected by:
  - a. different ROI sizes.
  - b. different water standoffs.
  - c. different SWE modes, i.e. standard or penetration modes.
  - d. different inclusion depths.
  
2. The Young's modulus measurements are affected by:
  - a. attenuating layers superficial to the ROI.

- b. changing the SWE gain.
  - c. breach or absence of pia mater.
  - d. application of pressure when scanning.
  - e. different inclusion sizes.
3. The Young's modulus measurements may be affected by the orientation of the transducer in anisotropic tissue such as the spinal cord and white matter.
4. Attenuating layers and structures that produce an acoustic shadow can result in lack of shear wave signals and lower Young's modulus measurements in the region posterior to them on standard SWE mode.
5. SWE showed characteristic artefacts for both adhered and mobile inclusion-background interfaces, which may in the future allow identification of the existence of a mobile interface.
6. The minimum sizes of cylindrical inclusions of contrast  $\pm 0.10$  detectable by SWE were 1mm and 3mm for hard and soft inclusions, respectively.
7. CTE values as a function of inclusion size for both stiff and soft inclusions demonstrated tendencies toward 0 dB with increasing size. The CTE is lower for soft inclusions compared with stiff inclusions for corresponding sizes. CTE is always less than perfect. However, unlike strain imaging, for SWE this is consistent with a partial volume explanation. Further work is required to refine the partial volume mathematics so as demonstrate better agreement between predicted and measured Young's modulus and CTE values.

## 6.6 Recommendations

Further research is needed to improve our understanding many of the above observed phenomena, good examples being a) low Young's modulus values obtained in regions of acoustic shadowing and b) shear wave dropout, neither of which were adequately explained. However, the results reported in this chapter are sufficient for the moment, to provide recommendations for "best practice" when clinical scanning, so as to obtain the most reliable SWE measurements of Young's modulus in tissue. From the above findings, the recommendations for optimising intra-operative SWE scanning are as follows:

1. As the standard SWE mode showed a lack of shear wave signal more frequently than the penetration mode, it is recommended that the penetration mode is used as this will reduce the incidence of shear wave dropouts. However, it should be noted that even in homogeneous backgrounds, the the minimum detectable size of inclusions of Young's modulus contrast of -0.10 is 5 mm for soft inclusions for this mode compared with 3 mm for standard mode. This chapter also demonstrated that the measured Young's modulus values were not affected by the different SWE modes.
2. Since different water standoffs do not affect the Young's modulus measurements, scanning should be performed with water standoff when possible. In cases where it is impossible to create water standoff, scanning should be performed with minimal pressure on the brain as application of pressure during scanning can result in increased Young's modulus measurement in the upper third of the scanned area. However, if the area of interest is deeper, then applying contact pressure that produces up to 15 mm surface displacement during scanning, to improve quality of shear wave penetration in the deeper regions, can be used as this was shown not to affect Young's modulus values obtained from the deeper regions.
3. For stiff lesions in a soft background, it should be remembered that for smaller lesions the Young's modulus could be underestimated due to partial volume effect. Conversely, for soft lesions in a stiff background, the Young's modulus of smaller lesions could be overestimated.

4. The attenuating tissue superficial to the area of interest, and other unknown mechanisms, can cause (a) shear wave signal dropout and (b) underestimation of the Young's modulus, which may be present alone or together, especially using standard mode. To minimise the occurrence of this effect, it is recommended that the scanning should be performed with penetration mode and areas that are attenuating should not be lying above the area of interest. Alternatively, if attenuation or dropout are unavoidable, then it should be remembered that the Young's modulus might be greater than the actual measurements and that lack of a displayed Young's modulus is not always due to lack of echo signal or the presence of a fluid-filled void.
5. Surgical manipulations can affect the Young's modulus of the tissue, so post-resection scans will be expected to display lower Young's modulus of the same tissue due to this effect. This effect was shown to be due to breach in pia mater. Retraction was not shown to decrease the Young's modulus measurements. Therefore, when using SWE to detect residual tumour, the surgeon has to remember that the remaining lesion tissue now will have a lower Young's modulus compared to the original.
6. The best SWE gain for intra-operative scanning is 70%, where there is dropout but minimal artefact. With lower SWE gain than this, there is a problem with reduced shear wave signal whilst with higher SWE gain, the dropout problem is not solved and there is a tendency for artefactual signals with high Young's modulus.
7. There is potential for SWE to differentiate adhered from mobile tumour-brain interface as shown in this chapter. Therefore, the soft 'brackets' should be looked out for, as it may be a sign of a slip plane.

The next 2 chapters report the findings from clinical scans that were performed with the above recommendations in place. Chapters 7 and 8 will be on intra-operative scans in tumour resection and epilepsy surgery, respectively.

## **Chapter 7**

# **Clinical Application of Intra-operative Shear Wave Elastography in Epilepsy Surgery**

This chapter describes the clinical application of intra-operative SWE during epileptogenic focus resection. It compares the SWE measurements of these lesions with surgical findings. It also compares the visibility of these lesions on intra-operative SWE with that on MRI scans based on the formal report by the neuroradiologist. It reports the seizure outcomes from resection of these lesions and concludes by reporting the correlation between SWE measurements and histological features of these lesions.

## 7.1 Introduction

As detailed in Chapter 2, about 15% of all patients with epilepsy are refractory to AEDs (Rosenow & Lüders, 2001). Epilepsy surgery has been shown to improve seizure outcomes in both temporal (Engel et al., 2012; Wiebe et al., 2001) and extratemporal epilepsy (Cohen-Gadol et al., 2004). The aim of epilepsy surgery is to remove the epileptogenic lesions (Rosenow & Lüders, 2001). For mesial temporal epilepsy, removal of the mesial temporal structures can lead to good seizure outcomes (Engel et al., 2012; Wiebe et al., 2001). However, for extratemporal and neocortical temporal epilepsy, there is no anatomical landmark to guide surgical resection and the success of surgery depends on the ability of the surgeon to delineate the epileptogenic lesions (Roper, 2009). This is further complicated by the fact that these lesions can involve multiple lobes (Frater et al., 2000) and do not show up on MRI scan in 16% to 43% of cases (Berg et al., 2003; Bien et al., 2009; McGonigal et al., 2007; Scott et al., 1999; Siegel et al., 2001). In these cases, the seizure outcomes are not as favourable as those for lesions that are visible on MRI (Jeha et al., 2007; Zentner et al., 1996). Therefore, for extratemporal epilepsy cases, to optimise surgical outcomes, presurgical workup is performed with FDG-PET (Chassoux et al., 2012), SPECT (Spencer, 1994), MSI (Wu X.-T. et al., 2012), and morphometric MRI postprocessing (Wang Z.I. et al., 2013). Although these presurgical investigations can assist in localising epileptogenic lesions, they are not real-time and are implemented intra-operatively through co-registration with MRI using neuronavigation. As shown by Dorward et al. (1998), there is a shift of brain structures of  $4.6 \text{ mm} \pm 4 \text{ mm}$  (mean  $\pm$  SD) after craniotomy, resulting in localisation inaccuracy. As scalp EEG is vulnerable to interference from the dura, skull and scalp (Rosenow & Lüders, 2001) and is not precise (Sweet et al., 2013), invasive intracranial recording is employed to localise the epileptogenic lesions. Frequently, the placement of invasive recording is performed using neuronavigation guidance, which is vulnerable to brain shift. Therefore, a real-time intra-operative imaging technique that can reliably detect the epileptogenic lesions would have the potential to overcome the inaccuracy associated with this shift. Miller et al. (2008) showed that IOUS was able to delineate focal cortical dysplasia with good resolution, thus showing the potential for guiding resection. However, in

MRI-defined non-lesional cases, IOUS may or may not detect the epileptogenic lesion, precluding its use for guiding placement of invasive recording or resection.

SWE is an ultrasound-based technique, as explained in Chapter 3. It is capable of providing real-time imaging intra-operatively, thereby overcoming the problem of brain shift after craniotomy. In addition to displaying US B-mode, SWE is also capable of mapping Young's modulus of the area of interest. Although epileptogenic lesions have been shown to be stiffer than brain (Uff, 2011), Chapter 5 also showed that there are lesions which were softer than brain. By exploiting the difference in the Young's modulus of epileptogenic lesions, SWE may detect these lesions intra-operatively, especially in MRI-negative cases.

## 7.2 Aims

The aims of this study are as follows:

1. To determine the correlation of SWE measurements of different epileptogenic lesions with surgical grading of stiffness.
2. To determine the ability of SWE to visualise epileptogenic lesions.
3. To determine whether SWE measurements of epileptogenic lesions are correlated with histological characteristics. This would assist understanding of what causes a given epileptogenic lesion to be hard or soft

## 7.3 Methods

### 7.3.1 Patient selection

Patients were recruited from Great Ormond Street Hospital for Children and The National Hospital for Neurology and Neurosurgery. The inclusion criteria were as follows:

1. They have focal symptomatic epilepsy, and

2. They have consented to undergo surgery for their epilepsy, and
3. They have given their consent for this study, or their parents have given their consent on their behalf for this study if they are under 16 years old.

The surgical procedures included invasive monitoring and implantation of subdural grids and depth electrodes, resection of lesions, functional hemispherectomy and/or temporal-parietal-occipital disconnection. Those who underwent solely functional hemispherectomy, temporal-parietal-occipital disconnection, or invasive monitoring without resection of lesions were excluded because the epileptogenic foci were not resected and the surgeon would therefore not be able to comment on the stiffness of the lesions.

### 7.3.2 Operating room protocol

The operating room setup is described in Chapter 3. After anaesthesia, the patient was transferred to the operating table and his/her head was pinned with Mayfield clamp to immobilise the head. Stealth neuronavigation registration was performed to plan the craniotomy placement. In cases where the lesion was obvious on the pre-operative MRI scan, the craniotomy placement was on the overlying skull. In those with subtle or absent lesions on the pre-operative MRI scan, the craniotomy was placed on the symptomatic side and subdural grid with or without depth electrodes were implanted. The location of implantation of the grids and electrodes was determined by the seizure semiology, SPECT, PET, EEG and/or MEG findings, and the decision from the epilepsy multidisciplinary meeting. The patient was then observed on the ward with the implants in situ for approximately 7 days, after which time they would be removed, and additional procedure on the lesion would be performed. The procedure performed was determined by the location of the lesion. If the lesion was located in an eloquent area, then the decision would either be non-resectional or disconnective surgery such as functional hemispherectomy and temporal-parietal-occipital disconnection. If the lesion was located away from eloquent cortex, then

resection of the lesion was carried out. The lesions were sent to the laboratory for histopathological results.

### 7.3.3 Data acquisition

After craniotomy, the ultrasound transducer was placed in a sterile sheath filled with acoustic coupling gel. The SWE mode on the SuperSonic Aixplorer® scanner was then activated. For MRI-defined lesional cases, the scans were performed around the lesions and on normal areas, whereas for MRI-defined non-lesional cases, the scans were performed on the exposed brain. The images were analysed after the operation by the author. Without having been informed of the SWE findings, the surgeon was asked to grade the stiffness of the lesions from 1 to 5 as follows:

1. The lesion is very soft like cyst.
2. The lesion is softer than brain.
3. The lesion is similar to brain.
4. The lesion is stiffer than brain.
5. The lesion is very stiff like cartilage.

For MRI-negative cases, SWE scans were again acquired prior to resection but after invasive recording to guide resection of the lesions. The Q-box function was used to measure the Young's modulus for the lesions and adjacent brain.

### 7.3.4 Data analysis

The Young's modulus measurements and Young's modulus contrast were compared with surgical findings. The epileptogenic lesions were divided into 'obvious', 'subtle' and 'absent' based on the MRI reported by a consultant neuroradiologist. As reported in Section 6.4.8, using phantoms with inclusions of varying sizes in a homogeneous background, the lowest Young's modulus contrast for inclusions to be detectable was  $\pm 0.10$ , which was used as the threshold for a lesion to be graded as 'visible'. From Section 6.4.9, using phantoms

with large inclusions (1-cm- to 2-cm-diameter inclusions), the lowest Young's modulus contrast for the large inclusions to be detectable was  $\pm 0.25$ , which was the value selected to be the threshold for a lesion to be graded as 'obvious'. Therefore, the epileptogenic lesions were graded as 'obvious', 'subtle' and 'absent' for those with Young's modulus contrast of greater than  $\pm 0.25$ , between  $\pm 0.10$  and  $\pm 0.25$ , and less than  $\pm 0.10$ , respectively. Comparison was then made between SWE and MRI images using these grading systems. For cases scanned at Great Ormond Street Hospital the Young's modulus measurements were also compared with histology to determine if there was any correlation with the presence of calcification, proliferation, cellularity and gliosis, as scored subjectively by Dr Tom Jacques, consultant neurohistopathologist. These were chosen because these were the common histological features that are commonly present in brain tumours. The cases scanned at The National Hospital for Neurology and Neurosurgery were not assessed in this way.

Statistical analysis using Spearman's rank correlation, a non-parametric statistical test, was performed for comparison of Young's modulus measurements and Young's modulus contrast with surgical findings, because the grading of stiffness was ordinal and discrete whereas Young's modulus and Young's modulus contrast were continuous. For paired data, Student's t-test and Wilcoxon signed-rank test were used for statistical analysis for a normally and non-normally distributed data, respectively. For independent data, Student's t-test and Mann Whitney U test were used for statistical analysis for a normally and non-normally distributed data, respectively.

## 7.4 Results

A total of 56 patients were recruited into the study. The summary of all the cases is illustrated in Table 7.1.

Research number	Age (y)	Gender	Diagnosis	Type of operation
GOSH 2	13.0	F	DNT <sup>§</sup>	Resection
GOSH 4	1.0	F	FCD <sup>§§</sup>	Resection
GOSH 6	13.0	F	FCD <sup>§§</sup>	Resection
GOSH 7	11.0	F	DNT <sup>§</sup>	Resection
GOSH 8	7.0	M	FCD <sup>§§</sup>	Resection
GOSH 9*	1.0	M	Polymicrogyria	Hemispherotomy
GOSH 11	7.0	M	Ganglioglioma	Resection
GOSH 12	2.0	F	Polymicrogyria	Resection
GOSH 13	16.0	M	FCD <sup>§§</sup>	Resection
GOSH 14	13.0	F	DNT <sup>§</sup>	Resection
GOSH 15*	16.0	F	Rasmussen's encephalitis	Hemispherotomy
GOSH 18*	16.0	M	Rasmussen's encephalitis	Hemispherotomy
GOSH 19*	6.0	M	Rasmussen's encephalitis	Hemispherotomy
GOSH 20	15.0	F	DNT <sup>§</sup>	Resection
GOSH 21*	6.0	M	MCD** (no histology)	TPO% disconnection
GOSH 22	11.0	F	Non-diagnostic appearance	Resection
GOSH 23*	17.0	F	Polymicrogyria	Hemispherotomy
GOSH 24*	0.6	M	FCD <sup>§§</sup> (biopsy)	TPO% disconnection
GOSH 26*	0.4	F	Hemimegalencephaly	TPO% disconnection
GOSH 27	15.0	M	Non-diagnostic appearance	Resection
GOSH 28	11.0	M	FCD <sup>§§</sup>	Resection
GOSH 30*	5.0	M	Polymicrogyria	TPO% disconnection
GOSH 33*	10.0	M	Porencephalic cyst	Hemispherotomy
GOSH 34*	2.0	M	FCD <sup>§§</sup> (no histology)	TPO% disconnection
GOSH 36*	11.0	F	Hemimegalencephaly	Hemispherotomy
GOSH 37	3.0	M	Inflammation	Resection
GOSH 38	16.0	M	FCD <sup>§§</sup>	Resection
GOSH 39	7.0	M	Ganglioglioma	Resection
GOSH 41	13.0	M	DNT <sup>§</sup>	Resection
GOSH 42*	8.0	M	Porencephalic cyst	Hemispherotomy
GOSH 43*	0.5	M	Hemimegalencephaly	TPO% disconnection
GOSH 44*	4.0	M	Hemimegalencephaly	TPO% disconnection
GOSH 46 <sup>§</sup>	10.0	F	Ganglioglioma	Resection
GOSH 48	17.0	F	Subpial gliosis	Resection
GOSH 50	3.9	F	DNT <sup>§</sup>	Resection
GOSH 51	1.3	M	Cavernoma	Resection
GOSH 54	17.0	M	FCD <sup>§§</sup>	Resection
GOSH 57	17.0	M	Cortical ischaemia / injury	Resection
GOSH 58	9.0	M	Subpial gliosis	Resection
GOSH 59	11.0	M	Ganglioglioma	Resection
GOSH 60	3.0	F	FCD <sup>§§</sup>	Resection
GOSH 62	16.0	F	FCD <sup>§§</sup>	Resection
GOSH 63	3.0	F	Polymicrogyria	Resection
GOSH 64*	3.0	F	FCD <sup>§§</sup> (no histology)	Hemispherotomy
GOSH 65	10.0	M	Recurrent ganglioglioma	Resection
GOSH 66	6.0	M	Ganglioglioma	Resection
NHNN 1	53.0	F	Cavernoma	Resection

NHNN 3	23.0	M	FCD <sup>§§</sup>	Resection
NHNN 6	49.0	M	DNT <sup>§</sup>	Resection
NHNN 9	44.0	F	Cavernoma	Resection
GOSH 69	14.0	F	Perivascular glial clustering	Resection
GOSH 70	9.0	F	Hippocampal sclerosis	Resection
GOSH 71	3.0	M	DNT <sup>§</sup>	Resection
GOSH 72	8.0	M	Hippocampal sclerosis	Resection
GOSH 74*	16.0	F	FCD <sup>§§</sup> (no histology)	Not done <sup>£</sup>
GOSH 75	2.0	F	Ganglioglioma	Resection

Table 7.1. Summary of epilepsy surgery cases recruited into the study. <sup>§</sup>Dysembryoplastic neuroepithelial tumour. <sup>§§</sup>Focal cortical dysplasia. <sup>\*\*</sup>Malformation of cortical development. <sup>£</sup>The resection was not performed due to location in the eloquent cortex. <sup>%</sup>Temporo-parieto-occipital. <sup>\*</sup>These cases underwent either hemispherotomy or TPO disconnection. <sup>§</sup>This case was not epileptogenic because it was in the posterior fossa.

Of the 56 cases, 17 cases were excluded because they underwent hemispherotomy or temporo-parieto-occipital (TPO) disconnection. One further case (GOSH 46) was also excluded because the ganglioglioma was located in the posterior fossa and thus not epileptogenic. Table 7.2 shows the summary of the cases included for analysis.

Research number	Diagnosis	YM (kPa) (mean $\pm$ SD <sup>¶</sup> )	YMC <sup>§</sup>	Stiffness grading	MRI grading	SWE grading	Seizure outcome <sup>£</sup>
GOSH 2	DNT <sup>§</sup>	170.6 $\pm$ 115.3	24.088	4	Obvious	Obvious	1
GOSH 4	FCD <sup>§§</sup>	44.8 $\pm$ 20.8	0.874	4	Subtle	Obvious	3
GOSH 6	FCD <sup>§§</sup>	22.5 $\pm$ 4	-0.205	4	Absent	Subtle	3
GOSH 7	DNT <sup>§</sup>	6.6 $\pm$ 1.3	-0.739	2	Obvious	Obvious	1
GOSH 8	FCD <sup>§§</sup>	74.7 $\pm$ 25.4	2.591	4	Absent	Obvious	1
GOSH 11	Ganglioglioma	117.17 $\pm$ 32.32	4.139	4	Subtle	Obvious	1
GOSH 12	Polymicrogyria	62.3 $\pm$ 13.5	1.871	4	Subtle	Obvious	3
GOSH 13	FCD <sup>§§</sup>	58.4 $\pm$ 7.8	1.905	4	Obvious	Obvious	2
GOSH 14	DNT <sup>§</sup>	16 $\pm$ 2.3	-0.333	2	Obvious	Obvious	4
GOSH 20	DNT <sup>§</sup>	32.6 $\pm$ 1.2	0.672	2	Obvious	Obvious	1
GOSH 22	Non diagnostic appearance	58.3 $\pm$ 2.5	1.872	4	Obvious	Obvious	3
GOSH 27	Non diagnostic appearance	32 $\pm$ 2.1	0.410	3	Obvious	Obvious	1
GOSH 28	FCD <sup>§§</sup>	58.95 $\pm$ 10.44	2.684	4	Subtle	Obvious	1
GOSH 37	Inflammation	58.4 $\pm$ 6.5	1.336	4	Subtle	Obvious	1
GOSH 38	FCD <sup>§§</sup>	55.9 $\pm$ 3.4	1.754	4	Subtle	Obvious	4
GOSH 39	Ganglioglioma	70 $\pm$ 3.2	3.000	4	Obvious	Obvious	1
GOSH 41	DNT <sup>§</sup>	20.8 $\pm$ 1.7	-0.249	2	Obvious	Subtle	1
GOSH 48	Subpial gliosis	76.6 $\pm$ 8.1	3.614	4	Obvious	Obvious	2
GOSH 50	DNT <sup>§</sup>	13.3 $\pm$ 1.4	-0.441	2	Obvious	Obvious	3
GOSH 51	Cavernoma	29.7 $\pm$ 3.1	1.583	4	Obvious	Obvious	1A
GOSH 54	FCD <sup>§§</sup>	50.2 $\pm$ 4.3	0.825	3	Subtle	Obvious	3
GOSH 57	Cortical ischaemia / injury	11.2 $\pm$ 3.1	-0.556	2	Obvious	Obvious	1
GOSH 58	Subpial gliosis	78.9 $\pm$ 8	2.985	N/A	Subtle	Obvious	1
GOSH 59	Ganglioglioma	17 $\pm$ 1.3	-0.227	2	Subtle	Subtle	1
GOSH 60	FCD <sup>§§</sup>	48.1 $\pm$ 13.9	0.537	4	Subtle	Obvious	3
GOSH 62	FCD <sup>§§</sup>	47.4 $\pm$ 0.8	1.873	4	Subtle	Obvious	1
GOSH 63	Polymicrogyria	86.2 $\pm$ 3.6	4.904	4	Obvious	Obvious	1

GOSH 65	Recurrent ganglioglioma	143.3 ± 84.8	3.841	2	Obvious	Obvious	1
GOSH 66	Ganglioglioma	66.6 ± 7.8	2.742	4	Obvious	Obvious	3
NHNN 1	Cavernoma	190.6 ± 94	5.807	4	Obvious	Obvious	1
NHNN 3	FCD <sup>§§</sup>	96.9 ± 17.4	4.601	4	Absent	Obvious	3
NHNN 6	DNT <sup>§</sup>	43.4 ± 12.8	2.417	4	Absent	Obvious	1
NHNN 9	Cavernoma	15.3 ± 5.1	-0.528	4	Obvious	Obvious	1
GOSH 69	Perivascular glial clustering	89.7 ± 14.7	2.385	4	Subtle	Obvious	1
GOSH 70	Hippocampal sclerosis	127 ± 36.5	4.962	4	Subtle	Obvious	2
GOSH 71	DNT <sup>§</sup>	17.6 ± 1.3	-0.438	2	Obvious	Obvious	1
GOSH 72	Hippocampal sclerosis	No signal	N/A	3	Obvious	N/A	1
GOSH 75	Ganglioglioma	253.5 ± 75.9	4.417	4	Obvious	Obvious	1

Table 7.2. The summary of cases included for analysis. <sup>§</sup>Dysembryoplastic neuroepithelial tumour. <sup>§§</sup>Focal cortical dysplasia. <sup>¶</sup>Standard deviation. <sup>§</sup>Young's modulus contrast. <sup>‡</sup>Engel's classification is used to group seizure outcomes.

### 7.4.1 Comparison of Young's modulus measurements with surgical findings

One patient with subpial gliosis (GOSH 58) did not have surgical grading as the patient underwent anterior temporal lobectomy, thus precluding the surgeon from palpating the lesion. Explanted temporal lobe palpation was not deemed accurate enough so it was excluded from the comparison.

Figure 7.1 illustrates the Young's modulus measurements according to different stiffness grading. There was a significant correlation between Young's modulus measurements and stiffness grading (Spearman's rank correlation coefficient ( $\rho$ ) = 0.582,  $p < 0.001$ ). Figure 7.2 shows the box and whiskers plot for the Young's modulus contrast with regards to stiffness grading, where there was also a significant correlation between the two ( $\rho$  = 0.622,  $p < 0.001$ ). There was one outlier (GOSH 65) in the softer-than-brain lesions, where the Young's modulus measurement and contrast were 143.3 kPa and 3.841, respectively, but the surgeon felt that the lesion was softer than brain. In one of the stiffer-than-brain lesions (NHNN 9), the Young's modulus measurement and contrast were only 15.3 kPa and -0.528, respectively. In another stiffer-than-brain lesion case (GOSH 6), the Young's modulus measurement and contrast were only 22.5 kPa and -0.205, respectively. The lesions that had similar stiffness to normal brain had higher Young's modulus measurements compared with normal brain.

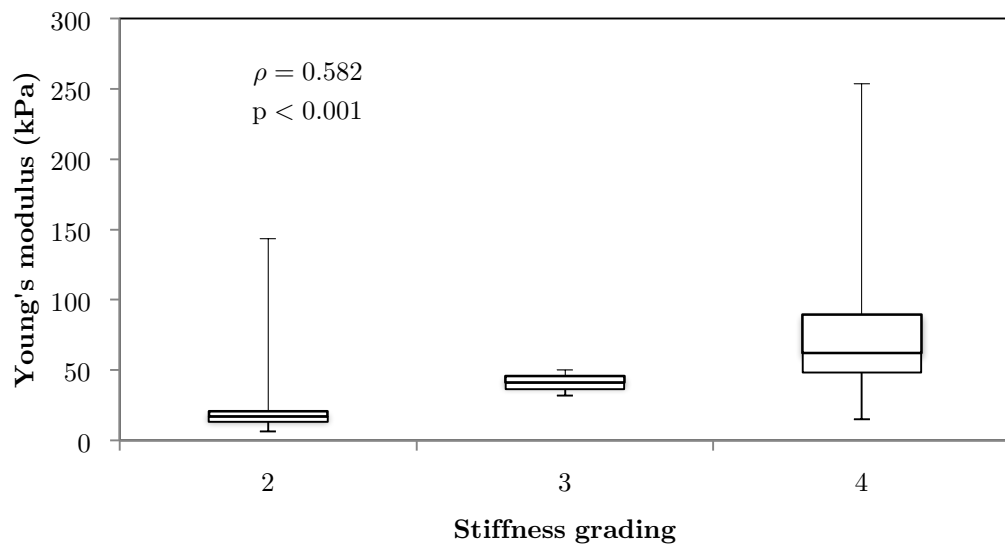


Figure 7.1: Box and whiskers plot for Young's modulus measurements according to different stiffness grading ( $n=37$ ). The upper and lower bounds of the box were the third and first quartiles, respectively while the line within the box was the median. The upper and lower whiskers were maximum and minimum values, respectively.

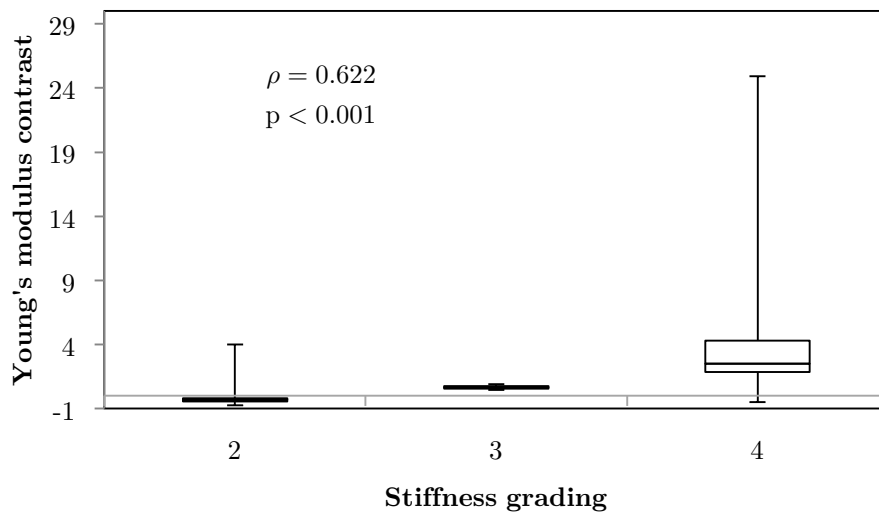


Figure 7.2: Box and whiskers plot for Young's modulus contrast according to different stiffness grading ( $n = 37$ ). The upper and lower bounds of the box were the third and first quartiles, respectively while the line within the box was the median. The upper and lower whiskers were maximum and minimum values, respectively.

### 7.4.2 Comparison between SWE and MRI gradings

There were 38 cases available for grading in the MRI group while there were only 37 cases for grading in the SWE group due to absence of signal (unexplained dropout) in GOSH 72 (Figure 7.3). Of those 38 cases in the MRI group, 4 cases were graded as ‘absent’, 13 cases ‘subtle’, and 21 ‘obvious’, whereas in the SWE group, 3 cases were graded as ‘subtle’ and 34 ‘obvious’, based on the Young’s modulus contrast cut-off. None of the SWE group was graded as ‘absent’ because all the lesions had a Young’s modulus contrast of higher than  $\pm 0.10$ .

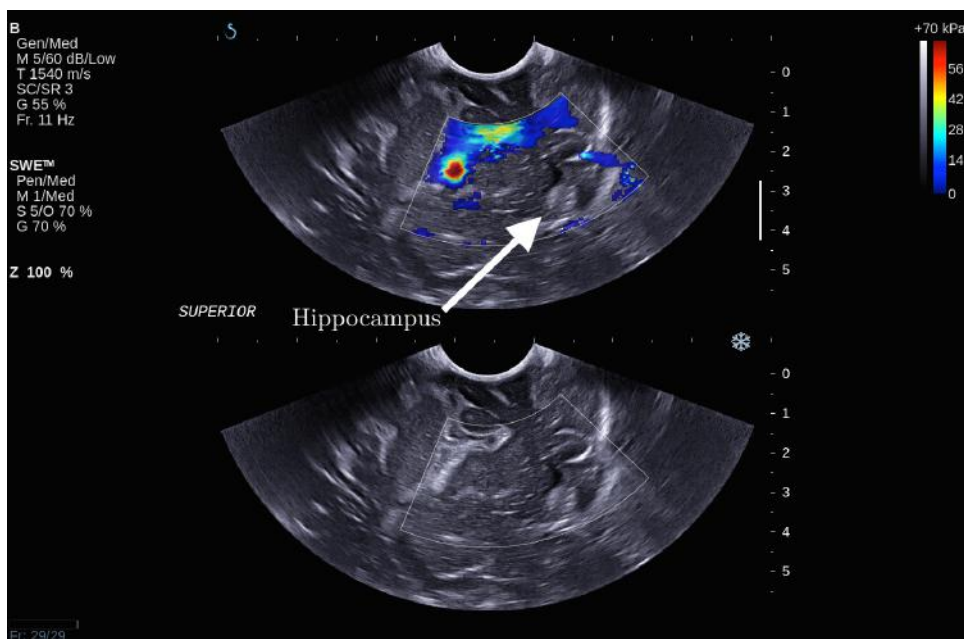


Figure 7.3: SWE of GOSH 72 showing the lack of SWE signal in the hippocampus. This scan was performed in the coronal plane with the left being superior. The stiff region (red) in the sylvian fissure was consistent with the pia effect, described in chapter 6.

#### 7.4.2.1 MRI-negative cases

There were 4 cases (GOSH 6, GOSH 8, NHNN 3 and NHNN 6) where MRI failed to show the epileptogenic lesions, that is, MRI-defined non-lesional cases. The MRI sequences used for these cases included T1-weighted, T2-weighted and FLAIR sequences, all of which did not show the epileptogenic lesions. Three of these lesions were graded as ‘obvious’ on SWE but were not visible on ultrasound B-mode. In contrast, one lesion was graded as

'subtle' on SWE and was visible on ultrasound B-mode. All these MRI-defined non-lesional cases were proven to be epileptogenic on invasive recordings.

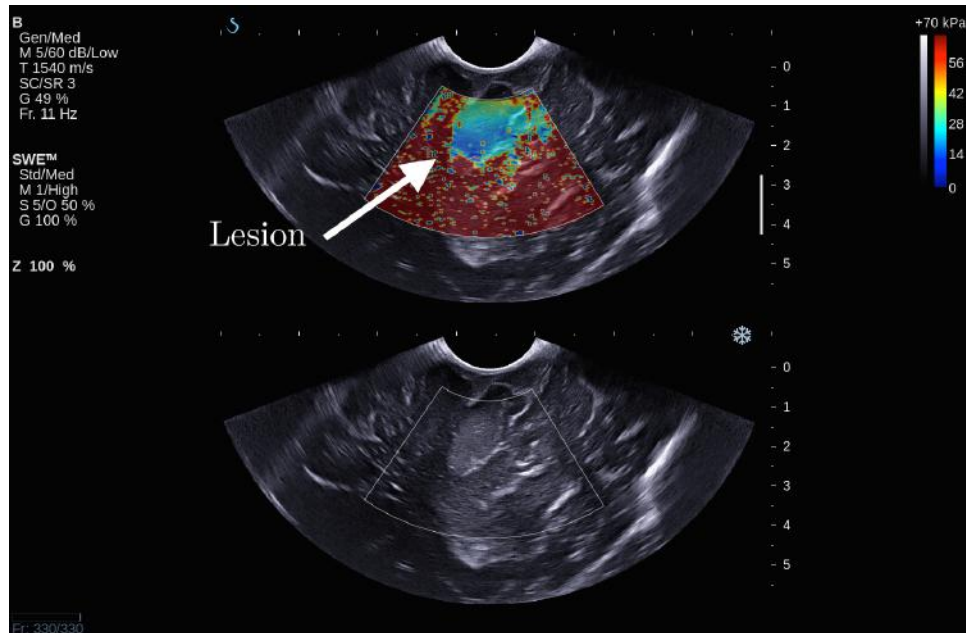


Figure 7.4: SWE for GOSH 6 showing the soft lesion relative to the surrounding brain. As this case was one of the earliest clinical cases, the SWE gain was set to 100%, thereby giving rise to artefactual stiff regions under the lesion.

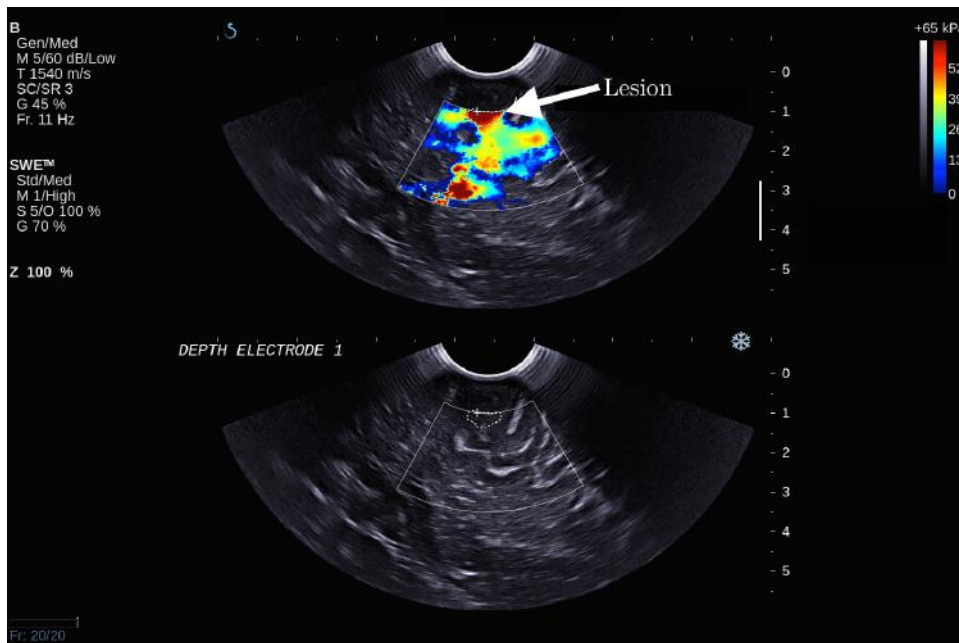


Figure 7.5: SWE for GOSH 8 showing the stiff lesion superficially. This case also demonstrated that the lesion was absent on ultrasound B-mode. The areas deeper down which were also stiff were probably due to anisotropy of deep white matter.

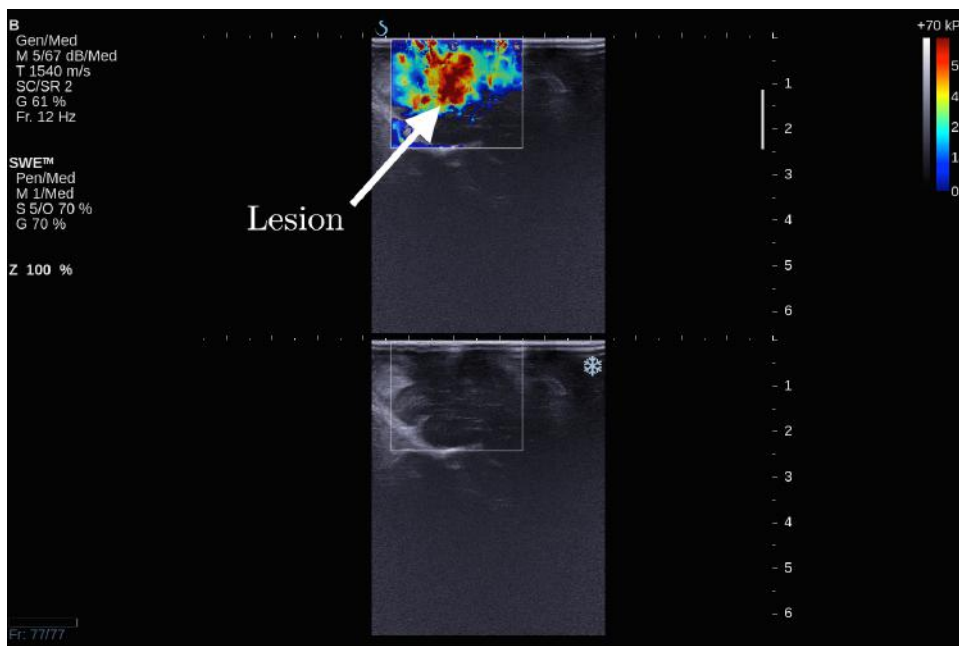


Figure 7.6: SWE for NHNN 3 showing the stiff lesion. This is another case demonstrating that the lesion was absent on ultrasound B-mode.

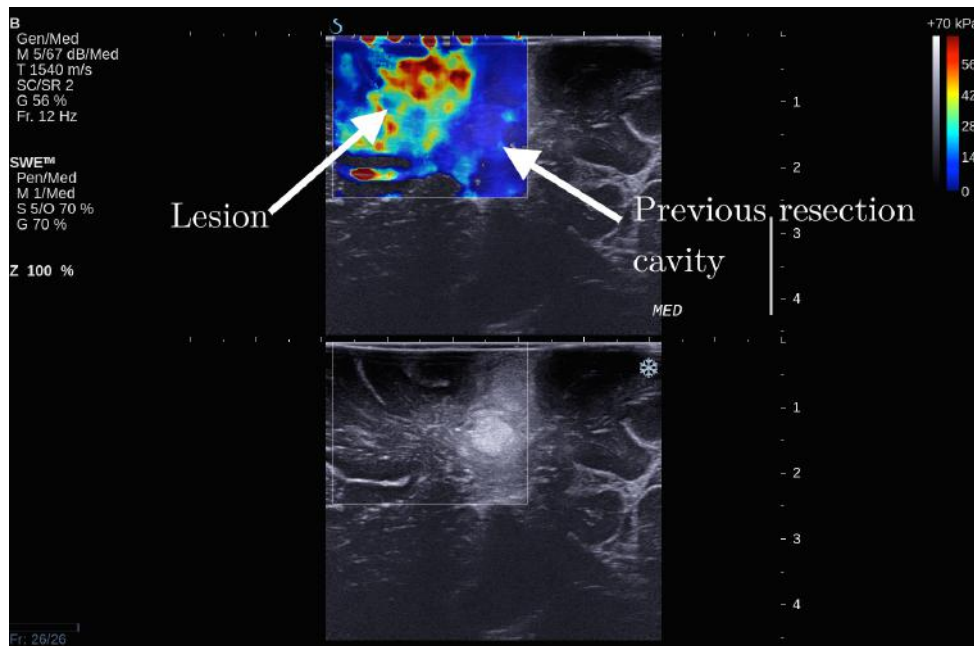


Figure 7.7: SWE for NHNN 6 showing the stiff lesion relative to surrounding brain. This case had previously undergone resection of DNT but seizure returned. The resection cavity was shown not to be epileptogenic but the adjacent area was, which appeared normal on MRI scan.

Figure 7.4 illustrates the SWE appearance of the lesion in GOSH 6. Due to this case being one of the earliest experiences, the SWE settings were not optimised. Therefore, there appeared to be stiff regions under the lesions, which were shown to be artefacts using porcine brain in Chapter 6 when the SWE gain was set to 100%. The lesion was also visible on ultrasound B-mode. The lesion was felt to be softer than brain, which did not agree with the Young's modulus measurement or contrast of 22.5 kPa and -0.205, respectively.

Figure 7.5 shows the SWE display of the lesion in GOSH 8. This case was also one of the earliest cases but fortunately, the SWE gain was not set to 100%. The Young's modulus range was set to 0 – 65 kPa, which was close to enough to the recommended setting of 0 – 70 kPa (Chapter 6). The lesion was not visible on US B-mode; therefore the resection was guided purely by electrophysiological results and SWE. The Young's modulus measurement and contrast of 74.7 kPa and 2.591, respectively, which agreed with surgical findings.

Figure 7.6 demonstrates the SWE appearance of the lesion in NHNN 3. This case was performed using a linear array transducer with a frequency bandwidth of 4 – 15 MHz, with a central frequency of 9.5 MHz. The scanner used at The National Hospital for Neurology and Neurosurgery was transferred from The Institute of Cancer Research, where the phantom studies were performed. Unfortunately, it only had the linear array transducer (SuperLinear SL15-4™); hence all the scans performed at this location were acquired with this transducer. The surgical findings agreed with Young's modulus measurements and contrast, which were 96.9 kPa and 4.601, respectively.

Figure 7.7 shows the SWE display of the lesion in NHNN 6. This patient underwent previous resection of DNT with good seizure outcome. However, the seizures returned and MRI scan just showed previous resection cavity but no new lesion. The patient underwent invasive recording and SWE scanning, the latter revealed a stiff region adjacent to the resection cavity. This region was later confirmed as being epileptogenic. The Young's modulus and contrast were 43.4 kPa and 2.417, respectively, which agreed with surgical findings.

#### **7.4.2.2 MRI-positive cases**

Of the 34 MRI-defined lesional cases, there were 21 'obvious' and 13 'subtle' MRI cases whereas there were 31 'obvious' and 3 'subtle' SWE cases. The examples for the cases with MRI-obvious-SWE-subtle, MRI-subtle-SWE-obvious, and MRI-subtle-SWE-subtle are illustrated here. For GOSH 41, the MRI FLAIR sequence demonstrated the lesion clearly (Figure 7.8), in contrast to the SWE appearance of subtle lesion with Young's modulus contrast of -0.249 (Figure 7.9). For GOSH 4, while the MRI FLAIR sequence showed a subtle lesion in the right motor strip (Figure 7.10), the corresponding SWE demonstrated the lesion clearly (Figure 7.11). For GOSH 59, the lesion appeared subtle on both the T2-weighted MRI sequence and SWE (Figure 7.12 and Figure 7.13, respectively). This lesion appeared hyperechoic on ultrasound B-mode.

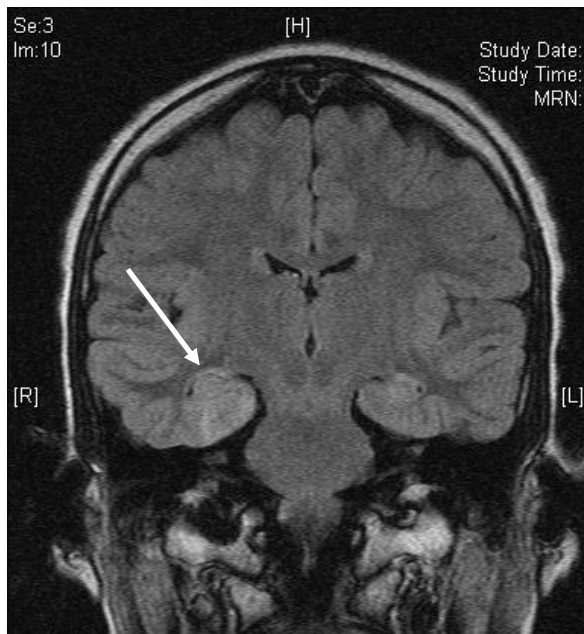


Figure 7.8: MRI FLAIR sequence for GOSH 41 showing clearly the lesion in the right mesial temporal lobe (arrow).

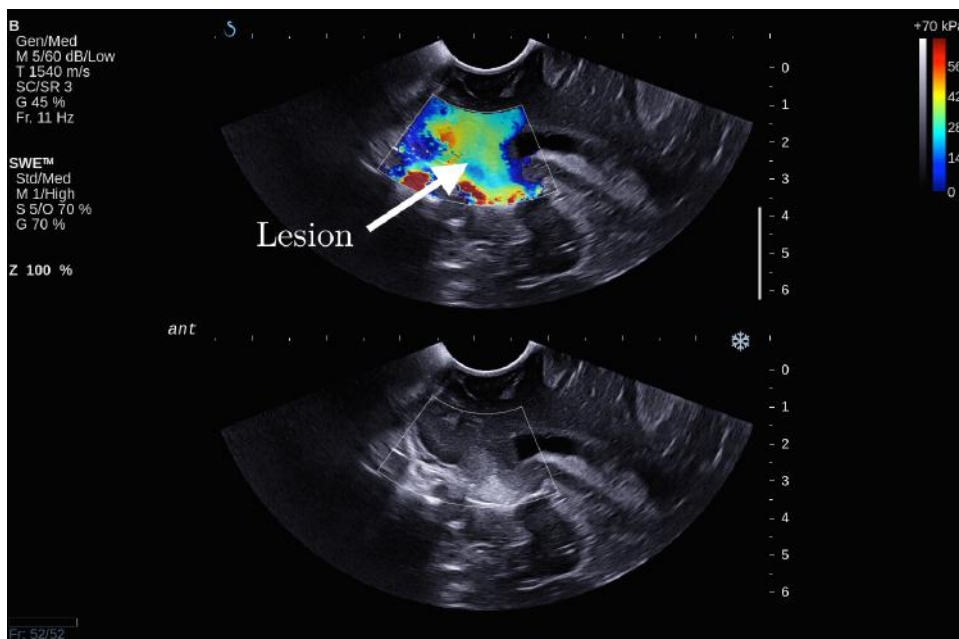


Figure 7.9: SWE for GOSH 41 showing a subtle soft lesion, which appeared as hyperechoic region on ultrasound B-mode.

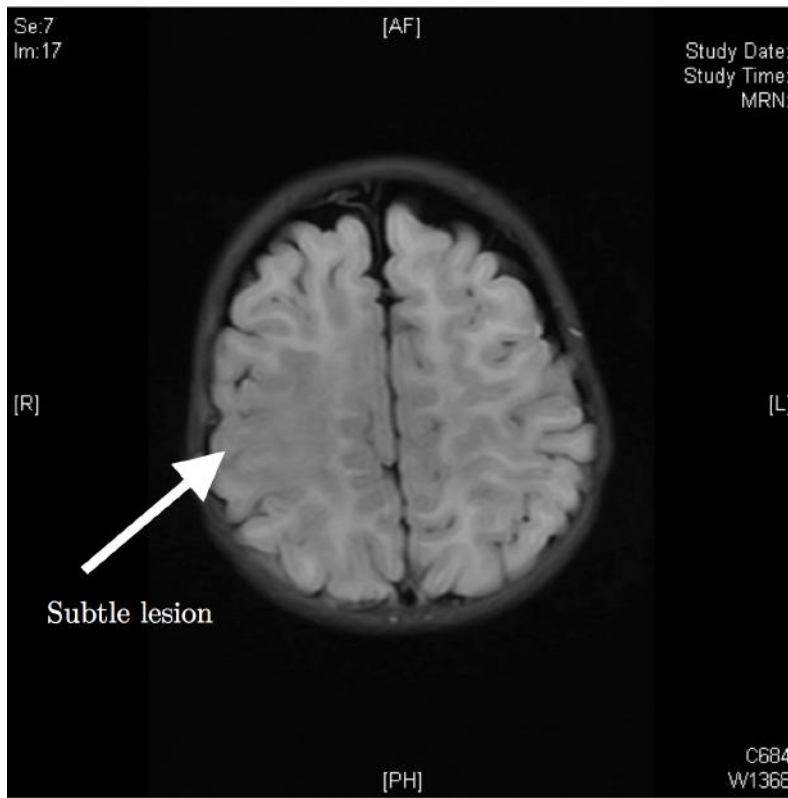


Figure 7.10: MRI FLAIR scan for GOSH 4 showing subtle lesion near the right motor strip.

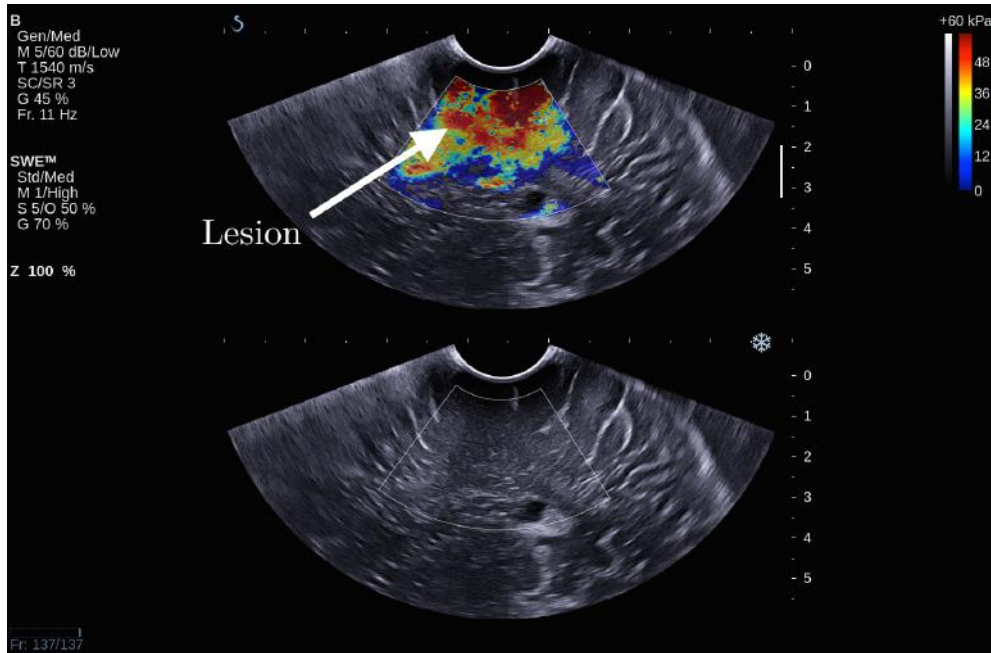


Figure 7.11: SWE for GOSH 4 showing the obvious stiff lesion.

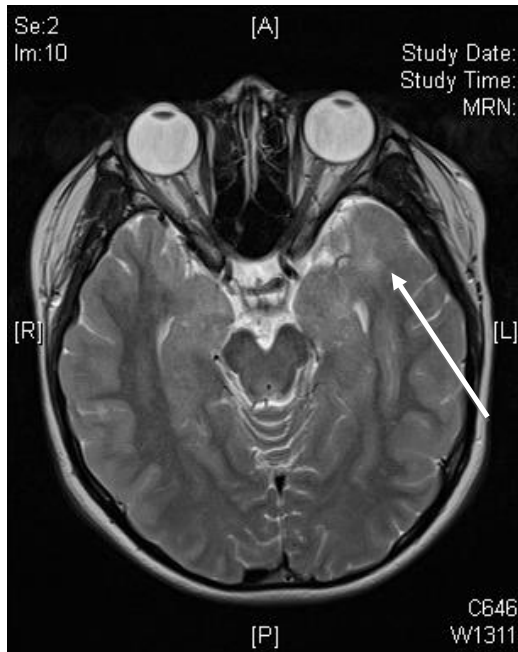


Figure 7.12: T2-weighted MRI sequence showing the subtle abnormality in the left temporal pole extending into the mesial temporal lobe (arrow).

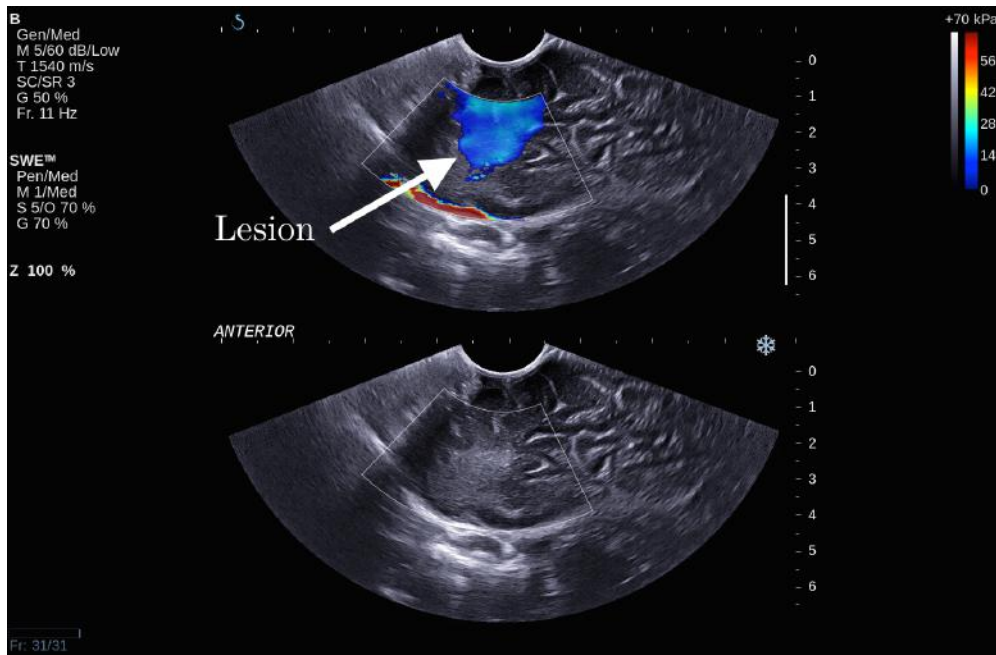


Figure 7.13: SWE for GOSH 59 showing a subtle soft lesion.

There were 2 cases (GOSH 22 and GOSH 27) where the lesions appeared obvious on both MRI and SWE but the histological results were non-diagnostic. One of them (GOSH 27) achieved seizure free status (Engel class 1) while the other one (GOSH 22) only achieved partial seizure control (Engel class 3). Figure 7.14 and Figure 7.15 illustrate the SWE for GOSH 22 and GOSH 27, respectively.

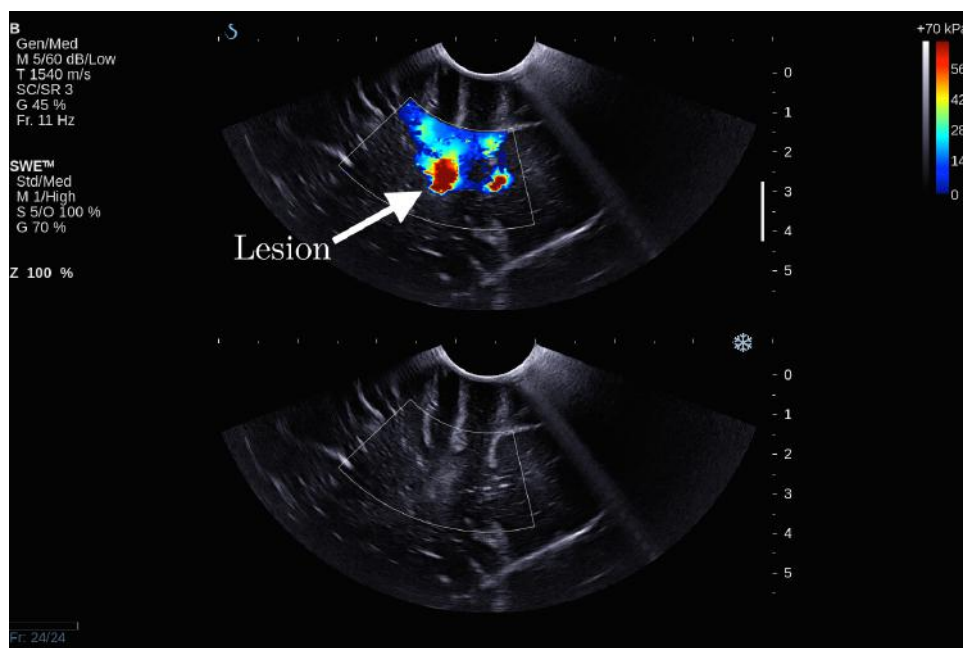


Figure 7.14: SWE for GOSH 22 showing an obvious stiff lesion with a non-diagnostic histological appearance.

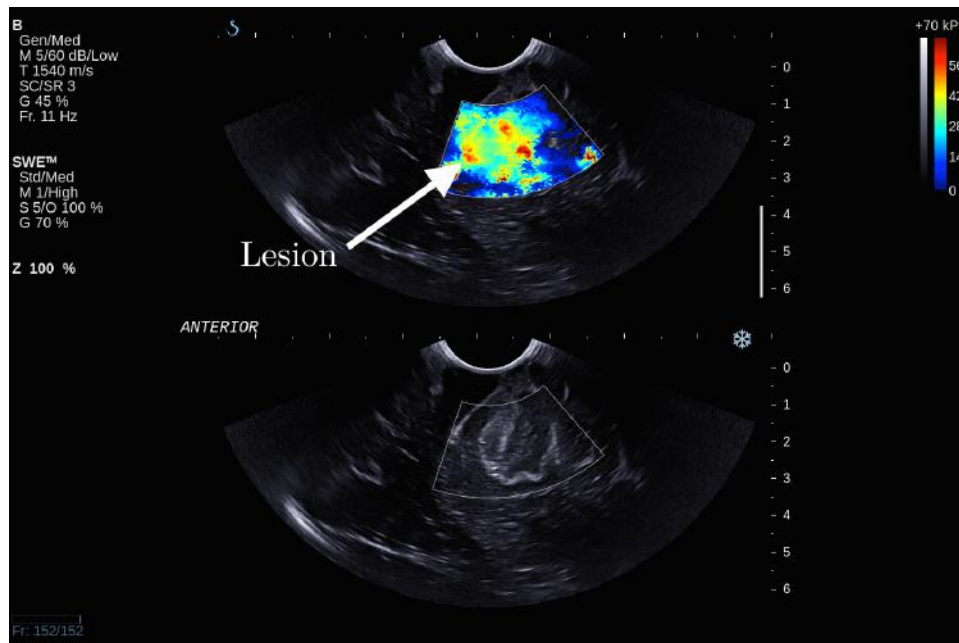


Figure 7.15: SWE for GOSH 27 showing an obvious stiff lesion with a non-diagnostic histological appearance.

#### 7.4.2.3 Overall comparison between SWE and MRI gradings

A total of 37 cases were compared for SWE and MRI gradings (Table 7.3). In Table 7.4, the Wilcoxon signed-rank test shows that the sum of signed ranks ( $W$ ) is +138.00 for SWE-MRI, meaning that SWE grades were significantly better than MRI ( $z = -3.499$ ,  $p < 0.001$ ). In other words, SWE was able to detect epileptogenic lesions better than MRI overall. When only lesional cases are analysed, the Wilcoxon signed-rank test shows that  $W$  is +77.00 for SWE-MRI, meaning that SWE grades were also significantly better than MRI ( $z = -3.051$ ,  $p = 0.002$ ), as shown in Table 7.5.

MRI \ SWE	Absent	Subtle	Obvious	Total
Absent	0	1	3	4
Subtle	0	1	12	13
Obvious	0	1	19	20
Total	0	3	34	37

Table 7.3: Contingency table for comparing SWE with MRI gradings.

		N	Mean Rank	Sum of Ranks
SWE - MRI	Negative Ranks	1 <sup>a</sup>	7.50	7.50
	Positive Ranks	16 <sup>b</sup>	9.09	145.50
	Ties	20 <sup>c</sup>		
	<b>Total</b>	<b>37</b>		<b>+137.00</b>

Table 7.4: The result of Wilcoxon signed-rank test overall. <sup>a</sup>SWE < MRI; <sup>b</sup>SWE > MRI; <sup>c</sup>SWE = MRI.

		N	Mean Rank	Sum of Ranks
SWE - MRI	Negative Ranks	1 <sup>a</sup>	7.00	7.00
	Positive Ranks	12 <sup>b</sup>	7.00	84.00
	Ties	20 <sup>c</sup>		
	<b>Total</b>	<b>33</b>		<b>+77.00</b>

Table 7.5: The result of Wilcoxon signed-rank test for just the lesional cases. <sup>a</sup>SWE < MRI; <sup>b</sup>SWE > MRI; <sup>c</sup>SWE = MRI.

### 7.4.3 Histopathological correlation

Figure 7.16 shows the Young's modulus distribution for normal brain and epileptogenic lesions. There was a significant difference between the Young's moduli for normal brain and epileptogenic lesion (median 21.9 kPa versus 58.3 kPa;  $p < 0.001$ ). The Young's modulus distribution for epileptogenic lesions grouped into tumours and non-tumours is illustrated in Figure 7.17. There was a significant difference between non-tumoural lesions and normal brain (median 21.1 kPa versus 58.4 kPa;  $p < 0.001$ ) but not for tumours and normal brain (median 23.3 kPa versus 38 kPa;  $p = 0.064$ ). Although the non-tumoural lesions seemed to have a higher Young's modulus than tumours, there was no significant difference ( $p = 0.467$ ). Wilcoxon's signed-rank test was used for statistical analysis as the data were paired and not normally distributed.

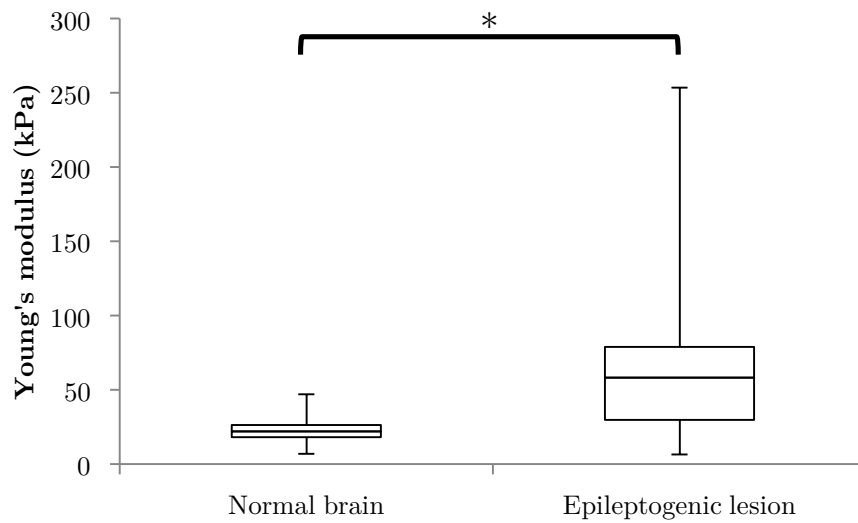


Figure 7.16: Box and whiskers plot for Young's modulus for normal brain and epileptogenic lesions. The upper and lower bounds of the box were the third and first quartiles, respectively while the line within the box was the median. The upper and lower whiskers were maximum and minimum values, respectively. \*There is statistically significant difference in the Young's modulus between normal brain and epileptogenic lesions ( $p < 0.001$ , Wilcoxon's signed-rank test).

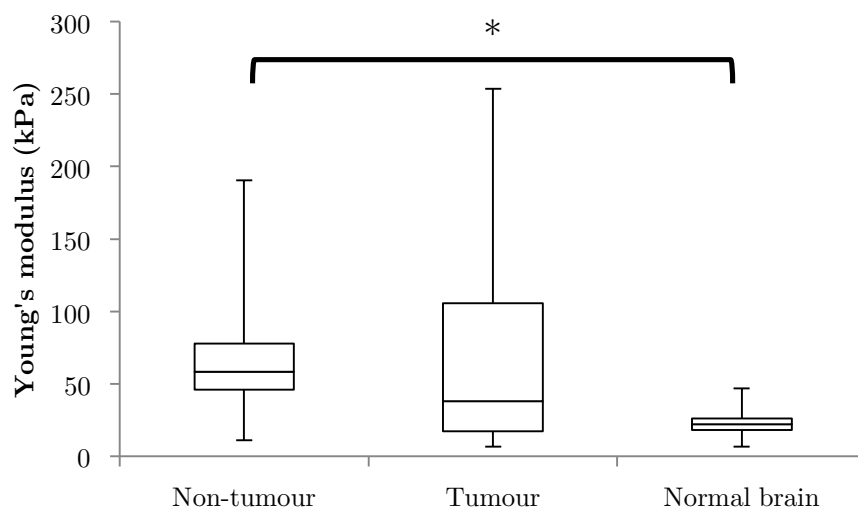


Figure 7.17: Box and whiskers plot of Young's modulus measurements for non-tumoural lesions, tumours, and normal brain. The upper and lower bounds of the box were the third and first quartiles, respectively while the line within the box was the median. The upper and lower whiskers were maximum and minimum values, respectively. \*There was a statistically significant difference in the Young's modulus between non-tumoural lesions and normal brain ( $p < 0.001$ ). There was no statistically significant difference between tumours and brain ( $p = 0.064$ ), and between tumour and non-tumour ( $p = 0.467$ ). Wilcoxon's signed-rank test was used for statistical analysis.

Further histological analyses were performed to look for cellularity, proliferation, calcification and gliosis. The Mann Whitney U test was used to perform the statistical analysis as the distribution was not Gaussian, as demonstrated in the box and whiskers plots below.

Figure 7.18 shows the Young's modulus statistical parameters for cellularity grading on histology. There was no significant Young's modulus difference between different cellularity gradings (median 59 kPa versus 56 kPa for not increased and increased cellularity, respectively;  $p = 0.699$ ).

Figure 7.19 demonstrates the Young's modulus statistical parameters measured for proliferation grading on histology. There was a non-significant increase in Young's modulus with proliferation (median 55 kPa versus 143 kPa;  $p = 0.071$ ).

Figure 7.20 is the corresponding plot for calcification grading on histology. There appeared to be a decrease in Young's modulus with the presence of calcification (median 58 kPa versus 13 kPa) but it was not significant ( $p = 0.286$ ).

Figure 7.21 illustrates the distribution of Young's modulus values for gliosis grading on histology. There seemed to be an increase in Young's modulus with gliosis (median 32 kPa versus 58 kPa) but it was not quite significant ( $p = 0.185$ ).

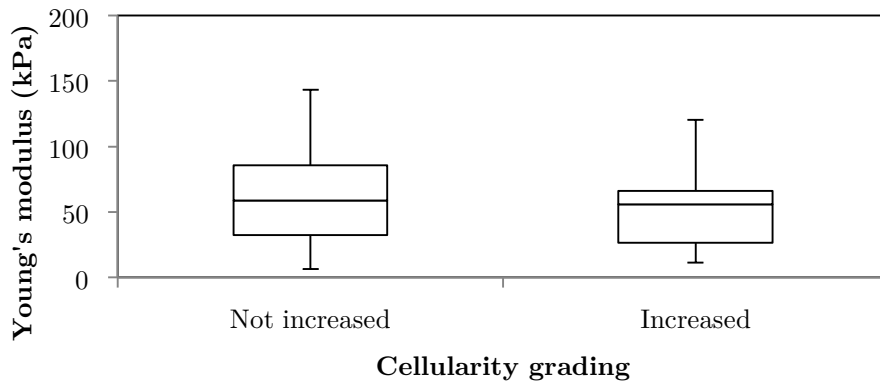


Figure 7.18: Box and whiskers plot of Young's modulus for epileptogenic lesions according to the grading of cellularity (n=29). The upper and lower bounds of the box were the third and first quartiles, respectively while the line within the box was the median. The upper and lower whiskers were maximum and minimum values, respectively. There was no statistically significant difference ( $p = 0.699$ , Mann Whitney U test).

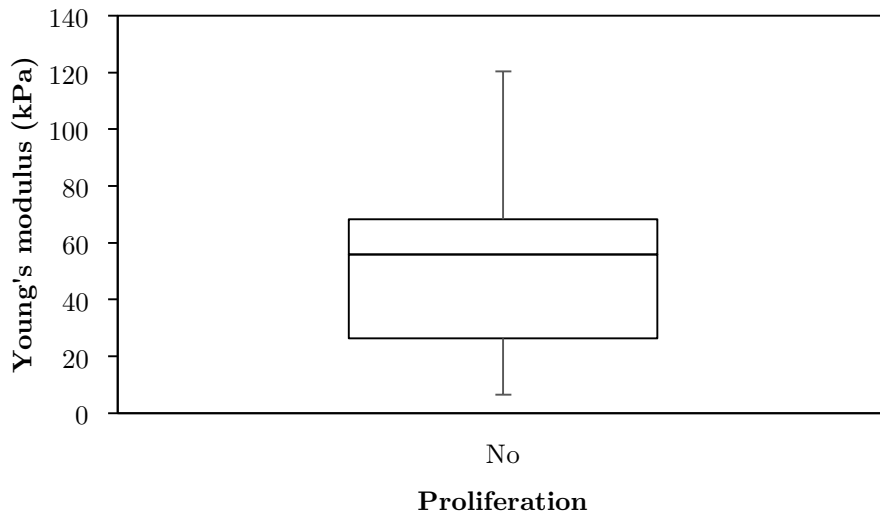


Figure 7.19: Box and whiskers plot of Young's modulus for epileptogenic lesions according to the presence of proliferation (n=28). 'No' in the horizontal axis indicates low proliferation. The upper and lower bounds of the box were the third and first quartiles, respectively while the line within the box was the median. The upper and lower whiskers were maximum and minimum values, respectively. There was only one patient (n=1) with increased proliferation with Young's modulus of 143.3kPa. Although the Young's modulus was higher in the patient with higher proliferation compared with those with lower proliferation, there was no statistically significant difference ( $p = 0.071$ , Mann Whitney U test).

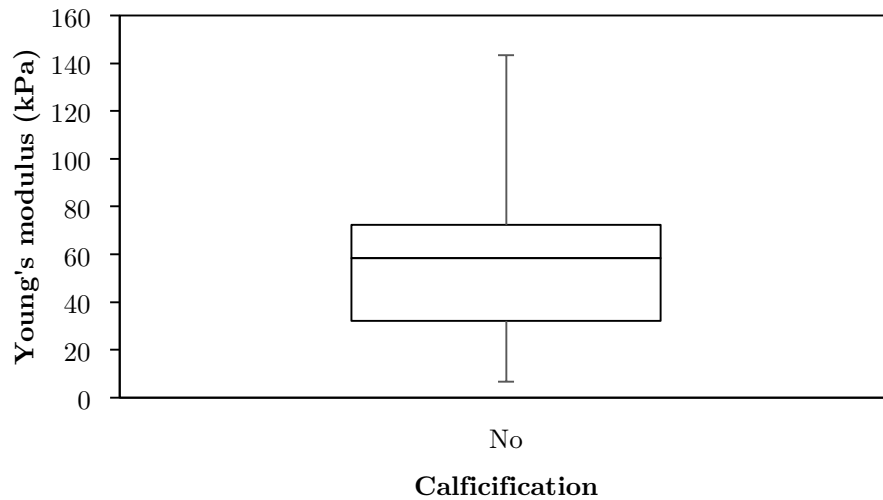


Figure 7.20: Box and whiskers plot of Young's modulus for epileptogenic lesions according to the presence of calcification ( $n=28$ ). The upper and lower bounds of the box were the third and first quartiles, respectively while the line within the box was the median. The upper and lower whiskers were maximum and minimum values, respectively. There was only one patient ( $n=1$ ) with the presence of calcification with Young's modulus of 13.3kPa. There was no statistically significant difference ( $p = 0.286$ , Mann Whitney U test).

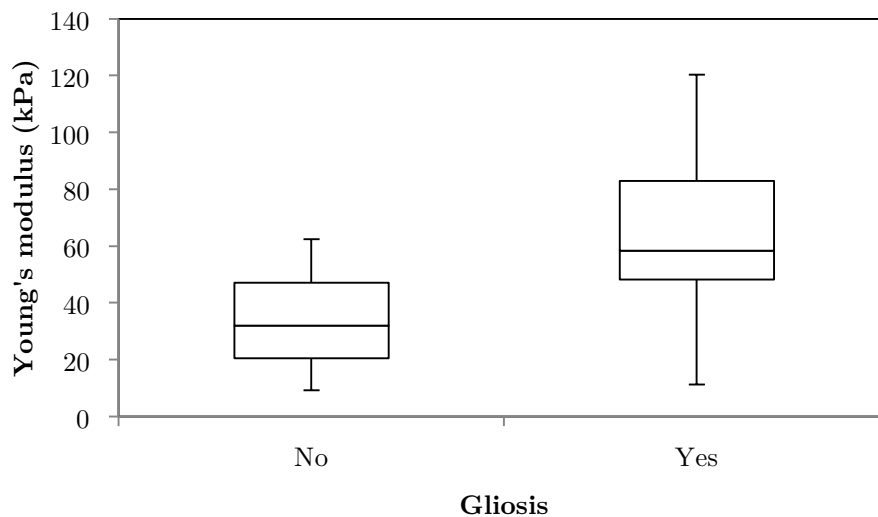


Figure 7.21: Box and whiskers plot of Young's modulus for epileptogenic lesions according to the presence of gliosis ( $n=21$ ). The upper and lower bounds of the box were the third and first quartiles, respectively while the line within the box was the median. The upper and lower whiskers were maximum and minimum values, respectively. There was no statistically significant difference ( $p = 0.185$ , Mann Whitney U test).

## 7.5 Discussion

### 7.5.1 Comparison of Young's modulus measurements with surgical findings

Overall, there was a significant correlation between Young's modulus measurements performed with SWE and surgical findings. The correlation was better for Young's modulus contrast than for Young's modulus measurements alone, which makes sense since the surgeon's grading was really a contrast grading. However, there were 4 cases where Young's modulus measurements disagreed with surgical findings.

For the softer-than-brain lesions, there was 1 case where the SWE measurement contradicted the stiffness grading. Figure 7.22 is the SWE for GOSH 65, where the lesion was felt to be softer than brain by the surgeon but the SWE was demonstrating a stiff lesion. One possible explanation is that the lesion was deep, with the superficial margin sitting approximately 2-3 cm from the brain surface. Judging from the SWE quality, there was good shear wave signal throughout, but as mentioned in Chapter 6 the depth of the lesion might cause the SWE estimation to be unreliable due to low SNR. Another possible explanation is that the surgeon was grading the stiffness of the lesion based on both visual and tactile feedback from surgical instruments deep in the surgical cavity. Therefore, there was a possibility that the tactile feedback was less accurate for deeper lesions (Perreault & Cao, 2006) and thus was subjected to variations between different surgeons. Thirdly, the surgeon who did this operation was different from the main surgeon who did the majority of the operations, thereby potentially contributing to the contradicting result (inter-operator variability).

For lesions with similar consistency to normal brain, the Young's modulus measurements were slightly higher than those in normal brain, indicating that surgical palpation was biased and tactile feedback could not differentiate the minor differences in the Young's modulus.

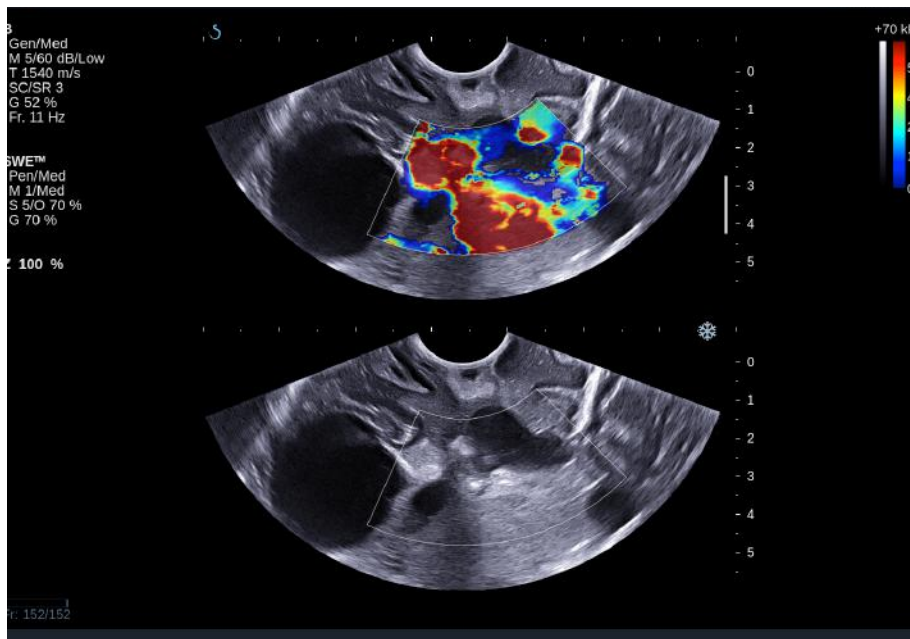


Figure 7.22. SWE of the lesion for GOSH 65 showing that the lesion was stiff (red) with its corresponding Young's modulus of  $143.3 \text{ kPa} \pm 84.8 \text{ kPa}$  (mean  $\pm$  SD). The lesion, which was recurrent ganglioglioma was hyperechoic on US B-mode.

For stiffer-than-brain lesions, there were 2 patients (GOSH 6 and NHNN 9), where SWE disagreed with surgical findings. For GOSH 6, Figure 7.4 shows that the lesion was softer than surrounding brain, which contradicted the surgical findings. As it was one of the earliest cases, the SWE settings had not been optimised. The SWE gain was set to 100%, which was shown to demonstrate artefactual stiff regions in areas of low SNR (Chapter 6). Also shown in Chapter 6, attenuating stiff layer could result in lower Young's modulus measurements in the area posterior to the layer, if 'standard' SWE mode was used. The 'standard' SWE mode was used in this case, thereby potentially giving rise to lower Young's modulus measurements, as there might be an overlying stiff cortex in this patient.

For NHNN 9, Figure 7.23 shows that the lesion was softer than adjacent brain, which appeared hyperechoic on ultrasound B-mode. The area adjacent to the hyperechoic region appeared stiff, therefore the surgeon could mistake the adjacent stiff areas for the lesion. Another possible explanation is that the hyperechoic region might be oedema (van

Velthoven & Auer, 1990), which would be soft, and the cavernoma might be isoechoic on ultrasound B-mode corresponding to the stiff region.

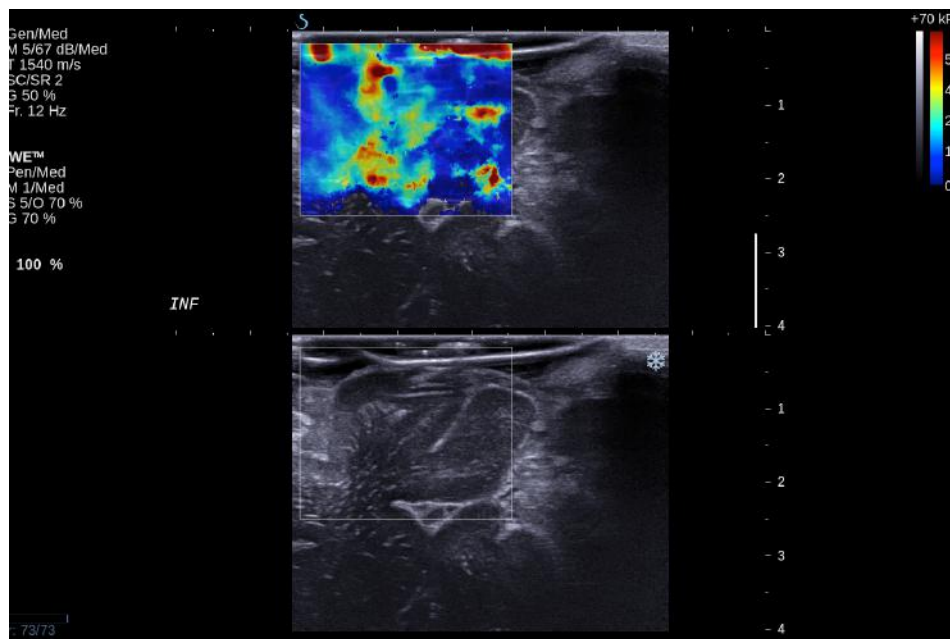


Figure 7.23. SWE of the lesion for NHNN 9 showing that the hyperechoic lesion appeared to have low Young's modulus (blue). The adjacent isoechoic region appeared to have high Young's modulus (red) compared to regions further to the right.

### 7.5.2 Comparison of SWE and MRI gradings

This study showed that SWE was superior to MRI in detecting epileptogenic lesions, based on SWE using the Young's modulus contrast criteria and MRI using the report by consultant neuroradiologist.

SWE was shown to be capable of detecting all four MRI-defined non-lesional cases with proven histological diagnosis and invasive electrophysiological recordings. All the MRI-defined non-lesional cases were located extratemporally with a 50% seizure-free outcome, which agreed with the outcomes of 14 – 63% in extratemporal cases (Ramey et al., 2013). All the lesions were stiffer than brain. Three out of four cases had Young's modulus measurement concordant with surgical findings. The one case that did not have concordance

was one of the earliest cases prior to optimisation of SWE settings. Nonetheless, the lesion was visible on SWE. In this small number of cases, it was demonstrated that SWE may be used as an intra-operative tool to guide electrode placements and resection.

In the lesional cases, SWE was superior to MRI in detecting epileptogenic lesions ( $p = 0.002$ ). In this group, 62% of the lesions were stiffer than brain, 9% similar to brain and 29% softer than brain. This finding did not agree with that of Uff (2011), who showed that all the lesions were stiffer than brain. This could be due to the small numbers in Uff (2011), as the majority of the lesions in the present study were stiffer than brain. There was one case where there was no signal in the hippocampus, thereby preventing the Young's modulus measurements. This could be due to the attenuating effect from the (abnormally stiff) temporal lobe (Figure 7.24). In this group, 65% and 73% achieved Engel class 1 and 2 status, respectively. This agreed with literature findings of 42 – 79% (Engel et al., 2012; Wiebe et al., 2001) and 64% (Wiebe et al., 2001) for Engel class 1 and 2, respectively.

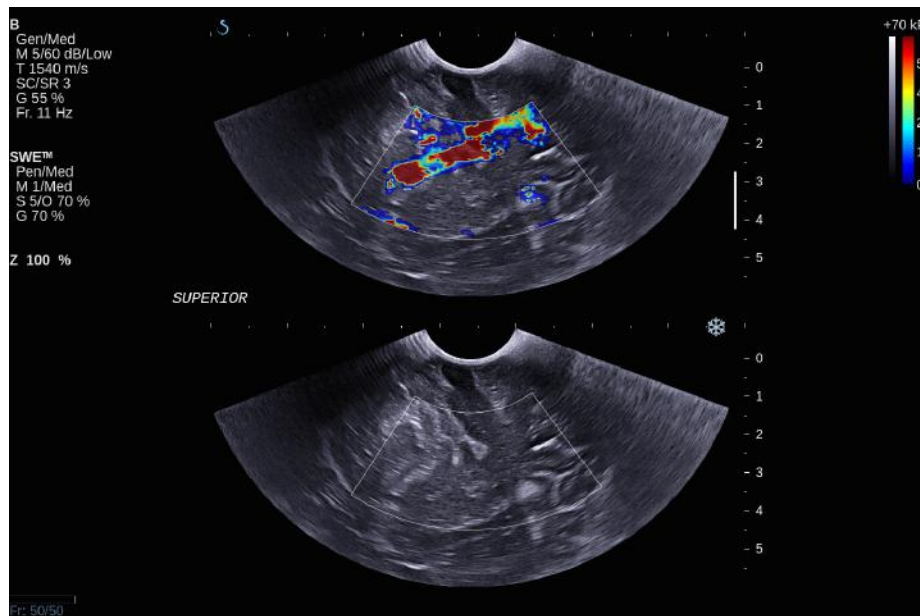


Figure 7.24: SWE for GOSH 72 showing stiff temporal lobe.

Overall, SWE was shown to be superior to MRI in detecting epileptogenic lesions ( $p = 0.001$ ). Currently, there has been no literature comparing SWE appearance with MRI for epileptogenic lesions. As the MRI grading was performed according to the report by the neuroradiologist on duty, the result might be subjected to bias. Therefore, in future, MRI grading should be done with multiple neuroradiologists for each MRI dataset to improve the robustness of the grading. As with SWE grading, the Young's modulus contrast cutoff seemed to be satisfactory but the Young's modulus contrast results were dependent on where the Q-box was placed. To improve the accuracy of Young's modulus measurements, the images could be exported into MATLAB® (MATLAB, 2010), and the area of interest could be outlined to include irregular regions.

### 7.5.3 Histopathological correlation

This study showed that the Young's moduli for epileptogenic lesions were significantly higher than normal brain in each case using paired analysis ( $p < 0.001$ ), thereby demonstrating that SWE measurement of Young's modulus was capable of differentiating epileptogenic lesions from surrounding normal brain. By further dividing the epileptogenic lesions into tumours and non-tumoural lesions, the Young's moduli for non-tumoural lesions were significantly higher than normal brain when compared using paired analysis ( $p < 0.001$ ). This means that SWE was capable of detecting non-tumoural epileptogenic lesions. The Young's moduli for epileptogenic tumours were also higher than normal brain, and it almost reached a statistical significance with paired analysis ( $p = 0.064$ ). The number of tumour cases was only 14 compared with 24 in non-tumoural cases. Therefore, further validation with more cases will be required to show the capability of SWE in detecting epileptogenic tumours. Currently, there has been no literature assessing the Young's modulus of epileptogenic lesions.

There were 2 lesional cases (GOSH 22 and GOSH 27), who had non-diagnostic appearance on histology. Although GOSH 22 had a non-diagnostic appearance on histology, further analysis showed the presence of gliosis. However, the seizure outcome was poor (Engel class 3), indicating that the epileptogenic lesion might have been incompletely

resected. Another possible explanation is that the actual lesion could have been absent on imaging and the lesion showing on both MRI and SWE was the surrounding brain with gliosis. GOSH 27 did not have any diagnostic features even on further histological analysis. Despite this, the patient achieved a seizure-free status (Engel class 1), which could mean that the lesion was completely resected and the specimen sent to the laboratory was not of the lesion.

Further analysis comparing histological features with Young's modulus failed to show any correlation. The Young's modulus did not change significantly between lower and higher cellularity grading. This could be due to the stiffness being contributed by the supporting stroma rather than the tumour cells *per se*. The Young's modulus seemed to increase with proliferation but the results failed to reach statistical significance ( $p = 0.071$ ). This agreed with the finding in colon tumours where  $|G^*|$  increased with proliferation, as shown by a significant increase in cellularity between the early and advanced stages in the ectopic model (Juge et al., 2012). The authors also showed that the  $|G^*|$  did not increase in the orthotropic model, where there was no significant increase in cellularity between the early and advanced stages (Juge et al., 2012).

The Young's modulus also showed a non-significant increase with gliosis ( $p = 0.185$ ). In a mechanically-induced injury in cultured astrocytes, reactive gliosis was shown to have lower Young's modulus than naïve astrocytes (Miller W.J. et al., 2009). This could be due to the gliosis process in epileptogenic lesions being more chronic compared to acutely injured astrocytes, giving rise to glial scar which involves active proliferation of astrocytes, which could result in increased elastic modulus. The Young's modulus showed a non-significant negative correlation with calcification, which was unusual but the numbers were very small, with only one specimen having calcification. Unfortunately, further histological analysis failed to show any correlation between Young's modulus and histological features. However, there was an almost significant correlation between Young's modulus and proliferation, so further study with more cases may confirm this finding.

## 7.6 Conclusions

The work reported in this chapter showed that the Young's modulus measurements and contrast correlated significantly with surgical findings. In all four cases where MRI reported an absence of a lesion, SWE was capable of detecting the lesions. SWE was shown to be superior to MRI in detecting epileptogenic lesions. There was significantly higher Young's modulus in epileptogenic lesions, especially non-tumoural lesions, compared to normal brain in the same patients, thus demonstrating that SWE measurements of Young's modulus was capable of differentiating epileptogenic lesions from normal brain. Although Young's modulus measurements seemed to have a positive correlation with proliferation and gliosis, which was almost significant, and therefore represent encouragement for further study with larger numbers.

## Chapter 8

# Clinical Application of Intra-operative Shear Wave Elastography in Brain Tumour Resection

This chapter presents the first evaluation of the clinical applicability of intra-operative SWE during brain tumour resection. It reports the comparison between SWE measurements and surgical findings. It also compares SWE findings of residual tumour with post-operative MRI scan. It concludes by reporting on the correlation between SWE measurements and histological features of the tumours.

## 8.1 Introduction

As elaborated in Chapter 2, the clinical outcomes for brain tumour resection have been shown to be significantly improved with increased extent of resection (Capelle et al., 2013; Claus et al., 2005; Hervey-Jumper & Berger, 2014; Keles et al., 2001; Lacroix et al., 2001; Laws et al., 2003; McGirt et al., 2008, 2009; Nakamura et al., 2000; Nomiya et al., 2007; Oszvald et al., 2012; Sanai et al., 2011; Shaw et al., 2002; Smith et al., 2008; Stummer et al., 2008; Ushio et al., 2005; Vuorinen et al., 2003; Yeh et al., 2005). To achieve this, neurosurgeons employ different intra-operative tools to improve the extent of resection of brain tumours (Gronningsaeter et al., 2000; Lunsford et al., 1984; Senft et al., 2011; Stummer et al., 2006). Although neuronavigation with pre-operative imaging is indispensable in providing useful information for craniotomy planning, it is susceptible to structural shift during resection (Dorward et al., 1998). Intra-operative MRI (iMRI) has been shown to significantly improve the extent of resection and clinical outcomes (Senft et al., 2011) of brain tumours by providing high resolution imaging. However, iMRI increases operative time by up to 107 minutes (Senft et al., 2011; Shah et al., 2012) and is not widely available, especially in the less affluent neurosurgical units. Furthermore, it provides only infrequent (one or two) opportunities to image during surgery. By providing real-time intra-operative imaging with nearly unlimited imaging opportunity and minimal effect on operative time, intraoperative US (IOUS) has also been shown to provide significant improvement the extent of resection (Hammoud et al., 1996; Le Roux et al., 1992), even without integration with neuronavigation (Renovanz et al., 2014). However, the artefacts of IOUS such as post-resection hyperechoic rim (Erdoğan et al., 2005; Woydt et al., 1996), post-surgical and post-radiation artefacts (Hammoud et al., 1996), acoustic shadowing from Surgicel (Erdoğan et al., 2005), peritumoural-oedema hyperechogenicity (van Velthoven & Auer, 1990), and hyperechoic blood (van Velthoven & Auer, 1990), may pose difficulty in IOUS interpretation.

Intra-operative ultrasound strain elastography has been shown to demonstrate better tumour-brain contrast than ultrasound B-mode (Selbekk et al., 2012), and is reliable in predicting tumour stiffness (Chakraborty et al., 2004; Scholz et al., 2007, 2005; Selbekk et al., 2010, 2005; Uff et al., 2009). In addition, QSE has been shown to characterise tumour-brain

interface through the appearance of high strain for the presence of slip plane (Chakraborty et al., 2012; Chakraborty, 2007; Uff, 2011). In Chapter 6, using gelatine phantoms, SWE was shown to possess soft ‘brackets’ features on either side of the inclusion which might eventually be characterise mobile inclusion-background interface. In Chapter 5, SWE measurements of brain lesions were shown to correlate well with surgical findings, supported by the preliminary study by Uff (2011), thereby providing quantitative elasticity imaging for brain tumours. Due to artefacts in IOUS (see above) and inaccuracies of neurosurgeons in estimating residual tumour intra-operatively (Albert et al., 1994; Orringer et al., 2012), SWE may be used to differentiate residual tumour from artefacts on IOUS and therefore, may serve as a useful adjunct to guide tumour resection..

## 8.2 Aims

The aims of this study are as follows:

1. To determine the level of agreement between SWE measurements of Young’s modulus in various brain tumours with surgical grading of stiffness.
2. To determine the accuracy of SWE in detecting tumour residual, using post-operative MRI as the ‘gold standard’.
3. To determine the ability of SWE to characterise tumour-brain interface clinically.
4. To determine whether SWE measurements of brain tumours are correlated with either tumour type, or with histological characteristics. The former would provide diagnostic information while the latter would assist understanding of what causes a given tumour to be hard or soft.

## 8.3 Methods

### 8.3.1 Patient selection

Patients were recruited from Great Ormond Street Hospital for Children and The National Hospital for Neurology and Neurosurgery. The inclusion criteria were as follows:

1. They were diagnosed with brain tumour, and
2. They had consented to undergo craniotomy and resection or open biopsy of the tumour, and
3. They have given their consent for this study, or their parents have given their consent on their behalf for this study if they are under 16 years old.

Those who had consented for craniotomy but underwent neuronavigation-guided biopsy (burr hole biopsy), were excluded because the surgeon would be unable to comment on the stiffness of the tumour, and it would not be possible to perform intra-operative SWE with the SuperSonic® Aixplorer.

### 8.3.2 Operating room protocol

The operating room setup is described in Chapter 3. After anaesthesia, the patient was transferred to the operating table and his/her head was pinned with a Mayfield clamp to immobilise the head. Stealth® neuronavigation registration was performed to plan the craniotomy placement. The location of the tumour was determined with neuronavigation. For intrinsic tumours, SWE was performed after durotomy and prior to corticotomy, whereas SWE was performed prior to durotomy for extrinsic tumours as they are often be adhered to the dura. After the initial scan, the resection was initiated. The resection was continued until such time when the surgeon felt that he wanted to check the extent of resection or to confirm the location of the tumour. At this time, IOUS was again performed with SWE simultaneously to assess the extent of resection or to confirm the location of the tumour. Final SWE was performed to assess the final extent of resection prior to closure of craniotomy.

### 8.3.3 Data acquisition

After craniotomy, the ultrasound transducer was placed in a sterile sheath filled with acoustic coupling gel. The SWE mode on the SuperSonic Aixplorer® scanner was then activated. The scans were performed on exposed cortex for intrinsic tumours and on closed dura for extrinsic tumours. Without informing the surgeon about the SWE findings beforehand, the surgeon was asked to grade the stiffness of the lesions from 1 to 5 as follows:

1. The lesion is very soft like cyst.
2. The lesion is softer than brain.
3. The lesion is similar to brain.
4. The lesion is stiffer than brain.
5. The lesion is very stiff like cartilage.

During the resection, the surgeon was also asked to grade the tumour-brain interface as mobile or adhered based on intraoperative findings. In both cases, the SWE appearance was analysed by the author to look for correlation with ‘soft bracket’ signs (Chapter 6).

After the resection was deemed complete by the surgeon, SWE was performed to determine if there was tumour residual. The tumour residual was graded by the author as either present or absent on both SWE and B-mode. The Q-box function was used to measure the Young’s modulus for the tumour bed and adjacent brain.

### 8.3.4 Data analysis

The Young’s modulus measurements and Young’s modulus contrast were compared with surgical findings. The tumour-brain interface on SWE was analysed and compared with surgical findings. The intra-operative findings by SWE, B-mode and the surgeon were compared with post-operative MRI. The Young’s modulus measurements were also compared with histology to determine if there was any correlation with tumour type. Further histological analysis was carried out by Dr Tom Jacques, consultant

neurohistopathologist at Great Ormond Street Hospital, to assess the presence of calcification, proliferation, cellularity and gliosis. These were chosen because these were the common histological features that are commonly present in brain tumours. For each case, the standard procedure was followed where tissue samples were sent to histology fixed in formalin, where sections were cut, stained and examined in the following way for subjective scoring of each of the histological characteristics. A single neurohistopathologist judged all cases, which allowed personal bias to influence the results but avoided interobserver variability. The histological scores were then compared with Young's modulus measurements.

Statistical analysis using Spearman's rank correlation, a non-parametric statistical test, was performed for comparison of Young's modulus measurements and Young's modulus contrast with surgical findings, because the grading of stiffness was ordinal and discrete whereas Young's modulus and Young's modulus contrast were continuous. McNemar's test was used to compare SWE, B-mode and surgeon's opinions with post-operative MRI, which was considered the 'gold standard', and also SWE with surgeon's opinions. This test uses  $2 \times 2$  contingency tables with dichotomous, that is either a 'Yes' or 'No' in this case, result for paired data. Statistical analysis was performed using Student's t-test and Mann Whitney U test to compare Young's modulus measurements for different histological diagnoses, when the Young's modulus distribution was Gaussian and non-Gaussian, respectively. For paired data comparing Young's modulus measurements for brain tumours and corresponding surrounding brain, paired Student's t-test and Wilcoxon signed-rank test were used for normally and non-normally distributed data. These statistical tests were selected after advice from Dr Zoe Fox, the statistician from Institute of Neurology, University College London.

## 8.4 Results

A total of 35 patients were recruited into the study. The summary of the cases is given in Table 8.1.

Research number	Age	Gender	Diagnosis	YM (kPa) (mean $\pm$ SD <sup>†</sup> )	YMC	Stiffness grading	Residual (Surgeon)	Residual (B-mode)	Residual (SWE)	Residual (MRI)
GOSH 1	12	M	Low grade astrocytoma	26.2 $\pm$ 3.1	0.297	2	No	Yes	No	No
GOSH 3	11	F	sPNET <sup>‡</sup>	35.6 $\pm$ 4.5	0.361	2	No	Yes	Yes	Yes
GOSH 5	1	F	Choroid plexus papilloma	13.2 $\pm$ 2.6	-0.064	2	No	Not done	Not done	No
GOSH 10	6	F	Epidermoid cyst	182.4 $\pm$ 15.6	0.772	4	No	No	No	Yes
GOSH 16	11	F	Residual sPNET <sup>‡</sup>	164.4 $\pm$ 48.4	0.692	4	No	No	No	No
GOSH 17	15	M	Pilomyxoid astrocytoma	9.7 $\pm$ 1.7	-0.224	2	Yes	Yes	Yes	Yes
GOSH 25 <sup>§</sup>	8	F	SEGA <sup>§§</sup>	300 $\pm$ 0	N/A	4	No	No	Yes	No
GOSH 29 <sup>§</sup>	6	F	SEGA <sup>§§</sup>	300 $\pm$ 0	N/A	4	No	No	No signal	No
GOSH 32	6	M	Metastasis from clear cell sarcoma of the kidney	241.6 $\pm$ 21	0.788	5	No	No	Yes	Yes
GOSH 35	15	M	GBM <sup>§§</sup>	154.4 $\pm$ 20.9	0.748	4	Yes	Yes	Yes	Yes
GOSH 40	2	F	Pilocytic astrocytoma	17.8 $\pm$ 1.5	-0.285	2	No	Yes	Yes	Yes
GOSH 45	2	M	ATRT <sup>&amp;‡</sup>	159.1 $\pm$ 82.3	0.802	5	Yes	No	Yes	Yes
GOSH 47	14	M	Recurrent pleomorphic xanthoastrocytoma	197.8 $\pm$ 2.4	0.681	N/A	Yes	Yes	Yes	Not done*
GOSH 49	1	F	ETANTR <sup>‡‡</sup>	4.2 $\pm$ 0.9	-0.720	2	Yes	Yes	Yes	Not done <sup>§</sup>
GOSH 52	3.3	M	Pineoblastoma	196.3 $\pm$ 23.6	0.920	4	Yes	Yes	Yes	Yes
GOSH 53	1.1	M	Choroid plexus papilloma	11.9 $\pm$ 5.9	-0.290	2	No	No	No	No
GOSH 55	7	F	Anaplastic ganglioglioma	11 $\pm$ 3.9	-0.102	2	No	No	No	No
GOSH 56	17	F	Pleomorphic xanthoastrocytoma with anaplasia	11.2 $\pm$ 1.4	-0.138	2	Yes	Yes	Yes	Yes

GOSH 61	15	M	Recurrent pilocytic astrocytoma	146.4 ± 14.1	0.889	4	Yes	Yes	Yes	Yes
NHNN 2	43	F	Meningioma	39.5 ± 1.2	0.771	4	No	Yes	No	No
GOSH 67	1	M	ATRT <sup>&amp;&amp;</sup>	33.6 ± 8.6	0.559	2	No	Yes	No	No
GOSH 68	1	F	Residual choroid plexus papilloma	178.9 ± 57.6	0.921	4	No	Yes	Yes	Yes
NHNN 4	53	M	GBM <sup>§§</sup>	7.3 ± 3.2	-0.170	2	No	No	Yes	Yes
NHNN 5 <sup>‡</sup>	39	M	Residual medulloblastoma	33.1 ± 8.6	0.458	3	No	N/A	N/A	No
NHNN 7	61	F	GBM <sup>§§</sup>	12.3 ± 1.3	0.070	2	No	No	Yes	Yes
NHNN 8	46	F	GBM <sup>§§</sup>	3 ± 0.9	-0.439	2	No	Yes	Yes	Yes
NHNN 10	62	M	Vestibular schwannoma	153.8 ± 56.3	0.870	4	Yes	Yes	Yes	Yes
NHNN 11	49	F	Meningioma	5.6 ± 2	-0.158	2	No	Yes	No signal	Yes
NHNN 12	40	M	GBM <sup>§§</sup>	9.9 ± 4.9	-0.823	2	No	Yes	No signal	Yes
NHNN 13	35	F	Pilocytic astrocytoma	31.8 ± 5.7	0.216	2	No	Yes	Yes	No
NHNN 14	49	F	Metastasis from breast	97.6 ± 42	0.711	4	No	Yes	Yes	Yes
NHNN 15	56	F	Meningioma	46.2 ± 24.2	0.505	4	No	No	No	No
GOSH 73	5	F	Pilocytic astrocytoma	11.4 ± 0.7	-0.088	2	No	Yes	Yes	Yes
GOSH 76	10	M	Anaplastic ependymoma	77.1 ± 11.4	0.858	2	No	No	No signal	No

Table 8.1: Summary of brain resection cases recruited into this study. <sup>¶</sup> Standard deviation. <sup>\*</sup> It was converted to biopsy due to excessive bleeding. <sup>§</sup> It was a case of known residual due to invasion into brainstem. <sup>‡</sup> The patient developed air embolus during surgery so the post-operative scan was abandoned. <sup>§</sup> The calculation of YMC for these cases was not possible as the lesions were subventricular and the adjacent brain was too deep for shear wave to penetrate. <sup>‡</sup> Supratentorial primitive neuroectodermal tumour. <sup>§§</sup> Subependymal giant cell astrocytoma. <sup>&&</sup> Atypical teratoid/rhabdoid tumour. <sup>§§</sup> Glioblastoma multiforme. <sup>‡‡</sup> Embryonal tumour with abundant neuropil and true rosettes.

### 8.4.1 Comparison of Young's modulus measurements with surgical findings

One patient (GOSH 47) was excluded for comparison because the surgeons could not ascertain the stiffness of the tumour due excessive bleeding upon opening the dura, which resulted in the operation being abandoned.

There was overall a significant correlation between Young's modulus measurements and surgical grading (Spearman's rank correlation coefficient ( $\rho$ ) = 0.845,  $p < 0.001$ ), illustrated in Figure 8.1. The correlation between the Young's modulus contrast and surgical grading was also significant ( $\rho = 0.780$ ,  $p < 0.001$ ), as illustrated in Figure 8.2. The calculation of Young's modulus contrast for GOSH 25 and GOSH 29 was not possible as the tumour, SEGA, was located under the ventricle and the adjacent brain could not be imaged with SWE due to lack of signal (see Figure 8.1 and Figure 8.2).

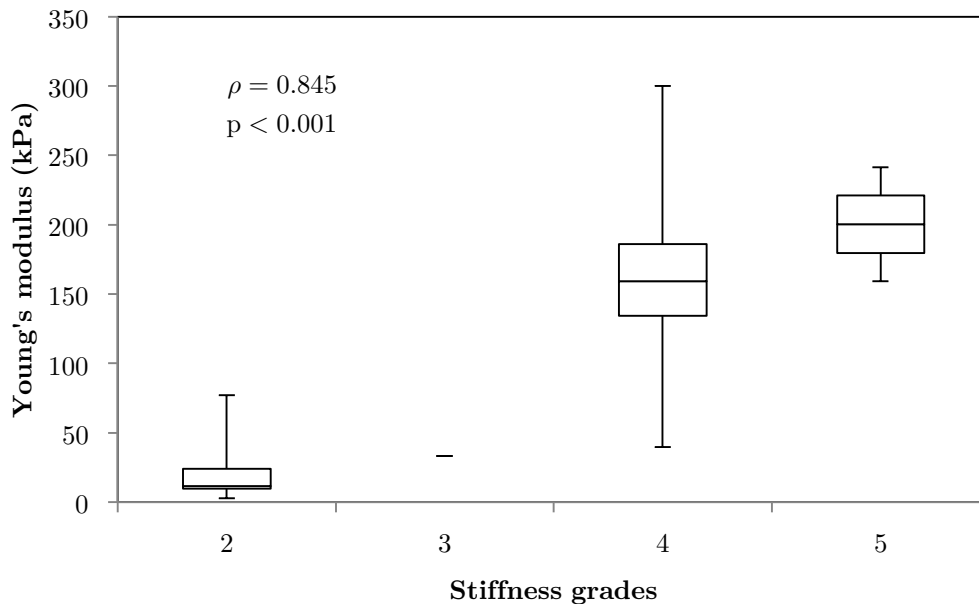


Figure 8.1: Box and whiskers plot for Young's modulus measurements according to stiffness grade assessed by independent surgical opinion ( $n=34$ ). The upper and lower bounds of the box were the third and first quartiles, respectively while the line within the box was the median. The upper and lower whiskers were maximum and minimum values, respectively.

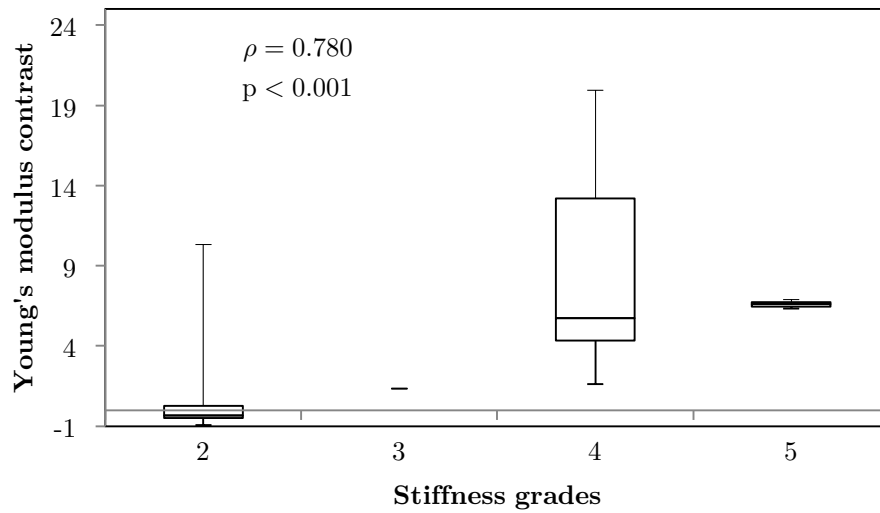


Figure 8.2: Box and whiskers plot for Young's modulus contrast according to stiffness grade assessed by independent surgical opinion (n=32). The upper and lower bounds of the box were the third and first quartiles, respectively while the line within the box was the median. The upper and lower whiskers were maximum and minimum values, respectively.

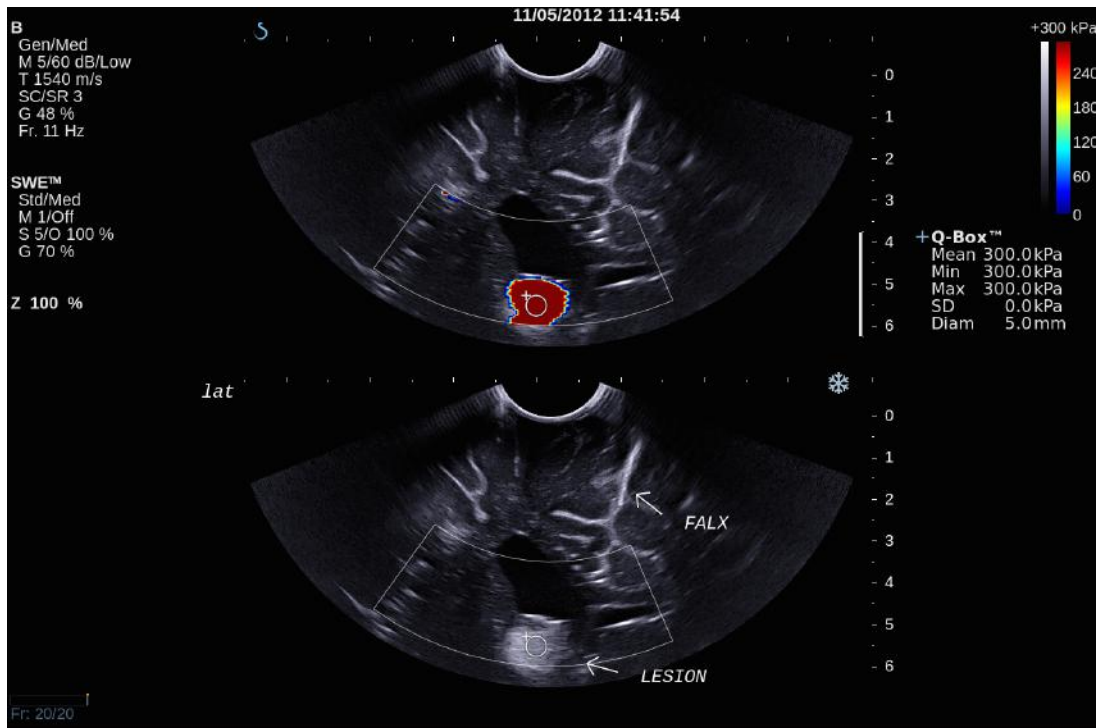


Figure 8.3: Intra-operative SWE for GOSH 25 showing the tumour lying under the ventricles. The adjacent deep grey matter did not have any SWE signal.

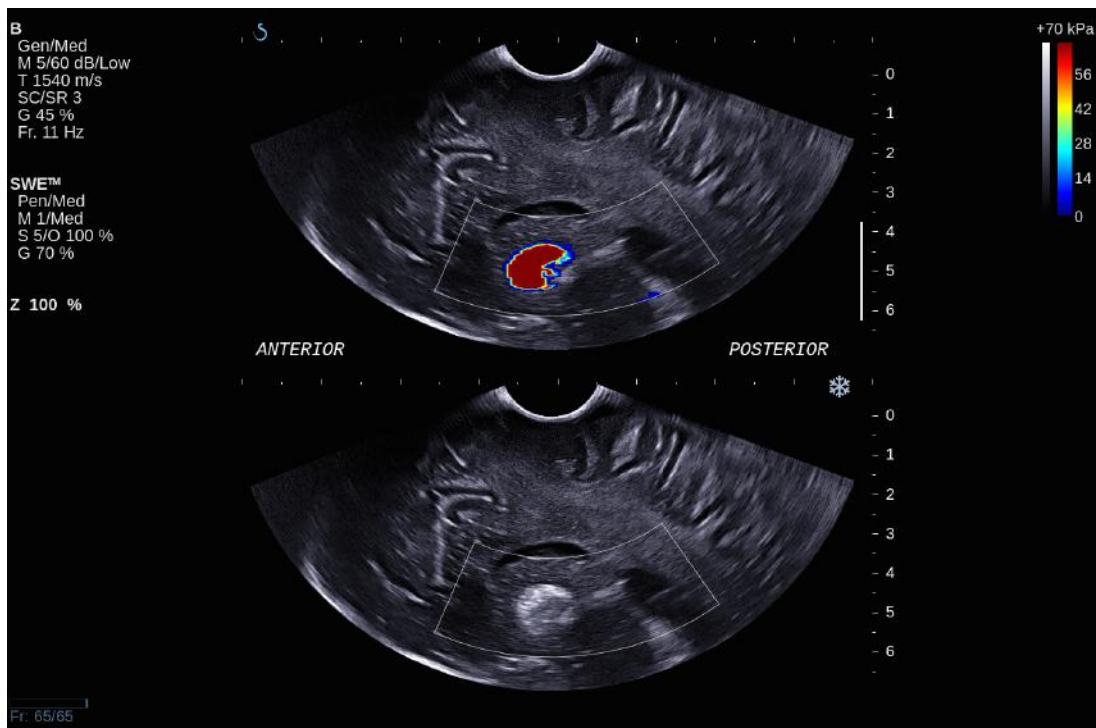


Figure 8.4: Intra-operative SWE for GOSH 29 showing the tumour lying under the ventricles at a depth of 5 cm from the transducer. There was a lack of SWE signal in the adjacent brain.

### 8.4.2 Residual tumour detection

Table 8.2 shows the 2×2 contingency table comparing SWE with MRI findings on the presence of residual tumour. Using MRI as the ‘gold standard’, the sensitivity and specificity of SWE for detection of residual tumour identified by MRI were 94% and 77%, respectively. McNemar’s test showed no statistically significant difference between SWE and MRI in the number of cases in which residual tumour was and was not detected ( $p = 1.000$ ).

SWE \ MRI	Residual tumour	No residual tumour	Total
Residual tumour	16	2	18
No residual tumour	1	7	8
Total	17	9	26

Table 8.2: McNemar's 2×2 contingency table comparing intra-operative SWE with post-operative MRI for detecting residual tumour. No statistically significant difference was detected between SWE and MRI for detecting residual tumour ( $p = 1.000$ ).

The sensitivity and specificity of US B-mode for the same task were 73% and 63%, respectively, using MRI as the ‘gold standard’ (see Table 8.3). McNemar’s test showed no statistically significance between US B-mode and MRI for for detecting residual tumour ( $p = 1.000$ ).

B-mode \ MRI	Residual tumour	No residual tumour	Total
Residual tumour	14	4	18
No residual tumour	5	7	12
Total	19	11	30

Table 8.3: McNemar's 2×2 contingency table for comparing intra-operative US B-mode with post-operative MRI scan in detecting residual tumour. No statistically significant difference was detected between US B-mode and MRI for detecting residual tumour ( $p = 1.000$ ).

When comparing surgeon’s findings with MRI, there was a statistically significant difference ( $p < 0.001$ ), as illustrated in Table 8.4. The sensitivity and specificity of surgeon’s opinion on whether residual tumour was present were 36% and 100%, respectively.

Surgeon \ MRI	Residual tumour	No residual tumour	Total
Residual tumour	7	0	7
No residual tumour	12	13	25

<b>Total</b>	<b>19</b>	<b>13</b>	<b>32</b>
--------------	-----------	-----------	-----------

Table 8.4: McNemar's  $2 \times 2$  contingency table for comparing surgeon's intra-operative opinion with post-operative MRI scan in detecting residual tumour. A statistically significant difference was detected between surgeons's opinion and MRI for determining whether there was residual tumour or not ( $p < 0.001$ ).

When comparing SWE with US B-mode, there was no statistically significant difference between them ( $p = 0.727$ ), as shown in Table 8.5.

<b>SWE \ B-mode</b>	<b>Residual tumour</b>	<b>No residual tumour</b>	<b>Total</b>
<b>Residual tumour</b>	15	5	<b>20</b>
<b>No residual tumour</b>	3	5	<b>8</b>
<b>Total</b>	<b>18</b>	<b>10</b>	<b>28</b>

Table 8.5: McNemar's  $2 \times 2$  contingency table for comparing intra-operative SWE with B-mode in detecting residual tumour. No statistically significant difference was detected for SWE and B-mode for detecting residual tumour ( $p = 0.727$ ).

When comparing SWE against surgeon's findings, there was a statistically significant difference between them ( $p = 0.001$ ), as shown in Table 8.6.

<b>SWE \ Surgeon</b>	<b>Residual tumour</b>	<b>No residual tumour</b>	<b>Total</b>
<b>Residual tumour</b>	9	11	<b>20</b>
<b>No residual tumour</b>	0	8	<b>8</b>
<b>Total</b>	<b>9</b>	<b>19</b>	<b>28</b>

Table 8.6: McNemar's  $2 \times 2$  contingency table for comparing intra-operative SWE and surgeon's opinion in detecting residual tumour. A statistically significant difference was detected for SWE and surgeon's opinion of the presence of residual tumour. ( $p = 0.001$ ).

### 8.4.3 Characterisation of tumour-brain interface

Of the 35 patients, there were only 4 cases with a slippery boundary at the tumour-brain interface detected intra-operatively during resection by the surgeons (NHNN 2, NHNN 11, NHNN 15 and GOSH 55). The intra-operative SWE images for these cases were analysed to determine if there was any evidence of the soft 'bracket' sign. For comparison,

the images for the remaining cases, where there was no slippery boundary detected intra-operatively by the surgeons, were also evaluated to look for the absence of this sign.

Of the 4 cases with a slippery boundary, 3 cases showed the presence of the soft 'bracket' sign. Figure 8.5, Figure 8.6, and Figure 8.7 are the SWE images for NHNN 2, NHNN 15 and GOSH 55, respectively, illustrating the soft 'bracket' sign. The case that did not demonstrate the sign did not produce enough SWE signal due to insufficient water standoff and because a small craniotomy precluding direct contact between the transducer and the dura. Figure 8.8 illustrates the lack of SWE signal. It was also noted that the B-mode image was not of good quality, most likely due to the same reason.

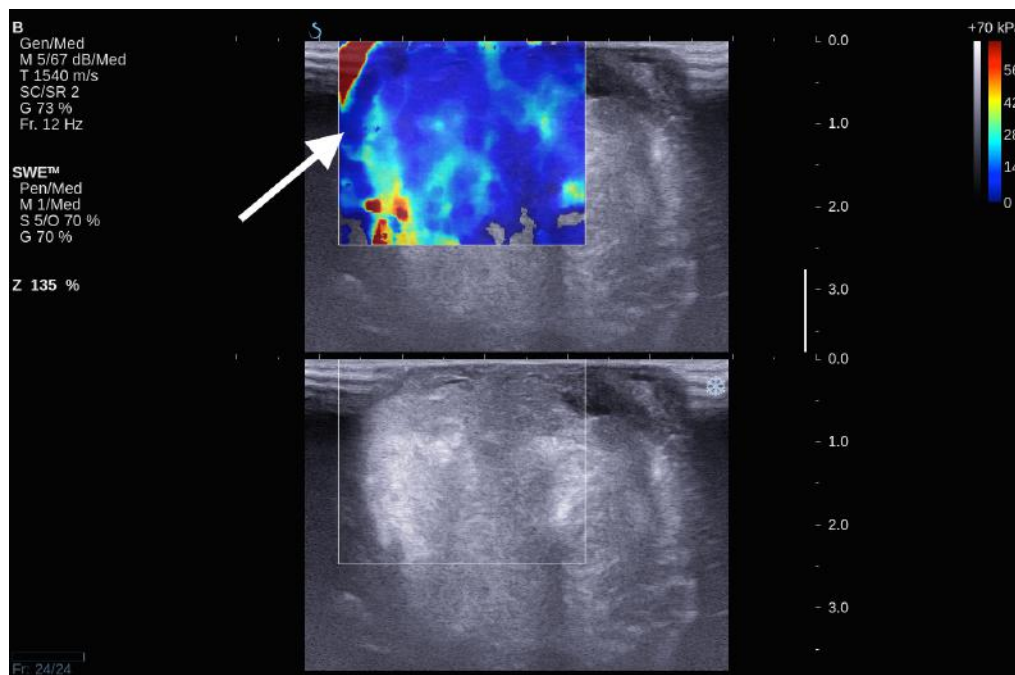


Figure 8.5: Intra-operative SWE for NHNN 2 showing a soft 'bracket' sign (white arrow). There was a cleavage plane, identified independently by the surgeon, in the corresponding area.

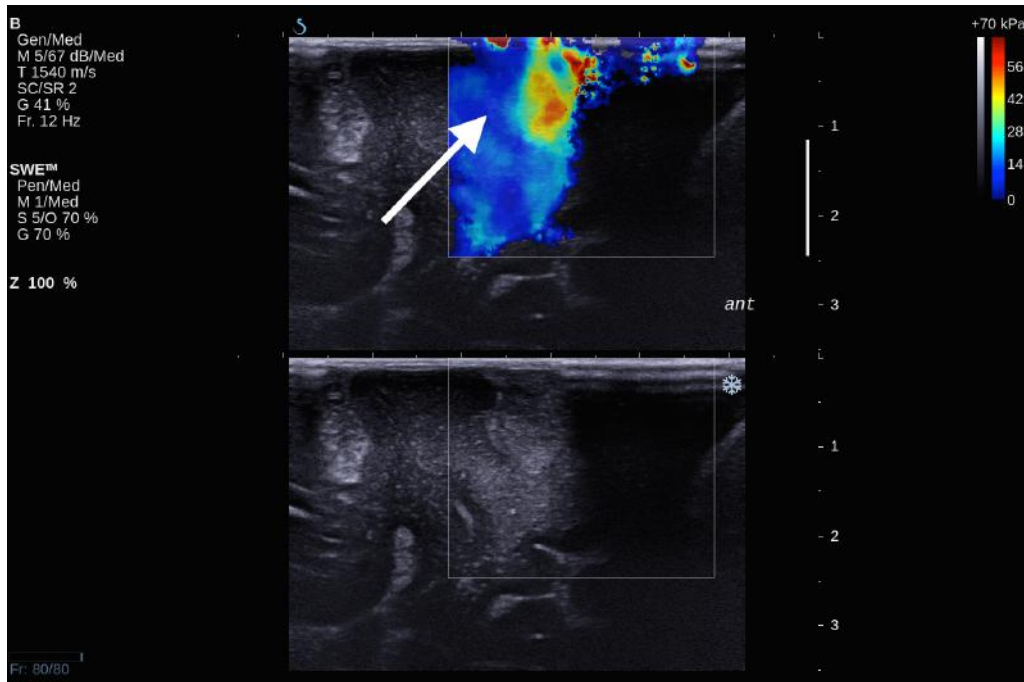


Figure 8.6: Intra-operative SWE for NHNN 15 showing a soft 'bracket' sign (white arrow), where there was a slippery boundary identified by the surgeon intra-operatively.

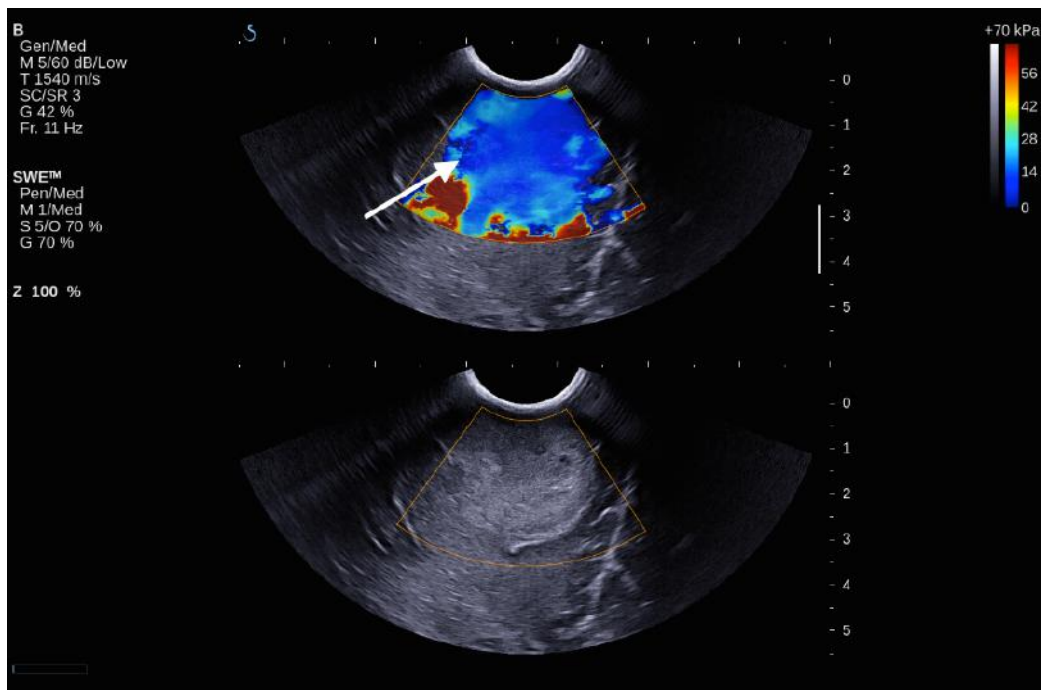


Figure 8.7: Intra-operative SWE for GOSH 55 showing a soft 'bracket' sign for slip plane (white arrow). Intra-operatively. There was a slippery boundary in the corresponding area.

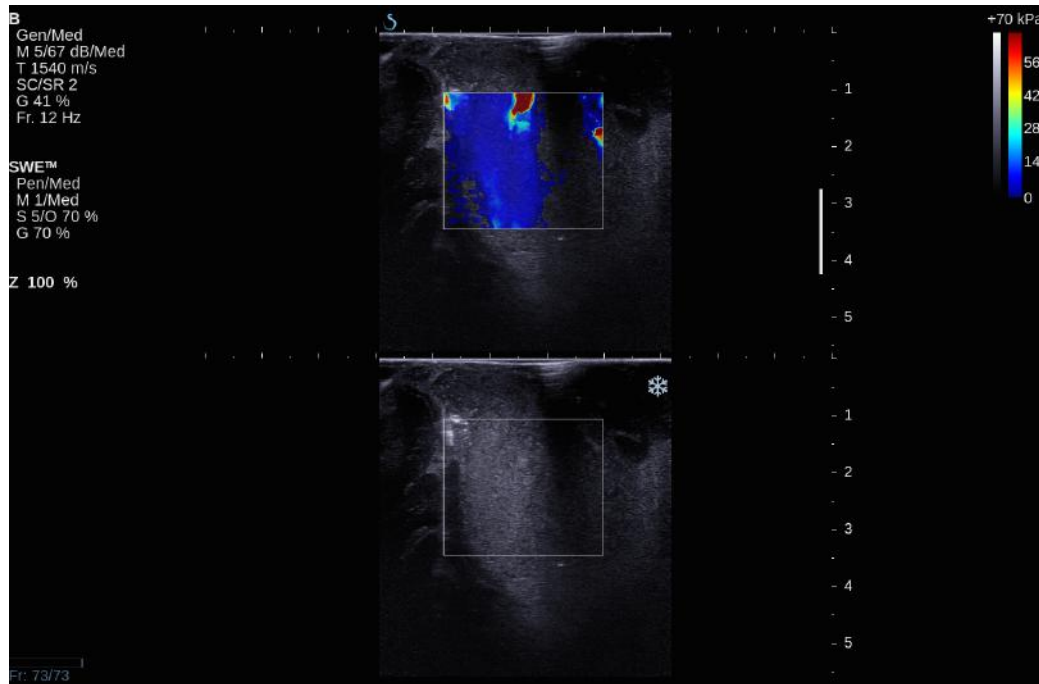


Figure 8.8: Intra-operative SWE of NHNN 11 showing insufficient signal generated due to insufficient water standoff.

#### 8.4.4 Histopathological correlation

Figure 8.9 shows the plot for Young's modulus of normal brain and all tumours. The median Young's modulus for the normal brain was 14.9 kPa, which was significantly lower than that for all tumours (median 33.5 kPa,  $p = 0.003$ ). Wilcoxon's signed-rank test was used to perform paired statistical analysis, as the values for both the tumour and normal brain were not normally distributed. Figure 8.10 shows the Young's modulus for various tumour types. The tumours with WHO grades of I and II were graded as low grade while those with WHO grades of III and IV were graded as high grade. As demonstrated, the low grade and high grade tumours were not normally distributed, hence the Mann Whitney U test was used to judge whether the difference between the values in the 2 groups were statistically significant. Low grade tumours tended to be stiffer than high grade tumours, and metastases even stiffer. However, differences between the Young's moduli were not significant for low grade versus high grade ( $p = 0.220$ ), low grade versus metastasis ( $p = 0.288$ ), and high grade versus metastasis ( $p = 0.101$ ).

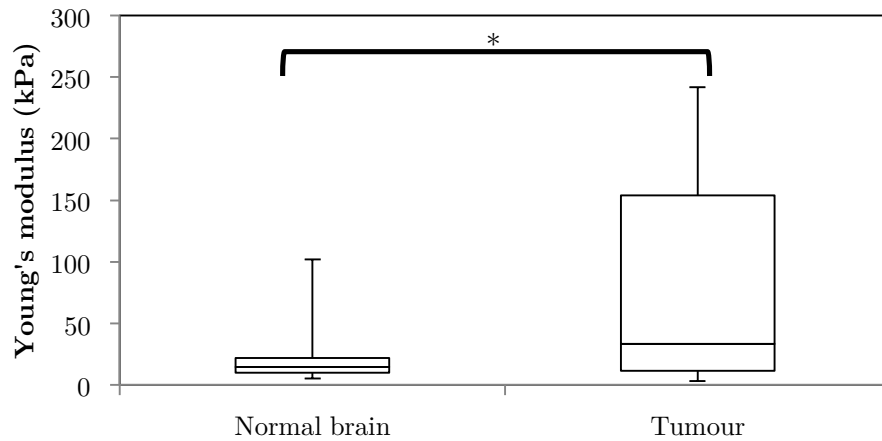


Figure 8.9: Box and whiskers plot for Young's modulus measurements of normal brain and tumour. The upper and lower bounds of the box were the third and first quartiles, respectively while the line within the box was the median. The upper and lower whiskers were maximum and minimum values, respectively. \*There was a significant difference between the 2 groups ( $p = 0.003$ , Wilcoxon's signed-rank test).

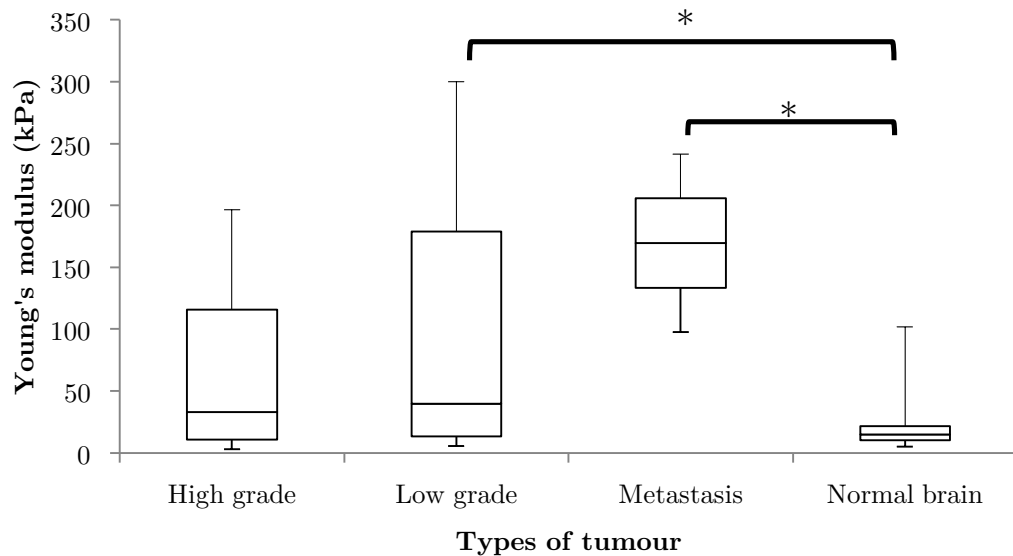


Figure 8.10: Box and whiskers plot of Young's modulus distributions for various tumour types. The upper and lower bounds of the box were the third and first quartiles, respectively while the line within the box was the median. The upper and lower whiskers were maximum and minimum values, respectively. \*There was a significant difference between the Young's modulus values for low grade tumour and normal brain ( $p = 0.036$ ) and between metastases and normal brain ( $p = 0.007$ ) but the differences between high grade and normal brain ( $p = 0.125$ ), high grade and low grade ( $p = 0.220$ ), metastases and high grade ( $p = 0.132$ ), and low grade and metastasis ( $p = 0.288$ ), were not significant. Mann Whitney U test was used to perform statistical analysis.

Further histological analyses were performed to look for cellularity, proliferation, calcification and gliosis. The Mann Whitney U test was used to perform the statistical analysis as the distribution was not Gaussian, as demonstrated in the box and whiskers plots below.

Figure 8.11 shows properties of the Young's modulus distributions for tumours classified on histology having cellularity that was increased and not increased. There seemed to be a decrease in Young's modulus when there was an increase in cellularity (median 162 kPa versus 35 kPa) but the difference between median values was not significant ( $p = 0.647$ ).

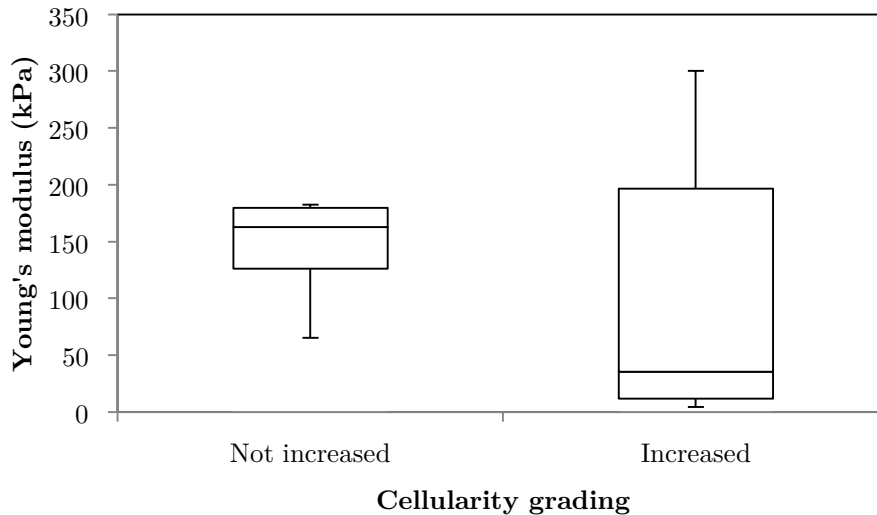


Figure 8.11: Box and whiskers plot for Young's modulus according to cellularity grading on histology ( $n=29$ ). The upper and lower bounds of the box were the third and first quartiles, respectively while the line within the box was the median. The upper and lower whiskers were maximum and minimum values, respectively. There was no statistically significant difference between the median values of the groups ( $p = 0.647$ , Mann Whitney U test).

Figure 8.12 shows the Young's modulus distribution properties for tissue sections graded as high proliferation and low proliferation on histology. There was an increase in the median Young's modulus with proliferation but this was not significant (median 65 kPa versus 161 kPa;  $p = 0.566$ ).

Figure 8.13 shows the plot for the presence of calcification on histology. There was an increase in the median Young's modulus with the presence of calcification (median 35 kPa

versus 162 kPa), but again the difference between median values was not significant ( $p = 0.356$ ).

Figure 8.14 shows the plot for the presence of gliosis on histology. There was a non-significant decrease in the median Young's modulus with gliosis (median 164 kPa versus 65 kPa;  $p = 0.400$ ).

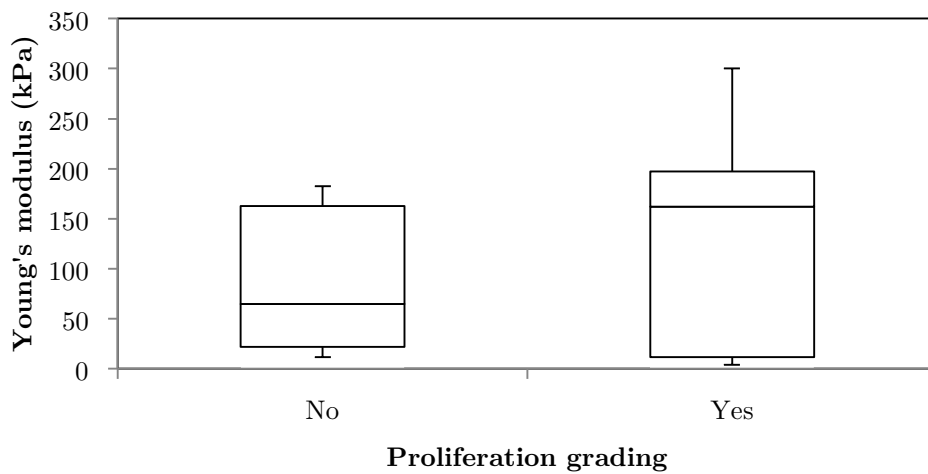


Figure 8.12: Box and whiskers plot for Young's modulus according to proliferation grading on histology ( $n=29$ ). The upper and lower bounds of the box were the third and first quartiles, respectively while the line within the box was the median. 'Yes' indicates high proliferation whereas 'No' indicates low proliferation. The upper and lower whiskers were maximum and minimum values, respectively. There was no statistically significant difference between the median values of the groups ( $p = 0.566$ , Mann Whitney U test).

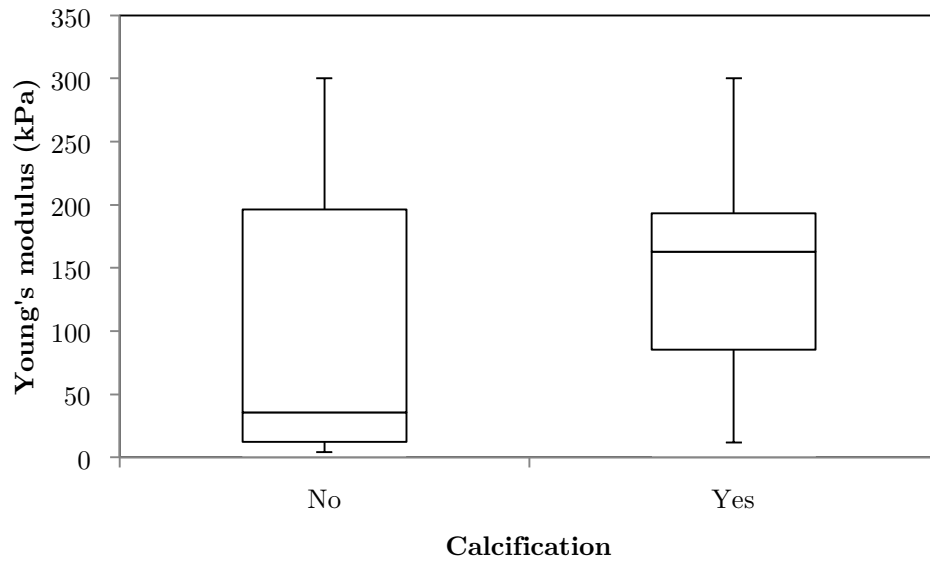


Figure 8.13: Box and whiskers plot for Young's modulus according to the presence of calcification on histology ( $n=29$ ). The upper and lower bounds of the box were the third and first quartiles, respectively while the line within the box was the median. The upper and lower whiskers were maximum and minimum values, respectively. 'Yes' and 'No' indicate the presence and absence of calcification, respectively. There was no statistically significant difference between the median values of the groups ( $p = 0.356$ , Mann Whitney U test).

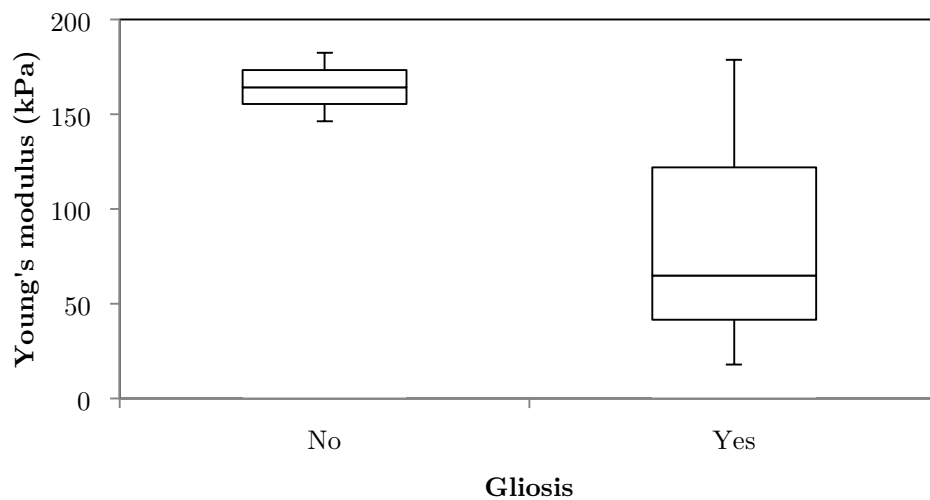


Figure 8.14: Box and whiskers plot for Young's modulus according to the presence of gliosis on histology ( $n=5$ ). The upper and lower bounds of the box were the third and first quartiles, respectively while the line within the box was the median. The upper and lower whiskers were maximum and minimum values, respectively. 'Yes' and 'No' indicate the presence and absence of gliosis, respectively. There was no statistically significant difference between the median values of the groups ( $p = 0.400$ , Mann Whitney U test).

#### 8.4.5 Correlation of Young's modulus and histopathological features for combined epileptogenic lesions and brain tumours

As demonstrated in Sections 7.4.3 and 8.4.4, there was no statistically significant correlation between Young's modulus and histopathological features, such as cellularity, proliferation, calcification and gliosis. Therefore, to have a larger sample number, this section attempts to combine the datasets from both the epileptogenic lesions and the brain tumours to determine if there is a statistically significant correlation.

Figure 8.15 shows properties of the Young's modulus distributions for tumours classified on histology having cellularity that was increased and not increased. There was no statistically significant difference between lower and higher cellularity (median 65 kPa versus 55.9 kPa;  $p = 0.816$ ).

Figure 8.16 shows the plot for Young's modulus according to the presence of proliferation on histology. There was a statistically significant increase in Young's modulus with proliferation (median 55.9 kPa versus 159.1 kPa;  $p = 0.007$ ).

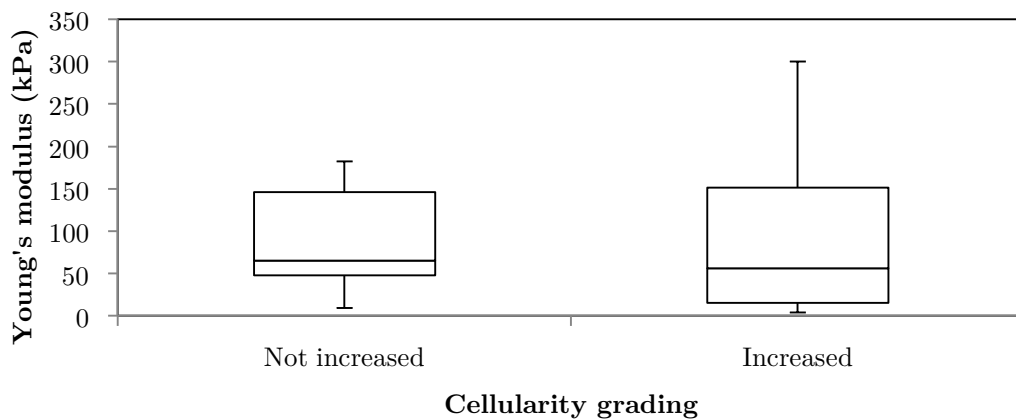


Figure 8.15: Box and whiskers plot of Young's modulus and cellularity grading on histology ( $n=56$ ). The upper and lower bounds of the box were the third and first quartiles, respectively while the line within the box was the median. The upper and lower whiskers were maximum and minimum values, respectively. There was no significant difference between lower and higher cellularity ( $p = 0.816$ , Mann Whitney U test).

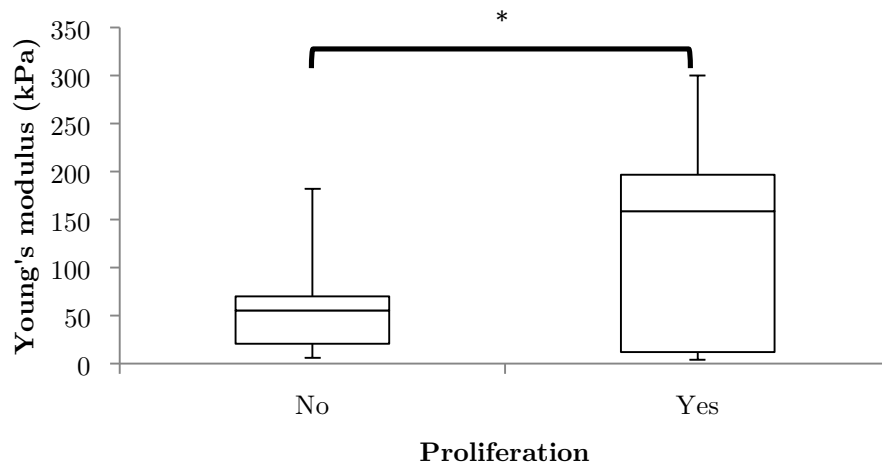


Figure 8.16: Box and whiskers plot of Young's modulus according to the presence of proliferation on histology (n=56). 'Yes' indicates high proliferation whereas 'No' indicates low proliferation. The upper and lower bounds of the box were the third and first quartiles, respectively while the line within the box was the median. The upper and lower whiskers were maximum and minimum values, respectively. There was a statistically significant increase in Young's modulus with proliferation ( $p = 0.007$ , Mann Whitney U test). \* $p < 0.05$

Figure 8.17 shows the plot for Young's modulus according to the presence of calcification on histology. There was an increase in the Young's modulus measurements with the presence of calcification (median 55.9 kPa (no calcification) versus 146.4 kPa (calcification)) but the increase was not statistically significant ( $p = 0.249$ ).

Figure 8.18 shows the plot for Young's modulus according to the presence of gliosis on histology. There was no significant difference in the Young's modulus measurements between those with gliosis (median 58.4 kPa) and those without gliosis (median 62.3 kPa;  $p = 0.533$ ).

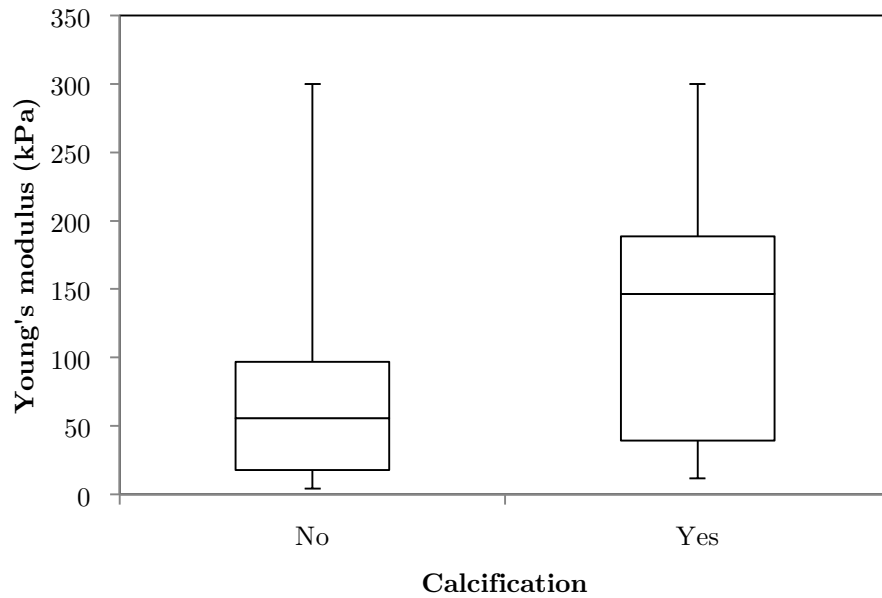


Figure 8.17: Box and whiskers plot of Young's modulus according to the presence of calcification on histology (n=56). 'Yes' and 'No' indicate the presence and absence of calcification. The upper and lower bounds of the box were the third and first quartiles, respectively while the line within the box was the median. The upper and lower whiskers were maximum and minimum values, respectively. There was a non-significant increase in Young's modulus with the presence of calcification ( $p = 0.249$ , Mann Whitney U test).

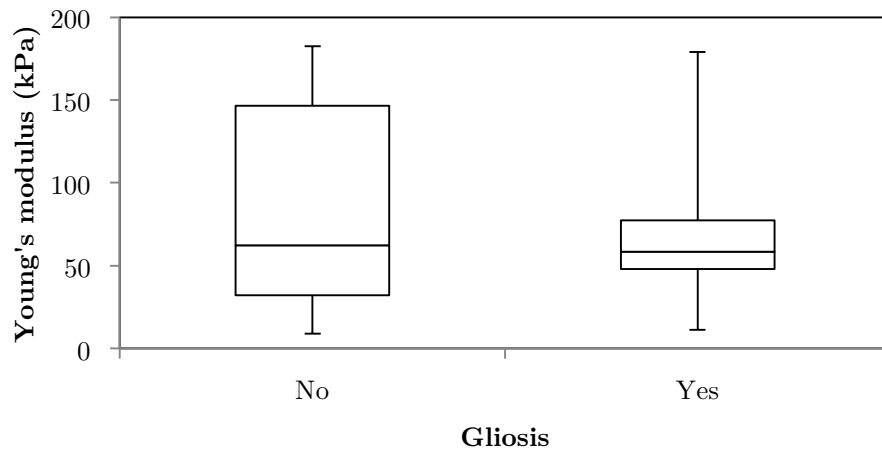


Figure 8.18: Box and whiskers plot for Young's modulus according to the presence of gliosis on histology (n=25). 'Yes' and 'No' indicate the presence and absence of gliosis. The upper and lower bounds of the box were the third and first quartiles, respectively while the line within the box was the median. The upper and lower whiskers were maximum and minimum values, respectively. There was no significant difference in the Young's modulus with the presence of gliosis ( $p = 0.533$ , Mann Whitney U test).

## 8.5 Discussion

### 8.5.1 Comparison of Young's modulus measurements with surgical findings

This study showed that there was significant correlation between both Young's modulus and Young's modulus contrast measured by SWE and surgical opinion of tumour stiffness relative to normal brain. In the brain tumours, the Young's modulus measurements agreed better than Young's modulus contrast with surgical grading of the stiffness. This is consistent with the findings in other studies using QSE where strain was correlated with surgical opinion on tumour stiffness (Chakraborty et al., 2006; Scholz et al., 2005; Selbekk et al., 2005; Uff, 2011). In GOSH 76, although the tumour was thought to be softer than brain by the surgeon, the Young's modulus measurement was  $77.1 \pm 11.4$  kPa (mean  $\pm$  SD) and Young's modulus contrast was 0.858, indicating that it was stiffer than brain by SWE. This could be due to undue pressure on the brain surface when performing the scan. The location of the tumour, which was parietal, was particularly vulnerable to saline irrigation flowing out making water standoff almost impossible. Therefore, in order to acquire a good quality B-mode or SWE, the surgeon might have applied too much pressure, which was known to cause artefactual stiffness due to the non-linear effects of precompression in the area of stress concentration caused by the transducer. As the lesion was superficial, this effect could be unintentionally produced by small pressure.

### 8.5.2 Residual tumour detection

Of the 35 patients, only 26 patients were included in the comparison between intra-operative SWE and post-operative MRI in detecting residual tumour. GOSH 47 and GOSH 49 were excluded because post-operative MRI was not performed. GOSH 47 developed excessive bleeding during surgery resulting in the surgeons abandoning the operation. GOSH 49 had extensive invasion into the brainstem on pre-operative MRI. Therefore, the surgeons decided to perform only debulking surgery with intended residual tumour. GOSH 29,

GOSH 40, GOSH 76, NHNN 11 and NHNN 12 did not have SWE signal post-operatively despite using ‘penetration mode’ and the probe being held as close to the cavity as possible. The tumour in GOSH 29 was situated at a depth of  $> 5$  cm, and there was no SWE signal. In contrast, GOSH 25, similar case to GOSH 29, had SWE signal down to a depth of 5 cm post-resection, but the signal was of questionable reliability as it gave a very high Young’s modulus of 300 kPa. For GOSH 76, the water standoff could not be maintained in the resection cavity. For NHNN cases, as the acquisition was performed using a linear array probe, which was a lot larger than the sector array probe, all the NHNN post-resection scans were performed with the probe above the cavity using a water standoff. NHNN 11 had Surgical® in the resection cavity prior to the scan because of excessive bleeding, thereby causing a lack of SWE signal. NHNN 12 had a large GBM prior to resection, resulting in a very deep post-resection cavity. Due to the large linear array probe, it was not possible to insert the probe in the cavity. GOSH 5 did not have a post-resection scan, as it was one of the earlier cases where the primary aim was to investigate the feasibility and determine the artefacts associated with clinical scanning. NHNN 5 did not have a post-resection scan as the patient developed an air embolus and the surgery had to be abandoned.

Using post-operative MRI as the ‘gold standard’, detection of residual tumour by SWE was shown to have a sensitivity and specificity of 94% and 77%, respectively. Currently, there has been no literature reporting the sensitivity and specificity of SWE in detecting residual brain tumour. SWE was shown to be comparable to post-operative MRI in detecting residual tumour.

Compared to post-operative MRI, US B-mode was shown to have a sensitivity and specificity of 73% and 63%, respectively, for detecting residual tumour. This result agrees with current literature results, which showed a sensitivity of 67 - 85% (Erdoğan et al., 2005; Hammoud et al., 1996; Le Roux et al., 1992). US B-mode was also shown to be comparable to both post-operative MRI findings and SWE in detecting residual tumour.

Surgeon’s intraoperative opinion of the presence or absence of residual tumour was shown to be significantly different from post-operative MRI findings. The sensitivity of surgeon’s opinion in detecting residual tumour was also lower than both SWE and US B-

mode. This agrees with Albert et al. (1994) and Orringer et al. (2012), where surgeons were less likely to detect residual tumour than post-operative MRI. The reason underpinning this could be that tumour can have similar appearance to normal surrounding brain, making visual inspection less reliable. Having said that, surgeons had a specificity of 100%, higher than both SWE and US B-mode, in detecting residual tumour. Therefore, using SWE in combination with surgeon's opinion may optimise the detection of residual tumour as SWE has a higher sensitivity than surgeon whilst the surgeon has a higher specificity than SWE.

### 8.5.3 Characterisation of tumour-brain interface

This study showed that SWE provided signs of the presence of a slippery boundary at the tumour-brain interface in 3 out of 4 cases. In fact, the SWE "soft bracket" signature was effectively present in 3 out of the 3 cases that could be assessed. The reason that 1 case could not be assessed was the insufficient water standoff and inability of the transducer to maintain contact with the brain surface.

As shown by Chakraborty (2007), Uff et al. (2009) and Uff (2011), a slippery boundary appears as a narrow band of high strain on QSE. As strain is inversely proportional to Young's modulus, this should appear as low Young's modulus on SWE. As shear waves generated by ARF only travel in the US lateral and elevational directions, it could be a possible reason for not having the low Young's modulus areas in the superior and inferior aspects of the tumour, thereby a soft 'bracket' sign instead of high strain in the tumour-brain interface. As shown by phantom study with mobile boundary in Chapter 6, the presence of 'soft bracket' sign, indicating the presence of mobile boundary, was demonstrated intraoperatively for tumours with slip plane. This is the first time slip plane was detected by SWE *in vivo*.

### 8.5.4 Histopathological correlation

This study showed that the Young's modulus for all tumour types was significantly higher than normal brain ( $p = 0.003$ ), thereby showing that SWE was capable of

differentiating various brain tumours from the surrounding brain. The paired statistical analysis, Wilcoxon's signed rank test in this case, showed that the difference in Young's modulus measurements was significant between brain tumours and normal brain. In this study low grade tumours tended to be stiffer than high grade tumours, and metastases stiffer still, although the differences between median values was not significant. However, the low grade tumours ( $p = 0.036$ ) and metastasis ( $p = 0.007$ ) were shown to be significantly stiffer than brain. Murphy et al. (2013) showed that meningiomas have shear modulus of 2 – 10 kPa, that is, Young's modulus of 6 – 30 kPa. As stated in Chapter 3, the Young's modulus is 3 times that of shear modulus. From Table 8.1, the meningioma cases (NHNN 2, NHNN 11 and NHNN 15) showed that the Young's modulus ranged from 5.6 – 46.2 kPa (mean 30.4 kPa; SD 21.8 kPa), which agreed with this literature. In a case of breast metastasis (NHNN 14), the Young's modulus was 97.6 kPa  $\pm$  42 kPa (mean  $\pm$  SD), which agrees with the reported values of 61 – 165 kPa in the literature (Chang et al., 2013; Youk et al., 2013). This study is the first that attempts to examine whether Young's modulus is characteristic of brain tumour type, showing that there is considerable variability within groups but due to small numbers of different tumour types, the result was not conclusive. This means that SWE was capable in distinguishing brain tumours from normal brain but was unable to separate different tumour types from each other intraoperatively prior to resection. Since the completion of my PhD project, there was a study that measures Young's modulus with SWE in brain tumours (Imbault et al., 2014). This paper showed that all tumours – high and low grade gliomas, meningiomas and metastasis – were significantly stiffer than normal brain. In this study the normal brain only had Young's modulus of 6.3 to 7.2 kPa, which was much lower than the findings from this thesis (median Young's modulus of 31.0 kPa and 18.8 kPa for grey and white matter, respectively). This study also showed that the different tumour types had significantly different Young's modulus, which was not shown by this thesis. This could be due to the much larger number of patients in this study (92 patients) than in Chapter 8 of this thesis (34 patients).

Further analysis comparing histological features with Young's modulus failed to show any correlation. Although it was not a significant relationship, the Young's modulus decreased with increased cellularity grading ( $p = 0.647$ ). This could be due to a softer

microenvironment promoting cellular proliferation, resulting in a higher cellular density, the stiffness being determined mainly by the supporting stroma rather than the tumour cells.

This study showed that proliferation may correlate positively with Young's modulus but it did not reach statistical significance ( $p = 0.566$ ). When the datasets for both brain tumours and epileptogenic lesions were combined, this tentative finding was confirmed, showing a significant correlation with proliferation ( $p = 0.007$ ). This is consistent with the finding by Juge et al. (2012) in colon tumours in mice, where the authors showed a positive correlation between  $|G^*|$  and proliferation.

Although it was also not statistically significant, Young's modulus may increase with calcification ( $p = 0.356$ ), which would be consistent with the general finding that the presence of calcium increases the stiffness of tissue.

Young's modulus decreased non-significantly with gliosis ( $p=0.400$ ), which could represent softer reactive gliosis following mechanically induced injury (W. J. Miller et al., 2009). This is in contrast to the findings in epileptogenic lesion in Chapter 7. This could be due to the difference in the duration of development of tumour and epileptogenic lesions, where the former would be shorter than the latter.

The numbers in this study were small, thus although showing some correlation, the results were not statistically significant.

## 8.6 Conclusions

This chapter showed that the SWE measurements of Young's modulus and Young's modulus contrast correlated significantly with surgical grading of stiffness. This means that clinically, the SWE measurements are reliable in predicting stiffness.

It also showed that there was high sensitivity and specificity of SWE in detecting residual tumour compared to post-operative MRI scan as the 'gold standard'. It also showed that when there is residual tumour, SWE is better than the surgeon at detecting residual

tumour by 2.5 times (94% versus 37%). When there is an absence of residual tumour, the surgeon is better at predicting the absence of residual tumour (100% versus 77%).

In three cases, a cleavage plane identified to by the surgeon to exist at the tumour-brain interface was associated with a soft 'bracket' sign on SWE. This provides the potential for SWE to be used intraoperatively to guide surgeon to identify the cleavage plane.

There was a significantly higher Young's modulus in brain tumours compared with surrounding brain, showing that SWE could differentiate brain tumours from surrounding brain based on Young's modulus measurements. With this small number, it was shown that low-grade tumours had significantly higher Young's modulus than surrounding brain. Although there seemed to be a correlation between histopathological features of proliferation, calcification and gliosis with Young's modulus, statistical significance was not reached due to the small numbers in this study. However, by combining both the epileptogenic lesion and the brain tumour dataset, Young's modulus was shown to correlate positively with proliferation, with statistical significance ( $p = 0.007$ ). This provides encouragement for future study with larger numbers.

## **Chapter 9**

### **Discussion and Conclusion**

This chapter summarises the main findings and describes the significance and limitations of the work reported in this thesis. It also highlights the novelty of this thesis and its contribution to knowledge. It then discusses the suggestions for improvement and the future directions of this project. Lastly, it summarises the hypotheses being tested and states whether the results from this thesis support or refute the hypotheses.

## 9.1 Introduction

- In low-grade gliomas, the 5-year survival significantly improved from 52 – 76% to 62.7 – 98.2% with increased resection (Chapter 2).
- In high-grade gliomas, the mean survival also significantly improved with increased extent of resection from 4 – 11.8 months and 12 – 34 months to 10.5 – 20 months and 20 – 62.6 months for GBM and AA, respectively (Chapter 2).
- IOUS offers real-time intra-operative imaging with the advantage of the absence of ionising radiation, easy application and affordability. However, IOUS images contain undesirable artefacts and do not provide information regarding tumour stiffness and tumour-brain interface conditions, which could help the surgeon to decide on starting point of resection.
- Clinical outcomes for epilepsy surgery also depend on the complete removal of the epileptogenic lesions (Chapter 2).
- However, about 16 – 43% of patients with epilepsy have lesions that are invisible on MRI, that is, they represent MRI-defined non-lesional cases (Chapter 2). This precludes the use of current intra-operative imaging techniques to locate and guide resection.
- In some of these cases, the lesions may be detected by pre-operative PET, SPECT, MSI and morphometric MRI postprocessing (Chapter 2). However, these techniques could be inaccurate due to brain shift intra-operatively, which render such images inaccurate.
- QSE was shown to improve the detection of brain tumours over IOUS B-mode and provide information on the tumour-brain interface whether it is mobile or adhered. However, it requires training and is susceptible to inter-operator variations and interpretations.
- SWE provides quantitative Young's modulus measurements. SWE does not need strain application so it more desirable as a neurosurgical tool as brain and spinal cord are vulnerable to damage if too much force is applied. SWE can be performed in real-time

using a commercial scanner such as the SuperSonic Aixplorer®, without requiring additional postprocessing with a computer.

- There are intra-operative artefacts in these images (Chapter 2) and unexplained disagreements between Young's modulus measurements and surgical findings (Chapter 5).
- SWE settings were neither standardised nor optimised and the artefacts in SWE images were not investigated.
- SWE appearances for different boundary conditions (mobile and adhered) have not been investigated and *in vivo* study specifically looking at tumour boundaries using SWE has not been performed.
- The overall aim of this thesis was to assess the potential value of intraoperative SWE in brain tumour and epilepsy surgery. This study sought to optimise SWE for intra-operative application in brain tumour and epilepsy surgery, through understanding the behaviour of SWE under a limited set of conditions. For much of the observations of behaviour, explanations were severely lacking, mainly because of a lack of understanding of both the physics and the proprietary technology within the device.

## 9.2 Summary, significance and limitations

As there was discussion in each of the result chapters, it will not be repeated in this section. Instead, a summary of the main findings, explaining their significance and limitations, is provided.

Chapter 4 described the laboratory experiments involving gelatine phantoms and post-mortem mouse brains to verify the Young's modulus measured using SWE with the SuperSonic Aixplorer®. By keeping temperature and incubation time constant, SWE measurements of gelatine phantoms correlated significantly with compressive rheometer measurements. With correction for frequency dispersion, SWE measurements were almost equal to Young's modulus measured with compressive rheometer. It also demonstrated that

SWE measurements of post-mortem mouse brains correlated extremely well with MRE measurements. As the MRE measurements were of shear modulus, which is a third of Young's modulus in a non-compressible material, SWE measurements were shown to be 3 times those of MRE. The results from this chapter showed that the Young's modulus measurements with SWE in both gelatine phantoms and brain tissue were reliable. One of the limitations of the mouse brain study was very few mice. Another limitation is that within normal brain, there was relatively little range of variation of YM from one mouse to another. A larger number of mice, and the study of brain pathology by both methods, would provide a more rigorous comparison between the two methods.

Having verified the SWE measurements of both gelatine phantoms and post-mortem brain tissue, Chapter 5 described clinical study on 10 patients to determine the accuracy of SWE measurements. This study showed that SWE measurements of various brain lesions were correlated significantly with surgical grading of tissue stiffness and those of normal brain agreed with and greatly extended the results in Uff (2011). This study also identified four main image artefacts with SWE, namely lack of shear wave signal, areas of increased Young's modulus when the SWE gain is set too high, decreased Young's modulus of both brain and tumour after manipulation, and increased Young's modulus of cortex when in contact with the ultrasound transducer. The implication from this study is that although SWE gave reasonably accurate measurements, there were artefacts in the images, which may lead to interpretation errors. Furthermore, SWE measurements of normal brain showed that grey matter had significantly higher Young's modulus than white matter (29.6 kPa versus 20.8 kPa,  $p = 0.008$ ). Current literature on brain stiffness was not consistent. Some literature showed that white matter was stiffer than grey matter (Hirakawa et al., 1981; Kruse et al., 2008; Uffmann et al., 2004) whereas some literature showed the opposite (Green et al., 2008; Uff, 2011). Therefore, based on the artefacts demonstrated in this chapter, laboratory experiments were carried out using gelatine phantoms and porcine brains and spinal cords to simulate clinical settings to investigate this further. The laboratory studies were described in Chapter 6.

Chapter 6 described the detailed laboratory experiments with gelatine phantoms, post-mortem porcine brains and spinal cords to study the artefacts highlighted by Chapter 5. This study demonstrated the factors that could affect SWE measurements:

1. Attenuating layers and regions of acoustic shadow were shown to result in a lack of shear wave signal and lower Young's modulus measurements using standard SWE mode. Therefore, to obtain a good shear wave signal and reliable Young's modulus measurements, attenuating layers and regions of acoustic shadowing should ideally be avoided, and if that is not possible, then scanning should be performed with SWE penetration mode.
2. If the SWE gain was set too high the an artefactually high Young's modulus would be displayed in regions which would otherwise have displayed no SWE signal. This study found that the optimal SWE gain setting for intra-operative scanning was 70%.
3. This study showed that surgical manipulations could result in lower Young's modulus measurements, implying that when performing a post-resection scan, the Young's modulus measurements may be lower for areas adjacent to resection cavity.
4. The application of pressure during scanning could result in higher Young's modulus measurements, thus recommending a water standoff or minimal pressure on the brain surface when acquiring intra-operative SWE images.
5. For inclusion of size less than 2 cm, in both 2D and 3D phantoms, the Young's modulus measurements were proportional to the size of the inclusion, which was shown to be consistent with expectations of a partial volume effect. An implication of this finding is that when interpreting SWE images for small residual tumour, its Young's modulus measurements might be lower than the original larger tumour.
6. Using *ex vivo* porcine spinal cords, although not statistically significant, SWE displayed higher Young's modulus measurements when the transducer

was oriented parallel to the spinal tracts than when the transducer was oriented perpendicular to them, thereby showing the potential of SWE in assessing anisotropy of tissue structure. This result has 2 potential implications: 1) If an area is deemed normal on US B-mode but has high Young's modulus measurements, repeat scanning in a perpendicular plane might be warranted to determine whether the abnormal Young's modulus measurement is due to tissue anisotropy or not. 2) By having the potential to detect anisotropy in deep white matter tracts, SWE could potentially be used to guide white matter tract sparing resection (Gil-Robles & Duffau, 2010).

7. Using 2D cylindrical inclusions, SWE demonstrated a characteristic 'soft brackets' in the inclusion-background interface in the mobile inclusions, thereby showing the potential for detecting cleavage plane in the tumour-brain interface *in vivo*, as demonstrated in Chapter 8.
8. SWE was shown to be capable of demonstrating cylindrical 2D inclusions as small as 1 mm diameter if they are stiff, and 3 mm they are soft, and of Young's modulus contrast at least  $\pm 0.10$ , thereby showing that SWE has potential for a high sensitivity for detecting residual tumour, which is better if the tumour is stiff rather than soft relative to the background.
9. The presence of pia mater has been shown to increase the Young's modulus measurement of grey matter in post-mortem porcine brains. This provided the possible explanation for higher Young's modulus measurements in grey matter compared to white matter, as shown in Chapter 5, Uff (2011) and Green et al. (2008).

Therefore, this chapter identified the factors that could affect SWE measurements, thus providing the basis for a carefully optimised clinical scanning protocol, and for understanding and interpreting SWE results in clinical scans.

A limitation of this study is that there was no verification of the SWE measurements with mechanical rheometer capable of measuring small amounts of material. Another drawback of this study is that it was technically not possible to create a smaller inclusion than 1 mm diameter, which prevented the study looking at the detectability of less than 1 mm inclusion. Due to small sample size in the anisotropy experiment, i.e. only 2 porcine spinal cords, the results of this experiment were not statistically significant.

Having identified the factors that could affect SWE measurements, clinical study was conducted using SWE in epilepsy (Chapter 7) and brain tumour (Chapter 8) surgery. In Chapter 7, SWE was shown to be capable of detecting epileptogenic lesions significantly better than MRI. Specifically in the four MRI-negative cases, SWE could detect all of the lesions. Furthermore, this chapter also showed that SWE could differentiate epileptogenic lesions from normal brain. The implication from these findings is that SWE could be a useful intra-operative tool in epilepsy surgery, especially in MRI-negative cases, to detect and differentiate epileptogenic lesions, which have different Young's modulus measurements, from normal brain and to guide placement of electrodes and/or resection of the lesions. A limitation of this study was that the grading of SWE images was based on Young's modulus contrast, which in turn was dependent on where the Q-box measurements were made. In heterogeneous lesions, this could affect the SWE grading. As most epileptogenic lesions were homogeneous, this problem was not encountered. Although the ultrasound transducer was not co-registered with neuronavigation in this study, the surgeon first confirmed the location and scan plane of the transducer with the neuronavigation before scanning the area of interest. MRI-negative cases are extremely rare and only a few were considered for invasive monitoring and surgical intervention. Therefore, future long-term studies would be required to recruit enough cases to show the efficacy of SWE in these cases. The study also failed to show any significant correlation between histopathological features and Young's modulus measurements. This could be due to insufficient numbers in this study, therefore suggesting that further study should be undertaken to continue this investigation. The histopathological grading could also be improved to provide quantitative results of the different features, such as 70% calcification rather than just the presence of calcification.

In Chapter 8, SWE was shown to be capable of detecting residual tumour significantly better than the intra-operative assessment by the surgeon but not US B-mode. Moreover, SWE appeared to demonstrate a slippery tumour-brain interface in three out of 35 cases. Using Young's modulus measurements, SWE was also capable of differentiating brain tumours from normal brain, especially low-grade glioma. This study implies that SWE could be a useful intra-operative tool to assist the neurosurgeon in identifying residual tumour and a slippery tumour-brain interface. As SWE could differentiate brain tumour from normal brain based on Young's modulus measurements, it could also be used to guide biopsy of heterogeneous tumours if resection is not intended. However, a limitation of this study is that some of the brain tumours were heterogeneous. Therefore, the position of the Q-box could affect the Young's modulus measurements. Another limitation of this study is that the residual tumour grading was performed by the author, based on Young's modulus measurements post-resection, the results could be biased. Therefore, future studies with multiple graders and comparison of receiver-operating characteristic (ROC) curves could eliminate this bias. As described in the previous paragraph, although the ultrasound transducer was not co-registered with neuronavigation in this study, the surgeon first confirmed the location and scan plane of the transducer with the neuronavigation before scanning the area of interest. As the SWE characteristics at the tumour-brain interface were only observed in three cases, further study with a much larger number of cases, multiple graders and ROC curves would be required to confirm this phenomenon. This study also failed to show any significant correlation between Young's modulus measurements and histopathological features. Again, this could be due to insufficient numbers. By combining both epileptogenic lesions and brain tumours, Young's modulus measurements significantly and positively correlated with the presence of proliferation (median 159 kPa with proliferation versus 56 kPa without proliferation;  $p = 0.007$ ). As discussed in the paragraph above, the quantitative grading of histopathological features could elucidate the correlation further.

## 9.3 Future work

### 9.3.1 Physics behind the ‘soft bracket’ sign in slip interfaces

It was encouraging that this thesis demonstrated that slippery interface between two gelatine surfaces and between tumour and brain *in vivo* was successfully shown by SWE with the appearance of the ‘soft bracket’ sign in the interface. Conversely, this thesis also demonstrated that the absence of slippery interface in both phantom studies and intraoperative setting did not have the appearance of the ‘soft bracket’ sign in the interface by SWE. However, the physics behind this finding is still puzzling. Simulation and experimental studies will be required to further understand this phenomenon. The commercial scanner SuperSonic Aixplorer® does not allow one to manually configure the settings involved in constructing the SWE images, thus limiting our ability to investigate the physics behind this phenomenon. Therefore, a research interface SWE scanner that allows manual configuration will be required to carry out the experimental studies.

### 9.3.2 Clinical studies using intra-operative SWE in neurosurgery

This thesis has set the foundation for implementing future clinical studies with intra-operative SWE in neurosurgery. As it can be performed using a reasonably priced commercial scanner, there is a possibility of integrating this technique to the current neurosurgical practice. In this way, the clinical studies in this thesis could provide the basis on which future clinical studies can be carried out.

Due to a very low incidence of MRI-defined non-lesional epilepsy cases, long-term studies in a quaternary epilepsy centre will be required to demonstrate the efficacy of SWE in detecting these lesions. As epileptogenic lesions and brain tumours included in this thesis were wide-ranged and small in numbers, it was not possible to correlate specific lesion types with Young’s modulus measurements. With long-term studies looking at individual lesion types, the correlation between these lesions and Young’s modulus measurements can be elucidated. If there is specific correlation, then a database of epileptogenic lesions and brain tumours with their corresponding Young’s modulus measurements can be created, thus

potentially facilitating guidance of biopsy of heterogeneous tumours and providing pre-biopsy diagnosis of different lesions.

### 9.3.3 Integrating MRE with intra-operative SWE

With MRI-defined non-lesional epileptogenic lesions being demonstrated on SWE and not on conventional MRI, there is a possibility of using MRE to image these patients to visualise these lesions. This thesis has shown that there was a strong correlation between MRE and SWE measurements in post mortem mouse brains, thereby providing the basis for translating the MRE measurements to SWE and vice versa. As this was only done with post-mortem mice, further studies looking at live mice and human brains will be required before the integration of pre-operative MRE with intra-operative SWE can be implemented. With MRE being capable of imaging intracranial lesions in pre-operative and outpatient settings, there is a possibility of using MRE for surgical planning and monitoring of such lesions, respectively.

### 9.3.4 Validation aspiration rheometer with SWE measurements

Schiavone et al. (2009) has demonstrated that *in vivo* brain elasticity measurements were possible with a light aspiration device. By deforming the brain surface by 1 – 3 mm through applying small suction pressure, it was shown that the elastic modulus of the brain could be calculated from the pressure required to cause the deformation and the amount of deformation caused. By adapting the device to measure brain tumour or epileptogenic lesions directly, both SWE and aspiration device measurements could be compared. However, before performing any clinical experiments, laboratory verification should be carried out using gelatine phantoms and *ex vivo* porcine brains. If SWE and aspiration rheometer measurements were found to be correlated, *in vitro* and *in vivo*, then the aspiration rheometer could be used to measure stiffness of tumour in spatially restricted regions, such as a pituitary tumour, through a transsphenoidal approach. Taking it one step further, the aspiration rheometer could be integrated with the Cavitron Ultrasonic Surgical

Aspirator (CUSA) to tailor the disruptive force emitted by the device according to the stiffness of the tumour.

## 9.4 Conclusions

I have shown that through laboratory studies, reliable data can be obtained in the clinical settings. This section summarises the hypotheses being tested and states whether or not they are confirmed.

### 9.4.1 Hypothesis 1: SWE can quantify stiffness of normal brain tissue, different epileptogenic lesions and brain tumours.

This hypothesis was confirmed. Firstly, SWE measurements were validated *in vitro* in gelatine phantoms and post-mortem mouse brains against 2 methods of measurements of mechanical properties – compressive rheometer and MRE, respectively (Chapter 4), showing that the SWE measurements can be trusted. Later, in the clinical studies, SWE measurements of epileptogenic lesions (Chapter 7) and brain tumours (Chapter 8) were shown to correlate significantly with surgical grading of stiffness relative to normal brain. SWE measurements of normal brain were shown to lie between the grading of softer and stiffer than brain.

### 9.4.2 Hypothesis 2: SWE measurements are different between epileptogenic lesions and normal brain.

This hypothesis was confirmed. SWE measurements of epileptogenic lesions were significantly different from normal brain through a paired Wilcoxon's signed ranks test (Chapter 7).

### **9.4.3 Hypothesis 3: SWE measurements are different between brain tumours and normal brain.**

This hypothesis was confirmed. SWE measurements of brain tumours were significantly different from normal brain through a paired Wilcoxon's signed ranks test (Chapter 8).

### **9.4.4 Hypothesis 4: SWE appearances are different for mobile and adhered interface.**

This hypothesis was confirmed. In 2D gelatine phantoms with adhered and mobile inclusions, SWE demonstrated the 'soft bracket' sign in both soft and stiff mobile inclusions (Chapter 6). In clinical study, SWE demonstrated the slip sign in three patients, where mobile interface was confirmed by the surgeon during surgery (Chapter 8).

### **9.4.5 Hypothesis 5: SWE can visualise epileptogenic lesions better than MRI.**

This hypothesis was confirmed. SWE was shown to be superior to MRI in detecting epileptogenic lesions based on the comparison between formal radiology report and Young's modulus contrast. SWE also managed to demonstrate all four MRI-negative epileptogenic lesions, thus showing the potential of SWE in guiding electrode placements and resection of MRI-defined non-lesional cases in the future.

### **9.4.6 Hypothesis 6: SWE-quantified elasticity of brain tumours and epileptogenic lesions is correlated with histopathological findings.**

This hypothesis was confirmed. Although SWE could differentiate brain tumours and epileptogenic lesions from normal brain, the numbers in each type of the brain tumours and epileptogenic lesions were small, thereby precluding conclusive correlation between individual

lesions and Young's modulus measurements. There was no correlation between Young's modulus measurements and histological features when brain tumours and epileptogenic lesions were analysed separately. However, when both groups (brain tumours and epileptogenic lesions) were analysed together, it was shown that Young's modulus was significantly correlated with proliferation (Chapter 8).

#### **9.4.7 Hypothesis 7: SWE can detect the residual tumour post-resection better than surgeon.**

This hypothesis was confirmed. Using post-operative MRI scan as 'gold standard', SWE was shown to have higher sensitivity (94% versus 36%) but lower specificity (77% versus 100%) than the surgeon. This means that when there is a residual tumour, SWE can detect the presence of residual tumour 2.5 times more than the surgeon. However, when there is no residual tumour, the surgeon is better at predicting the absence of residual tumour.

#### **9.4.8 Hypothesis 8: SWE can detect the residual tumour post-resection better than ultrasound B-mode.**

This hypothesis was disconfirmed. Using post-operative MRI scan as 'gold standard', SWE was shown to have higher sensitivity (94% versus 73%) and specificity (77% versus 63%) than ultrasound B-mode. However, this was shown to be statistically not significant ( $p=0.727$ ), i.e. SWE and ultrasound B-mode have the same sensitivity and specificity.

## Chapter 10

### References

- Albert, F. K., Forsting, M., Sartor, K., Adams, H.-P., & Kunze, S. (1994). Early Postoperative Magnetic Resonance Imaging after Resection of Malignant Glioma: Objective Evaluation of Residual Tumor and Its Influence on Regrowth and Prognosis. *Neurosurgery*, *34*(1), 45–61.
- Arbogast, K. B., & Margulies, S. S. (1998). Material characterization of the brainstem from oscillatory shear tests. *J Biomech*, *31*(9), 801–7.
- Bamber, J., Cosgrove, D., Dietrich, C. F., Fromageau, J., Bojunga, J., Calliada, F., ... Piscaglia, F. (2013). EFSUMB Guidelines and Recommendations on the Clinical Use of Ultrasound Elastography. Part 1: Basic Principles and Technology. *Ultraschall Med*, *34*, 169–184.
- Barr, R. G., & Zhang, Z. (2012). Effects of precompression on elasticity imaging of the breast: development of a clinically useful semiquantitative method of precompression assessment. *Journal of Ultrasound in Medicine : Official Journal of the American Institute of Ultrasound in Medicine*, *31*(6), 895–902.
- Bercoff, J., Tanter, M., & Fink, M. (2004a). Sonic boom in soft materials: The elastic Cerenkov effect. *Applied Physics Letters*, *84*(12), 2202.
- Bercoff, J., Tanter, M., & Fink, M. (2004b). Supersonic Shear Imaging : A New Technique for Soft Tissue Elasticity Mapping. *IEEE Trans Ultrason Ferroelectr Freq Control*, *51*(4), 396–409.
- Berg, A. T., Vickrey, B. G., Langfitt, J. T., Sperling, M. R., Walczak, T. S., Shinnar, S., ...

- Spencer, S. S. (2003). The multicenter study of epilepsy surgery: recruitment and selection for surgery. *Epilepsia*, *44*(11), 1425–33.
- Bergin, P. S., Fish, D. R., Shorvon, S. D., Oatridge, A., DeSouza, N. M., & Bydder, G. M. (1995). Magnetic resonance imaging in partial epilepsy: additional abnormalities shown with the fluid attenuated inversion recovery (FLAIR) pulse sequence. *J Neurol Neurosurg Psychiatry*, *58*(4), 439–443.
- Berry, G. P., Bamber, J. C., Armstrong, C. G., Miller, N. R., & Barbone, P. E. (2006). Towards an acoustic model-based poroelastic imaging method: I. Theoretical Foundation. *Ultrasound in Medicine and Biology*, *32*(4), 547–567.
- Berry, G. P., Bamber, J. C., Miller, N. R., Barbone, P. E., Bush, N. L., & Armstrong, C. G. (2006). Towards an acoustic model-based poroelastic imaging method: II. experimental investigation. *Ultrasound in Medicine and Biology*, *32*(12), 1869–1885.
- Berry, G. P., Bamber, J. C., Mortimer, P. S., Bush, N. L., Miller, N. R., & Barbone, P. E. (2008). The Spatio-Temporal Strain Response of Oedematous and Nonoedematous Tissue to Sustained Compression In Vivo. *Ultrasound in Medicine and Biology*, *34*(4), 617–629.
- Bien, C. G., Szinay, M., Wagner, J., Clusmann, H., Becker, A. J., & Urbach, H. (2009). Characteristics and surgical outcomes of patients with refractory magnetic resonance imaging-negative epilepsies. *Archives of Neurology*, *66*(12), 1491–9.
- Black, P. M., Moriarty, T., Alexander, E. I., Stieg, P., Woodard, E. J., Gleason, P. L., ... Jolesz, F. A. (1997). Development and Implementation of Intraoperative Magnetic Resonance Imaging and Its Neurosurgical Applications. *Neurosurgery*, *41*(4), 831–845.
- Blauwblomme, T., Ternier, J., Romero, C., Pier, K. S. T., D’Argenzio, L., Pressler, R., ... Harkness, W. (2011). Adverse events occurring during invasive electroencephalogram recordings in children. *Neurosurgery*, *69*(2 Suppl Operative), ons169–75; discussion ons175.
- Bloch, O., Han, S. J., Cha, S., Sun, M. Z., Aghi, M. K., McDermott, M. W., ... Parsa, A. T. (2012). Impact of extent of resection for recurrent glioblastoma on overall survival. *Journal Of Neurosurgery*, *117*(December), 1032–1038.
- Brain, other CNS and intracranial tumours incidence statistics. (2013). Retrieved from <http://www.cancerresearchuk.org/cancer-info/cancerstats/types/brain/incidence/#source1>
- Capelle, L., Fontaine, D., Mandonnet, E., Taillandier, L., Golmard, J. L., Bauchet, L., ... Duffau, H. (2013). Spontaneous and therapeutic prognostic factors in adult hemispheric

- World Health Organization Grade II gliomas: a series of 1097 cases: clinical article. *Journal of Neurosurgery*, 118(6), 1157–68.
- Catheline, S., Wu, F., & Fink, M. (1999). A solution to diffraction biases in sonoelasticity: the acoustic impulse technique. *The Journal of the Acoustical Society of America*, 105(5), 2941–50.
- Chakraborty, A. (2007). *The development of intra-operative ultrasound elasticity imaging techniques to assist during brain tumour resection*. PhD thesis, Academic Department of Clinical Neuroscience, University of London.
- Chakraborty, A., Bamber, J. C., Berry, G., Bush, N., & Dorward, N. L. (2004). Intra-operative ultrasound elastography and registered MRI of brain tumours: a feasibility study. *Proc. 3rd Int Conf on the Ultrasonic Measurement and Imaging of Tissue Elasticity, Oct. 17-20, 2004*.
- Chakraborty, A., Bamber, J. C., & Dorward, N. L. (2012). Slip elastography: a novel method for visualising and characterizing adherence between two surfaces in contact. *Ultrasonics*, 52(3), 364–376.
- Chakraborty, A., Berry, G., Bamber, J., & Dorward, N. (2006). Intra-operative Ultrasound Elastography and Registered Magnetic Resonance Imaging of Brain Tumours: A Feasibility Study. *Ultrasound*, 14(1), 43–49.
- Chakraborty, A., Uff, C., & Harkness, W. (2011). Ultrasound elastography is superior to MRI at identifying epileptogenic areas intra-operatively. In *International Society of Paediatric Neurosurgery*.
- Chandler, W. F., & Rubin, J. M. (1987). The application of ultrasound during brain surgery. *World Journal of Surgery*, 11(5), 558–69.
- Chandrasoma, P. T., Smith, M. M., & Apuzzo, M. L. J. (1989). Stereotactic Biopsy in the Diagnosis of Brain Masses: Comparison of Results of Biopsy and Resected Surgical Specimen. *Neurosurgery*, 24(2), 160–165.
- Chang, J. M., Moon, W. K., Cho, N., & Kim, S. J. (2011). Breast Mass Evaluation: Factors Influencing the Quality of US Elastography. *Radiology*, 259(1), 59–64.
- Chang, J. M., Park, I. A., Lee, S. H., Kim, W. H., Bae, M. S., Koo, H. R., ... Moon, W. K. (2013). Stiffness of tumours measured by shear-wave elastography correlated with subtypes of breast cancer. *European Radiology*, 23(9), 2450–8.
- Chassoux, F., Landré, E., Mellerio, C., Turak, B., Mann, M. W., Daumas-Duport, C., ... Devaux, B. (2012). Type II focal cortical dysplasia: electroclinical phenotype and surgical outcome related to imaging. *Epilepsia*, 53(2), 349–58.

- Chaturvedi, P., Insana, M. F., & Hall, T. J. (1998). 2-D Companding for Noise Reduction in Strain Imaging. *IEEE Trans Ultrason Ferroelectr Freq Control*, 45(1), 179–191.
- Claus, E. B., Horlacher, A., Hsu, L., Schwartz, R. B., Dello-Iacono, D., Talos, F., ... Black, P. M. (2005). Survival rates in patients with low-grade glioma after intraoperative magnetic resonance image guidance. *Cancer*, 103(6), 1227–33.
- Cohen-Gadol, A. A., Ozduman, K., Bronen, R. A., Kim, J. H., & Spencer, D. D. (2004). Long-term outcome after epilepsy surgery for focal cortical dysplasia. *Journal of Neurosurgery*, 101(1), 55–65.
- Cossu, M., Cardinale, F., Castana, L., Citterio, A., Francione, S., Tassi, L., ... Lo Russo, G. (2005). Stereoelectroencephalography in the Presurgical Evaluation of Focal Epilepsy: A Retrospective Analysis of 215 Procedures. *Neurosurgery*, 57(4), 706–718.
- Cossu, M., Schiariti, M., Francione, S., Fuschillo, D., Gozzo, F., Nobili, L., ... Russo, G. Lo. (2012). Stereoelectroencephalography in the presurgical evaluation of focal epilepsy in infancy and early childhood. *Journal of Neurosurgery. Pediatrics*, 9(3), 290–300.
- Crescenti, R. A. (2009). *Backscatter ultrasound readout of radiation-sensitive gels for radiation dosimetry*. PhD thesis, Institute of Cancer Research and The Royal Marsden Hospital, University of London.
- Deffieux, T., Gennisson, J., Bercoff, J., & Tanter, M. (2011). On the Effects of Reflected Waves in Transient Shear Wave Elastography. *IEEE Transactions on Ultrasonics Ferroelectrics and Frequency Control*, 58(10), 2032–5.
- Deffieux, T., Gennisson, J.-L., Larrat, B., Fink, M., & Tanter, M. (2012). The variance of quantitative estimates in shear wave imaging: theory and experiments. *IEEE Transactions on Ultrasonics, Ferroelectrics, and Frequency Control*, 59(11), 2390–410.
- Donnelly, B. R., & Medige, J. (1997). Shear properties of human brain tissue. *Journal of Biomechanical Engineering*, 119(4), 423–32.
- Dorward, N. L., Alberti, O., Palmer, J. D., Kitchen, N. D., & Thomas, D. G. (1999). Accuracy of true frameless stereotaxy: in vivo measurement and laboratory phantom studies. Technical note. *Journal of Neurosurgery*, 90(1), 160–8.
- Dorward, N. L., Alberti, O., Velani, B., Gerritsen, F. A., Harkness, W. F., Kitchen, N. D., & Thomas, D. G. (1998). Postimaging brain distortion: magnitude, correlates, and impact on neuronavigation. *J Neurosurg*, 88(4), 656–662.
- Doyley, M. M., Bamber, J. C., Fuechsel, F. F., & Bush, N. L. (2001). A Freehand Elastographic Imaging Approach For Clinical Breast Imaging: System Development And Performance Evaluation. *Ultrasound in Medicine & Biology*, 27(10), 1347–1357.

- Engel, J. J., Mcdermott, M. P., Wiebe, S., Langfitt, J. T., Stern, J. M., Dewar, S., ... Group, E. R. S. E. T. (ERSET) S. (2012). Early Surgical Therapy for Drug-Resistant Temporal Lobe Epilepsy: A Randomized Trial. *JAMA*, *307*(9), 922–930.
- Engle, D. J., & Lunsford, L. D. (1987). Brain tumor resection guided by intraoperative computed tomography. *Journal of Neuro-Oncology*, *4*(4), 361–70.
- Englot, D. J., Breshears, J. D., Sun, P. P., Chang, E. F., & Auguste, K. I. (2013). Seizure outcomes after resective surgery for extra-temporal lobe epilepsy in pediatric patients. *Journal of Neurosurgery. Pediatrics*, *12*(2), 126–33.
- Erdoğan, N., Tucer, B., Mavili, E., Menkü, A., & Kurtsoy, A. (2005). Ultrasound Guidance in Intracranial Tumor Resection: Correlation with Postoperative Magnetic Resonance Findings. *Acta Radiologica*, *46*(7), 743–749.
- Fallenstein, G. T., Hulce, V. D., & Melvin, J. W. (1969). Dynamic mechanical properties of human brain tissue. *J Biomech*, *2*, 217–226.
- Ferry, J. D. (1948). Mechanical properties of substances of high molecular weight; rigidities of gelatin gels; dependence on concentration, temperature and molecular weight. *J Am Chem Soc*, *70*, 2244–2249.
- Focke, N. K., Symms, M. R., Burdett, J. L., & Duncan, J. S. (2008). Voxel-based analysis of whole brain FLAIR at 3T detects focal cortical dysplasia. *Epilepsia*, *49*(5), 786–93.
- Frater, J. L., Prayson, R. A., Morris III, H. H., & Bingaman, W. E. (2000). Surgical pathologic findings of extratemporal-based intractable epilepsy: a study of 133 consecutive resections. *Arch Pathol Lab Med*, *124*(4), 545–549.
- Fung, Y. C. (1993). *Biomechanics Mechanical Properties of Living Tissues* (Second Ed.). New York: Springer-Verlag, New York.
- Gennisson, J.-L., Catheline, S., Chaffai, S., & Fink, M. (2003). Transient elastography in anisotropic medium: application to the measurement of slow and fast shear wave speeds in muscles. *J Acoust Soc Am*, *114*(1), 536–541.
- Gennisson, J.-L., Deffieux, T., Macé, E., Montaldo, G., Fink, M., & Tanter, M. (2010). Viscoelastic and anisotropic mechanical properties of in vivo muscle tissue assessed by supersonic shear imaging. *Ultrasound Med Biol*, *36*(5), 789–801.
- Gerganov, V. M., Samii, A., Giordano, M., Samii, M., & Fahlbusch, R. (2011). Two-dimensional high-end ultrasound imaging compared to intraoperative MRI during resection of low-grade gliomas. *J Clin Neurosci*, *18*(5), 669–673.
- Gil-Robles, S., & Duffau, H. (2010). Surgical management of World Health Organization

- Grade II gliomas in eloquent areas: the necessity of preserving a margin around functional structures. *Neurosurgical Focus*, 28(2), E8.
- Giuliodori, M. J., Lujan, H. L., Briggs, W. S., Palani, G., & DiCarlo, S. E. (2009). Hooke's law: applications of a recurring principle. *Advances in Physiology Education*, 33(4), 293–296.
- Golfinos, J. G., Fitzpatrick, B. C., Smith, L. R., & Spetzler, R. F. (1995). Clinical use of a frameless stereotactic arm: results of 325 cases. *Journal of Neurosurgery*, 83(2), 197–205.
- Green, M. A., Bilston, L. E., & Sinkus, R. (2008). In vivo brain viscoelastic properties measured by magnetic resonance elastography. *NMR in Biomedicine*, 21(7), 755–764.
- Gronningsaeter, A., Kleven, A., Ommedal, S., Aarseth, T. E., Lie, T., Lindseth, F., ... Unsgård, G. (2000). SonoWand, an ultrasound-based neuronavigation system. *Neurosurgery*, 47(6), 1373–9; discussion 1379–80.
- Hammoud, M. a, Ligon, B. L., elSouki, R., Shi, W. M., Schomer, D. F., & Sawaya, R. (1996). Use of intraoperative ultrasound for localizing tumors and determining the extent of resection: a comparative study with magnetic resonance imaging. *Journal of Neurosurgery*, 84(5), 737–41.
- Hart, M., Metcalfe, S., & Grant, R. (2014). Biopsy versus resection for high grade glioma ( Review ). *Cochrane Database of Systematic Reviews 2000*, (2).
- Hart, Y. M., & Shorvon, S. D. (1995). The nature of epilepsy in the general population. I. Characteristics of patients receiving medication for epilepsy. *Epilepsy Research*, 21(1), 43–9.
- Hegi, M. E., Diserens, A.-C., Gorlia, T., Hamou, M.-F., de Tribolet, N., Weller, M., ... Stupp, R. (2005). MGMT gene silencing and benefit from temozolomide in glioblastoma. *The New England Journal of Medicine*, 352(10), 997–1003.
- Hervey-Jumper, S. L., & Berger, M. S. (2014). Role of surgical resection in low- and high-grade gliomas. *Current Treatment Options in Neurology*, 16(4), 284.
- Hirakawa, K., Hashizume, K., & Hayashi, T. (1981). [Viscoelastic property of human brain - for the analysis of impact injury (author's transl)]. *No To Shinkei*, 33(10), 1057–65.
- Imbault, M., Demene, C., Mossad, M., Gennisson, J.-L., Tanter, M., Chauvet, D., ... Boch, A.-L. (2014). Intraoperative Quantitative Measurement of Brain Tumor Stiffness and Intracranial Pressure Assessment using Ultrasound Shear Wave Elastography. *IEEE International Ultrasound Symposium Proceedings*, 201–204.

- Jackson, R. J., Fuller, G. N., Abi-Said, D., Lang, F. F., Gokaslan, Z. L., Shi, W. M., ... Sawaya, R. (2001). Limitations of stereotactic biopsy in the initial management of gliomas. *Neuro-Oncology*, 3(3), 193–200.
- Jakola, A. S., Myrmet, K. S., Kloster, R., Torp, S. H., Lindal, S., Unsgård, G., & Solheim, O. (2012). Comparison of a strategy favoring early surgical resection vs a strategy favoring watchful waiting in low-grade gliomas. *JAMA : The Journal of the American Medical Association*, 308(18), 1881–8.
- Jamin, Y., Boulton, J. K. R., Li, J., Popov, S., Garteiser, P., Ulloa, J. L., ... Robinson, S. P. (2015). Exploring the Biomechanical Properties of Brain Malignancies and their Pathological Determinants with Magnetic Resonance Elastography. *Cancer Res*, 75(7), 1216–24.
- Jayakar, P., Duchowny, M., & Resnick, T. J. (1994). Subdural Monitoring in the Evaluation of Children for Epilepsy Surgery. *Journal of Child Neurology*, 9(2 Suppl), 2S61–2S66.
- Jeha, L. E., Najm, I., Bingaman, W., Dinner, D., Widdess-Walsh, P., & Lüders, H. (2007). Surgical outcome and prognostic factors of frontal lobe epilepsy surgery. *Brain : A Journal of Neurology*, 130(Pt 2), 574–84.
- Johannesen, T. B., Langmark, F., & Lote, K. (2003). Progress in long-term survival in adult patients with supratentorial low-grade gliomas: a population-based study of 993 patients in whom tumors were diagnosed between 1970 and 1993. *Journal of Neurosurgery*, 99(5), 854–62.
- Juge, L., Doan, B.-T., Seguin, J., Albuquerque, M., Benoit, L., Mignet, N., ... Sinkus, R. (2012). Colon Tumor Growth and Antivascular Treatment in Mice: Complementary Assessment with MR Elastography and Diffusion-weighted MR Imaging. *Radiology*, 264(2), 436–444.
- Kallel, F., Prihoda, C., & Ophir, J. (2001). Contrast-Transfer Efficiency for Continuously Varying Tissue Moduli: Simulation and Phantom Validation. *Ultrasound in Medicine & Biology*, 27(8), 1115–1125.
- Kallel, F., Varghese, T., Ophir, J., & Bilgen, M. (1997). The Nonstationary Strain Filter Lateral and Elevational in Elastography: Part II. Lateral and Elevational Decorrelation. *Ultrasound*, 23(9), 1357–1369.
- Keles, G. E., Chang, E. F., Lamborn, K. R., Tihan, T., Chang, C.-J., Chang, S. M., & Berger, M. S. (2006). Volumetric extent of resection and residual contrast enhancement on initial surgery as predictors of outcome in adult patients with hemispheric anaplastic astrocytoma. *Journal of Neurosurgery*, 105(1), 34–40.

- Keles, G. E., Lamborn, K. R., & Berger, M. S. (2001). Low-grade hemispheric gliomas in adults: a critical review of extent of resection as a factor influencing outcome. *Journal of Neurosurgery*, *95*(5), 735–45.
- Keles, G. E., Lamborn, K. R., & Berger, M. S. (2003). Coregistration accuracy and detection of brain shift using intraoperative sononavigation during resection of hemispheric tumors. *Neurosurgery*, *53*(3), 554–556.
- Knake, S., Triantafyllou, C., Wald, L. L., Wiggins, G., Kirk, G. P., Larsson, P. G., ... Grant, P. E. (2005). 3T phased array MRI improves the presurgical evaluation in focal epilepsies: a prospective study. *Neurology*, *65*(7), 1026–31.
- Konofagou, E. E., Harrigan, T. P., Ophir, J., & Krouskop, T. a. (2001). Poroelastography: Imaging the poroelastic properties of tissues. *Ultrasound in Medicine and Biology*, *27*(10), 1387–1397.
- Konofagou, E., & Ophir, J. (1998). A New Elastographic Method for Estimation and Imaging of Lateral Displacements, Lateral Strains, Corrected Axial Strains and Poisson' Ratios in Tissues. *Ultrasound in Medicine & Biology*, *24*(8), 1183–1199.
- Krouskop, T. A., Wheeler, T. M., Kallel, F., Garra, B. S., & Hall, T. (1998). Elastic Moduli of Breast and Prostate Tissues under Compression. *Ultrasonic Imaging*, *20*(4), 260–274.
- Kruse, S. a, Rose, G. H., Glaser, K. J., Manduca, A., Felmlee, J. P., Jack, C. R., & Ehman, R. L. (2008). Magnetic resonance elastography of the brain. *NeuroImage*, *39*(1), 231–7.
- Kubben, P. L., ter Meulen, K. J., Schijns, O. E. M. G., ter Laak-Poort, M. P., van Overbeeke, J. J., & van Santbrink, H. (2011). Intraoperative MRI-guided resection of glioblastoma multiforme: a systematic review. *The Lancet Oncology*, *12*(11), 1062–70.
- Kwan, P., & Brodie, M. J. (2002). Refractory epilepsy: a progressive, intractable but preventable condition? *Seizure*, *11*(2), 77–84.
- Lacroix, M., Abi-Said, D., Fourney, D. R., Gokaslan, Z. L., Shi, W., DeMonte, F., ... Sawaya, R. (2001). A multivariate analysis of 416 patients with glioblastoma multiforme: prognosis, extent of resection, and survival. *Journal Of Neurosurgery*, *95*(2), 190–198.
- Laws, E. R., Parney, I. F., Huang, W., Anderson, F., Morris, A. M., Asher, A., ... Chang, S. (2003). Survival following surgery and prognostic factors for recently diagnosed malignant glioma: data from the Glioma Outcomes Project. *Journal of Neurosurgery*, *99*(3), 467–73.
- Le Roux, P. D., Berger, M. S., Wang, K., Mack, L. A., & Ojemann, G. a. (1992). Low grade gliomas: comparison of intraoperative ultrasound characteristics with preoperative imaging studies. *Journal of Neuro-Oncology*, *13*(2), 189–98.

- Le Roux, P. D., Winter, T. C., Berger, M. S., Mack, L. A., Wang, K., & Elliott, J. P. (1994). A comparison between preoperative magnetic resonance and intraoperative ultrasound tumor volumes and margins. *J Clin Ultrasound*, 22(1), 29–36.
- Leighton, B. C., Fisher, B., Bauman, G., Depiero, S., Stitt, L., Macdonald, D., & Cairncross, G. (1997). Supratentorial Low-Grade Glioma in Adults: An Analysis of Prognostic Factors and Timing of Radiation. *Journal of Clinical Oncology*, 15(4), 1294–1301.
- Lerner, R. M., Huang, S. R., & Parker, K. J. (1990). “Sonoelasticity” images derived from ultrasound signals in mechanically vibrated tissues. *Ultrasound in Medicine & Biology*, 16(3), 231–239.
- Levine, D. N. (1999). The pathogenesis of normal pressure hydrocephalus: a theoretical analysis. *Bulletin of Mathematical Biology*, 61(5), 875–916.
- Li, J. (2015). *Non-invasive imaging of tissue biomechanical properties with magnetic resonance elastography in vivo*. PhD thesis, Institute of Cancer Research and The Royal Marsden Hospital, University of London.
- Li, J., Jamin, Y., Boulton, J. K., Cummings, C., Waterton, J. C., Ulloa, J., ... Robinson, S. P. (2014). Tumour biomechanical response to the vascular disrupting agent ZD6126 in vivo assessed by magnetic resonance elastography. *Br J Cancer*, 110(7), 1727–1732.
- Lunsford, L. D., Parrish, R., & Albright, L. (1984). Intraoperative Imaging with a Therapeutic Computed Tomographic Scanner. *Neurosurgery*, 15(4), 559–561.
- Macé, E., Cohen, I., Montaldo, G., Miles, R., Fink, M., & Tanter, M. (2011). In vivo mapping of brain elasticity in small animals using shear wave imaging. *IEEE Transactions on Medical Imaging*, 30(3), 550–558.
- Manduca, A., Lake, D. S., Kruse, S. A., & Ehman, R. L. (2003). Spatio-temporal directional filtering for improved inversion of MR elastography images. *Medical Image Analysis*, 7(4), 465–73.
- Martín, A., Macé, E., Boisgard, R., Montaldo, G., Thézé, B., Tanter, M., & Tavitian, B. (2012). Imaging of perfusion, angiogenesis, and tissue elasticity after stroke. *Journal of Cerebral Blood Flow and Metabolism Official Journal of the International Society of Cerebral Blood Flow and Metabolism*, 32(8), 1496–507.
- MATLAB. (2010). version 7.10.0 (R2010b). Natick, Massachusetts: The Mathworks Inc.
- McGirt, M. J., Chaichana, K. L., Attenello, F. J., Weingart, J. D., Than, K., Burger, P. C., ... Quinoñes-Hinojosa, A. (2008). Extent of surgical resection is independently associated with survival in patients with hemispheric infiltrating low-grade gliomas. *Neurosurgery*, 63(4), 700–7; author reply 707–8.

- McGirt, M. J., Chaichana, K. L., Gathinji, M., Attenello, F. J., Than, K., Olivi, A., ... Quiñones-Hinojosa, A. R. (2009). Independent association of extent of resection with survival in patients with malignant brain astrocytoma. *Journal of Neurosurgery*, *110*(1), 156–62.
- McGirt, M. J., Villavicencio, A. T., Bulsara, K. R., & Friedman, A. H. (2003). MRI-guided stereotactic biopsy in the diagnosis of glioma: comparison of biopsy and surgical resection specimen. *Surgical Neurology*, *59*(4), 279–283.
- McGonigal, A., Bartolomei, F., Régis, J., Guye, M., Gavaret, M., Trébuchon-Da Fonseca, A., ... Pe, J. (2007). Stereoelectroencephalography in presurgical assessment of MRI-negative epilepsy. *Brain*, *130*(Pt 12), 3169–3183.
- Miller, D., Knake, S., Bauer, S., Krakow, K., Pagenstecher, A., Sure, U., & Rosenow, F. (2008). Intraoperative ultrasound to define focal cortical dysplasia in epilepsy surgery. *Epilepsia*, *49*(1), 156–158.
- Miller, W. J., Leventhal, I., Scarsella, D., Haydon, P. G., Janmey, P., & Meaney, D. F. (2009). Mechanically induced reactive gliosis causes ATP-mediated alterations in astrocyte stiffness. *Journal of Neurotrauma*, *26*(5), 789–97.
- Muller, M., Gennisson, J.-L., Deffieux, T., Tanter, M., & Fink, M. (2009). Quantitative viscoelasticity mapping of human liver using supersonic shear imaging: preliminary in vivo feasibility study. *Ultrasound Med Biol*, *35*(2), 219–229.
- Murphy, M. C., Huston, J., Glaser, K. J., Manduca, A., Meyer, F. B., Lanzino, G., ... Ehman, R. L. (2013). Preoperative assessment of meningioma stiffness using magnetic resonance elastography. *Journal of Neurosurgery*, *118*(3), 643–8.
- Nakamura, M., Konishi, N., Tsunoda, S., Nakase, H., Tsuzuki, T., Aoki, H., ... Sakaki, T. (2000). Analysis of prognostic and survival factors related to treatment of low-grade astrocytomas in adults. *Oncology*, *58*(2), 108–16.
- Nightingale, K., Soo, M. S., Nightingale, R., & Trahey, G. (2002). Acoustic radiation force impulse imaging: in vivo demonstration of clinical feasibility. *Ultrasound in Medicine & Biology*, *28*(2), 227–35.
- Nimsky, C., Ganslandt, O., Cerny, S., Hastreiter, P., Greiner, G., & Fahlbusch, R. (2000). Quantification of, visualization of, and compensation for brain shift using intraoperative magnetic resonance imaging. *Neurosurgery*, *47*(5), 1070–9; discussion 1079–80.
- Nomiya, T., Nemoto, K., Kumabe, T., Takai, Y., & Yamada, S. (2007). Prognostic significance of surgery and radiation therapy in cases of anaplastic astrocytoma:

- retrospective analysis of 170 cases. *Journal of Neurosurgery*, 106(4), 575–81.
- O'Brien, T. J., So, E. L., Mullan, B. P., Hauser, M. F., Brinkmann, B. H., Jack, C. R., ... Sharbrough, F. W. (1999). Subtraction SPECT co-registered to MRI improves postictal SPECT localization of seizure foci. *Neurology*, 52(1), 137–137.
- Onal, C., Otsubo, H., Araki, T., Chitoku, S., Ochi, A., Weiss, S., ... Logan, W. (2003). Complications of invasive subdural grid monitoring in children with epilepsy. *Journal of Neurosurgery*, 98(5), 1017–26.
- Ophir, J., Alam, S. K., Garra, B. S., Kallel, F., Konofagou, E. E., Krouskop, T., ... Souchon, R. (2002). Elastography: Imaging the Elastic Properties of Soft Tissues with Ultrasound. *J Med Ultrasonics*, 29(4), 155–171.
- Ophir, J., Cespedes, I., Ponnekanti, H., Yazdi, Y., & Li, X. (1991). Elastography: a quantitative method for imaging the elasticity of biological tissues. *Ultrason Imaging*, 13(2), 111–34.
- Orringer, D., Lau, D., Khatri, S., Zamora-Berridi, G., Zhang, K., Wu, C., ... Sagher, O. (2012). Extent of resection in patients with glioblastoma: limiting factors, perception of resectability, and effect on survival. *J Neurosurg*, 117(5), 851–859.
- Oszvald, A., Güresir, E., Setzer, M., Vatter, H., Senft, C., Seifert, V., & Franz, K. (2012). Glioblastoma therapy in the elderly and the importance of the extent of resection regardless of age. *Journal of Neurosurgery*, 116(2), 357–64.
- Parker, K. J., Huang, S. R., Musulin, R. a, Lerner, R. M., & Musulin. (1990). Tissue Response to Mechanical Vibrations for “Sonoelastic Imaging.” *Ultrasound in Medicine and Biology*, 16(3), 241–46.
- Perreault, J. O., & Cao, C. G. L. (2006). Effects of vision and friction on haptic perception. *Human Factors*, 48(3), 574–86.
- Perucca, E. (1998). Pharmacoresistance in Epilepsy How Should It Be Defined? *CNS Drugs*, 10(3), 171–179.
- Pesavento, A., & Emert, H. (1998). Time-Efficient and Exact Algorithms for Adaptive Temporal Stretching and 2D-Correlation for Elastographic Imaging using Phase Information. *Proceedings of the 1998 IEEE Ultrasonic Symposium*, 1765–1768.
- Pesavento, A., Lorenz, A., Siebers, S., & Ermert, H. (2000). New real-time strain imaging concepts using diagnostic ultrasound. *Phys Med Biol*, 45, 1423–1435.
- Ponnekanti, H., Ophir, J., Huang, Y., & Cespedes, I. (1995). Fundamental Mechanical Limitations on the Visualization of Elasticity Contrast in Elastography. *Ultrasound in*

- Medicine & Biology*, 21(4), 533–543.
- Pope, W. B., Sayre, J., Perlina, A., Villablanca, J. P., Mischel, P. S., & Cloughesy, T. F. (2005). MR imaging correlates of survival in patients with high-grade gliomas. *AJNR. American Journal of Neuroradiology*, 26(10), 2466–74.
- Pouratian, N., & Schiff, D. (2010). Management of low-grade glioma. *Current Neurology and Neuroscience Reports*, 10(3), 224–31.
- Ramey, W. L., Martirosyan, N. L., Lieu, C. M., Hasham, H. a, Lemole, G. M., & Weinand, M. E. (2013). Current management and surgical outcomes of medically intractable epilepsy. *Clinical Neurology and Neurosurgery*, 115(12), 2411–8.
- Raza, S., Odulate, A., Ong, E., Chikarmane, S., & Harston, C. (2010). Using real-time tissue elastography for breast lesion evaluation: our initial experience. *J Ultrasound Med*, 29(4), 551–563.
- Regula, J., MacRobert, A. J., Gorchein, A., Buonaccorsi, G. A., Thorpe, S. M., Spencer, G. M., ... Bown, S. G. (1995). Photosensitisation and photodynamic therapy of oesophageal, duodenal, and colorectal tumours using 5 aminolaevulinic acid induced protoporphyrin IX--a pilot study. *Gut*, 36(1), 67–75.
- Renovanz, M., Hickmann, A., Henkel, C., Nadji-Ohl, M., & Hopf, N. (2014). Navigated versus Non-Navigated Intraoperative Ultrasound: Is There Any Impact on the Extent of Resection of High-Grade Gliomas? A Retrospective Clinical Analysis. *J Neurol Surg A Cent Eur Neurosurg.*, 75(3), 224-30.
- Roper, S. N. (2009). Surgical treatment of the extratemporal epilepsies. *Epilepsia*, 50 Suppl 8, 69–74.
- Rosenow, F., & Lüders, H. (2001). Presurgical evaluation of epilepsy. *Brain*, 124, 1683–1700.
- Rubí, S., Setoain, X., Donaire, A., Bargalló, N., Sanmartí, F., Carreño, M., ... Pons, F. (2011). Validation of FDG-PET/MRI coregistration in nonlesional refractory childhood epilepsy. *Epilepsia*, 52(12), 2216–24.
- Ruggieri, P. M., Najm, I., Bronen, R., Campos, M., Cendes, F., Duncan, J. S., ... Theodore, W. H. (2004). Neuroimaging of the cortical dysplasias. *Neurology*, 62(6 Suppl 3), S27–9.
- Sabin, H. I., & Whittle, I. R. (1990). Stereotactic craniotomy and intraoperative lesion localisation using the Brown-Robert-Wells frame. Technical note. *Acta Neurochirurgica*, 102(3-4), 137–40.
- Sanai, N., Polley, M.-Y., McDermott, M. W., Parsa, A. T., & Berger, M. S. (2011). An extent of resection threshold for newly diagnosed glioblastomas. *Journal of*

- Neurosurgery*, 115(1), 3–8.
- Sandrin, L., Fourquet, B., Hasquenoph, J.-M., Yon, S., Fournier, C., Mal, F., ... Palau, R. (2003). Transient elastography: a new noninvasive method for assessment of hepatic fibrosis. *Ultrasound in Medicine & Biology*, 29(12), 1705–13.
- Sarvazyan, A. P., & Hill, C. R. (2004). Physical Principles of Medical Ultrasonics. In J. Wiley (Ed.), (Second Ed.). Chichester.
- Sarvazyan, A. P., Rudenko, O. V, Swanson, S. D., Fowlkes, J. B., & Emelianov, S. Y. (1998). Shear wave elasticity imaging: a new ultrasonic technology of medical diagnostics. *Ultrasound in Medicine Biology*, 24(9), 1419–1435.
- Sato, S., & Smith, P. D. (1985). Magnetoencephalography. *Journal of Clinical Neurophysiology*, 2(2), 173–192.
- Schiavone, P., Chassat, F., Boudou, T., Promayon, E., Valdivia, F., & Payan, Y. (2009). In vivo measurement of human brain elasticity using a light aspiration device. *Medical Image Analysis*, 13(4), 673–8.
- Schneider, C. A., Rasband, W. S., & Eliceiri, K. W. (2012). NIH Image to ImageJ: 25 years of image analysis. *Nature Methods*, 9, 671–675.
- Schneider, F., Irene Wang, Z., Alexopoulos, A. V, Almubarak, S., Kakisaka, Y., Jin, K., ... Burgess, R. C. (2013). Magnetic source imaging and ictal SPECT in MRI-negative neocortical epilepsies: additional value and comparison with intracranial EEG. *Epilepsia*, 54(2), 359–69.
- Scholz, M., Lorenz, A., Pesavento, a, Brendel, B., Khaled, W., Engelhardt, M., ... Schmieder, K. (2007). Current status of intraoperative real-time vibrography in neurosurgery. *Ultraschall in Der Medizin (Stuttgart, Germany : 1980)*, 28(5), 493–7.
- Scholz, M., Noack, V., Pechlivanis, I., Engelhardt, M., Fricke, B., Linstedt, U., ... Harders, A. (2005). Vibrography during tumor neurosurgery. *J Ultrasound Med*, 24(7), 985–992.
- Scott, C. a, Fish, D. R., Smith, S. J., Free, S. L., Stevens, J. M., Thompson, P. J., ... Harkness, W. F. (1999). Presurgical evaluation of patients with epilepsy and normal MRI: role of scalp video-EEG telemetry. *Journal of Neurology, Neurosurgery, and Psychiatry*, 66(1), 69–71.
- Selbekk, T., Bang, J., & Unsgaard, G. (2005). Strain processing of intraoperative ultrasound images of brain tumours: initial results. *Ultrasound Med Biol*, 31(1), 45–51.
- Selbekk, T., Brekken, R., Indergaard, M., Solheim, O., & Unsgård, G. (2012). Comparison of contrast in brightness mode and strain ultrasonography of glial brain tumours. *BMC*

- Medical Imaging*, 12(1), 11.
- Selbekk, T., Brekken, R., Solheim, O., Lydersen, S., Hernes, T. A. N., & Unsgaard, G. (2010). Tissue motion and strain in the human brain assessed by intraoperative ultrasound in glioma patients. *Ultrasound Med Biol*, 36(1), 2–10.
- Senft, C., Bink, A., Franz, K., Vatter, H., Gasser, T., & Seifert, V. (2011). Intraoperative MRI guidance and extent of resection in glioma surgery: a randomised, controlled trial. *The Lancet Oncology*, 12(11), 997–1003.
- Shah, M. N., Leonard, J. R., Inder, G., Gao, F., Geske, M., Haydon, D. H., ... Limbrick, D. D. (2012). Intraoperative magnetic resonance imaging to reduce the rate of early reoperation for lesion resection in pediatric neurosurgery. *Journal of Neurosurgery. Pediatrics*, 9(3), 259–64.
- Shaw, E., Arusell, R., Scheithauer, B., O'Fallon, J., O'Neill, B., Dinapoli, R., ... Abrams, R. (2002). Prospective Randomized Trial of Low- Versus High-Dose Radiation Therapy in Adults With Supratentorial Low-Grade Glioma: Initial Report of a North Central Cancer Treatment Group/Radiation Therapy Oncology Group/Eastern Cooperative Oncology Group Study. *Journal of Clinical Oncology*, 20(9), 2267–2276.
- Shiina, T., Nightingale, K. R., Palmeri, M. L., Hall, T. J., Bamber, J. C., Barr, R. G., ... Kudo, M. (2015). WFUMB Guidelines and Recommendations for Clinical Use of Ultrasound Elastography: Part 1: Basic Principles and Terminology. *Ultrasound in Medicine & Biology*, 41(5), 1126–1147.
- Siegel, a M., Jobst, B. C., Thadani, V. M., Rhodes, C. H., Lewis, P. J., Roberts, D. W., & Williamson, P. D. (2001). Medically intractable, localization-related epilepsy with normal MRI: presurgical evaluation and surgical outcome in 43 patients. *Epilepsia*, 42(7), 883–8.
- Smith, J. S., Chang, E. F., Lamborn, K. R., Chang, S. M., Prados, M. D., Cha, S., ... Berger, M. S. (2008). Role of extent of resection in the long-term outcome of low-grade hemispheric gliomas. *Journal of Clinical Oncology*, 26(8), 1338–45.
- Smits, A., & Duffau, H. (2011). Seizures and the natural history of World Health Organization Grade II gliomas: a review. *Neurosurgery*, 68(5), 1326–33.
- Soffietti, R., Chio, A., Giordana, M. T., Vasario, E., & Schiffer, D. (1989). Prognostic Factors in Well-Differentiated Cerebral Astrocytomas in the Adult. *Neurosurgery*, 24(5), 686–691.
- Spencer, S. S. (1994). The relative contributions of MRI, SPECT, and PET imaging in epilepsy. *Epilepsia*, 35 Suppl 6, S72–89.

- Støylen, A. (2014). Basic ultrasound, echocardiography and Doppler for clinicians.
- Strandberg, M., Larsson, E.-M., Backman, S., & Källén, K. (2008). Pre-surgical epilepsy evaluation using 3T MRI. Do surface coils provide additional information? *Epileptic Disorders : International Epilepsy Journal with Videotape*, 10(2), 83–92.
- Stummer, W., Pichlmeier, U., Meinel, T., Wiestler, O. D., Zanella, F., & Reulen, H.-J. (2006). Fluorescence-guided surgery with 5-aminolevulinic acid for resection of malignant glioma: a randomised controlled multicentre phase III trial. *The Lancet Oncology*, 7(5), 392–401.
- Stummer, W., Reulen, H.-J., Meinel, T., Pichlmeier, U., Schumacher, W., Tonn, J.-C., ... Group, A.-G. S. (2008). Extent of Resection and Survival in Glioblastoma Multiforme: Identification of and Adjustment for Bias. *Neurosurgery*, 62(3), 564–576.
- Stummer, W., Stocker, S., Wagner, S., Stepp, H., Fritsch, C., Goetz, C., ... Reulen, H. J. (1998). Intraoperative Detection of Malignant Gliomas by 5-Aminolevulinic Acid-induced Porphyrin Fluorescence. *Neurosurgery*, 42(3), 518–526.
- SuperSonic Imagine. (2010). *Aixplorer MultiWave User's Guide*.
- Surbeck, W., Bouthillier, A., Weil, A. G., Crevier, L., Carmant, L., Lortie, A., ... Nguyen, D. K. (2011). The combination of subdural and depth electrodes for intracranial EEG investigation of suspected insular (perisylvian) epilepsy. *Epilepsia*, 52(3), 458–66. doi:10.1111/j.1528-1167.2010.02910.x
- Sweet, J. a, Hdeib, A. M., Sloan, A., & Miller, J. P. (2013). Depths and grids in brain tumors: implantation strategies, techniques, and complications. *Epilepsia*, 54 Suppl 9, 66–71.
- Uff, C. E. (2011). *The evaluation of advanced ultrasound elastographic techniques in neurosurgery*. PhD thesis, Institute of Cancer Research and The Royal Marsden Hospital, University of London.
- Uff, C. E., Garcia, L., Fromageau, J., Dorward, N., & Bamber, J. C. (2009). Real-time ultrasound elastography in neurosurgery. *IEEE International Ultrasound Symposium Proceedings*, 467–470.
- Uffmann, K., Maderwald, S., Greiff, A. De, & Ladd, M. E. (2004). Determination of Gray and White Matter Elasticity with MR Elastography. In *Proceedings of International Society for Magnetic Resonance in Medicine* (p. 1768). Kyoto, Japan.
- Ushio, Y., Kochi, M., Hamada, J., Kai, Y., & Nakamura, H. (2005). Effect of surgical removal on survival and quality of life in patients with supratentorial glioblastoma. *Neurologia Medico-Chirurgica*, 45(9), 454–60; discussion 460–1.

- van Velthoven, V., & Auer, L. M. (1990). Practical application of intraoperative ultrasound imaging. *Acta Neurochirurgica*, *105*(1-2), 5–13.
- Varghese, T., & Ophir, J. (1997). A Theoretical Framework for Performance Characterization of Elastography: The Strain Filter. *IEEE Trans Ultrason Ferroelectr Freq Control*, *44*(1), 164–172.
- Vuorinen, V., Hinkka, S., Färkkilä, M., & Jääskeläinen, J. (2003). Debulking or biopsy of malignant glioma in elderly people - a randomised study. *Acta Neurochirurgica*, *145*(1), 5–10. doi:10.1007/s00701-002-1030-6
- Wang, J., Liu, X., Ba, Y. M., Yang, Y. L., Gao, G. D., Wang, L., & Duan, Y. Y. (2012). Effect of sonographically guided cerebral glioma surgery on survival time. *J Ultrasound Med*, *31*(5), 757–762.
- Wang, Z. I., Ristic, A. J., Wong, C. H., Jones, S. E., Najm, I. M., Schneider, F., ... Alexopoulos, A. V. (2013). Neuroimaging characteristics of MRI-negative orbitofrontal epilepsy with focus on voxel-based morphometric MRI postprocessing. *Epilepsia*, 1–9. doi:10.1111/epi.12390
- Ward, A. G., & Saunders, P. R. (1958). Rheology: Theory and Applications. In F. R. Eirich (Ed.), *2* (pp. 313 – 362). Academic Press Inc., Publishers.
- Wetjen, N., Cohen-Gadol, A., Maher, C., Marsh, R., Meyer, F., & Cascino, G. (2002). Frontal lobe epilepsy: diagnosis and surgical treatment. *Neurosurgical Review*, *25*(3), 119–138. doi:10.1007/s101430100174
- WFUMB Symposium on Safety of Ultrasound in Medicine. Kloster-Banz, G. 14-19 A. 1996. (1998). Update on Thermal Bioeffects Issues. *Ultrasound in Medicine & Biology*, *24*(Supplement 1), S1–S10.
- Wiebe, S., Blume, W., Girvin, J., & Eliasziw, M. (2001). A randomised, controlled trial of surgery for temporal-lobe epilepsy. *New England Journal of Medicine*, *345*(5), 311–318.
- Willems, P. W. A., Taphoorn, M. J. B., Burger, H., van der Sprenkel, J. W. B., & Tulleken, C. A. F. (2006). Effectiveness of neuronavigation in resecting solitary intracerebral contrast-enhancing tumors: a randomized controlled trial. *Journal of Neurosurgery*, *104*(3), 360–8.
- Wolf, P., Rieger, E., & Kerl, H. (1993). Topical photodynamic therapy with endogenous porphyrins after application of 5-aminolevulinic acid. *Journal of the American Academy of Dermatology*, *28*(1), 17–21.
- Woodworth, G., McGirt, M. J., Samdani, A., Garonzik, I., Olivi, A., & Weingart, J. D. (2005). Accuracy of frameless and frame-based image-guided stereotactic brain biopsy

- in the diagnosis of glioma: comparison of biopsy and open resection specimen. *Neurological Research*, 27(4), 358–62.
- Woydt, M., Krone, A., Becker, G., Schmidt, K., Roggendorf, W., & Roosen, K. (1996). Correlation of intra-operative ultrasound with histopathologic findings after tumour resection in supratentorial gliomas. A method to improve gross total tumour resection. *Acta Neurochir (Wien)*, 138(12), 1391–1398.
- Wu, X.-T., Rampp, S., Buchfelder, M., Kuwert, T., Blümcke, I., Dörfler, a, ... Stefan, H. (2012). Interictal magnetoencephalography used in magnetic resonance imaging-negative patients with epilepsy. *Acta Neurologica Scandinavica*, (5), 1–7.
- Wu, Z., Hoyt, K., Rubens, D. J., & Parker, K. J. (2006). Sonoelastographic imaging of interference patterns for estimation of shear velocity distribution in biomaterials. *The Journal of the Acoustical Society of America*, 120(1), 535.
- Xu, Z. S., Lee, R. J., Chu, S. S., Yao, A., Paun, M. K., Murphy, S. P., & Mourad, P. D. (2013). Evidence of Changes in Brain Tissue Stiffness After Ischemic Stroke Derived From Ultrasound-Based Elastography. *Journal of Ultrasound in Medicine*, 32, 485–494.
- Yeh, S.-A., Ho, J.-T., Lui, C.-C., Huang, Y.-J., Hsiung, C.-Y., & Huang, E.-Y. (2005). Treatment outcomes and prognostic factors in patients with supratentorial low-grade gliomas. *British Journal of Radiology*, 78(927), 230–235.
- Yoon, J. H., Jung, H. K., Lee, J. T., & Ko, K. H. (2013). Shear-wave elastography in the diagnosis of solid breast masses: what leads to false-negative or false-positive results? *Eur Radiol*, 23, 2432–2440.
- Yoon, J., Kim, M., Kim, E., Moon, H., & Choi, J. (2013). Discordant elastography images of breast lesions: how various factors lead to discordant findings. *Ultraschall Med*, 34(3), 266–271.
- Youk, J. H., Gweon, H. M., Son, E. J., Kim, J.-A., & Jeong, J. (2013). Shear-wave elastography of invasive breast cancer: correlation between quantitative mean elasticity value and immunohistochemical profile. *Breast Cancer Research and Treatment*, 138(1), 119–26.
- Yuan, J., Chen, Y., & Hirsch, E. (2012). Intracranial electrodes in the presurgical evaluation of epilepsy. *Neurological Sciences: Official Journal of the Italian Neurological Society and of the Italian Society of Clinical Neurophysiology*, 33(4), 723–9.
- Zentner, J., Hufnagel, a, Ostertun, B., Wolf, H. K., Behrens, E., Campos, M. G., ... Schramm, J. (1996). Surgical treatment of extratemporal epilepsy: clinical, radiologic, and histopathologic findings in 60 patients. *Epilepsia*, 37(11), 1072–80.

## Appendix A

### The Correction of SWE for Frequency Dispersion

As shown by Muller et al. (2009), the frequency dispersion of shear wave speed is observable in tissue using data from the Aixplorer®, due to the dependence of shear wave speed on shear wave frequency in a viscoelastic material such as liver (Figure A.1). As compressive rheometer (Instron®) measurements were performed in a quasistatic fashion, they were not subjected to a varying strain rate that would cause the frequency dependence of Young's modulus measurements to be apparent in a viscoelastic material. As gelatine phantoms were viscoelastic, they would exhibit frequency dispersion of shear wave speed. In order to compare SWE measurements with compressive rheometer measurements, a frequency-dependence correction was applied to the former.

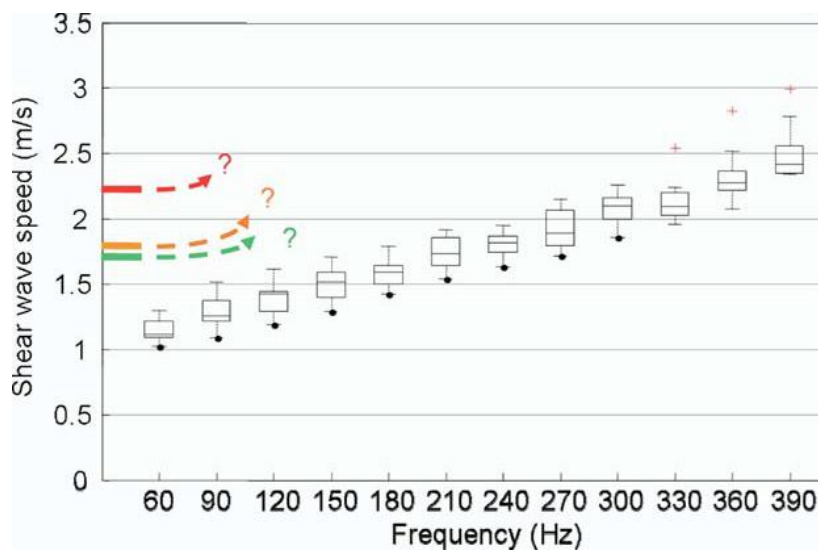


Figure A.1: Frequency dispersion of shear wave speed measured using the Aixplorer® in the livers of 10 healthy volunteers. The shear wave speed is directly proportional to its frequency. (Reproduced from Muller et al. (2009))

The frequency content of the shear wave pulse generated by the Axlplorer is unknown, and indeed will be tissue dependent. However, the data provided by Muller et al, for liver (Figure A.1) may be used as a first approximation. From this, it can be seen that the central frequency was approximately 225 Hz, as calculated below:

$$\frac{60 + 390}{2} = \frac{450}{2} = 225 \text{ Hz} \quad (\text{A.1})$$

The straight line obtained as a least squares best fit to the frequency dispersion curve in liver was:

$$c_s = 3.60f_s + c_0 \text{ (mm/s)}, \quad (\text{A.2})$$

where  $c_s$  is the shear wave speed in liver,  $f_s$  is the shear wave frequency and  $c_0$  is the zero frequency intercept of the extrapolated straight line. Under the assumption that the frequency dispersion curve for liver has a similar slope to that for gelatine, this intercept was used to derive the corrected shear wave speed, and hence the corrected Young's modulus, for a frequency of 0 Hz, the effective frequency associated with the near static axial compression applied by the Instron® machine. Assuming that the average frequency at which the Young's modulus was measured in the present work using the Aixplorer® was also 225 Hz:

$$c_s = 3.60 \times 225 + c_0 \text{ (mm/s)} \quad (\text{A.3})$$

$$c_s = 810 + c_0 \text{ (mm/s)}$$

$$c_s = 0.81 + c_0 \text{ (m/s)} \quad (\text{A.4})$$

$$\therefore c_0 = c_s - 0.81 \text{ (m/s)} \quad (\text{A.5})$$

Assuming  $E_0 \approx 3\rho c_0^2$  and  $\nu \approx 0.5$ , where  $E_0$  is the calculated Young's modulus at 0 Hz, and  $\rho \approx 1000\text{kg/m}^3$ ,

$$E_0 = 3 \times 1000 \times c_0^2 \quad (\text{A.6})$$

$$E_0 = 3000 \times (c_s - 0.81)^2 \quad (\text{A.7})$$

Similarly, from Equation A.6,

$$E_s = 3 \times 1000 \times c_s^2 \Rightarrow c_s = \sqrt{\frac{E_s}{3000}}, \quad (\text{A.8})$$

where  $E_s$  is the calculated Young's modulus from uncorrected shear wave speed  $c_s$ .

Substituting  $c_s$  into Equation A.7,

$$E_0 = 3000 \times \left( \sqrt{\frac{E_s}{3000}} - 0.81 \right)^2 \quad (\text{Pa}) \quad (\text{A.9})$$

$$E_0 = 3 \times \left( \sqrt{\frac{E_s}{3}} - 0.81 \right)^2 \quad (\text{kPa}) \quad (\text{A.10})$$

Therefore, in Chapter 4, the so-called corrected Young's modulus ( $E_0$ ) was calculated using Equation A.13, and was used to compare with compressive rheometer measurements.

## Appendix B

### List of Publications originating from this thesis

#### B.1 Peer-reviewed paper (from work described in chapter 7)

Chan HW, Pressler R, Uff C, Gunny R, St Piers K, Cross H, Bamber J, Dorward N, Harkness W, Chakraborty A (2014) A novel technique of detecting MRI-negative lesion in focal symptomatic epilepsy: Intraoperative ShearWave elastography. *Epilepsia* **55**(4), e30-33.

**B.2 Presentations with published abstracts**

Chan HW, Uff C, Bamber J, Chakraborty A, Dorward N. Ultrasound elastography superior to MRI for intraoperative identification of epileptogenic foci. Oral presentation at 2015 Spring Meeting of the Society of British Neurological Surgeons jointly with, as invited guests, the German Society of Neurosurgery (DGNC – Deutsche Gesellschaft für Neurochirurgie), April 22-24, 2015. (Winner for best oral presentation).

[from work described in Chapter 7]

Chan HW. Reliability of quantitative elastography. Invited talk at 46<sup>th</sup> Annual Scientific Meeting of the British Medical Ultrasound Society, Manchester, UK, December 9-11, 2014.

[from work described in Chapters 4, 5 & 6]

Chan HW, Uff C, Chakraborty A, Dorward N, Bamber JC. Investigating the effect of pia on the young's modulus measurements of grey and white matter in *ex vivo* porcine brains using shear wave elastography. Oral presentation at Thirteenth International Tissue Elasticity Conference, Utah, USA, September 7-10, 2014.

[from work described in Chapter 6]

Chan HW, Uff C, Chakraborty A, Dorward N, Bamber JC. Detecting MRI-negative epileptogenic lesions with intra-operative shear wave elastography. Oral presentation at Thirteenth International Tissue Elasticity Conference, Utah, USA, September 7-10, 2014.

[from work described in Chapter 7]

Chan HW, Li J, Cummings C, Sinkus R, Uff C, Chakraborty A, Dorward N, Robinson S, Jamin Y, Bamber JC. Cross-validation of elasticity imaging using magnetic resonance elastography and ultrasound shear wave elastography in post-mortem mouse brains. Oral presentation at Twelfth International Tissue Elasticity Conference, Surrey, UK, October 1-4, 2013.

[from work described in Chapter 4]

Chan HW, Uff C, Chakraborty A, Bamber J, Dorward N, Harkness W. Guiding tumour resection with intra-operative ultrasound augmented by shear wave elastography: Preliminary results. Oral presentation at Fifteenth World Federation of Neurosurgical Societies' World Congress of Neurological Surgery, Seoul, South Korea, September 8-13, 2013.

[from work described in Chapter 8]

Chan HW, Uff C, Chakraborty A, Bamber J, Dorward N, Harkness W. Visualising epileptogenic zones in children with intra-operative shear wave elastography. Oral presentation at Fifteenth World Federation of Neurosurgical Societies' World Congress of Neurological Surgery, Seoul, South Korea, September 8-13, 2013.

[from work described in Chapter 7]

Chan HW, Chakraborty A, Uff CE, Dorward NL, Bamber JC, Harkness W. A novel technique of detecting magnetic resonance imaging (MRI)-negative epileptogenic lesions in focal symptomatic epilepsy: A case report using intraoperative shear wave elastography. Oral presentation at Eleventh International Tissue Elasticity Conference, Deauville, France, October 2-5, 2012.

[from work described in Chapter 7]

Chan HW, Chakraborty A, Dorward NL, Bamber JC, Harkness W. Shear wave elastography of pediatric epileptogenic tumors: preliminary results. Oral presentation at Eleventh International Tissue Elasticity Conference, Deauville, France, October 2-5, 2012.

[from work described in Chapter 7]

### **B.3 Book Chapter**

Chan HW, Bamber J, Dorward N, Chakraborty A, Uff C. Ultrasound Elastography. In: Prada F, Solbiati L, Martegani A, DiMeco F eds. *Intraoperative Ultrasound (IOUS) in Neurosurgery: From Standard B-mode to Elastosonography*. Springer International Publishing, pp. 173-187.

## Appendix C

# Guide to setting up Supersonic Aixplorer® for intraoperative shear wave elastography in neurosurgery

This appendix is created as a guide for any neurosurgeons who wish to set up the Supersonic Aixplorer® scanner for intraoperative use. The step-by-step guide below is replicated from Chapter 3. The figures referred here can be found in Chapter 3. The sequence for setting up the scanner is as follows:

1. Turn on the scanner in the top left hand corner next to the speaker.
2. Press the ‘PROBE’ button situated leftmost on the second row. This will allow you select the preset configuration for the probe.
3. Press on the ‘PATIENT’ button situated on the right of the probe button. This will allow you to enter the patient details.
4. This step is performed after the transducer is draped with sterile sheath and the first scan is about to be acquired. The focus and the depth of the scan can be adjusted with the 2 rightmost grey knobs ‘FOCUS’ and ‘DEPTH’, respectively. To obtain an optimal sonogram, the focus needs to be deeper than the area of interest (see Figure 3.19). When the surgeon places the draped transducer on the brain, press the ‘AUTO TGC’ button, which is the fourth button from the bottom on the right. This will allow the sonogram image to be automatically optimised for acoustic

attenuation in the tissue. This allows better visualisation of the structures on sonogram but does not affect the SWE mode.

5. Press the ‘SWE’ orange knob, which is the third knob from the left. This will change the display from a single image to 2 images. The top image is the elastogram superimposed on the sonogram while the bottom image is solely the sonogram. Ensure that the SWE gain is set to 70%, which is the preset value (see Figure 3.19). But if it is not, then set it to 70% by turning the ‘SWE’ orange knob clockwise or counter-clockwise to increase or decrease the gain, respectively. SWE gain is the threshold mask, which determines whether the SWE signal is displayed on the screen (according to its quality). If the SWE gain is set at 100%, then the threshold mask is set at its lowest, thus allowing even very noisy SWE signal to be displayed. This implies that the SWE estimates are not reliable. If the SWE gain is set at 0%, then the threshold mask is set at its highest, thus potentially not displaying any SWE signal. The manufacturer recommended SWE gain at 70%, which is the optimal setting to use. Changing the setting could result in unwanted artefacts as shown in Chapter 6.

When acquiring the SWE images, the surgeon needs to place the transducer lightly on the brain as pressure on the brain can cause artefactually high Young’s modulus, as shown in this thesis. However, if the region of interest is deeper than about 7 mm, these artefacts are no longer significant. Another consideration when performing the scan is to hold the transducer still for about 3 seconds to allow the generation and stabilisation of the SWE signal.

When the region of interest is deeper (from the brain surface) than 2 cm, the SWE mode should be set to ‘PEN’ to allow maximal SWE signal, by turning the leftmost grey knob situated just beneath the display clockwise (see Figure 3.20).

6. As the normal brain Young’s modulus is around 30 kPa, as shown in Uff (2011) and in this thesis, and the range for lesions is 3 kPa to 300 kPa, the SWE scale should be set at 0 to 70 kPa (see Figure 3.19) by turning the grey knob on the rightmost

- situated just beneath the screen (see Figure 3.20). With this scale, the normal brain should appear as cyan in colour.
7. The region-of-interest (ROI) box, which is rectangular, is adjusted to the maximum to the allow largest possible elasticity map (see Figure 3.19). This can be adjusted by swiping your finger clockwise on the grey ring circling the trackball. The ROI box can be placed at the desired location by using the trackball.
  8. To capture the desired image, press the 'FREEZE' button first, which is situated in the bottom right hand side. Then, using the trackball, you can select the frame(s) you want to save. To save, press the 'SAVE IMAGE' button situated above the 'FREEZE' button.
  9. If a video clip is required, then press 'SAVE CLIP' button situated on the bottom left above the arrow button. This needs to be pressed before acquiring the clip.
  10. Once the images are saved, Young's modulus measurement can be performed. To perform measurements in the same sitting as image acquisition, simply press the 'REVIEW' button, the second button on the second row on the right, and select the image you want to analyse. Press 'MEAS.' button left of the grey ring will display a Q-box (see Figure 3.19). Q-box is a circle that can be placed anywhere within the ROI to give the mean, minimum, maximum, and standard deviation of the Young's modulus measurement and the diameter of the Q-box. Press the 'SELECT' button situated just on top of the grey ring, to fix the placement of the Q-box. To obtain another Q-box, simply press the 'MEAS.' button once again and repeat the process above. A maximum of four Q-box measurements can be displayed at one time. After four Q-box's, the fifth Q-box measurement will replace the first Q-box measurement on the display. Therefore, it is advised to save the image and then

reselect the image using the 'PREVIEW' button to start measurements of new regions.

To make measurements in a later setting, press the 'PREVIEW' button and select the image set required. Press 'CONTINUE' on the touch screen display to allow Q-box measurements and saving of images.

11. Once the scan acquisition is finished, simply press the 'END EXAM.' button, the third button from the left on the second row, and the images including the Q-box measurements will be saved.